Cooperative Vehicle Control, Feature Tracking and Ocean Sampling

Edward A. Fiorelli

A Dissertation

Presented to the Faculty

of Princeton University

in Candidacy for the Degree

of Doctor of Philosophy

Recommended for Acceptance

by the Department of

Mechanical & Aerospace Engineering

November, 2005

Abstract

This dissertation concerns the development of a feedback control framework for coordinating multiple, sensor-equipped, autonomous vehicles into mobile sensing arrays to perform adaptive sampling of observed fields. The use of feedback is central; it maintains the array, i.e. regulates formation position, orientation, and shape, and directs the array to perform its sampling mission in response to measurements taken by each vehicle. Specifically, we address how to perform autonomous gradient tracking and feature detection in an unknown field such as temperature or salinity in the ocean.

Artificial potentials and *virtual bodies* are used to coordinate the autonomous vehicles, modelled as point masses (with unit mass). The virtual bodies consist of linked, moving reference points called *virtual leaders*. Artificial potentials couple the dynamics of the vehicles and the virtual bodies. The dynamics of the virtual body are then prescribed allowing the virtual body, and thus the vehicle group, to perform maneuvers that include translation, rotation and contraction/expansion, while ensuring that the formation error remains bounded. This methodology is called the Virtual Body and Artificial Potential (VBAP) methodology.

We then propose how to utilize these arrays to perform autonomous gradient climbing and front tracking in the presence of both correlated and uncorrelated noise. We implement various techniques for estimation of gradients (first-order and higher), including finite differencing, least squares error minimization, averaging, and Kalman filtering. Furthermore, we illustrate how the estimation error can be used to optimally choose the formation size.

To complement our theoretical work, we present an account of sea trials performed with a fleet of autonomous underwater gliders in Monterey Bay during the Autonomous Ocean Sampling Network (AOSN) II project in August 2003. During these trials, Slocum

autonomous underwater gliders were coordinated into triangle formations, and various orientation schemes and inter-vehicle spacing sequences were explored. The VBAP methodology, modified for implementation on Slocum underwater gliders, was utilized. Various operational issues such as speed constraints, external currents, communication constraints, asynchronous surfacings and intermittent feedback were addressed.

for Diane

"She'll be the one,

when the party's over."

Acknowledgements

The work presented herein would not exist without Professor Naomi Ehrich Leonard, my advisor, to whom I am forever grateful for her unending patience, support, and inspiration. She has been a source of invaluable insight and assistance in my dissertation work and it has been a great privilege and honor to work with her.

I've had the pleasure of meeting countless talented individuals while at Princeton. My fellow students at Princeton University, namely, Pradeep Bhatta, Erik Christiansen, Josh Graver, Juan Melli, Ben Nabet, Sujit Nair, Derek Paley, Troy Smith, and Craig Woolsey have been great friends. I would especially like to thank Pradeep for his contributions to our work for the Autonomous Ocean Sampling Network II (AOSN II) project and for providing assistance whenever needed. I am indebted to Petter Ögren for his contributions and collaboration in my research on cooperative vehicle control and adaptive sampling, specifically on the Virtual Body and Artificial Potentials methodology and least squares estimation. I also cannot thank Francois Lekien enough for his participation in countless discussions and always being there to straighten out my thinking when it had gone awry. You truly were selfless with your time, and I value our friendship as much as our technical collaboration. I would like to thank Fumin Zhang for providing technical expertise whenever called upon. Furthermore, I would like to thank my buddies Ron Bennington and Fez Whatley for the laughs, and always being there one way or another.

I would like to thank Dr. David Fratantoni of the Woods Hole Oceanographic Institution for his assistance and use of his Slocum underwater gliders.

I would like to acknowledge my dissertation readers Professor Clancy Rowley and Professor Ralf Bachmayer. Their comments have improved this thesis considerably and I appreciate their time and insight. I would also like to thank my graduate committee, Professor

Phil Holmes and Professor Rob Stengel.

Finally, I thank my family for their love, understanding, and persistent encouragement. My parents, Edward and Maria Fiorelli, and my sisters, Donna and Priscilla, have always been a great source of inspiration. Most of all I thank my wife Diane, I don't think I would have gotten very far without you.

Contents

1 Introduction **1**

2 Coordinated Control: Virtual Bodies and Artificial Potentials **13**

2.1 Formation Framework 15

2.2 Potentials to Regulate Relative Distance 18

2.2.1 Vehicle-to-Vehicle Interaction 18

2.2.2 Vehicle-to-Virtual Leader Interaction 21

2.2.3 Formation Design with Distance Regulation 22

2.3 Potentials to Regulate Relative Orientation 35

2.3.1 Planar Formations. 36

2.3.2 Formations in $\mathbb{R}^3$. 39

2.4 Potentials to Regulate Relative Position 41

2.5 Formation Stability 42

3 Dynamic Formations **46**

3.1 Formation Trajectories 47

3.1.1 Translation and Rotation 48

3.1.2 Expansion and Contraction 48

3.1.3 Deformation 49
3.1.4 Deformation and Expansion/Contraction Alternative 50
3.1.5 Sensor Driven Trajectories 50
3.2 Formation Speed 52
3.3 Simulation: Formation Translation and Rotation 54

4 Adaptive Sampling with Vehicle Arrays 60
4.1 Adaptive Ocean Sampling with Multiple AUVs 61
4.1.1 Sampling Objectives 64
4.1.2 Problem Domain 67
4.2 Derivative Estimation from Distributed Measurements 70
4.2.1 Finite Differencing 70
4.2.2 Least-Squares Approximation 75
4.2.3 Gradient-of-the-Average Approximation 80
4.3 Discrete-Time Kalman Filter for Mean Field Estimation 84
4.4 Gradient Climbing and Feature Tracking 93
4.4.1 Gradient Climbing 93
4.4.2 Front Tracking 97

5 Cooperative Control of Autonomous Underwater Glider Fleets 102
5.1 The Autonomous Underwater Glider 103
5.2 VBAP and Coordinating Slocum Gliders at AOSN II 107
5.2.1 VBAP with a Constant Speed Constraint 109
5.2.2 External Currents 115
5.2.3 Intermittent Feedback 118

5.2.4 Latency . . . 118
5.2.5 Surfacing Asynchronicity . . . 119
5.3 AOSN II VBAP Operational Summary . . . 121
5.4 Simulations . . . 124
5.4.1 Truth and Model fields . . . 125
5.4.2 Setup and Results . . . 127

6 Sea Trials: AOSN II, Monterey Bay Summer 2003 **134**
6.1 Brief Review of Operations during AOSN II . . . 135
6.2 Discussion of Metrics . . . 137
6.3 August 6, 2003: Glider Formation at Upwelling Event . . . 140
6.4 August 16, 2003: Multi-Asset Demonstration . . . 147

7 Summary and Future Work **157**
7.1 Summary . . . 157
7.2 Future Work . . . 160

A Proof of Theorem 3.2.1 [64] **163**

B Kalman Filter Derivation **165**

C Glider Simulator Details **168**

D Virtual Body Steering for Cross Track Error Reduction **171**

References **174**

List of Figures

1.1 Robotic Vehicles with Fully Autonomous Capability Available Today. . . . 2

2.1.1 Notation for Framework. 16

2.2.1 Vehicle-to-Vehicle Interaction Potentials. 19

2.2.2 Bump Function. 20

2.2.3 Vehicle-to-Virtual Leader Interaction Potentials. 21

2.2.4 Single Virtual Leader Equilibrium Formations for Example 2.2.2. 25

2.2.5 Perturbation from Equilibrium Formation. 29

2.2.6 Double Virtual Leader Equilibrium Formations for Example 2.2.3. 30

2.2.7 Equilibria Formations in $\mathbb{R}^3$. 32

2.2.8 Hexagonal Lattice. 33

2.2.9 Hexagonal Lattice with Virtual Leader. 34

2.2.10 V-formation from Hexagonal Lattice. 35

2.3.1 Defining Relative Orientation. 36

2.3.2 Potentials Regulating Orientation in the Plane. 38

2.3.3 Potentials Regulating Orientation in $\mathbb{R}^3$. 41

2.4.1 Potentials Regulating Relative Position. 42

3.3.1 Formation Rotation. 56

3.3.2 Simulation Trajectories. 58

3.3.3 Formation Error Function 59

3.3.4 Virtual Body Dynamics. 59

4.1.1 Front Definition. 68

4.2.1 Effects of Nonzero Covariance on Optimal Vehicle Separation. 73

4.2.2 The Ω Disc. 81

4.3.1 Past and Previous Formations. 85

4.3.2 Kalman Filtering for Mean Field Estimation Simulation. 91

4.3.3 Kalman Filtering Results. 92

4.4.1 Projected Gradient Descent. 94

4.4.2 Simulated Mean Field, Gaussian Noise and Formation Trajectories. 95

4.4.3 Gradient Estimates. 96

4.4.4 Front Tracking Simulation. 99

4.4.5 Thermal Front Parameter Estimate and Correct Heading Histogram. 100

5.1.1 Webb Research Corporation Slocum glider. 104

5.1.2 AOSN II VBAP Communication Summary. 106

5.2.1 Virtual Body Direction in Response to Current. 117

5.2.2 Planning Scenarios. 122

5.3.1 AOSN II VBAP Operational Scenario. 123

5.4.1 Sea Surface Temperature (SST) in Monterey Bay. 126

5.4.2 ICON Depth Averaged Current Vector Field, Monterey Bay, August 17, 2000 16:00 local time. 127

5.4.3 Coordinated Glider Simulations. 130

5.4.4 Simulated Glider SST Profiles. 131

5.4.5 Inter-Vehicle Spacing Error. 132

6.1.1 Autonomous Glider Tracks in Monterey Bay During AOSN II. 136

6.3.1 Satellite Sea Surface Temperature (degrees Celsius) in Monterey Bay for August 6, 2003 19:02 UTC. 141

6.3.2 Glider Trajectories, Formation Snapshots, and Virtual Body Trajectory for August 6 Demonstration. 142

6.3.3 VBAP and Glider Trajectories for August 6 Demonstration. 143

6.3.4 Virtual Leader Tracking Error for August 6 Demonstration. 144

6.3.5 Formation Centroid Error ϵ vs. Time for August 6 Demonstration. 145

6.3.6 Magnitude of Inter-Glider Distance Error vs. Time for August 6 Demonstration. 146

6.3.7 Magnitude of Orientation Error vs Time for August 6 Demonstration. . . . 147

6.3.8 Glider Formation and Negative of the Least-Square Gradient Estimates for August 6 Demonstration. 148

6.4.1 August 16 Demonstration. 149

6.4.2 Glider Formation Snapshots for August 16 Demonstration. 150

6.4.3 Glider Trajectories for August 16 Demonstration. 151

6.4.4 Virtual Leader Trajectories for August 16 Demonstration. 152

6.4.5 VBAP and Glider Trajectories for August 16 Demonstration. 153

6.4.6 Virtual Leader Tracking Error for August 16 Demonstration. 154

6.4.7 Formation Centroid Error ϵ vs. Time for August 16 Demonstration. 154

6.4.8 Alternate Formation Centroid Error ε' vs. Time for August 16 Demonstration. 155

6.4.9 Magnitude of Inter-Glider Distance Error vs. Time for August 16 Demonstration. 155

6.4.10 Magnitude of Orientation Error vs Time for August 16 Demonstration. . . 156

D.1 Cross Track Error Diagram. 172

Chapter 1

Introduction

For some time now, it has been recognized that mobile autonomous robots have the potential to perform a multitude of tasks which may be impractical, costly, dangerous, or just too mundane for humans. For example, the Woods Hole Autonomous Benthic Explorer (ABE) is an autonomous underwater vehicle (AUV), see Figure 1.1, designed to monitor the deep ocean over long periods of time. ABE can survey bottom environments at depths of 5000 meters with a variety of sensors and tools, and has been used to study geothermal vent formations, a dangerous environment where hot lava is expelled at the intersection of tectonic plates [16].

Today, mobile autonomous robots that operate on land, in sea, and in the air are available for military and commercial applications, see Figure 1.1. However their autonomous capabilities are often relegated to navigation and low-level control functions, e.g. keeping the autonomous aircraft aloft. A human is often in the loop making high-level control decisions to direct the vehicle in completing its tasks. A critical challenge for automating high-level control is translating the task requirements and the current state of the vehicle into a metric from which the vehicle can correctly decide how to respond.

Figure 1.1: **Robotic Vehicles with Fully Autonomous Capability Available Today.** Top left: Woods Hole Oceanographic Institution's ABE vehicle studies the deep sea. Top right: Silver Arrow Hermes 450 unmanned air vehicle (UAV) performs military and homeland security operations. Bottom left: Autonomous Solutions' Gator unmanned ground vehicle (UGV) is at home on the farm. Bottom right: Webb Research's Slocum Glider autonomous underwater vehicle (AUV) has been successfully deployed in large-scale oceanographic survey operations.

With the apparent utility of a single mobile autonomous robot, it is natural to question what gains can result by using multiple robots cooperatively. There are a number of tasks a single robot or vehicle cannot effectively perform. For example, for meteorological or oceanographic surveys where vehicles equipped with sensors serve as mobile sensor platforms, the spatial and temporal scales present in the field of interest may be too dynamic for a single vehicle to provide adequate sampling. Cooperating vehicles can serve as a mobile sensor array that can change as needed in response to changing dynamics. Another example is multiple vehicles serving in a communication relay; numerous vehicles may be necessary to provide adequate range. In addition to expanded capabilities, utilizing multiple vehicles may provide robustness against mission failures should a component or vehicle fail.

The work presented in this thesis focuses on developing a control framework for coordinating groups of autonomous robots into mobile sensor arrays to perform adaptive sampling of observed fields. In particular we derive control laws that not only coordinate the vehicles into useful formations but use the acquired spatially distributed measurements to direct the array in gradient tracking and feature detection in an unknown field. The use of feedback is central to both objectives. Feedback is used to maintain the array, i.e. regulate formation position, orientation, and shape, and to direct the dynamics of the array to perform its mission.

Our goals can be listed as follows:

1. Develop an approach which provides a systematic procedure for generating provably stable control laws to coordinate multiple agents using local, relatively simple agent interactions. A main focus is on multiple *vehicle* systems.

2. Derive control laws that exploit the capabilities of multiple vehicles to serve in mobile and reconfigurable sensor arrays. These arrays adapt in response to the local measurements taken by the constituent vehicles to perform tasks such as gradient climbing and feature tracking.

3. Demonstrate coordinated fleets of autonomous underwater gliders at sea given real-world implementation constraints.

Our approach to coordinated control relies on *artificial potentials* and *virtual bodies* to coordinate groups of vehicles modelled as point masses (with unit mass). The virtual body consists of linked, moving reference points called *virtual leaders*. Artificial potentials couple the dynamics of the vehicles and the virtual body by regulating desired vehicle-to-vehicle spacing and vehicle-to-virtual-leader spacing. Potentials can also be designed to enforce a

desired orientation of vehicle position relative to a fixed frame attached to a virtual leader. The stabilizing control law for each vehicle is simply the negative gradient of the sum of artificial potentials with an additional dissipative term. The gradient is taken with respect to the vehicle's configuration; for a point mass the configuration is its position. The work is developed for particles each in $\mathbb{R}^3$ with some results specialized to $\mathbb{R}^2$.

With artificial potentials in place to stabilize the vehicles about the virtual body, the dynamics of the virtual body are then prescribed as part of the multi-vehicle control design problem. Indeed we parameterize the virtual body dynamics in such a way as to permit a decoupling of the formation stabilization and the formation maneuver/mission control subproblems. The methodology allows the virtual body, and thus the vehicle group, to perform maneuvers that include translation, rotation and contraction/expansion, all the while ensuring that the formation error remains bounded. In the case that the vehicles are equipped with sensors to measure the environment, the maneuvers can be driven by measurement-based estimates of the environment. This permits the vehicle group to perform as an adaptable sensor array.

The use of artificial potentials is inspired in part by biologists who study animal aggregations. These biologists have proposed that animals use simple traffic rules at the individual level to regulate spacing, alignment, and speed relative to their local neighbors, and these yield structure at the level of the aggregate [66, 37, 69, 19]. From these local actions emerge complicated group-level behaviors that increase the group's effectiveness in performing a variety of tasks such as foraging and predator avoidance. In the seminal work of Reynolds [74], simulated flocks using rules motivated from biology are observed performing remarkable maneuvers. This work has inspired many control theorists and roboticists to further explore coordination with only local level interactions.

Our artificial potentials are designed to emulate the social forces described by the biologists. Much like animals in a flock or herd, vehicles attempt to maintain specified distances from neighboring vehicles and virtual leaders. Models for the traffic rules that govern fish schools and animal groups found in the literature provide motivation for control synthesis. The methodology presented herein has the following desirable features:

- No specific ordering or numbering of the vehicles is required.
- Vehicular control laws which rely only on local interactions are possible.
- Controller design for formation shape regulation is decoupled from the design of the controller that regulates formation maneuvers.
- Stability of the formation is automatic from the construction.

A principal motivating application of coordinated autonomous vehicles is adaptive ocean sampling. The central theme of our adaptive sampling strategies is the use of feedback that integrates distributed in-situ measurements into our coordinated control methodology to affect sampling paths and formation patterns. For example, observations of environmental fields relevant to ocean science such as temperature, salinity, and bioluminescence, are collected by individual members of the sensor array and used to compute gradients and directions of maximum gradient variation. This is done not only to direct the network to fronts and features of interest but also to dictate how the network should respond while sampling along and about them. For example, we enable adaptive sensing resolution by way of formation expansion (or contraction) in response to flat, i.e. mostly constant, (or steep) measurements from the network. We also present filtering and averaging techniques for use with vehicle networks, e.g. least square estimates, discrete averaging, or Kalman filtering, to reduce the influence of noise and improve estimates.

Autonomous sampling networks provide an exciting opportunity with numerous important applications. In the ocean, these opportunities are enabled by autonomous underwater vehicles (AUVs). The Autonomous Ocean Sampling Network II (AOSN II) project [2] was devised to build a coupled observation/prediction system where ocean models would assimilate observations made by AUVs. The goal is to improve the models' skill at providing estimates and predictions of physical variables such as temperature and salinity, and biochemical signatures such as chlorophyll. Our contributions to the AOSN paradigm, described in this thesis, include demonstrating (1) how AUVs can be controlled as coherent arrays in a dynamic ocean environment and (2) how formations of AUVs serving in mobile sensor arrays can improve sampling of local features, e.g. by detecting and tracking the associated frontal boundaries and biological plumes. In August 2003 the first experimental component of AOSN II was performed in Monterey Bay, CA with the deployment of 12 Webb Slocum autonomous underwater gliders and 5 Scripps Spray gliders. Autonomous underwater gliders are a class of energy efficient AUVs designed for continuous, long-term deployment.

A goal of the month-long experiment was to study the physical and biochemical response to upwelling events. During an upwelling event cold, nutrient-rich water rises to the surface leading to increased biological activity in the vicinity of the upwelled water. In Monterey Bay, onset of upwelling events are marked by cold water appearing at the surface at the northern mouth of the bay which proceeds to spread south closing off the bay.

A major objective of our participation in the AOSN II experiment in summer 2003 was to demonstrate and evaluate coordinated AUV arrays in the ocean. To this effect we developed from our coordinated control theory, a methodology specific to underwater gliders with a number of operational constraints. For example, our approach had to be a plug-in solution

given a currently existing glider command structure. We also addressed issues related to glider control and actuation in the presence of external currents, planning and information latencies, and asynchronicities in communication. We performed several demonstrations at sea in Monterey Bay in August 2003. In this thesis we describe the implementation and evaluate the performance of coordinated glider formations using this methodology.

The earliest work regarding coordination of mobile robots dates back to the mid-to-late 1960s involving the study of one-dimensional strings of inter-connected vehicles [53, 70, 57]. Interestingly, many authors posed the problem in an optimal control framework citing the historic, and then recent, work of Kalman. The purpose of this work was to devise controllers which regulated inter-vehicle spacing and attenuated propagating disturbances along the string. Work on vehicle strings continued into the 1970s.

During the 1980s work on coordination in higher dimensions began to appear. In literature reviews, Erdmann [26] and Tournassoud [93] point out several concurrent lines of work on multiple movable objects. The first direction was taken by roboticists who sought optimal paths and both linear and non-linear controllers for multiple robotic arms [3, 76]. A second direction was taken by the computer science and artificial intelligence (AI) community where algorithms were devised to move multiple movable disks or polygonal objects from an initial configuration to a final configuration in bounded regions [80, 72]. This work is an extension of the classic "Piano Movers" problem. In [72], for example, the configuration space of multiple disks in a cluttered environment is transformed into a graph and searching for collision-free path is reduced to a graph-searching problem. In a third direction, the multiple moving object problem is decomposed into two subproblems [26]. First, paths which avoid collisions with static objects are planned for each movable object one at a time. Then the speed of each moving object along these trajectories is adjusted to avoid

collisions.

In 1989, Wang [96] took a more dynamical systems perspective by treating the robots as dynamic, interacting particles. Wang proposed using repulsive potentials between vehicles to avoid collisions and an attracting force directed towards static destinations, which although not explicitly stated, can be also be derived from a potential. Wang also introduces a vehicle's "cone of visibility" in which neighboring vehicles must lie to be sensed. Wang did not however consider attracting potentials between vehicles.

In the 1990s, the AI community proposed explicit behavior-based methodologies [55, 9, 5]. Here, each robot derives its control from a weighted average of behaviors, e.g. maintain formation, move towards goal, avoid obstacles, etc. We note that the work of Wang can also be described as behavior based. In [55, 10] learning was also implemented where the behavior weights would be adjusted based on the success of past actions and the present state of the vehicle and its environment. Artificial potentials were proposed for coordinated control in [98, 56] where control laws for agents were explicitly derived from the gradients of potentials. Work on multiple manipulators continued and was extended to consider moving manipulators [42, 23, 91]. Leader-follower algorithms where vehicles are divided into two sets: leaders and followers, were proposed in [97, 24]. Often in this setting the leaders are given pre-planned missions and the focus of study is on stabilizing control laws for the followers. Virtual structures, entities similar to our virtual bodies, were used in [89, 12]. Their construction differs from ours in that the virtual structure is a rigid template whose position and orientation is redefined at each iteration to best fit the current vehicle configuration. Our virtual body has continuous dynamics and evolves as a function of formation error.

From the late 1990s to the present research on coordinated multi-agent systems has

expanded drawing from graph theory [88, 29, 27, 68], hybrid control [30], and real-time optimization theory [25], among others. In Young et al [101] translation, rotation and expansion of a group is treated using a virtual structure which has dynamics dependent on a formation error function. Although similar in spirit to the work in this thesis, the formation control laws and the dynamics of the virtual structure differ from those presented here, and an ordering of vehicles is imposed. In Ögren et al [63] control Lyapunov functions are used for multi-agent coordination where vehicles track reference points similar to our virtual leaders. However, these reference points follow predefined trajectories. This theory was extended in [65] with the introduction of the virtual body and dynamic virtual body trajectories which enable missions such as gradient climbing.

Artificial potentials play an important role in our construction. In robotics, they have been extensively used to produce feedback control laws [41, 43, 75, 73] for avoidance of stationary obstacles as well as obstacles in motion [60] and have been used in motion planning [11]. In the modelling of animal aggregations, forces that derive from potentials are used to define local interactions between individuals (see [66] and references therein). In more recent work along these lines, the authors of [35, 90, 58] investigate swarm stability under various potential function profiles. Artificial potentials have also been exploited to derive control laws for autonomous, multi-agent, robotic systems [98]. In [56, 51, 67] convergence proofs to desired configurations are explicitly provided.

Lately, research on the subject of sampling using autonomous vehicle groups has been drawing much attention. In particular, gradient climbing with a vehicle network is a topic of growing interest in the literature (see, for example, [8, 35]). In [54] gradient climbing is performed in the context of distributing vehicle networks about environmental boundaries. In [18], the authors use Voronoi diagrams and *a priori* information about an environment

to design control laws for a vehicle network to optimize sensor coverage in, e.g. surveillance applications.

Coordinated AUV fleets have also been a topic of recent research. In 2004, the IEEE AUV 2004 workshop was dedicated to multi-AUV coordination; our contribution can be found in [32]. In the literature, one paper of note by Curtin et al in 1993 [20] presents a vision of how AUVs would participate in AOSNs and would later lead to AOSN II initiated in 2002 [31]. Recent theoretical work on coordinating constellations of AUVs can be found in [38] where linear control is used in conjunction with a derived formation error. In [6] a more practical leader-follower algorithm is introduced to induce coordination using local acoustic ranging from the leader, acoustic communication and Kalman filtering. However, there are fewer examples of full-scale, cooperative multiple-AUV demonstrations in the water. One example by Schultz et al is described in [79] where a group of AUVs was used to map salinity distributions.

In Chapters 2 and 3 we present the framework for the Virtual Body and Artificial Potential (VBAP) multi-vehicle control methodology. We first introduce virtual leaders and virtual bodies along with artificial potentials and present control laws which stabilize point-mass formations at rest or those strictly translating. The control law for each vehicle is derived from the gradient of the artificial potentials. We present a variety of artificial potentials and show how they are used to construct stable formations elucidating the role of virtual leaders in symmetry breaking. Hexagonal lattices are presented as an avenue to systematically produce various formation shapes.

In Chapter 3 this methodology is extended to allow the virtual body, and thus vehicle group, to perform maneuvers that include translation, rotation and contraction/expansion,

all the while ensuring that a formation error remains bounded[1] . Stability of the complete closed-loop system is proven using a Lyapunov function that sums the system kinetic and potential energies.

With a framework for coordinating vehicles into dynamic sensor arrays in place, in Chapter 4 we investigate how to use these arrays to achieve the scientific objective of adaptive ocean sampling. We first define the adaptive ocean sampling problem using mobile sensor arrays and motivate the specific sampling problems to be addressed, namely gradient climbing and front tracking. We then define the problem domain in which subsequent analysis will be based. We discuss how to estimate gradients utilizing finite differencing and review least squares gradient estimates using scalar measurements taken by each vehicle. We also discuss how measurement noise and estimates of the field's higher order spatial derivatives can dictate optimum sensor array resolution. We then describe an alternate approach to gradient estimation using the gradient of the average value of the field contained within a closed region. As shown by Uryasev [94], this average can be expressed as a function of the field values along only the boundary of the closed region. We present cases in which this approach is equivalent to a least-squares estimate, elucidating when it can be viewed as an averaging process. Estimation by finite differencing and least-squares optimization are point-wise in time in that they only utilize present information. To further improve these estimates in the presence of noise we develop a Kalman filter that utilizes both past and present information. Lastly we present our gradient climbing and front tracking algorithms and demonstrate their effectiveness through simulation.

The theory presented in Chapters 2 and 3 does not directly address various operational constraints and realities associated with working with real vehicles in the sea. In Chapter 5

[1]This research was conducted jointly with Petter Ögren [65, 64] who is now with the Swedish Defense Research Agency (FOI)

we address a number of these issues in a presentation of our implementation of the VBAP methodology for a fleet of Slocum underwater gliders in Monterey Bay. For example, the control laws are modified to accommodate constant speed constraints consistent with glider motion and to cope with external currents. The implementation also treats underwater gliders which can only track waypoints and can only communicate every few hours while at the surface. To test and refine our methodology prior to sea trials, we performed a series of simulations in realistic settings implementing communication constraints, computational limitations, and constrained vehicle kinematics and dynamics. We simulated an autonomous glider fleet performing cooperative temperature front tracking. Innovative Coastal-Ocean Observation Network (ICON) model data [83] provided current data and the gliders took measurements from aircraft-observed sea surface temperature (SST) data.

Chapter 6 presents and evaluates the coordination demonstrations performed during the AOSN II experiment at Monterey Bay in August 2003. We describe two demonstrations and present an evaluation of the coordination performance. The sea-trials performed on August 6, 2003 and August 16, 2003 demonstrate our ability to coordinate a group of three Slocum underwater gliders into triangle formations. In both cases, we used our VBAP methodology with a single virtual leader serving as the virtual body. We explored various orientation schemes and inter-vehicle spacing sequences as the formation made its way through the bay. The metrics we evaluate relate to virtual body trajectory tracking error, inter-vehicle spacing error, orientation error, and group center of mass tracking error.

Chapter 7 summarizes the major findings and contributions, and suggests directions for future research.

Chapter 2

Coordinated Control: Virtual Bodies and Artificial Potentials

This chapter discusses our multi-vehicle control framework developed to coordinate vehicles into regular formations using *virtual leaders* and *artificial potentials*. Virtual leaders are mobile reference points which provide a mechanism for constructing a vast array of formation shapes and drive formation translations and rotations. Essentially, virtual leaders are implemented to break symmetries, giving us control over the formation's shape, location and orientation with respect to a fixed inertial frame. When linked, virtual leaders constitute a *virtual body*. In this chapter we present vehicle control laws that stabilize a formation with respect to either a fixed virtual body or one moving at a velocity $\boldsymbol{v_0}(t)$ with respect to a fixed inertial frame. In Chapter 3 we discuss how to achieve any combination of formation translation, re-scaling, and rotation by assigning dynamics to the virtual body.

Artificial potentials couple the dynamics of the vehicles and the virtual body by imposing desired vehicle-to-vehicle spacing and vehicle-to-virtual-leader spacing. The forces that derive from the potentials emulate the social forces described by biologists. Much like

animals in a flock or herd, vehicles attempt to maintain specified distances from neighboring vehicles and virtual leaders. Potentials are also designed to enforce a desired orientation of vehicle position relative to a fixed frame attached to a virtual leader. This orientation control between vehicles and virtual leaders is an extension of the biological theme. A key feature of our potentials is that interactions can be limited to finite neighborhoods about each vehicle and virtual leader; thus, long range interactions (atypical in biological groups) can be prohibited. Furthermore, there is no ordering of vehicles required; any vehicle is interchangeable with any other. Lastly, a benefit of using artificial potentials for control design is that they provide a guide for choosing Lyapunov functions. In this chapter we present a variety of artificial potentials useful for constructing and regulating formations.

The artificial potentials are realized by means of the vehicle control actuation; the control law for each vehicle is derived from the gradient of the artificial potentials. We consider fully actuated, double integrator, point mass vehicle models. This model may be simple but it is not without merit. For example, it has been shown for a certain class of non-holonomic wheeled vehicles with differential drive, e.g., when drive wheels can be independently actuated and are located on a single axis, the kinematics of an off-wheel axis point are indeed holonomic [46]. Through feedback linearization, fully actuated double integrator dynamics can be derived for an off-axis point. In Chapter 5 we present how our model was adapted for use in coordinating autonomous underwater gliders at sea. There we specialize to first-order dynamics with vehicle speed constraints.

In Section 2.1 we present our framework in detail and important notation used throughout. In Sections 2.2, 2.3, and 2.4 we present a variety of artificial potentials and show how they are used to construct stable formations elucidating the role of virtual leaders in symmetry breaking. Specifically, in Section 2.2 we present potentials to regulate relative

distances between vehicle pairs and vehicle and virtual leader pairs. We also show how a variety of formation shapes can be constructed using vehicles and virtual leaders in hexagonal lattices. In Section 2.3 we present potentials that only break the rotational symmetry between virtual leaders and vehicles. In Section 2.4 we present potentials that regulate relative position between vehicles and virtual leaders. This chapter concludes with Section 2.5 in which we discuss stability for general formations using the framework presented herein.

2.1 Formation Framework

Let the position of the ith vehicle in a group of N vehicles, with respect to an inertial frame, be given by a vector $\boldsymbol{x}_i \in \mathbb{R}^p, p = 2, 3$, and $i = 1, \ldots, N$ as shown in Figure 2.1.1. Let the corresponding velocity be given by $\boldsymbol{v}_i = \dot{\boldsymbol{x}}_i$. The position of the lth virtual leader with respect to the inertial frame is $\boldsymbol{b}_l \in \mathbb{R}^p$, for $l = 1, \ldots, M$. The virtual leaders are linked and the position vector from the origin of the inertial frame to the center of mass of the virtual body is denoted $\boldsymbol{r} \in \mathbb{R}^p$, where $\boldsymbol{r} = 1/M \sum_{m=1}^{M} \boldsymbol{b}_m$. Let $\boldsymbol{x}_{ij} = \boldsymbol{x}_i - \boldsymbol{x}_j \in \mathbb{R}^p$ and $\boldsymbol{h}_{il} = \boldsymbol{x}_i - \boldsymbol{b}_l \in \mathbb{R}^p$. Finally define the configuration for all vehicles and virtual leaders as $\boldsymbol{X} = (\boldsymbol{x}_1^T, \ldots, \boldsymbol{x}_N^T, \boldsymbol{b}_1^T, \ldots, \boldsymbol{b}_M^T)^T \in \mathbb{R}^{p(N+M)}$. Throughout **bold** characters indicate column vectors and the same variable in normal font refers to its magnitude, for example $x_{ij} = \|\boldsymbol{x}_{ij}\|$. The hat character indicates that a vector has been normalized, e.g. $\hat{\boldsymbol{x}}_{ij} = \frac{\boldsymbol{x}_{ij}}{x_{ij}}$ for $x_{ij} \neq 0$.

The control force on the ith vehicle is given by $\boldsymbol{u}_i \in \mathbb{R}^p$. For now we assume full actuation and the dynamics can be written for $i = 1, \ldots, N$ as

$$\begin{aligned} \dot{\boldsymbol{x}}_i &= \boldsymbol{v}_i \\ \ddot{\boldsymbol{x}}_i &= \boldsymbol{u}_i. \end{aligned} \tag{2.1.1}$$

In Chapter 5 we consider additional forcings arising from ocean currents.

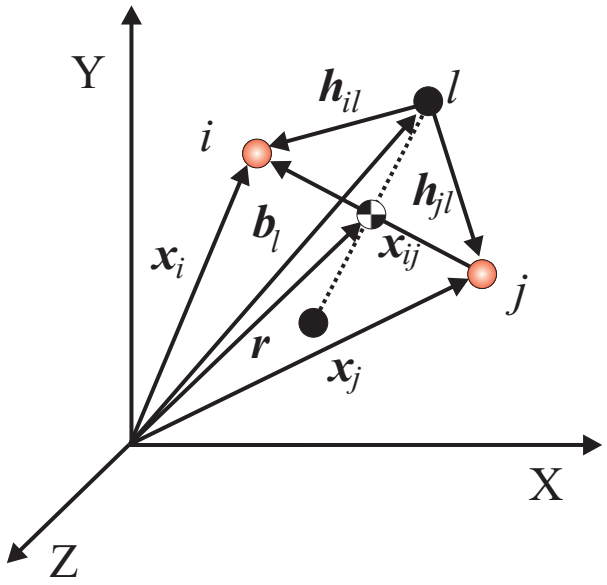

Figure 2.1.1: **Notation for Framework.** Shaded dots are vehicles, solid dots are virtual leaders.

The control force for each vehicle, $\boldsymbol{u}_i$, is the negative gradient of an artificial potential, $V_i : \mathbb{R}^{p(N+M)} \rightarrow \mathbb{R}^+$, with respect to $\boldsymbol{x}_i$ plus an additional control force which is not necessarily derived from a potential, i.e.

$$\boldsymbol{u}_i = -\nabla_{\boldsymbol{x}_i} V_i - \boldsymbol{f}_{\boldsymbol{v}i}. \tag{2.1.2}$$

$\boldsymbol{f}_{\boldsymbol{v}i}$ serves to provide *asymptotic* convergence to the desired formation geometry. The particular functional form of $\boldsymbol{f}_{\boldsymbol{v}i}$ will depend on the virtual body motion prescribed. For example, we will show that for a stationary virtual body, equating $\boldsymbol{f}_{\boldsymbol{v}i} = \dot{\boldsymbol{x}}_i$, i.e. the vehicle's absolute velocity, is sufficient to provide local asymptotic convergence to a desired formation shape. For a virtual body under strict translation, i.e. $\dot{\boldsymbol{r}} = \dot{\boldsymbol{b}}_1 = \ldots = \dot{\boldsymbol{b}}_M = \boldsymbol{v_0}(t), \ddot{\boldsymbol{r}} = \ddot{\boldsymbol{b}}_1 = \ldots = \ddot{\boldsymbol{b}}_M = \dot{\boldsymbol{v}}_{\boldsymbol{0}}(t)$, we can use

$$\boldsymbol{f}_{\boldsymbol{v}i} = \alpha_v(\dot{\boldsymbol{x}}_i - \dot{\boldsymbol{r}}) - \ddot{\boldsymbol{r}}, \tag{2.1.3}$$

where $\alpha_v > 0$ is a constant parameter, to prove asymptotic convergence to the desired formation shape about the translating virtual body.

To establish a systematic procedure for obtaining a desired formation geometry, we define

$$V = \sum_{i=1}^{N} V_i, \tag{2.1.4}$$

and restrict V_i to be of the form

$$V_i = \sum_{j \neq i}^{N} V_I(x_{ij}; \boldsymbol{\mu_I}) + \sum_{l=1}^{M} V_h(\boldsymbol{x}_i, \boldsymbol{b}_l; \boldsymbol{\mu_h}),$$

where

$$V_h(\boldsymbol{x}_i, \boldsymbol{b}_l; \boldsymbol{\mu_h}) = V_h^c(h_{il}; \boldsymbol{\mu_h^c}) + V_h^o(\boldsymbol{x}_i, \boldsymbol{b}_l; \boldsymbol{\mu_h^o}) + V_h^p(\boldsymbol{x}_i, \boldsymbol{b}_l; \boldsymbol{\mu_h^p}).$$

V is designed such that the desired formation is a global minimizer for a prescribed vector $\boldsymbol{\mu}$ of design parameters.

V_I is a potential that defines vehicle-to-vehicle interactions with parameters given by $\boldsymbol{\mu_I}$. It acts to regulate relative distance between vehicle pairs. Likewise, V_h is a potential which defines virtual leader-to-vehicle interactions with parameters given by $\boldsymbol{\mu_h}$. It is comprised of the sum of three potentials V_h^c, V_h^o, and V_h^p. V_h^c is a potential that acts to regulate distance between vehicles and virtual leaders. V_h^o is a potential that acts to regulate the orientation of a vehicle's relative position vector, e.g. $\boldsymbol{h}_{il}$, with respect to a fixed frame attached to a virtual leader. Lastly, V_h^p is a potential that regulates relative position between vehicles and virtual leaders. Common to all potentials is a limited range of effect. Vehicles more than a distance $d_1 > 0$ apart, and virtual leaders and vehicles more than $h_1 > 0$ apart do not interact. An important distinction between these potentials is their role in symmetry breaking and in the next three subsections we further elaborate on their nature and their role in controller design for stable formations.

2.2 Potentials to Regulate Relative Distance

2.2.1 Vehicle-to-Vehicle Interaction

To regulate relative distance between pairs of vehicles i and j, we define an artificial potential $V_I(x_{ij}; \alpha_I, d_0, d_1)$ which is only a function of the relative distance x_{ij} between the ith and jth vehicle. The scalar $d_0 > 0$ specifies the desired inter-vehicle distance. In turn, we design the potential V_I such that it has a global minimum at $x_{ij} = d_0$. The force derived from this potential will be a central force acting along the line connecting the two vehicles. Define $f_I(\boldsymbol{x}_{ij})$ as

$$\begin{aligned} -\nabla_{\boldsymbol{x}_i} V_I &= -f_I(\boldsymbol{x}_{ij})\hat{\boldsymbol{x}}_{ij} \\ &= f_I(\boldsymbol{x}_{ij})\hat{\boldsymbol{x}}_{ji}. \end{aligned}$$

The interaction force regulates relative distance by attracting vehicles that are too far apart and repelling vehicles that are too close together. Furthermore, to aid in formation design we require that the force be zero for vehicles separated by scalar $d_1 > 0, d_1 > d_0$. The scalar α_I is a multiplicative scaling which allows us to adjust the magnitude of gradients.

For example, consider the potential defined for any pair of vehicles i and j given by

$$V_I(x_{ij}; \alpha_I, d_0, d_1) = \begin{cases} \alpha_I \left(\frac{1}{3} x_{ij}^3 - d_0^3 \ln x_{ij} - \frac{1}{3} d_0^3 + d_0^3 \ln d_0 \right) & 0 < x_{ij} \leq d_1 \\ 0 & x_{ij} > d_1 \end{cases} \tag{2.2.1}$$

which is plotted in Figure 2.2.1a. The nonzero component of the force derived from this potential is given by the expression

$$f_I(\boldsymbol{x}_{ij}) = \begin{cases} \nabla_{x_{ij}} V_I & 0 < x_{ij} \leq d_1 \\ 0 & x_{ij} > d_1 \end{cases} \tag{2.2.2}$$

and thus,

$$f_I(\boldsymbol{x}_{ij}) = \begin{cases} \alpha_I(x_{ij}^2 - \frac{d_0^3}{x_{ij}}) & 0 < x_{ij} \leq d_1 \\ 0 & x_{ij} > d_1 \end{cases}$$

where we have explicitly defined the force at $x_{ij} = d_1$ (the discontinuity in V_I). As indicated in Figure 2.2.1a, if $x_{ij} < d_0$ then $f_I(\boldsymbol{x}_{ij}) < 0$ and yields a repelling force between the ith and jth vehicles (since the corresponding control term for the ith vehicle is $-\nabla_{\boldsymbol{x}_i} V_I$). In fact for this particular potential, as $x_{ij} \to 0, f_I(\boldsymbol{x}_{ij}) \to \infty$ which is intended to prevent vehicle-to-vehicle collisions. If $d_0 < x_{ij} \leq d_1$ then $f_I(\boldsymbol{x}_{ij}) > 0$ and yields an attractive force between the ith and jth vehicles. If $x_{ij} > d_1$ then $f_I(\boldsymbol{x}_{ij}) = 0$ and the ith and jth vehicles do not affect each other.

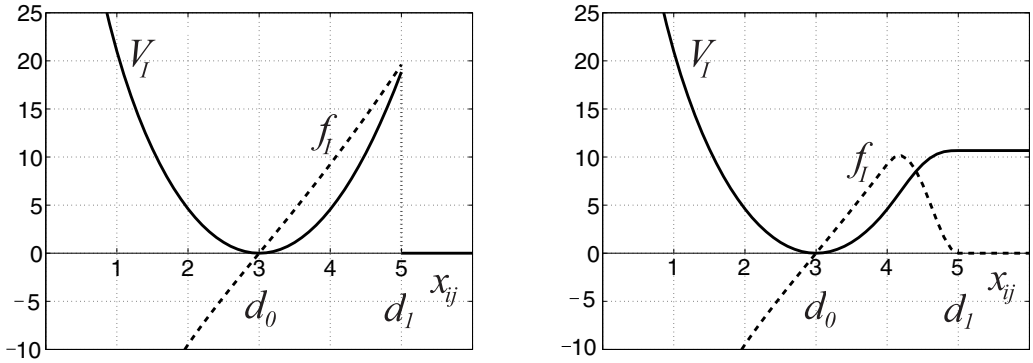

Figure 2.2.1: **Vehicle-to-Vehicle Interaction Potentials.** Solid lines indicate potential profile and dashed lines indicate its gradient. (a) Profile of potential given in (2.2.1) with $\alpha_I = 1, d_0 = 3$, and $d_1 = 5$. (b) Profile of numerically integrated potential whose gradient is given in (2.2.3) with $\alpha_I = 1, d_0 = 3$, $d_1 = 5, a = 4$ and $b = 5$.

This potential is clearly discontinuous at $x_{ij} = d_1$, as is its gradient. This does not create a problem for our immediate purposes in proving local stability of our resulting controllers, i.e. for x_{ij} initially sufficiently close to d_0. However, to avoid the discontinuity at d_1 we can scale the potential by a bump function $\beta(x_{ij}) \in [0, 1]$ so that the resulting potential is at

least C^1. A common example of a C^1 bump function (so named for its shape) is given by

$$\beta(x) = \begin{cases} 1 & x \leq a \\ \sin^2(\frac{\pi}{2}\frac{x-b}{a-b}) & a < x \leq b \\ 0 & x > b \end{cases}$$

where a and b are constants (see Figure 2.2.2).

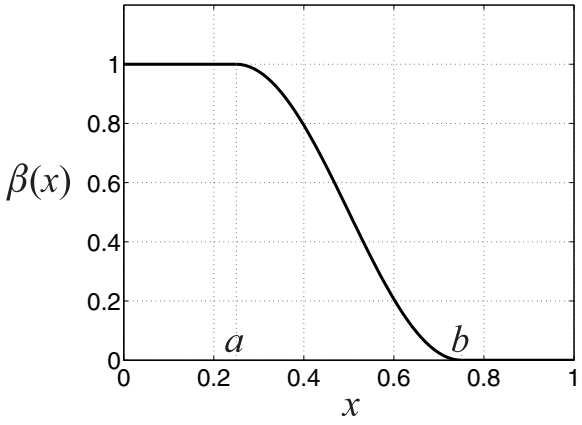

Figure 2.2.2: **Bump Function.**

We now scale f_I by $\beta(x_{ij})$ so as to make the potential C^1. We take $b = d_1$, $a \in (d_0, d_1)$ and define the force to be,

$$f_I = \alpha_I \beta(x_{ij}) \left(x_{ij} - \frac{d_0^2}{x_{ij}} \right), \; x_{ij} > 0. \tag{2.2.3}$$

The potential is then obtained by integrating (2.2.3) with respect to x_{ij}. In this example, no anti-derivative exists due to a $\cos x_{ij}/x_{ij}$ term in the integrand. However, the value of the potential at any x_{ij} (to within an additive constant) can be found by numerical integration. For example, in Figure 2.2.1b we have plotted the continuous f_I and the associated potential obtained by numerical integration.

2.2.2 Vehicle-to-Virtual Leader Interaction

Regulating relative distance between the ith vehicle and lth virtual leader is achieved by using an artificial potential, $V_h^c(h_{il}; \alpha_h^c, h_0, h_1)$. This potential will yield a force similar to the vehicle-to-vehicle interaction force where scalar $h_0 \geq 0$ now specifies the desired vehicle-to-virtual leader distance and $h_1 > 0$ specifies the radius of interaction. The force derived from this potential will be a central force acting along the line connecting the vehicle and virtual leader. Since virtual leaders are only reference points, collisions with vehicles are not a concern and we do allow h_0 to be zero. That is, we permit desired formation geometries where a vehicle may coincide with a virtual leader.

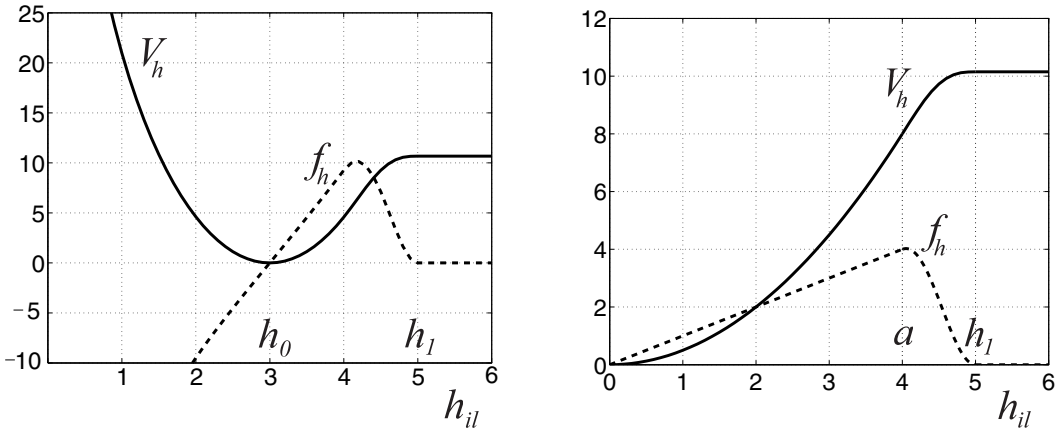

(a) (b)

Figure 2.2.3: **Vehicle-to-Virtual Leader Interaction Potentials.** Solid lines indicate potential profile and dashed lines indicate its gradient. (a) Profile of potential analogous to that given by numerically integrating (2.2.3) with $\alpha_h^c = 1, h_0 = 3$, and $h_1 = 5$. (b) Profile of smooth quadratic potential given in (2.2.4) with $\alpha_h^c = 1, h_0 = 0$, $h_1 = 5, a = 4$ and $b = 5$.

Two virtual leader interaction force profiles are shown in Figure 2.2.3. In the left pane we plot the potential and its gradient analogous to that found in (2.2.3) where x_{ij}, α_I, d_0,

and d_1 are replaced by h_{il}, α_h^c, h_0, and h_1, respectively. That is,

$$f_h^c(\boldsymbol{h}_{il}) = \begin{cases} \nabla_{h_{il}} V_h^c & 0 < h_{il} \leq h_1 \\ 0 & h_{il} > h_1, \end{cases}$$

where $-\nabla_{\boldsymbol{x}_i} V_h^c = -f_h^c(\boldsymbol{h}_{il})\hat{\boldsymbol{h}}_{il}$.

Virtual leaders affect real vehicles in their neighborhood through f_h^c by repelling them if they are at a relative distance, h_{il}, less than h_0 and attracting them if they are at a relative distance greater than h_0 but less than h_1. In the right pane we plot f_h^c for a quadratic potential when h_0 is zero. The force (scaled by β) is given by

$$f_h^c(\boldsymbol{h}_{il}) = \alpha_h^c h_{il} \beta(h_{il}),$$

which is the gradient with respect to $\boldsymbol{x}_i$ in the direction $-\hat{\boldsymbol{h}}_{il}$ of the potential

$$V_h^c(h_{il}) = \begin{cases} \frac{\alpha_h^c}{2}\, h_{il}^2 & h_{il} \leq a \\ \alpha_h^c \left(\frac{h_{il}^2}{4} + \frac{h_{il}}{2\pi}(a - h_1)\sin\gamma - \frac{(a-h_1)^2}{2\pi^2}\cos\gamma + \frac{a^2}{4} - \frac{(a-h_1)^2}{2\pi^2} \right) & a < h_{il} \leq h_1 \\ \frac{\alpha_h^c}{4}\, h_1^2 + \frac{\alpha_h^c}{4} a^2 - \frac{\alpha_h^c}{\pi^2}(a - h_1)^2 & h_{il} > h_1, \end{cases} \tag{2.2.4}$$

where $\gamma = \pi \frac{h_1 - h_{il}}{a - h_1}$.

2.2.3 Formation Design with Distance Regulation

We are now ready to present examples of formation design using only the potentials we have just discussed. The first three examples are simple structures that illustrate the use of our potentials and associated parameters. In the last example we show how we can build upon these simple structures to systematically construct varied formations by utilizing a hexagonal lattice arrangement of vehicles and virtual leaders.

The potentials and resulting control laws presented in Section 2.2.1 and Section 2.2.2 are equally valid in both planar formations and formations in $\mathbb{R}^3$. In this subsection we

provide details for planar formation design and in concluding remarks we briefly touch upon how these results relate to formation design in $\mathbb{R}^3$. The virtual body is fixed in the inertial frame and throughout we take $\boldsymbol{f}_{\boldsymbol{v}_i} = \dot{\boldsymbol{x}}_i$.

Example 2.2.1. Two Vehicles Only

In this example we consider a formation of only two vehicles (and no virtual leaders) which is essentially the classical two body problem [36] with dissipation. The desired formation consists of the vehicles separated by a distance d_0; this can be achieved by introducing a single potential, $V_I(x_{12})$. The resulting dynamics are given by

$$\begin{aligned}
\ddot{\boldsymbol{x}}_1 &= -\nabla_{\boldsymbol{x}_1} V_I(x_{12}) - \boldsymbol{f}_{\boldsymbol{v}1} \\
&= -f_I(x_{12})\hat{\boldsymbol{x}}_{12} - \dot{\boldsymbol{x}}_1 \\
\ddot{\boldsymbol{x}}_2 &= -\nabla_{\boldsymbol{x}_2} V_I(x_{21}) - \boldsymbol{f}_{\boldsymbol{v}2} \\
&= f_I(x_{12})\hat{\boldsymbol{x}}_{12} - \dot{\boldsymbol{x}}_2.
\end{aligned}$$

Assuming $x_{12} \neq 0$ this simple system has equilibria, i.e. $\ddot{\boldsymbol{x}}_i = \dot{\boldsymbol{x}}_i = 0$, when $f_I(x_{12}) = 0$. Using a potential V_I of the form defined in Section 2.2.1 implies either $x_{12} = d_0$ or $x_{12} \geq d_1$. In both instances we have a continuous set of equilibria due to the $SE(2)$ symmetry in the control law; the control law is a function of relative distance only which is invariant under $SE(2)$ actions. To see this, let $(R, c) \in SE(2)$ where $R \in SO(2), \boldsymbol{c} \in \mathbb{R}^2$ and define $\boldsymbol{x'}_i = R\boldsymbol{x}_i + \boldsymbol{c}$. Then $x'_{12} = \|\boldsymbol{x}_1{}' - \boldsymbol{x}_2{}'\| = \|R\boldsymbol{x}_1 - R\boldsymbol{x}_2\| = x_{12}$ since multiplication by an element of $SO(2)$ preserves length.

Given the $SE(2)$ symmetry, we will only examine the dynamics of $\boldsymbol{x}_{12}$. These are

$$\begin{aligned}
\ddot{\boldsymbol{x}}_{12} &= \ddot{\boldsymbol{x}}_1 - \ddot{\boldsymbol{x}}_2 \\
&= -2f_I(x_{12})\hat{\boldsymbol{x}}_{12} - \dot{\boldsymbol{x}}_{12}
\end{aligned}$$

which has an isolated equilibrium at $x_{12} = d_0$. This equilibrium can be proven to be asymptotically stable by use of Lyapunov stability analysis with application of LaSalle's invariance principle. The Lyapunov function is given by $\Phi(\boldsymbol{x}_{12}) = 1/2\|\dot{\boldsymbol{x}}_{12}\|^2 + 2V_I(x_{12})$. A continuous set of neutrally stable equilibria exists for $x_{12} \geq d_1$. Clearly a drawback of vehicle-to-vehicle interaction only is the innability to break the $SE(2)$ symmetry. In the next example we introduce a single virtual leader to break the translational symmetry.

Example 2.2.2. Two Vehicles, One Virtual Leader

In Example 2.2.1 there was an $SE(2)$ symmetry in the control law. In this example we show how virtual leaders are used to break the translational symmetry. Let the virtual leader be stationary and located at the origin of an inertial frame, i.e. $\boldsymbol{b}_1 = \boldsymbol{r} = 0$. The desired formation geometry consists of two vehicles to be separated by a distance d_0 with the formation center of mass located at the origin (see Figure 2.2.4a). Consider three potentials, $V_I(x_{12}), V_h^c(h_{11})$, and $V_h^c(h_{21})$. We choose $h_0 = d_0/2$ and select $d_1 \gg d_0$ and $h_1 \gg d_0$ such that the desired configuration will be a minimum of V_I and V_h^c. The dynamics for each vehicle are written

$$\begin{aligned} \ddot{\boldsymbol{x}}_1 &= -\nabla_{\boldsymbol{x}_1} V_h^c(h_{11}) - \nabla_{\boldsymbol{x}_1} V_I(x_{12}) - \boldsymbol{f}_{\boldsymbol{v}1} \\ &= -f_h^c(h_{11})\hat{\boldsymbol{h}}_{11} - f_I(x_{12})\hat{\boldsymbol{x}}_{12} - \dot{\boldsymbol{x}}_1 \qquad (2.2.5) \\ \ddot{\boldsymbol{x}}_2 &= -\nabla_{\boldsymbol{x}_2} V_h^c(h_{21}) - \nabla_{\boldsymbol{x}_2} V_I(x_{21}) - \boldsymbol{f}_{\boldsymbol{v}2} \\ &= -f_h^c(h_{21})\hat{\boldsymbol{h}}_{21} + f_I(x_{12})\hat{\boldsymbol{x}}_{12} - \dot{\boldsymbol{x}}_2. \qquad (2.2.6) \end{aligned}$$

Equating $\ddot{\boldsymbol{x}}_i = \dot{\boldsymbol{x}}_i = 0$ above we find the condition for equilibria

$$f_h^c(h_{11})\ \hat{\boldsymbol{h}}_{11} = -f_I(x_{12})\ \hat{\boldsymbol{x}}_{12} = -f_h^c(h_{21})\ \hat{\boldsymbol{h}}_{21}. \qquad (2.2.7)$$

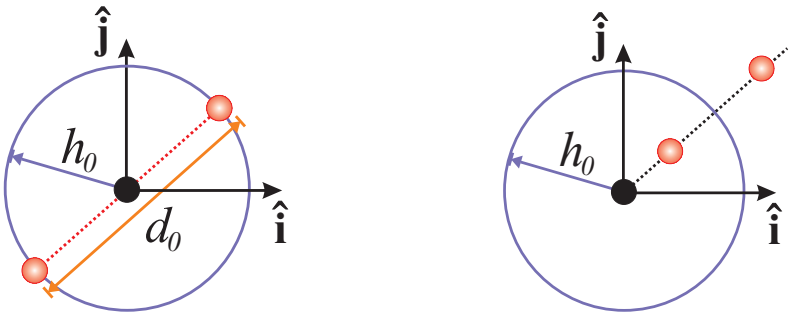

(a) (b)

Figure 2.2.4: **Single Virtual Leader Equilibrium Formations for Example 2.2.2.** Shaded dots are vehicles, solid dots are virtual leaders. (a) Desired vehicle configuration corresponding to the minimum of all acting potentials. (b) Spurious equilibrium corresponding to a saddle point in the net potential field (formation persists under perturbation in the radial direction).

Assuming that $x_{12} < d_1$ and $h_{i1} < h_1, i = 1, 2$, an equilibrium set exists at the desired formation, i.e. the desired formation is any point in the set $\Sigma = \{\boldsymbol{x}_1 \in \mathbb{R}^2, \boldsymbol{x}_2 \in \mathbb{R}^2, \dot{\boldsymbol{x}}_1 = \dot{\boldsymbol{x}}_2 = 0 | x_{12} = d_0, h_{11} = h_{21} = h_0\}$ (shown in Figure 2.2.4a). Furthermore, any other equilibria must be one in which the vehicles are co-linear along a line that passes through the origin, such an example is illustrated in Figure 2.2.4b. It follows from the conditions specified in (2.2.7) that the translational symmetry has been broken; however, rotational symmetry about the origin persists. That is, the conditions in (2.2.7) are preserved under a rotation of $\boldsymbol{x}_1$ and $\boldsymbol{x}_2$ by $R \in SO(2)$. To illustrate why, suppose that $\boldsymbol{x}_1{}^*$ and $\boldsymbol{x}_2{}^*$ are vehicle positions that satisfy (2.2.7). Then for any $R \in SO(2)$, $\boldsymbol{x}_1{}^{*'} = R\boldsymbol{x}_1{}^*$ and $\boldsymbol{x}_2{}^{*'} = R\boldsymbol{x}_2{}^*$ are solutions of (2.2.7) as well. Furthermore,

$$
\begin{aligned}
x_{12}^{*'} &= \|\boldsymbol{x}_1{}^{*'} - \boldsymbol{x}_2{}^{*'}\| = \|R\boldsymbol{x}_1{}^{*} - R\boldsymbol{x}_2{}^{*}\| = x_{12}^{*} \\
h_{11}^{*'} &= \|\boldsymbol{x}_1{}^{*'}\| = \|R\boldsymbol{x}_1{}^{*}\| = h_{11}^{*} \\
h_{21}^{*'} &= \|\boldsymbol{x}_2{}^{*'}\| = \|R\boldsymbol{x}_2{}^{*}\| = h_{21}^{*} \\
\hat{\boldsymbol{x}}_{12}{}^{*'} &= \frac{\boldsymbol{x}_1{}^{*'} - \boldsymbol{x}_2{}^{*'}}{\|\boldsymbol{x}_1{}^{*'} - \boldsymbol{x}_2{}^{*'}\|} = R\frac{\boldsymbol{x}_1{}^{*} - \boldsymbol{x}_2{}^{*}}{\|R\boldsymbol{x}_1{}^{*} - R\boldsymbol{x}_2{}^{*}\|} = R\hat{\boldsymbol{x}}_{12}{}^{*} \\
\hat{\boldsymbol{h}}_{11}{}^{*'} &= \frac{\boldsymbol{x}_1{}^{*'}}{\|\boldsymbol{x}_1{}^{*'}\|} = R\frac{\boldsymbol{x}_1{}^{*}}{\|R\boldsymbol{x}_1{}^{*}\|} = R\hat{\boldsymbol{h}}_{11}{}^{*} \\
\hat{\boldsymbol{h}}_{21}{}^{*'} &= \frac{\boldsymbol{x}_2{}^{*'}}{\boldsymbol{x}_2{}^{*'}} = R\frac{\boldsymbol{x}_2{}^{*}}{\|R\boldsymbol{x}_2{}^{*}\|} = R\hat{\boldsymbol{h}}_{21}{}^{*}.
\end{aligned}
$$

Thus,

$$
\begin{aligned}
f_h^c(h_{11}^{*'})\,\hat{\boldsymbol{h}}_{11}{}^{*'} &= Rf_h^c(h_{11}^{*})\,\hat{\boldsymbol{h}}_{11}{}^{*} \\
f_I(x_{12}^{*'})\,\hat{\boldsymbol{x}}_{12}{}^{*'} &= Rf_I(x_{12}^{*})\,\hat{\boldsymbol{x}}_{12}{}^{*} \\
f_h^c(h_{21}^{*'})\,\hat{\boldsymbol{h}}_{21}{}^{*'} &= Rf_h^c(h_{21}^{*})\,\hat{\boldsymbol{h}}_{21}{}^{*}.
\end{aligned}
$$

Now $\boldsymbol{x}_1{}^{*}$ and $\boldsymbol{x}_2{}^{*}$ are such that (2.2.7) is satisfied, i.e.

$$
f_h^c(h_{11}^{*})\,\hat{\boldsymbol{h}}_{11}{}^{*} = -f_I(x_{12}^{*})\,\hat{\boldsymbol{x}}_{12}{}^{*} = -f_h^c(h_{21}^{*})\,\hat{\boldsymbol{h}}_{21}{}^{*},
$$

and multiplying through by R we also have

$$
Rf_h^c(h_{11}^{*})\,\hat{\boldsymbol{h}}_{11}{}^{*} = -Rf_I(x_{12}^{*})\,\hat{\boldsymbol{x}}_{12}{}^{*} = -Rf_h^c(h_{21}^{*})\,\hat{\boldsymbol{h}}_{21}{}^{*},
$$

which is equivalent to

$$
f_h^c(h_{11}^{*'})\,\hat{\boldsymbol{h}}_{11}{}^{*'} = -f_I(x_{12}^{*'})\,\hat{\boldsymbol{x}}_{12}{}^{*'} = -f_h^c(h_{21}^{*'})\,\hat{\boldsymbol{h}}_{21}{}^{*'}.
$$

Thus, formation rotation preserves (2.2.7) and rotational symmetry persists.

We can prove asymptotic stability of this equilibrium (the set Σ) modulo $\mathrm{S}^1 \approx SO(2)$, i.e., to the formation shown in Figure 2.2.4a. Define $\boldsymbol{\chi} = (\boldsymbol{x}_1^T, \boldsymbol{x}_2^T, \dot{\boldsymbol{x}}_1^T, \dot{\boldsymbol{x}}_2^T)^T \in \mathbb{R}^8$ and

consider the candidate Lyapunov function

$$\Phi(\boldsymbol{\chi}) = \frac{1}{2}\sum_{i=1}^{2}\left(\|\dot{\boldsymbol{x}}_i\|^2 + \sum_{j\neq i}^{2} V_I(x_{ij}) + 2\, V_h^c(h_{i1})\right).$$

Taking the time derivative of Φ yields

$$\dot{\Phi} = \dot{\boldsymbol{x}}_1 \cdot \ddot{\boldsymbol{x}}_1 + \dot{\boldsymbol{x}}_2 \cdot \ddot{\boldsymbol{x}}_2 + \nabla_{\boldsymbol{x}_1} V_I(x_{12}) \cdot \dot{\boldsymbol{x}}_{12} + \nabla_{\boldsymbol{x}_1} V_h^c(h_{11}) \cdot \dot{\boldsymbol{x}}_1 + \nabla_{\boldsymbol{x}_2} V_h^c(h_{21}) \cdot \dot{\boldsymbol{x}}_2.$$

Now,

$$\begin{aligned}
\dot{\boldsymbol{x}}_1 \cdot \ddot{\boldsymbol{x}}_1 + \dot{\boldsymbol{x}}_2 \cdot \ddot{\boldsymbol{x}}_2 &= \dot{\boldsymbol{x}}_1 \cdot (-\nabla_{\boldsymbol{x}_1} V_I(x_{12}) - \nabla_{\boldsymbol{x}_1} V_h^c(h_{11}) - \dot{\boldsymbol{x}}_1) \\
&\quad + \dot{\boldsymbol{x}}_2 \cdot (-\nabla_{\boldsymbol{x}_2} V_I(x_{21}) - \nabla_{\boldsymbol{x}_2} V_h^c(h_{21}) - \dot{\boldsymbol{x}}_2) \\
&= -\dot{\boldsymbol{x}}_1 \cdot \nabla_{\boldsymbol{x}_1} V_h^c(h_{11}) - \dot{\boldsymbol{x}}_2 \cdot \nabla_{\boldsymbol{x}_2} V_h^c(h_{21}) - \nabla_{\boldsymbol{x}_1} V_I(x_{12}) \cdot \dot{\boldsymbol{x}}_{12} - \|\dot{\boldsymbol{x}}_1\|^2 - \|\dot{\boldsymbol{x}}_2\|^2
\end{aligned}$$

Thus,

$$\dot{\Phi} = -\|\dot{\boldsymbol{x}}_1\|^2 - \|\dot{\boldsymbol{x}}_2\|^2 \leq 0,$$

which is negative semi-definite. To prove asymptotic stability of the set Σ we invoke LaSalle's invariance principle. Note that $\Phi \geq 0$ and is identically 0 *only* when $\|\dot{\boldsymbol{x}}_1\| = \|\dot{\boldsymbol{x}}_2\| = 0$ and $x_{12} = d_0, h_{11} = h_{21} = h_0$. Furthermore, $\dot{\Phi} \leq 0$ and identically 0 only at equilibria. We prove asymptotic stability of the set of desired formation Σ by proving it is the only member of an invariant set to which all trajectories converge when starting within some region of attraction.

Let Σ' denote the set of all equilibria $\boldsymbol{\chi}$ which satisfy (2.2.7) other than the desired formations contained in Σ, i.e.

$$\Sigma' = \{\, \boldsymbol{\chi} \notin \Sigma \mid f_h^c(h_{11})\, \hat{\boldsymbol{h}}_{11} = -f_I(x_{12})\, \hat{\boldsymbol{x}}_{12} = -f_h^c(h_{21})\, \hat{\boldsymbol{h}}_{21} \,\}.$$

Let $c' = \min_{\boldsymbol{\chi}\in\Sigma'} \Phi(\boldsymbol{\chi})$, that is, c' is the least value of Φ corresponding to some equilibrium other than the desired formations contained in Σ (recall by design the set of desired formations Σ

is the global minimizer of Φ). We assert that there exist potentials as presented in Figure 2.2.1 and 2.2.3a for which $c' > 0$ (and bounded away from 0). Choose a c such that $c < c'$ and define $\Omega_c = \{ \boldsymbol{\chi} \mid \Phi(\boldsymbol{\chi}) \leq c\}$. Since $\dot{\Phi} \leq 0$ in Ω_c, Ω_c is a positively invariant[1] set.

Let E be the set of all points in Ω_c where $\dot{\Phi}(\boldsymbol{\chi}) = 0$ and let M be the largest invariant set in E, i.e. $M \subset E \subset \Omega_c$. By Theorem 4.4 in [40], every solution starting in Ω_c approaches M as $t \to \infty$. All points in E satisfy $\dot{\Phi} = -\|\dot{\boldsymbol{x}}_1\|^2 - \|\dot{\boldsymbol{x}}_2\|^2 = 0$ and thus M, being an invariant set within E, only contains equilibria. Since $\boldsymbol{\chi} \in \Sigma$ are the only equilibria in Ω_c, the set M only consists of $\boldsymbol{\chi} \in \Sigma$. Thus, by Theorem 4.4 of [40] the equilibria formations in Σ are asymptotically stable.

When $x_{12} < d_1$ and $h_{11}, h_{21} < h_1$, the conditions in (2.2.7) permit an equilibrium associated with $|f_h^c(h_{11})| = |f_I(x_{12})| = |f_h^c(h_{21})| \neq 0$ and $\boldsymbol{h}_{11}, \boldsymbol{h}_{21}$ and $\boldsymbol{x}_{12}$ co-linear (see Figure 2.2.4b). Denote the positions of each vehicle at this equilibrium as $\boldsymbol{x}_1{}^*$ and $\boldsymbol{x}_2{}^*$ and define $\boldsymbol{\chi}^* = (\boldsymbol{x}_1{}^{*T}, \boldsymbol{x}_2{}^*, 0, 0)^T \in R^8$. Furthermore, define the set of equilibria $\Sigma^* = \{(R\boldsymbol{x}_1{}^{*T}, R\boldsymbol{x}_2{}^{*T}, 0, 0)^T | R \in SO(2)\}$. The equilibrium set, Σ^*, is in fact unstable. Given any neighborhood of radius ϵ about an equilibrium $\boldsymbol{\chi}^* \in \Sigma^*$, for $\boldsymbol{\chi}^*$ to be stable we must be able to produce a $\delta(\epsilon) > 0$ such that $\|\boldsymbol{\chi}(0) - \boldsymbol{\chi}^*\| < \delta \Rightarrow \|\boldsymbol{\chi}(t) - \boldsymbol{\chi}^*\| < \epsilon, \forall t \geq 0$ [40]. Denote the open disc of radius ϵ about $\boldsymbol{\chi}^*$ as B_ϵ, i.e., $B_\epsilon = \{\boldsymbol{\chi} \in \mathbb{R}^8 \mid \|\boldsymbol{\chi} - \boldsymbol{\chi}^*\| < \epsilon\}$. Suppose we choose ϵ small enough such that the equilibria shown in Figure 2.2.4a, the desired formation equilibria, are not contained within B_ϵ (we assume our potentials are constructed in a manner that this is indeed possible). Thus, since $\Phi(\boldsymbol{\chi})$ is continuous and $\boldsymbol{\chi}^* \in \Sigma^*$ is not the global minimizer of Φ for any $\boldsymbol{\chi}^*$ within B_ϵ, Φ is bounded from below by some $a > 0$, for $\boldsymbol{\chi} \in B_\epsilon$, i.e. $\Phi(\boldsymbol{\chi}) > a, \forall \boldsymbol{\chi} \in B_\epsilon$.

We will now construct a family of initial conditions arbitrarily close to $\boldsymbol{\chi}^*$ such that

[1] A set Q is said to be a positively invariant set with respect to (2.2.5)-(2.2.6) if $\boldsymbol{\chi}(0) \in Q \Rightarrow \boldsymbol{\chi}(t) \in Q, \forall t \geq 0$ [40].

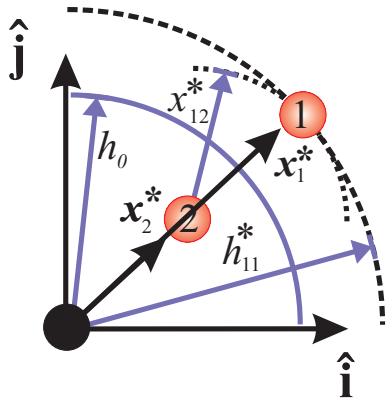

Figure 2.2.5: **Perturbation from Equilibrium Formation.** Shaded dots are vehicles, solid dot is the virtual leader. Solid circular arc has radius h_0, dashed circular arc has radius h^*_{11}. Dotted arc has radius x^*_{12}.

there exists no $\delta(\epsilon) > 0$ that guarantees $\|\boldsymbol{\chi}(t) - \boldsymbol{\chi}^*\| < \epsilon, \forall\, t \geq 0$.

For the equilibrium $\boldsymbol{\chi}^* = (\boldsymbol{x}_1{}^{*T}, \boldsymbol{x}_2{}^{*T}, 0, 0)^T$, denote $h^*_i = \|\boldsymbol{x}_i{}^*\|$, $i = 1, 2$, $x^*_{12} = \|\boldsymbol{x}_1{}^* - \boldsymbol{x}_2{}^*\|$ and denote the perturbation as $\boldsymbol{\chi}' = (\boldsymbol{x}_1{}'^T, \boldsymbol{x}_2{}'^T, 0, 0)^T$, with $h'_i = \|\boldsymbol{x}_i{}'\|$, $i = 1, 2$, $x'_{12} = \|\boldsymbol{x}_1{}' - \boldsymbol{x}_2{}'\|$. Referring to Figure 2.2.5, consider holding vehicle 2 fixed, i.e. $h'_{21} = \|\boldsymbol{x}_2{}'\| = h^*_{21}$, and perturb vehicle 1 to any location along a circular arc about vehicle 2 of radius x^*_{12} (indicated by the dotted curve) such that $h'_{11} = \|\boldsymbol{x}_1{}'\| < h^*_{11}$ and $h'_{11} > h_0$. Note that $x'_{12} = \|\boldsymbol{x}_1{}' - \boldsymbol{x}_2{}'\| = x^*_{12}$. Note that $\boldsymbol{\chi}' \in B_\epsilon$ cannot be an equilibrium solution of (2.2.7) because the virtual leader and the two vehicles are not all co-linear.

Since $h_0 < h'_{11} < h^*_{11} < h_1$, $V^c_h(h'_{11}) < V^c_h(h^*_{11})$ from which it follows $\Phi(\boldsymbol{\chi}') < \Phi(\boldsymbol{\chi}^*)$ for $\boldsymbol{\chi}^* \in \Sigma^*$. Furthermore, any trajectory, $\boldsymbol{\chi}(t)$, with $\boldsymbol{\chi}(0) = \boldsymbol{\chi}'$ cannot return to the Σ^* set since $\Phi(\boldsymbol{\chi}(0)) < \Phi(\boldsymbol{\chi}^*)$ and $\dot{\Phi}(\boldsymbol{\chi}(t)) \leq 0, \forall\, t \geq 0$. Define M as the invariant set for which $\dot{\Phi} = 0$ for $\boldsymbol{\chi}(0) \in B_\epsilon$. M only contains the equilibria set Σ^*. Therefore, since $\Phi > a > 0$ on B_ϵ and Σ^* is both unreachable and the sole member of M, all trajectories must leave B_ϵ. A perturbation $\boldsymbol{\chi}'$ produced in the manner described above can be produced no matter how small ϵ, therefore, $\boldsymbol{\chi}^*$ is not stable.

Example 2.2.3. Two Vehicles, Two Virtual Leaders

In Example 2.2.2 we saw how the addition of a virtual leader broke the translational symmetry but not the S^1 symmetry. Here we include an additional virtual leader and demonstrate that the full $SE(2)$ symmetry can be broken. Again we wish the desired vehicle pair to be separated by a distance d_0 with center of mass at the origin. However, in addition we now wish the line connecting the two vehicles to be oriented along the y-axis ($\hat{\mathbf{j}}$) as indicated in Figure 2.2.6.

A virtual body configuration that makes this desired formation an equilibrium corresponds to placing each virtual leader along the x-axis ($\hat{\mathbf{i}}$) at $\boldsymbol{b}_l = \pm\sqrt{h_0^2 - 1/4d_0^2}\,\hat{\mathbf{i}}$ as shown in Figure 2.2.6. The virtual body center is therefore located at the origin, $\boldsymbol{r} = 0$.

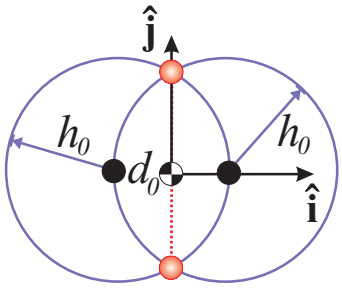

Figure 2.2.6: **Double Virtual Leader Equilibrium Formations for Example 2.2.3.** Shaded dots are vehicles, solid dots are virtual leaders. Virtual body center of mass is indicated by hatched dot. Desired vehicle configuration corresponding to the minimum of all acting potentials.

We consider five potentials $V_I(x_{12}), V_h^c(h_{11}), V_h^c(h_{12}), V_h^c(h_{21})$, and $V_h^c(h_{22})$. The minimum of potentials $V_h^c(h_{i1})$ and $V_h^c(h_{i2})$ alone define the desired formation geometry with broken $SE(2)$ symmetry; however, to ensure no vehicle collisions we include $V_I(x_{12})$, the vehicle interaction potential. The vehicle interaction potential also helps ensure that two vehicles will not try to converge to the same minimum of the virtual leader interaction potentials since vehicles repel when they are too close. As in the previous two examples, the desired formation geometry is by design a minimum of the sum of the artificial potentials

and can be shown to be a stable equilibrium. The dynamics for each vehicle are written

$$\begin{aligned}
\ddot{\boldsymbol{x}}_1 &= -\nabla_{\boldsymbol{x}_1} V_h^c(h_{11}) - \nabla_{\boldsymbol{x}_1} V_h^c(h_{12}) - \nabla_{\boldsymbol{x}_1} V_I(x_{12}) - \boldsymbol{f}_{\boldsymbol{v}1} \\
&= -f_h^c(h_{11})\hat{\boldsymbol{h}}_{11} - f_h^c(h_{12})\hat{\boldsymbol{h}}_{12} - f_I(x_{12})\hat{\boldsymbol{x}}_{12} - \dot{\boldsymbol{x}}_1 \qquad (2.2.8) \\
\ddot{\boldsymbol{x}}_2 &= -\nabla_{\boldsymbol{x}_2} V_h^c(h_{21}) - \nabla_{\boldsymbol{x}_2} V_h^c(h_{22}) - \nabla_{\boldsymbol{x}_2} V_I(x_{21}) - \boldsymbol{f}_{\boldsymbol{v}2} \\
&= -f_h^c(h_{21})\hat{\boldsymbol{h}}_{21} - f_h^c(h_{22})\hat{\boldsymbol{h}}_{22} + f_I(x_{12})\hat{\boldsymbol{x}}_{12} - \dot{\boldsymbol{x}}_2 \qquad (2.2.9)
\end{aligned}$$

which yield the following equations at equilibrium

$$\begin{aligned}
0 &= -f_h^c(h_{11})\hat{\boldsymbol{h}}_{11} - f_h^c(h_{12})\hat{\boldsymbol{h}}_{12} - f_I(x_{12})\hat{\boldsymbol{x}}_{12} \\
0 &= -f_h^c(h_{21})\hat{\boldsymbol{h}}_{21} - f_h^c(h_{22})\hat{\boldsymbol{h}}_{22} + f_I(x_{12})\hat{\boldsymbol{x}}_{12}.
\end{aligned}$$

As expected these equations permit the desired formation geometry as a solution. Another set of (unstable) equilibria are the solutions where all $\hat{\boldsymbol{h}}_{i1}$ and $\hat{\boldsymbol{x}}_{12}$ lie along the x-axis ($\hat{\mathbf{i}}$).

Formation Design in $\mathbb{R}^3$

Formation design in $\mathbb{R}^3$ follows the same methodology as we have presented for formations in $\mathbb{R}^2$: (1) interaction potentials between vehicles prevent collisions and dictate vehicle spacings and (2) virtual leaders with their respective interaction potentials break symmetries. However, designing appropriate potentials for desired patterns in $\mathbb{R}^3$ is much more challenging given the increased number of degrees of freedom. For the two vehicle case considered in Example 2.2.1 the symmetry is now an $SE(3)$ symmetry. Introducing a virtual leader (as in Example 2.2.2) breaks the translational symmetry but leaves an S^2 or spherical symmetry about the virtual leader. Adding a second virtual leader is not sufficient to completely fix the orientation of the formation as rotation about the line connecting the

two virtual leaders is unconstrained (see Figure 2.2.7a). As indicated in Figure 2.2.7b a virtual body consisting of three virtual leaders can fully break the symmetry.

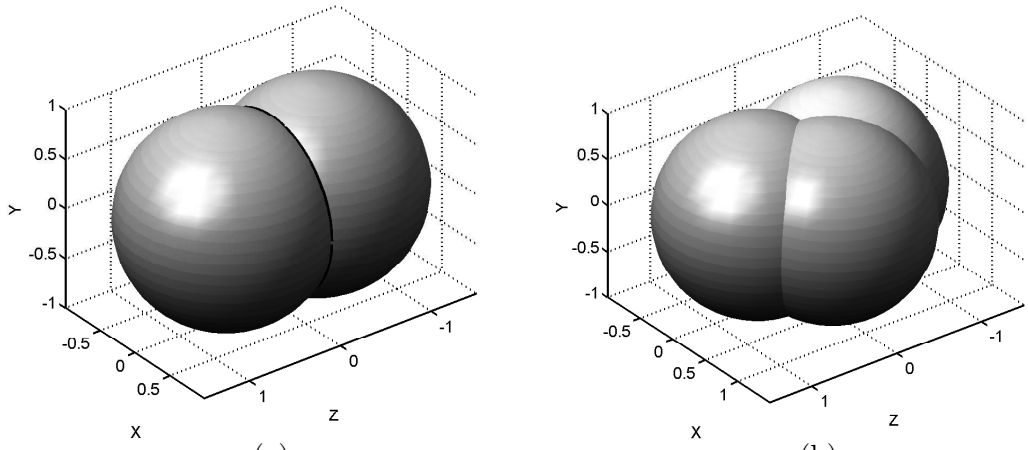

Figure 2.2.7: **Equilibria Formations in $\mathbb{R}^3$.** Gray spheres indicate radius h_0 about each virtual leader. (a) Two virtual leaders at $(\pm 0.5, 0, 0)$ with $h_0 = 1$. The black circle at the intersection of the spheres indicates non-isolated minima of sum of potentials $V_h^c(h_{il})$. (b)Three virtual leaders at $(\pm 0.5, 0, 0)$ and (0, 0.5, 0) with $h_0 = 1$. Two isolated equilibria at $(0, \pm\frac{\sqrt{3}}{2}, 0)$ exist at the minima of the sum of all three potentials (intersection of all three spheres).

It can be difficult, especially in $\mathbb{R}^3$, to find virtual leader configurations to break rotational symmetry in a systematic manner. In the next section we introduce potentials with the specific purpose of breaking this symmetry for $N > 2$. These potentials depend on relative position vectors and make it possible to fix formations with only a single virtual leader.

Example 2.2.4. Formation Arrays: Hexagonal Lattices

In this example we present a method for constructing formation arrays for many vehicles, $N > 2$. These arrays take the form of hexagonal lattices. Given N vehicles with interaction

potential, $V_I(x_{ij})$ and desired spacing d_0, we choose $d_0 < d_1 < d_0\sqrt{3}$. This yields hexagonal lattice equilibria in which $x_{ij} = d_0$ for $i, j = 1, \ldots, N$ as shown in Figure 2.2.8. About each vehicle there is a maximum of six vehicles lying evenly spaced around a circle of radius d_0.

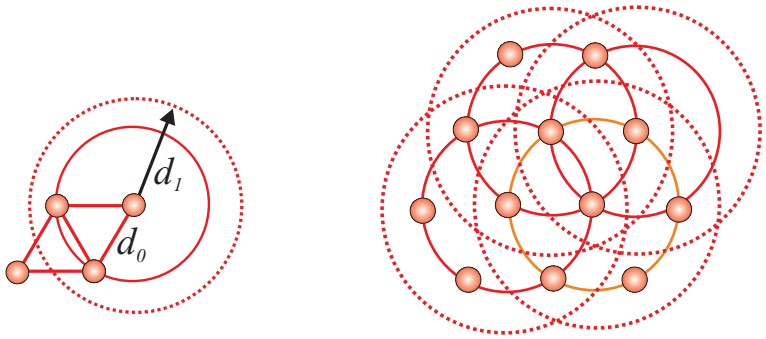

(a) (b)

Figure 2.2.8: **Hexagonal Lattice.** Shaded dots are vehicles. Solid circles have radius d_0, dashed circles have radius d_1. (a) Lattice with four vehicles. (b) Lattice with twelve vehicles.

We can break the translational symmetry by introducing a virtual leader in place of a vehicle. Alternatively, to keep the lattice intact we can place the virtual leader at the center of a three vehicle group as shown in Figure 2.2.9. This is achieved by choosing $h_0 = d_0\sqrt{3}/3$ and $h_0 < h_1 < 2d_0\sqrt{3}/3$. In this case, three vehicles now lie in an equilateral triangle on the circle of radius h_0 about the virtual leader.

Note that near this equilibrium (in phase space) only three vehicles will be aware of and influenced by the virtual leader. Similarly, near this equilibrium, each vehicle will in general interact with at most six neighboring vehicles. With one virtual leader there remains an S^1 symmetry. This can, of course, be broken with the addition of other virtual leaders as in Example 2.2.2 or by using artificial potentials of the form to be discussed in Section 2.3.

For groups with $N > 3$ we can extend these ideas to artificial potential design for stable

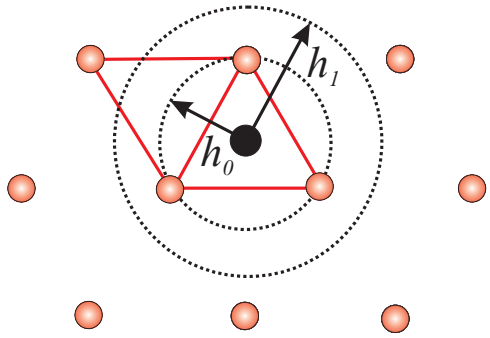

Figure 2.2.9: **Hexagonal Lattice with Virtual Leader.** Shaded dots are vehicles. The solid dot is the virtual leader.

equilibria that corresponds to more varied group geometries of interest such as vehicles moving in a circle (e.g., to escort another vehicle), in a line, in a V-shape, etc. One way to do this is to start with the hexagonal lattice set-up and impose a virtual leader in any position where no real vehicle should be present. For example, if we have five vehicles and want them to form a V-shape, we would place a virtual leader in each position in the lattice of Figure 2.2.9 that is not part of the V-shape. In Figure 2.2.10 we have shown five of these "occupier" virtual leaders (smaller black dots). For these we assign $h_0 = d_0$ and $h_1 = d_1$. For the virtual leader near the apex of the V-shape (the larger black dots in Figure 2.2.10) we assign $h_0 = d_0\sqrt{3}/3$ and $h_0 < h_1 < 2d_0\sqrt{3}/3$. Then, the five vehicles (shaded dots) in the V formation are in equilibrium and the virtual leaders "use up" spaces so no real vehicle can occupy them.

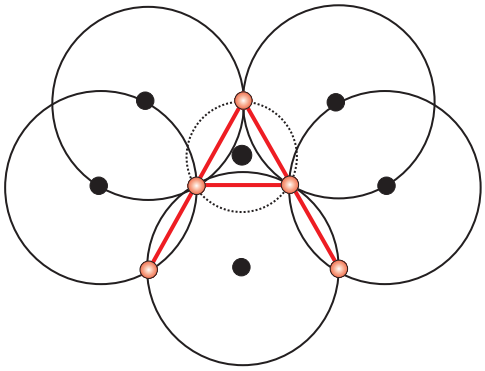

Figure 2.2.10: **V-formation from Hexagonal Lattice.** Shaded dots are vehicles and black dots are virtual leaders. Solid circles around each virtual leader have radius h_0.

2.3 Potentials to Regulate Relative Orientation

In Section 2.2 we introduced potentials between vehicles and vehicle-virtual leader pairs which are functions of relative distance only. The resulting control forces are central forces acting along the line between pairings. In Section 2.2.3 with a single virtual leader and potentials that regulate inter-vehicle distance alone, it was demonstrated that a desired formation can only be stabilized to within an S^1 symmetry about the virtual leader. To break that symmetry we introduced a second virtual leader. For the same two-vehicle formation in $\mathbb{R}^3$, an S^2 symmetry exists about a single virtual leader; it was illustrated that three virtual leaders are needed to break all symmetries and define isolated minima.

In this section we introduce potentials that intrinsically serve to break these S^1 and S^2 symmetries for planar and $\mathbb{R}^3$ formations, respectively. To do so, we first assume that $h_{il} \neq 0$ for all $i = 1, \ldots, N$ and $l = 1, \ldots, M$, i.e. no vehicle can be at the same position as a virtual leader. We then define the *relative orientation* of the ith vehicle and lth virtual leader as the orientation of the relative position vector ($\boldsymbol{h}_{il}$). This relative orientation is denoted $\Theta_{il} \in S^{p-1}_{h_{il}}, p = 2, 3$ where $S^1_{h_{il}}$ is the circle of radius h_{il} and $S^2_{h_{il}}$ is the sphere of radius h_{il}. For orientation in the plane, it is convenient to use polar coordinates (h_{il}, θ_{il})

where $\Theta_{il} = \theta_{il} \in [0, 2\pi)$ with $\theta_{il} = 0$ corresponding to $\boldsymbol{h}_{il}$ pointing in the $\hat{\mathbf{i}}$ direction. For orientation in $\mathbb{R}^3$ we will use spherical coordinates. The *desired* relative orientation will be denoted with the superscript "*d*" as $\Theta_{il}^d \in \mathrm{S}^{p-1}$. The symmetry breaking potentials we define in this section depend on these relative orientations and are denoted $V_h^o(\Theta_{il})$ or sometimes $V_h^o(\Theta_{il}; \alpha_h^o, \Theta_l^d, h_1)$ where α_h^o is a scalar design parameter. The range of influence of these potentials is limited to $h_{il} \leq h_1$. *In this section we retain the discontinuity at* $h_{il} = h_1$ *and explicitly define the potential and gradient to be zero for* $h_{il} \geq h_1$.

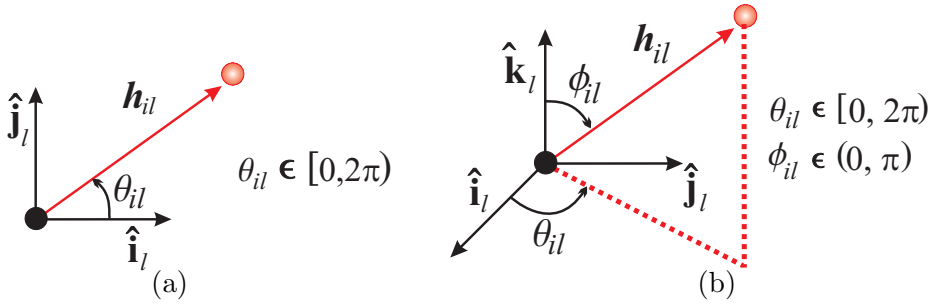

Figure 2.3.1: **Defining Relative Orientation.** Vehicle orientation relative to virtual leader (a) in the plane and (b) in $\mathbb{R}^3$. Black circle is the virtual leader, shaded circle is the vehicle.

2.3.1 Planar Formations.

Consider formations restricted to the plane. As described above, we identify the orientation of the *ith* vehicle with respect to the *lth* virtual leader with the polar coordinate $\theta_{il} \in [0, 2\pi)$. This is shown in Figure 2.3.1 where we have fixed a frame $\hat{\mathbf{i}}_l, \hat{\mathbf{j}}_l$ to the virtual leader with orientation the same as the inertial frame. When designing potentials on S^1, we must ensure our potentials are C^1 with respect to our parametrization by verifying that $\left(\frac{\partial V_h^o}{\partial \theta_{il}}\right)_{\theta_{il}=0} = \left(\frac{\partial V_h^o}{\partial \theta_{il}}\right)_{\theta_{il} \to 2\pi}$. The examples presented in what follows are all C^1 for $\theta_{il} \in [0, 2\pi)$.

For formation design we will introduce potentials, $V_h^o(\theta_{il})$, that are strictly functions

of θ_{il} and yield gradients which are perpendicular to $\boldsymbol{f}_{\boldsymbol{h}}^{\boldsymbol{c}}(h_{il})$. Therefore these potentials only break the S^1 symmetry and do not influence the radial dynamics between vehicle and virtual leader. The gradient of this potential with respect to $\boldsymbol{x}_i$ is given by

$$\begin{aligned} \nabla_{\boldsymbol{x}_i} V_h^o(\theta_{il}) &= \frac{\partial V_h^o}{\partial \theta_{il}} \frac{\partial \theta_{il}}{\partial \boldsymbol{x}_i} \\ &= f_h^o(\theta_{il})\, \boldsymbol{h}_{il}^{\perp} \end{aligned}$$

where we have defined

$$\boldsymbol{h}_{il}^{\perp} \equiv \frac{\partial \theta_{il}}{\partial \boldsymbol{x}_i} = \frac{1}{h_{il}} \left(-\sin\theta_{il}\, \hat{\mathbf{i}}_l + \cos\theta_{il}\, \hat{\mathbf{j}}_l \right).$$

In light of the well known formula for the gradient in planar polar coordinates, it is not surprising that $\|\boldsymbol{h}_{il}^{\perp}\| = \|\boldsymbol{h}_{il}\|^{-1}$. Furthermore, $\boldsymbol{h}_{il}^{\perp}$ is indeed perpendicular to $\boldsymbol{h}_{il}$.

Consider the potential given by

$$V_h^o(\theta_{il}) = \alpha_h^o \sin^2 \frac{1}{2}(\theta_{il} - \theta^d) \tag{2.3.1}$$

which acts to align θ_{il} to a chosen reference angle, θ^d. This potential has a unique minimum at $\theta_{il} = \theta^d$, see Figure 2.3.2a. The gradient is given by $\nabla_{\boldsymbol{x}_i} V_h^o(\theta_{il}) = \frac{\alpha_h^o}{2} \sin(\theta_{il} - \theta^d)\, \boldsymbol{h}_{il}^{\perp}$. A simple modification of the potential of (2.3.1) is given by

$$V_h^o(\theta_{il}) = \alpha_h^o \sin^2 \frac{r}{2}(\theta_{il} - \theta^d). \tag{2.3.2}$$

The potential of (2.3.2) has r isolated global minima, evenly spaced at angles $\theta^d + 2\pi t/r$, for $t = 0, \ldots, r-1$ (see Figure 2.3.2b). This potential is especially suited to breaking the S^1 symmetry for a formation with r vehicles about a single virtual leader where the desired formation geometry is an $r-1$ sided regular polygon. More generally, given r desired orientations $\theta_q^d, q = 1, \ldots, r$ about the virtual leader (not necessarily evenly spaced about 2π), the potential

$$V_h^o(\theta_{il}) = \alpha_h^o \prod_{q=1}^{r} \sin^2 \frac{1}{2}(\theta_{il} - \theta_q^d)$$

has an isolated minimum at each $\theta_q^d, q = 1, \ldots, r$.

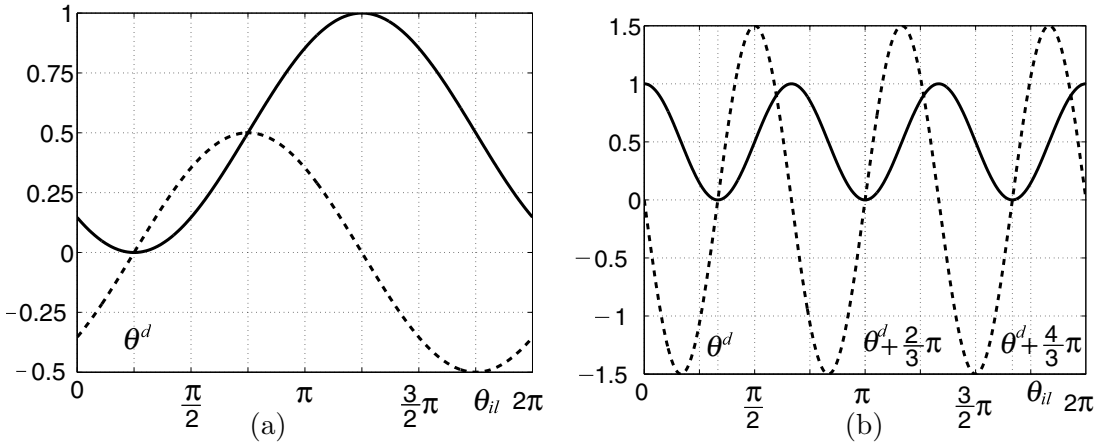

Figure 2.3.2: **Potentials Regulating Orientation in the Plane.** Solid lines indicate potential profile and dashed lines indicate the nonzero component of its gradient. (a) Profile of potential given in (2.3.1) with $\alpha_h^o = 1$ and $\theta^d = \pi/4$. (b) Profile of potential given in (2.3.2) with $\alpha_h^o = 1, \theta^d = \pi/4$, and $r = 3$.

Alternatively, since S^1 is isomorphic to $SO(2)$ we can map $\theta_{il} \in [0, 2\pi)$ to $R_{il} \in SO(2)$ and the desired orientation $\theta^d \in \mathrm{S}^1$ to $R^d \in SO(2)$, i.e.

$$R_{il} = \begin{pmatrix} \cos\theta_{il} & -\sin\theta_{il} \\ \sin\theta_{il} & \cos\theta_{il} \end{pmatrix}, \quad R^d = \begin{pmatrix} \cos\theta^d & -\sin\theta^d \\ \sin\theta^d & \cos\theta^d \end{pmatrix}.$$

In [85], given two vehicles, A and B, with orientation defined by $R^A \in SO(3)$ and $R^B \in SO(3)$, control laws are sought to align the vehicles body frames by seeking to drive $R^A = R^B$. In [85], control laws derived from the potential

$$V = \mathrm{Tr}(\mathbb{I} - (R^A)^T R^B) \tag{2.3.3}$$

are shown to solve this vehicle alignment problem. The potential in (2.3.1) and (2.3.3) are identical when setting $R^A = R^d$ and $R^B = R_{il}$ in the latter equation.

2.3.2 Formations in $\mathbb{R}^3$.

For formations in three dimensions, the orientation of the ith vehicle relative to the lth virtual leader, Θ_{il}, is an element of S^2. Unlike for S^1, no single parametrization can cover S^2. To ease matters, we assume that we may disregard the north and south poles on S^2. A useful parametrization for our purposes is then $(\rho, \theta_{il}, \phi_{il})$-spherical coordinates with radius $\rho = h_{il}$. In this parametrization the orientation of a vehicle relative to a virtual leader is described by a pair of angles, (θ_{il}, ϕ_{il}), where $\theta_{il} \in [0, 2\pi)$ and $\phi_{il} \in [0, \pi]$ (see Figure 2.3.1). These angles are measured with respect to a reference frame attached to the lth virtual leader and oriented as the inertial frame. In light of our assumption, we only consider $\phi_{il} \in (0, \pi)$.

As in the planar case, $V_h^o(\theta_{il}, \phi_{il})$ yields gradients which are perpendicular to $\boldsymbol{f_h}(h_{il})$. Therefore these potentials only break the S^2 symmetry and do not influence the radial dynamics between vehicle and virtual leader. The gradient of this potential with respect to $\boldsymbol{x}_i$ is given by

$$\begin{aligned} \nabla_{\boldsymbol{x}_i} V_h^o(\theta_{il}, \phi_{il}) &= \frac{\partial V_h^o}{\partial \theta_{il}} \frac{\partial \theta_{il}}{\partial \boldsymbol{x}_i} + \frac{\partial V_h^o}{\partial \phi_{il}} \frac{\partial \phi_{il}}{\partial \boldsymbol{x}_i} \\ &= f_h^\theta(\theta_{il}, \phi_{il})\, \boldsymbol{h}_{il}{}^{\boldsymbol{\theta}\perp} + f_h^\phi(\theta_{il}, \phi_{il})\, \boldsymbol{h}_{il}{}^{\boldsymbol{\phi}\perp} \end{aligned}$$

where we have defined

$$f_h^\theta(\theta_{il}, \phi_{il}) \equiv \frac{\partial V_h^o}{\partial \theta_{il}},$$

$$f_h^\phi(\theta_{il}, \phi_{il}) \equiv \frac{\partial V_h^o}{\partial \phi_{il}},$$

$$\boldsymbol{h}_{il}{}^{\boldsymbol{\theta}\perp} \equiv \frac{\partial \theta_{il}}{\partial \boldsymbol{x}_i} = \frac{1}{h_{il}} \left(-\frac{\sin\theta_{il}}{\sin\phi_{il}}\, \hat{\mathbf{i}}_l + \frac{\cos\theta_{il}}{\sin\phi_{il}}\, \hat{\mathbf{j}}_l \right)$$

and

$$\boldsymbol{h}_{il}{}^{\boldsymbol{\phi}\perp} \equiv \frac{\partial \theta_{il}}{\partial \boldsymbol{x}_i} = \frac{1}{h_{il}} \left(\cos\phi_{il} \cos\theta_{il}\, \hat{\mathbf{i}}_l + \cos\phi_{il} \sin\theta_{il}\, \hat{\mathbf{j}}_l - \sin\phi_{il}\, \hat{\mathbf{k}}_l \right).$$

$\boldsymbol{h}_{il}{}^{\boldsymbol{\theta}\perp}$ and $\boldsymbol{h}_{il}{}^{\boldsymbol{\phi}\perp}$ lie in the plane whose normal is given by $\boldsymbol{h}_{il}$. Thus, neither f_h^θ nor f_h^ϕ have influence in the radial direction. Furthermore, $\boldsymbol{h}_{il}{}^{\boldsymbol{\theta}\perp}$ and $\boldsymbol{h}_{il}{}^{\boldsymbol{\phi}\perp}$ are orthogonal to each other.

Now consider the potential

$$V_h^o(\theta_{il}, \phi_{il}) = \alpha_h^o \left(1 - \cos(\theta_{il} - \theta^d) \sin\phi_{il} \sin\phi^d - \cos\phi_{il} \cos\phi^d\right) \tag{2.3.4}$$

which is positive definite and has a unique isolated global minimum at $(\theta_{il}, \phi_{il}) = (\theta^d, \phi^d)$, see Figure 2.3.3. This potential is indeed C^0 even at the poles, $\phi_{il} = 0, \pi$. Taking partials with respect to θ_{il} and ϕ_{il}, i.e.

$$\begin{aligned} \frac{\partial V_h^o}{\partial \theta_{il}} &= \alpha_h^o \sin(\theta_{il} - \theta^d) \sin\phi_{il} \sin\phi^d \\ \frac{\partial V_h^o}{\partial \phi_{il}} &= \alpha_h^o \left(\sin\phi_{il} \cos\phi^d - \cos(\theta_{il} - \theta^d) \cos\phi_{il} \sin\phi^d\right) \end{aligned}$$

illustrates how the gradient is undefined at the poles since $\frac{\partial V_h^o}{\partial \phi_{il}}\big|_{\phi_{il}=0} = \frac{\partial V_h^o}{\partial \phi_{il}}(\theta_{il}, \phi_{il})$ and thus our removal of the poles. Also, as in the planar case $\left(\frac{\partial V_h^o}{\partial \theta_{il}}\right)_{\theta_{il}=0} = \left(\frac{\partial V_h^o}{\partial \theta_{il}}\right)_{\theta_{il}\to 2\pi}$.

Given r desired orientations $(\theta_q^d, \phi_q^d), q = 1, \ldots, r$ about the virtual leader, we design a potential given by

$$V_h^o(\theta_{il}, \phi_{il}) = \alpha_h^o \prod_{q=1}^{r} \left(1 - \cos(\theta_{il} - \theta_q^d) \sin\phi_{il} \sin\phi_q^d - \cos\phi_{il} \cos\phi_q^d\right) \tag{2.3.5}$$

which has r isolated minima, one at each of the desired orientations (see Figure 2.3.3).

S^2 is not isomorphic to $SO(3)$. However, we can define $R_{il}(\theta_{il}, \phi_{il}) = R_y(\phi_{il}) R_z(\theta_{il})$ where $R_z(\theta_{il}) \in SO(3)$ represents rotation about the z-axis $(\hat{\mathbf{k}}_{\boldsymbol{l}})$ by an amount θ_{il} and $R_y(\phi_{il}) \in SO(3)$ represents rotation about the y-axis $(\hat{\mathbf{j}}_{\boldsymbol{l}})$ by an amount ϕ_{il}. Then, $\hat{\boldsymbol{h}}_{\boldsymbol{il}} = R_{il} \hat{\boldsymbol{k}}_{\boldsymbol{l}}$. Given a desired orientation $(\theta_{il}^d, \phi_{il}^d)$ we define $R^d = R_{il}(\theta_{il}^d, \phi_{il}^d) \in SO(3)$ and derive a control law from the potential presented in (2.3.3). In this setting, quaternions provide a singularity free parametrization for both R_{il} and R^d.

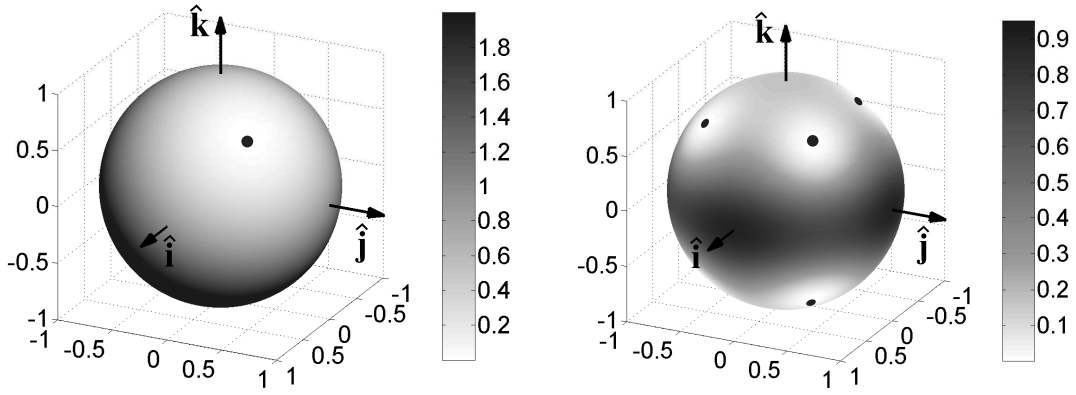

(a) (b)

Figure 2.3.3: **Potentials Regulating Orientation in $\mathbb{R}^3$.** Gray scale corresponds to value of the potential. Black dots indicate global minima. (a) Surface plot of the potential given in (2.3.4) on the sphere modulo north and south poles with $(\theta^d, \phi^d) = (\pi/4, \pi/4)$ and $\alpha_h^o = 1$. (b) Surface plot of the potential given in (2.3.5) on the sphere modulo north and south poles with eight minima at $(\theta^d, \phi^d) = (\pi/4 + p\pi/2, \pi/4), (\pi/4 + p\pi/2, -\pi/4)$ for $p = 0, 1, 2, 3$ and $\alpha_h^o = 1$.

2.4 Potentials to Regulate Relative Position

In Section 2.2 and Section 2.3 we presented methods for breaking selected symmetries using virtual leaders and various artificial potentials. In this section we present a single potential to break the $SE(p), p = 2, 3$ symmetries about a virtual leader. These potentials will be denoted $V_h^p(\boldsymbol{h}_{il}; \boldsymbol{d}, \alpha_p)$ and have minima when the relative vehicle position, $\boldsymbol{h}_{il}$, is equal to desired relative position vector $\boldsymbol{d} \in \mathbb{R}^p$. As in Section 2.3 in what follows we impose the discontinuous cutoff for $h_{il} > h_1$.

The simple quadratic potential

$$V_h^p = \frac{\alpha_p}{2} \|\boldsymbol{h}_{il} - \boldsymbol{d}\|^2$$

has a unique and isolated minimum when $\boldsymbol{h}_{il} = \boldsymbol{d}$. If there are r desired locations about

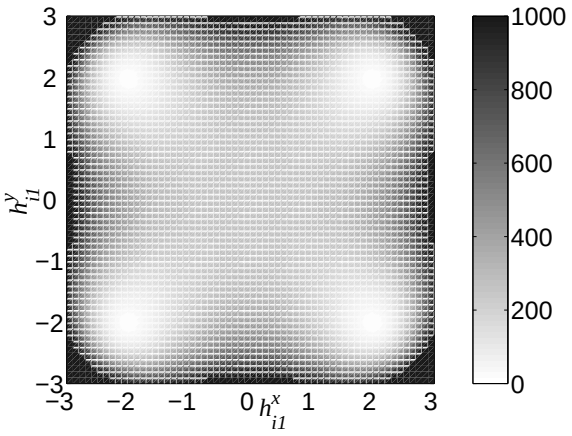

Figure 2.4.1: **Potentials Regulating Relative Position.** Potential in (2.4.1) with minima at vertices of the square defined by $d_1 = (2,2), d_2 = (2,-2), d_3 = (-2,-2)$, and $d_4(-2,2)$. Axis are defined by $\boldsymbol{h}_{i1} = (h^x_{i1}, h^y_{i1})$.

the virtual leader denoted $\boldsymbol{d}_q, q = 1, \ldots, r$, the potential

$$V_h^p = \frac{\alpha_p}{2^r} \prod_{q=1}^{r} \|\boldsymbol{h}_{il} - \boldsymbol{d}_q\|^2 \tag{2.4.1}$$

suffices having r minima at each d_q. For example, in Figure 2.4.1 we show the resulting potential field associated with (2.4.1) for a square formation in the plane about a virtual leader at the origin.

2.5 Formation Stability

In Example 2.2.2 we used Lyapunov's Second Method and invoked LaSalle's invariance principle to prove asymptotic stability of the two vehicle, one stationary virtual leader formation modulo an S^1 symmetry about the virtual leader. In general, a benefit of using artificial potentials for control design is that they provide a guide for choosing Lyapunov functions. In particular, a Lyapunov function for proving stability and robustness of the group motion can be constructed as the sum of each vehicle's kinetic energy and the artificial potentials. That is, local asymptotic stability of $\boldsymbol{\chi} = (\boldsymbol{x}_1^T, \ldots, \boldsymbol{x}_N^T, \dot{\boldsymbol{x}}_1^T, \ldots, \dot{\boldsymbol{x}}_N^T)^T = \boldsymbol{\chi}^*$

corresponding to the vehicles at rest and at the global minimum of the sum of the artificial potentials is proven with the Lyapunov function

$$\Phi = \frac{1}{2}\sum_{i=1}^{N}\left[\|\dot{\boldsymbol{x}}_i\|^2 + \sum_{j\neq i}^{N} V_I(x_{ij}) + 2\sum_{l=1}^{M}\left(V_h^c(h_{il}) + V_h^o(\Theta_{il}) + V_h^p(\boldsymbol{x}_i, \boldsymbol{b}_l)\right)\right]. \tag{2.5.1}$$

Without dissipation, the examples provided in Section 2.2.3 are all stable in the sense of Lyapunov. When there is an S^1 symmetry, the stability is modulo S^1. Stability follows from the fact that in each of these cases, by design, the equilibrium described is a global minimum of the total artificial potential. Recall that the local potential $V_I(x_{ij})$ is designed so that it has a global minimum at $x_{ij} = d_0$ and V_h has a global minimum at $h_{il} = h_0, \Theta_{il} = \Theta^d$ and/or $\boldsymbol{h}_{il} = \boldsymbol{d}$. In all of these cases, the desired equilibrium corresponds to these minimum values. Thus, the sum of the local potentials has a global minimum at the equilibrium.

In general, the Lyapunov function corresponding to total kinetic energy plus artificial potential energy (Φ in the example above) can be used further to select a controlled dissipation force $\boldsymbol{f_v}$ and to prove local asymptotic stability. The derivative of Φ with respect to time is

$$\begin{aligned}\dot{\Phi} &= \sum_{i=1}^{N}\dot{\boldsymbol{x}}_i \cdot \left(\boldsymbol{u}_i + \sum_{j\neq i}^{N}\nabla_{\boldsymbol{x}_i} V_I(x_{ij}) + \sum_{l=1}^{M}\nabla_{\boldsymbol{x}_i} V_h(\boldsymbol{x}_i, \boldsymbol{b}_l)\right) \\ &= \sum_{i=1}^{N}\dot{\boldsymbol{x}}_i \cdot \boldsymbol{f}_{\boldsymbol{v}i}\end{aligned}$$

where we have used the expression (2.1.2) for the control law $\boldsymbol{u_i}$ and we have assumed there is a neighborhood about the equilibrium in which the control law remains smooth. Thus, if we choose

$$\boldsymbol{f}_{\boldsymbol{v}i} = a_i\dot{\boldsymbol{x}}_i, \quad a_i > 0 \tag{2.5.2}$$

for $i = 1, \ldots, N$, then $\dot{\Phi}$ is negative semi-definite being equal to zero if and only if $\dot{\boldsymbol{x}}_i = 0$ for all i. By the LaSalle invariance principle we can conclude that an equilibrium that has

been made stable without dissipation will be asymptotically stabilized with this form of dissipation.

In the case where the virtual body is not stationary but rather strictly translating with a velocity $\boldsymbol{v}_0(t)$, i.e. $\dot{\boldsymbol{r}} = \dot{\boldsymbol{b}}_1 = \ldots = \dot{\boldsymbol{b}}_M = \boldsymbol{v_0}(t), \ddot{\boldsymbol{r}} = \ddot{\boldsymbol{b}}_1 = \ldots = \ddot{\boldsymbol{b}}_M = \dot{\boldsymbol{v}}_{\boldsymbol{0}}(t)$, an $\boldsymbol{f_v}$ which asymptotically stabilizes a desired formation that is at rest with respect to the moving virtual body is given by,

$$\boldsymbol{f}_{\boldsymbol{v}i} = \alpha_v(\dot{\boldsymbol{x}}_i - \dot{\boldsymbol{r}}) - \ddot{\boldsymbol{r}}$$

where $\alpha_v > 0$ is a constant parameter. A Lyapunov function that can prove asymptotic stability and has a global minimum at the desired formation is given by

$$\Phi' = \frac{1}{2}\sum_{i=1}^{N}\sum_{l=1}^{M}\left[\|\dot{\boldsymbol{h}}_{il}\|^2 + 2M\left(V_h^c(h_{il}) + V_h^o(\Theta_{il}) + V_h^p(\boldsymbol{x}_i, \boldsymbol{b}_l)\right) + \sum_{j\neq i}^{N} V_I(x_{ij})\right]. \tag{2.5.3}$$

Clearly, $\Phi' > 0$ and $\Phi' = 0$ only when each vehicle is at rest with respect to the virtual body (i.e. each virtual leader) and at positions relative to the virtual body such that the sum of artificial potentials is zero. The Lyapunov function, (2.5.1), used to prove stability when the virtual body is stationary, i.e. $\dot{\boldsymbol{h}}_{il} = \dot{\boldsymbol{x}}_i$, is identical to (2.5.3) except for how the sums over the virtual leaders, i.e. sums over l, are nested. With vehicle dynamics given in (2.1.1) and control law given in (2.1.2), the time derivative of Φ is given by

$$\dot{\Phi}' = \sum_{i=1}^{N}\sum_{l=1}^{M} -\alpha_v\|\dot{\boldsymbol{h}}_{il}\|^2. \tag{2.5.4}$$

$\dot{\Phi}'$ is only negative semi-definite but stability of the desired formation equilibrium can be proven by invoking LaSalle's invariance principle (see Example 2.2.2).

We conclude with a proposition about the stability of formations constructed with the artificial potentials discussed throughout this chapter, with vehicle dynamics as given in (2.1.1), and control law given in (2.1.2).

Proposition 2.5.1. *Consider a group of N vehicles with dynamics defined by (2.1.1) and the control law given by (2.1.2) and (2.5.2) and let the virtual body be strictly translating with respect to a fixed inertial frame, i.e.* $\dot{\boldsymbol{r}} = \dot{\boldsymbol{b}}_1 = \ldots = \dot{\boldsymbol{b}}_M = \boldsymbol{v_0}(t), \ddot{\boldsymbol{r}} = \ddot{\boldsymbol{b}}_1 = \ldots = \ddot{\boldsymbol{b}}_M = \dot{\boldsymbol{v}}_{\mathbf{0}}(t)$. *Let the equilibrium of interest be one in which* $\dot{\boldsymbol{h}}_{il} = 0$ *and a global minimum of the sum of artificial potentials given in (2.1.4). Then, the equilibrium is locally asymptotically stable for the closed-loop dynamics. In the case in which there is no symmetry, stability is achieved in the full state space. In the case in which there is symmetry, the relative velocity of all vehicles will go to zero and each symmetry variable will be stabilized to an arbitrary (constant) value. We assume that* h_1 *and* d_1 *have been defined so that there is a neighborhood about the equilibrium in which the control law remains smooth.*

Proposition 2.5.1 can be used to prove asymptotic stability of all of the equilibria described in this chapter. This excludes, of course, the unstable equilibria shown in Figure 2.2.4b and others.

It should be emphasized that stability results are generally local. A major disadvantage of potentials is that there can be many local minima and other critical points. This is true even for relatively small N (as illustrated in Example 2.2.2). Often it is impossible to catalog all possible equilibria and thus stating anything global about stability is prohibited.

Chapter 3

Dynamic Formations

In Chapter 2 we presented a methodology for designing stable vehicle formations using artificial potentials and a virtual body. Vehicle control laws comprised of the gradients of these artificial potentials and the fed-forward virtual body dynamics were introduced to stabilize the vehicle formation about a translating virtual body. Central to a stability proof was a Lyapunov function that serves as a meaningful measure of the formation error. In this chapter we enable the virtual body to rotate, expand/contract, and deform and we describe control laws that drive the virtual body, and thus the vehicle group, to perform these maneuvers in a stable manner. These control laws regulate the speed of the virtual body to ensure bounded formation error. In the construction presented herein, we use the formation design tools and vehicle control laws presented in Chapter 2, that stabilize a formation of vehicles about a *stationary* virtual body.

In Section 3.1 virtual body maneuvers (and thus desired vehicle formation maneuvers) are identified with trajectories in an extended virtual body configuration space. Motion along these trajectories, i.e. virtual body motion, is achieved by parameterizing these trajectories by a time-like variable s. In Section 3.2, formation stabilization is achieved by

specifying a feedback control to regulate the speed, $\dot{s}$, at which the virtual body traverses the mission trajectories to ensure that formation error remains below a specified upper bound.

The parametrization of the virtual body dynamics by s permits a decoupling of the formation stabilization and the formation maneuver/mission control subproblems. By appropriate choice of vehicle control law and the proposed $\dot{s}$ control law, it can be shown that formation error will remain bounded regardless of virtual body maneuver direction.

The vehicle control laws must be designed to asymptotically stabilize the formation about a stationary virtual body. A Lyapunov function used to prove asymptotic stability then serves as the formation error function by which we regulate $\dot{s}$. The interpretation of this function as a meaningful measure of formation error *during* the formation maneuver is limited since the function may be inherently biased from zero when the vehicles have nonzero velocity. This will be addressed and demonstrated in Section 3.3 where we present a simulation of the virtual body translating and rotating.

Much of the work in this chapter was first presented in [64] and [61]. The presentation of Section 3.1 and Section 3.2 closely follows [64]. The development that allows the vehicle group to deform using potentials presented in Section 2.3 and Section 2.4, remarks regarding the controller performance, and Section 3.3 are all new since [64] and [61].

3.1 Formation Trajectories

As presented in Chapter 2, the position of the lth virtual leader with respect to an inertial frame is given by $\boldsymbol{b}_l \in \mathbb{R}^p$ and the virtual body center of mass is given by $\boldsymbol{r} \in \mathbb{R}^p$, where $p = 2$ or 3. Denote the orientation of the virtual body with respect to a fixed inertial frame as $R \in SO(p)$.

3.1.1 Translation and Rotation

When virtual leaders are constrained to maintain fixed relative position between each other, it is natural to view the virtual body as a *rigid body* and define its configuration as an element of $SE(p)$, i.e. $(R, \boldsymbol{r}) \in SE(p)$ where $R \in SO(p)$ is the $p \times p$ rotation matrix. *Translation* and *rotation* of the virtual body are then defined by a trajectory in this space. To achieve motion these trajectories are parameterized by the time-like variable s, i.e. $(R(s), \boldsymbol{r}(s))$ where $s \in [s_s, s_f]$. The dynamics of the virtual body are then described by the relations

$$\dot{\boldsymbol{r}} = \widehat{\frac{d\boldsymbol{r}}{ds}}\dot{s}, \quad \dot{R} = \frac{dR}{ds}\dot{s}, \tag{3.1.1}$$

and the trajectory for the lth virtual leader is

$$\boldsymbol{b}_l(s) = R(s)\bar{\boldsymbol{b}}_l + \boldsymbol{r}(s), \quad l = 1, \ldots, M,$$

where $\bar{\boldsymbol{b}}_l = \boldsymbol{b}_l(s_s) - \boldsymbol{r}(s_s)$, i.e. the initial relative position, and $R(s_s)$ is the $p \times p$ identity matrix.

For example, the choice

$$\widehat{\frac{d\boldsymbol{r}}{ds}} = \begin{pmatrix} 1 \\ \\ 0 \end{pmatrix}, \quad \frac{dR}{ds} = 0,$$

produces a formation with its center of mass moving in a straight line in the $(1, 0)$ direction in the plane with fixed orientation. Stability of the formation during the maneuver is guaranteed by the choice of $\dot{s}$ presented in Section 3.2.

3.1.2 Expansion and Contraction

Expansion and *contraction* are achieved by scaling the distances between virtual leaders and the desired separation parameters in each artificial potential, $(d_i, h_i), i = 0, 1$, by a scalar variable $k^e(s)$. We now define the virtual body configuration as an element of $SE(p) \times \mathbb{R}$

and the s-parameterized trajectory is defined by the triplet $(R, \boldsymbol{r}, k^e) \in SE(p) \times \mathbb{R}$ where

$$\begin{aligned} \boldsymbol{b}_l(s) &= k^e(s)R(s)\bar{\boldsymbol{b}}_l + \boldsymbol{r}(s), \\ h_i(s) &= k^e(s)\bar{h}_i, \\ d_i(s) &= k^e(s)\bar{d}_i, \end{aligned}$$

with $k^e(s_s) = 1, \bar{h}_i = h_i(s_s)$ and $\bar{d}_i = d_i(s_s)$. The dynamics of a virtual body which can translate, rotate, and expand and contract are now described by the relations

$$\dot{\boldsymbol{r}} = \widehat{\frac{d\boldsymbol{r}}{ds}}\dot{s}, \quad \dot{R} = \frac{dR}{ds}\dot{s}, \quad \dot{k}^e = \frac{dk^e}{ds}\dot{s}. \tag{3.1.2}$$

3.1.3 Deformation

In Section 2.3 we introduced artificial potentials, denoted V_h^o, designed to regulate the orientation of the relative position vectors of virtual leaders and vehicles. This was accomplished by designing the potential associated with the lth virtual leader to have Z_l isolated minima at the angles $\phi_{lz}^d, z = 1, \ldots, Z_l$ for formations in $\mathbb{R}^2$ and at the angles $(\theta_{lz}^d, \phi_{lz}^d), z = 1, \ldots, Z_l$, for formations in $\mathbb{R}^3$. The superscript "d" refers to *deformation* which is the maneuver resulting from the introduction of dynamics to the $(p-1)\sum_{i=1}^{M} Z_i$ desired angles, $(\theta_{lz}^d, \phi_{lz}^d)$, by parameterizing them by s. For example, in the plane we can define the scaling

$$\phi_{lz}^d(s) = k_{lz}^d(s)\bar{\phi}_{lz}^d$$

with $k_{lz}^d(s_s) = 1$, and $\bar{\phi}_{lz}^d = \phi_{lz}^d(s_s)$. If we introduce the desired orientations into an extended virtual body configuration space defined by $(R, \boldsymbol{r}, k^e, \boldsymbol{k^d}) \in (SE(p) \times \mathbb{R} \times \mathbb{R}^{\sum_{n=1}^{M} Z_n}$, where

$$\boldsymbol{k^d} = (k_{11}^d, \ldots, k_{1Z_1}^d, \ldots, k_{M1}^d, \ldots, k_{MZ_M}^d)^T,$$

the dynamics of this virtual body are defined by

$$\dot{\boldsymbol{r}} = \widehat{\frac{d\boldsymbol{r}}{ds}}\dot{s}, \quad \dot{R} = \frac{dR}{ds}\dot{s}, \quad \dot{k}^e = \frac{dk^e}{ds}\dot{s}, \quad \dot{\boldsymbol{k}}^{\boldsymbol{d}} = \frac{d\boldsymbol{k}^{\boldsymbol{d}}}{ds}\dot{s}. \tag{3.1.3}$$

Note that the term *deformation* is to used to describe the effect of this maneuver on the vehicle formation, not on the virtual body. That is, this maneuver does not affect the position of the virtual leaders in any way.

3.1.4 Deformation and Expansion/Contraction Alternative

In Section 2.4 we introduced a potential, denoted V_h^p, designed to regulate relative position of the vehicles about virtual leaders. These potentials act to drive $\boldsymbol{h}_{il}$ towards a desired relative position vector $\boldsymbol{d}_{lz}$ where $i = 1, \ldots, N$ identifies the vehicle, $l = 1, \ldots, M$ identifies the virtual leader and $z = 1, \ldots, Z_l$. By introducing dynamics to $\boldsymbol{d}_{lz}$ formations can be made to simultaneously deform and expand/contract. Parameterizing these dynamics by s yields

$$\dot{\boldsymbol{d}}_{lz}(s) = \frac{d\boldsymbol{d}_{lz}}{ds}\dot{s}.$$

When these potentials are utilized, extended virtual body configuration space is defined by $(R, \boldsymbol{r}, \boldsymbol{d}) \in SE(p) \times \mathbb{R}^{p\sum_{n=1}^{M} Z_n}$, where

$$\boldsymbol{d} = (\boldsymbol{d}_{11}^T, \ldots, \boldsymbol{d}_{1Z_1}^T, \ldots, \boldsymbol{d}_{M1}^T, \ldots, \boldsymbol{d}_{MZ_M}^T)^T,$$

with virtual body dynamics given by

$$\dot{\boldsymbol{r}} = \widehat{\frac{d\boldsymbol{r}}{ds}}\dot{s}, \quad \dot{R} = \frac{dR}{ds}\dot{s}, \quad \dot{\boldsymbol{d}}_{lz} = \frac{d\boldsymbol{d}}{ds}\dot{s}. \tag{3.1.4}$$

(3.1.4) provides the same maneuver capabilities as those provided in (3.1.3); they vary only in the type of potentials used to construct the formation.

3.1.5 Sensor Driven Trajectories

In Section 3.1.1 we presented an example where the virtual body trajectory was prescribed to generate translation in a fixed direction with fixed orientation. With the developments in

this chapter, the virtual body trajectory can be prescribed with many more degrees of freedom. Furthermore, the specification of virtual body direction, i.e. $dR/ds, \widehat{d\boldsymbol{r}}/ds, dk^e/ds$, etc., can be chosen to be a function of the measurements taken by sensors on the vehicles. For instance, suppose that we have underwater vehicles and each can measure a scalar environmental field T such as temperature, salinity, or biomass concentration. These measurements can be used to estimate the gradient of the field ∇T_{est} at the center of mass of the group. If the mission is to move the vehicle group to a maximum in the field T, e.g. hot spots or high concentration areas, an appropriate choice of direction for the virtual body dynamics is

$$\widehat{\frac{d\boldsymbol{r}}{ds}} = \nabla T_{\text{est}} \, .$$

This drives the virtual body, and thus the vehicle group, to a local maximum in T. Proof of convergence to a maximum with gradient climbing using least-squares estimation of gradients (with the option of Kalman filtering to use past measurements) are presented in [64]. The optimal formation (shape and size) that minimizes the least-square gradient estimation error is also developed in [64]. Adaptive gradient climbing is then possible; for example, the diameter of the formation (spatial resolution of the sensor array) can be changed in response to measurements for optimal estimation of the field.

The approach to gradient climbing can be extended to drive formations to and along fronts and boundaries of features. For example, measurements of a scalar field can be used to compute second and higher-order derivatives in the field, necessary for estimating front locations (e.g. locations of maximum gradient). This will be discussed in Chapter 4.

3.2 Formation Speed

In Section 3.1 we explained how various formation maneuvers can be implemented by defining trajectories in the virtual body's (extended) configuration space. These trajectories are parameterized by a scalar variable s and in each case we showed how the virtual body dynamics (in time) can be written as the product of virtual body direction and virtual body speed $\dot{s}$. For example, for group translation we parameterize the position of the virtual body center of mass $\boldsymbol{r} = \boldsymbol{r}(s)$ such that its dynamics can be written $\dot{\boldsymbol{r}} = (\widehat{d\boldsymbol{r}}/ds)\ \dot{s}$. In this section we present a control law for $\dot{s}$ which guarantees that a formation error remains below a user-specified upper bound as s evolves from s_s to some final s_f. This control law also allows the specification of a desired virtual body speed, v_0, which will bound $\dot{s}$ and be obtained as the formation error approaches zero [62].

Denote the state of the vehicle group as $\boldsymbol{\chi} = (\boldsymbol{x}_1^T, \ldots \boldsymbol{x}_N^T, \dot{\boldsymbol{x}}_1^T, \ldots \dot{\boldsymbol{x}}_N^T)^T \in \mathbb{R}^{2Np}$ and the desired equilibrium configuration $\boldsymbol{\chi}^* \in \mathbb{R}^{Np}$. Suppose a vehicle control law is known which provides asymptotic stability of $\boldsymbol{\chi} = \boldsymbol{\chi}^*$ when the virtual body is *stationary* , i.e. when $\dot{s} = 0$. By Lyapunov converse theorems (e.g. see Theorem 4.16 in [40]) we know there exists a Lyapunov function to prove asymptotic stability of $\boldsymbol{\chi}^*$ for s fixed. Suppose one such function is given by $\Phi(\boldsymbol{\chi})$ and thus $\dot{\Phi} = \frac{\partial \Phi}{\partial \boldsymbol{\chi}}^T \dot{\boldsymbol{\chi}} \leq 0$, and $\dot{\Phi} = 0$ if and only if $\boldsymbol{\chi} = \boldsymbol{\chi}^*$, for all $\boldsymbol{\chi} \in B_c$ where B_c is the ball of radius c about $\boldsymbol{\chi}^*$. By introducing virtual body maneuvers, s will no longer be constant. This implicitly makes the desired formation configuration a function of s, i.e. $\boldsymbol{\chi}^* \equiv \boldsymbol{\chi}^*(s)$. Since the Lyapunov function also depends on the virtual body motion, we have $\Phi \equiv \Phi(\boldsymbol{\chi}, s)$. The following theorem presents a control law for $\dot{s}$ which guarantees that $\Phi(\boldsymbol{\chi}, s) < \Phi_U$ (the user specified upper bound) given $\Phi(\boldsymbol{\chi}(t_0), s_s) < \Phi_U$. The s-dependent function $\Phi(\boldsymbol{\chi}, s)$ is interpreted as the *formation error.*

Theorem 3.2.1. (Convergence and Boundedness) [64] *Let $\Phi(\boldsymbol{\chi}, s)$ be a Lyapunov function for every fixed choice of s with $\Phi(\boldsymbol{\chi}^*(s), s) = 0$. Let Φ_U be a desired upper bound on the value of this Lyapunov function such that the set $\{\boldsymbol{\chi} : \Phi(\boldsymbol{\chi}, s) \leq \Phi_U\}$ is bounded. Let v_0 be a nominal desired formation speed and δ a small positive scalar. Let $h : \mathbb{R}^+ \to \mathbb{R}^+$ be a continuous function with compact support in $\{\Phi \mid \Phi \leq \Phi_U/2\}$ and $h(0) > 0$. If the endpoint is not reached, i.e. for $s < s_f$, let $\dot{s}$ be given by*

$$\dot{s} = \min\left\{ v_0,\ h(\Phi(\boldsymbol{\chi}, s)) + \frac{-\left(\frac{\partial \Phi}{\partial \boldsymbol{\chi}}\right)^T \dot{\boldsymbol{\chi}}}{\delta + |\frac{\partial \Phi}{\partial s}|} \frac{(\delta + \Phi_U)}{(\delta + \Phi(\boldsymbol{\chi}, s))} \right\} \tag{3.2.1}$$

with initial condition $s(t_0) = s_s$. At the endpoint and beyond, i.e. for $s \geq s_f$, set $\dot{s} = 0$. Then, the coupled vehicle-virtual body system asymptotically converges to $(\boldsymbol{\chi}, s) = (\boldsymbol{\chi}^*(s_f), s_f)$. Furthermore, if at initial time t_0, $\Phi(\boldsymbol{\chi}(t_0), s(t_0)) \leq \Phi_U$, then $\Phi(\boldsymbol{\chi}, s) \leq \Phi_U$ for all $t \geq t_0$ and thus bounded.

Proof: See Appendix A.

Remark 3.2.1. *A typical choice of $h(\Phi)$ is*

$$h(\Phi) = \begin{cases} \frac{1}{2} v_0 \left(1 + \cos\left(\pi \frac{2}{\Phi_U} \Phi\right)\right) & \text{if } |\Phi| \leq \frac{\Phi_U}{2} \\ 0 & \text{if } |\Phi| > \frac{\Phi_U}{2} \end{cases}$$

Here, $h(0) = v_0 > 0$ guaranteeing asymptotic stability and giving $\dot{s} = v_0$ at $\Phi = 0$. $\dot{s} \leq v_0$ because of the min-operator in (3.2.1). Its support is limited to $|\Phi| \leq \frac{\Phi_U}{2}$ thus not affecting the $\Phi \leq \Phi_U$ property.

Remark 3.2.2. *The typical effect of the second term within the min function in (3.2.1) is to slow the virtual body dynamics to guarantee that Φ does not exceed Φ_U.*

Remark 3.2.3. *The choice of mission trajectory appears in the control law for $\dot{s}$ implicitly through the term $\frac{\partial \Phi}{\partial s}$. This highlights the decoupling between the design of trajectories to*

meet mission requirements and the design of virtual body dynamics to ensure formation stabilization during the maneuver.

Remark 3.2.4. *Consider the case in which vehicle control laws are derived from artificial potentials, e.g. as in Chapter 2. Suppose that the desired formation equilibria correspond to isolated minima of these potentials. Since* $\Phi(\boldsymbol{\chi}, s)$ *is a Lyapunov function for the s-frozen system,* $\boldsymbol{\chi}^*$ *must be of the form* $\boldsymbol{\chi}^* = ({\boldsymbol{x}_1}^{*T}, \ldots, {\boldsymbol{x}_N}^{*T}, 0, \ldots, 0)^T$ *where* ${\boldsymbol{x}_i}^*$ *denotes any desired equilibrium position for the ith vehicle as long as* $({\boldsymbol{x}_1}^*, \ldots, {\boldsymbol{x}_N}^*)$ *is the desired formation configuration. During the maneuver when* $\dot{s} > 0$*, on average* $\dot{\boldsymbol{x}}_i \neq 0$ *and thus* $\Phi(\boldsymbol{\chi}, s) > 0$ *since* $\boldsymbol{\chi} \neq \boldsymbol{\chi}^*$*.*

Remark 3.2.5. *Selection of* Φ_U *should be consistent with* v_0 *and* $\Phi(\boldsymbol{\chi}, s) > 0$ *during the maneuver. For example, during a pure virtual body translation where* $s_f >> s_s$*, if* $\dot{s}$ *converges to* v_0 *and subsequently* $\dot{\boldsymbol{x}}_i$ *converges to* $v_0 \frac{\widehat{d\boldsymbol{r}}}{ds}$*,* Φ_U *should be at least equal to* $\Phi(\boldsymbol{\chi}^\dagger, s)$ *where* $\boldsymbol{\chi}^\dagger = ({\boldsymbol{x}_1}^{*T}, \ldots, {\boldsymbol{x}_N}^{*T}, v_0 \frac{\widehat{d\boldsymbol{r}}}{ds}^T, \ldots, v_0 \frac{\widehat{d\boldsymbol{r}}}{ds}^T)^T$*.*

3.3 Simulation: Formation Translation and Rotation

To demonstrate this controller and motivate a discussion of its performance, a simulation of a two-vehicle planar rotation and translation using a virtual body composed of two virtual leaders is presented. Starting from rest, the virtual body is made to translate in a straight line for 5 units of time. The line connecting the two virtual leaders is parallel to the direction of motion. After 5 time units the virtual body is made to rotate 90° counterclockwise while the virtual body is still translating. To effect rotation about the center of mass of the virtual body, we parameterize a trajectory in $SO(2)$ by s. The $\dot{s}$ dynamics are prescribed by equation (3.2.1) with h as suggested in Remark 3.2.1. After 23 time units the virtual

body is halted by setting $\dot{s} = 0$.

In this example, the distance between the two virtual leaders is chosen to be $2\sqrt{h_0^2 - d_0^2/4}$. The center of mass of the virtual body is initially at the origin of the inertial frame, i.e. $\boldsymbol{r} = 0 \in \mathbb{R}^2$. The simulation is started with the two virtual leaders in a line along the horizontal as shown in Figure 3.3.1a. Initially, the two vehicles are in the stable configuration corresponding to the global minimum of the sum of the artificial potentials, i.e., they sit at a distance d_0 from one another and a distance h_0 from each of the virtual leaders.

Virtual body translation to the right is specified by choosing $\frac{\widehat{d\boldsymbol{r}}}{ds} = (1, 0) \in \mathbb{R}^2$. The objective of the rotation is to produce the formation shown in Figure 3.3.1b. The path of the virtual body is counterclockwise rotation $R(s) \in SO(2)$, equivalently $\theta(s)$ (see Figure 3.3.1b) will go from 0 to $\pi/2$ by choosing

$$\frac{d\theta}{ds} = k_\beta(\beta(t; t_l, t_u) - 1)(\theta(s) - \pi/2).$$

where k_β is a constant gain. The $(\beta - 1)$ term is included to activate rotation at t_l. Recall that we define the bump function $\beta(t; t_l, t_u)$ (see Figure 2.2.2) such that $\beta = 1$ for $t < t_l$, $\beta = 0$ for $t \geq t_u$ and β decreases monotonically for $t \in (t_l, t_u]$. In this simulation, we choose $t_l = 5$ time units , $t_u = 10$ time units and $k_\beta = 0.5$.

The nominal desired speed was chosen as $v_0 = 1$ space units per time unit. At $t = 23$ the virtual body is halted and the vehicles should then converge to the new equilibrium configuration corresponding to the global minimum of the sum of the artificial potentials. This is the formation shown in Figure 3.3.1b.

The controlled dynamics for each vehicle are given by

$$\begin{aligned}
\ddot{\boldsymbol{x}}_1 &= -\nabla V_I(x_{12}) - \nabla V_h^c(h_{11}) - \nabla V_h^c(h_{12}) - \alpha_v \dot{\boldsymbol{x}}_1 \\
\ddot{\boldsymbol{x}}_2 &= -\nabla V_I(x_{21}) - \nabla V_h^c(h_{21}) - \nabla V_h^c(h_{22}) - \alpha_v \dot{\boldsymbol{x}}_2.
\end{aligned}$$

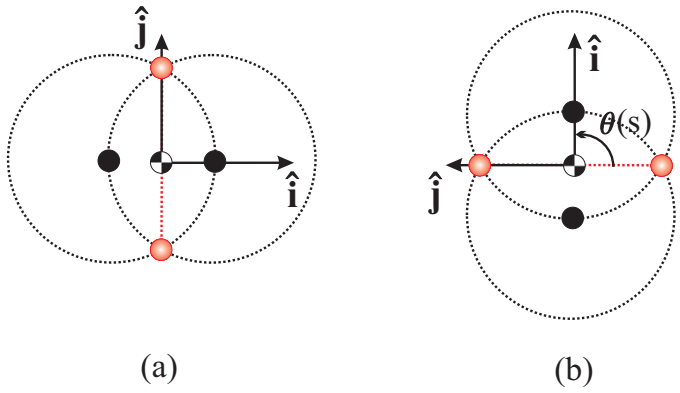

Figure 3.3.1: **Formation Rotation.** Shaded dots are vehicles and solid dots are virtual leaders. The dotted circle around each virtual leader has radius h_0. a) Formation initially at global minimum of total potential. b) Formation after rotation by 90°.

The artificial potentials used in this simulation are

$$V_h^c = \begin{cases} \alpha_h \left(\frac{1}{3}h_{il}^3 - h_0^3 \ln h_{il} - \frac{1}{3}h_0^3 + h_0^3 \ln h_0\right) & 0 < h_{il} \leq h_1 \\ 0 & h_{il} > h_1 \end{cases} \tag{3.3.1}$$

$$V_I = \begin{cases} \alpha_I \left(\frac{1}{3}x_{ij}^3 - d_0^3 \ln x_{ij} - \frac{1}{3}d_0^3 + d_0^3 \ln d_0\right) & 0 < x_{ij} \leq d_1 \\ 0 & x_{ij} > d_1. \end{cases} \tag{3.3.2}$$

We also use

$$\Phi(\boldsymbol{\chi}, s) = \frac{1}{2}\sum_{i=1}^{2}\left[\|\dot{\boldsymbol{x}}_i\|^2 + \sum_{j\neq i}^{2} V_I(x_{ij}) + 2\sum_{l=1}^{2} V_h^c(h_{il})\right]. \tag{3.3.3}$$

For fixed s, $\Phi(\boldsymbol{\chi}, s)$ is the Lyapunov function presented in Chapter 2 to prove stability for vehicle convergence with a stationary virtual body. This is extended to the variable s by including the s-dependence of $h_{il} = x_i(t) - b_l(s(t))$ in (3.3.3). Following Remark 3.2.5 the upper bound Φ_U is set at $\Phi_U = 1.1$. This follows from the fact that $\Phi \geq \frac{1}{2}\sum_{i=1}^{2}\|\dot{\boldsymbol{x}}_i\|^2$ so that if the virtual body is to converge to v_0 while translating, then $\Phi \geq v_0^2 = 1$.

The equations of motion were integrated in MATLAB using a Runge-Kutta 4th order integrator for 30 time units with parameters $\alpha_I = 10$, $\alpha_h = 10$, $d_0 = 2\sqrt{3}$, and $h_0 = 2$. The damping coefficient α_v was taken to be $\alpha_v = 2I$, where I is the identity matrix. We take d_1

and h_1 to be 100 so that neither x_{ij} nor h_{il} will approach the discontinuities at d_1 and h_1, respectively. The resulting vehicle and virtual body trajectories are plotted in Figure 3.3.2. In the top left pane we show the initial formation and the evolution for the first 2 time units, during which the vehicles and virtual body start from rest and translate in the $+X$ direction (refer to Figure 3.3.2). In the top right pane we show the trajectories for $t = 5$ to $t = 10$. During this interval the virtual body begins to rotate. In the bottom left pane we show the trajectories for $t = 10$ to $t = 20$. During this interval the virtual body completes the rotation. In the bottom right pane we show the trajectories for $t = 20$ to $t = 30$.

Figure 3.3.3 shows the evolution of $\Phi(\boldsymbol{\chi}, s)$ (the formation error function) during the controlled translation and rotation of the two-vehicle formation. Initially, $\Phi(\boldsymbol{\chi}, s) = 0$ since we start the vehicle at the equilibrium configuration. During the rotation, $\Phi(\boldsymbol{\chi}, s)$ increases, but as expected $\Phi(\boldsymbol{\chi}, s) \leq \Phi_U$ throughout. At roughly $t = 12$ we see that Φ dips below Φ_U and converges to some value below it. Finally at $t = 23$ when the virtual body is halted and Φ converges to 0.

In Figure 3.3.4 we plot $\dot{s}$ versus t in the left pane and θ versus t in the right pane. Notice that before the rotation, $\dot{s}$ converges to a value less than v_0 (the dashed line). This illustrates one limitation of the controller (3.2.1). In this example, v_0 serves only as an upper bound for $\dot{s}$. This is a result of the statement made in Remark 3.2.4. That is, suppose $\dot{s}$ was driven towards v_0 (from below). This implies that $\Phi \geq v_0^2$. However, $\dot{s}$ has only been shown to converge to v_0 as $\Phi \to 0$. There is no guarantee that $\dot{s}$ will converge to v_0 otherwise.

When the virtual body rotation is initiated there is a decrease in $\dot{s}$. At this time Φ remains unchanged at the Φ_U bound. This indicates that the controller in (3.2.1) is working as designed by slowing the virtual body dynamics to ensure Φ does not exceed Φ_U. Once the rotation is near completion the second argument of the "min" function in (3.2.1)

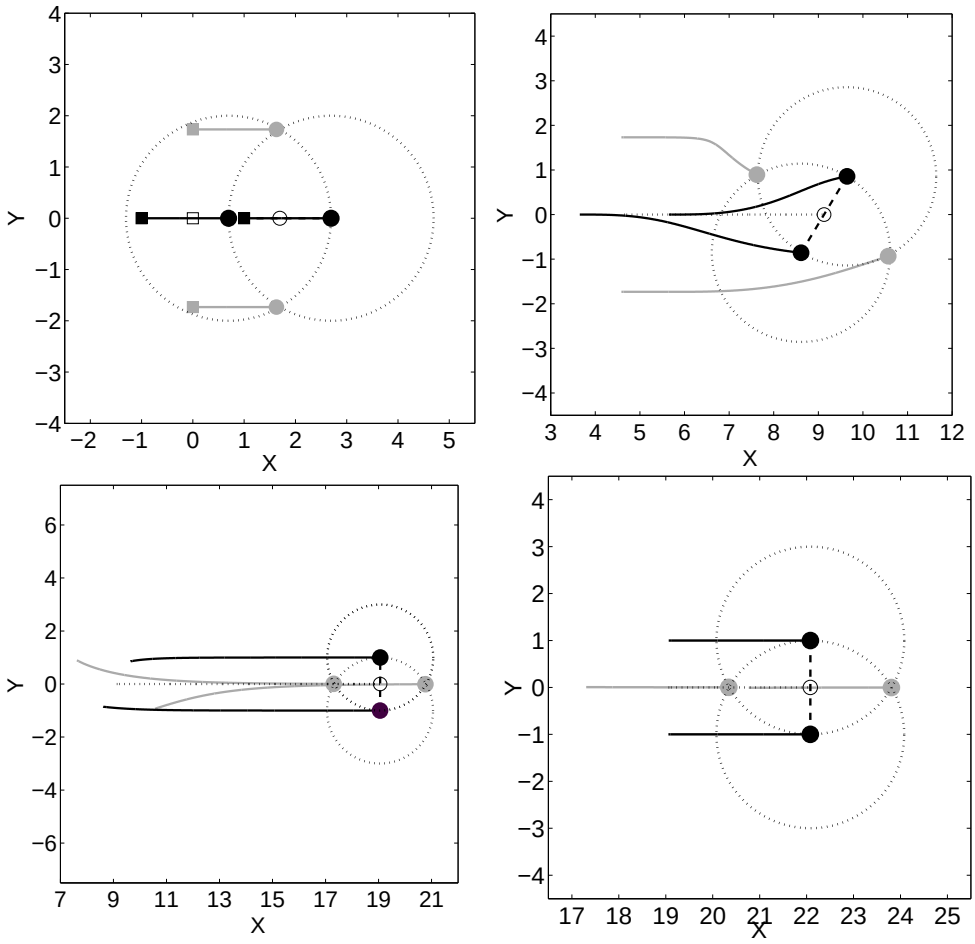

Figure 3.3.2: **Simulation Trajectories.** Shaded dots are vehicles and solid dots are virtual leaders. Lines are their respective trajectories. Dotted circles about virtual leaders have radius h_0. Small circle illustrates virtual body center of mass. Dotted line is its respective trajectory. The squares in the top left pane illustrate initial conditions.

exceeds v_0 and thus $\dot{s}$ becomes equal to v_0. In this case, limiting $\dot{s}$ results in Φ converging to a value less than Φ_U (at $t = 12$).

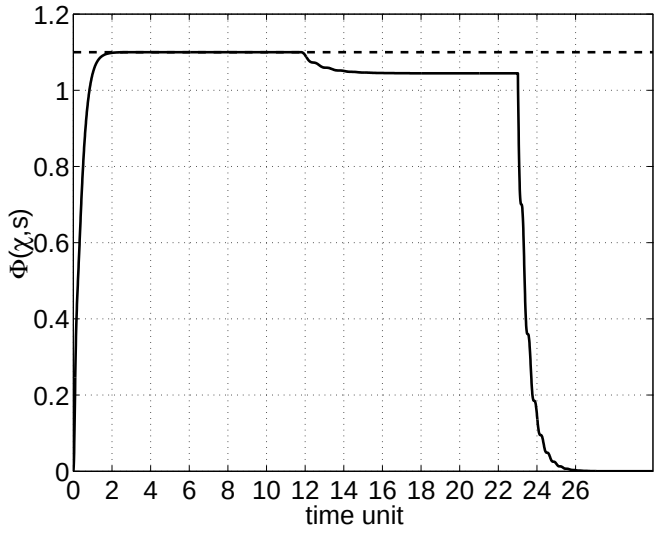

Figure 3.3.3: **Formation Error Function.** $\Phi(\boldsymbol{\chi}, s)$ versus time. Dashed line indicates $\Phi_U = 1.1$.

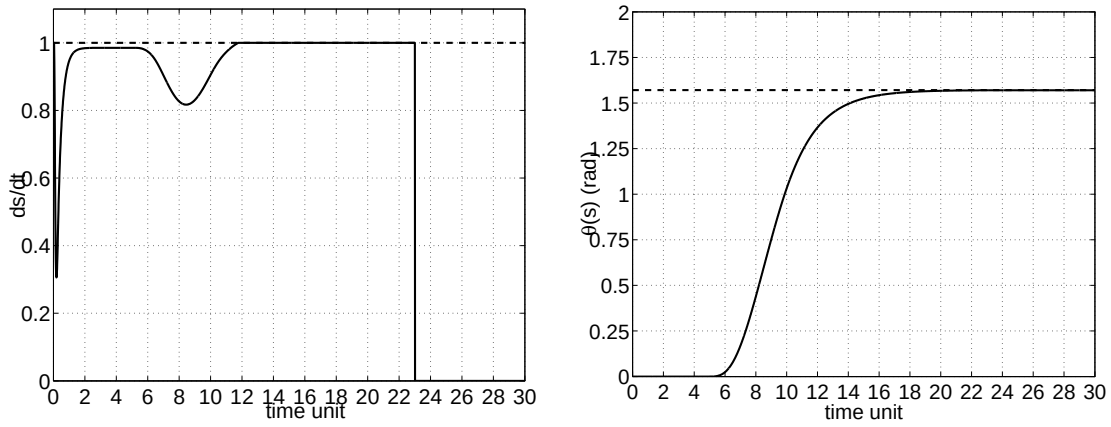

(a) (b)

Figure 3.3.4: **Virtual Body Dynamics.** (a) $\dot{s}$ versus time. Dashed line indicates $v_0 = 1.0$. (b) $\theta(s)$ versus time. Dashed line indicates $\theta = \pi/2$.

Chapter 4

Adaptive Sampling with Vehicle Arrays

With a framework for coordinating vehicle groups into dynamic sensor arrays in place, we now investigate how to use these arrays to achieve the scientific objective of adaptive ocean sampling. Recall that our control technique provides a decoupling of the formation stabilization problem from the mission planning problem. Thus we are free to select mission parameters such as direction of travel and formation spacing independently of formation stabilization considerations. In this chapter we examine the roles of these parameters in enabling adaptive sampling using vehicle fleets. Our context will be oceanographic and we specialize to the problem of feature tracking. This is just one subproblem of the large field of ocean sampling.

In Section 4.1 we define the adaptive ocean sampling problem using mobile sensor arrays. We also motivate the specific adaptive sampling problems to be addressed, namely gradient climbing and front tracking, and define the problem domain in which subsequent analysis will be based. In Section 4.2 we present techniques for estimating derivatives of our ocean

model from noisy measurements taken by each vehicle in the array, and we present an optimal formation problem in terms of the estimate error covariance. These derivatives are necessary ingredients of the gradient climbing and front tracking strategies. We then present a Kalman filter in Section 4.3 that uses past information with present information to improve estimates. Lastly, in Section 4.4 we present our gradient climbing and front tracking algorithms and demonstrate their effectiveness through simulation.

4.1 Adaptive Ocean Sampling with Multiple AUVs

"A central objective in ocean sampling experiments is to collect the data that best reveals the ocean processes of interest given available resources. There are a number of metrics that can be used to help define what is meant by the best data set, and the appropriate choice of metric will typically depend on the spatial and temporal scales of interest. For example, for a broad area, the goal might be to collect data that minimizes estimation error of the process of interest. For smaller scales, the goal may be to collect data in and around features of interest, e.g., to sample at locations of greatest dynamic variability. A fundamental problem is to choose the paths of available mobile sensor platforms, notably sensor-equipped AUVs, in an optimal way. These paths, however, do not need to be predetermined, but instead can be adapted in response to sensor measurements. This is what we refer to as *adaptive sampling*" [32]. In this chapter we focus on sampling at smaller spatial scales and address the problems of gradient climbing and front tracking.

Feedback control is implicit in adaptive sampling. For example, in covering a broad region, the AUV's should be controlled to appropriately explore the region and avoid approaching one another (in which case they might become redundant sensors). For adaptive feature tracking, the formation control described in Chapters 2 and 3 are merged with the

gradient climbing and front tracking algorithms described in this chapter. A central theme is that feedback plays multiple critical roles in managing uncertainty. First, feedback can be used to redesign paths in response to new sensor measurements. As new information about the environment becomes available, the AUVs should react accordingly and not be constrained by plans designed *a priori* . Of equal importance, feedback is needed to manage the uncertainty inherent in the dynamics of the vehicles in the water.

Suppose there is a scalar field $T : \mathbb{R}^2 \to \mathbb{R}$ and consider the following motivating example for adaptive sampling where each vehicle in a sensor array can compute and communicate the gradient of T at its current position. In the following lemma, we propose an algorithm for gradient descent of a three-vehicle triangular formation in a planar quadratic field $T(\boldsymbol{x}) = \frac{1}{2}\boldsymbol{x}^T P\boldsymbol{x}$, $\boldsymbol{x} \in \mathbb{R}^2$ and prove convergence to the minimum of this field.

Lemma 4.1.1 (Gradient Descent in Quadratic Field)**.** *Consider three vehicles and a single virtual leader with artificial potentials defined with global minimum corresponding to the vehicles in a triangular formation about the virtual leader. Let the control law be given by equation (2.1.2). Consider the gradient field* $T(\boldsymbol{x}) = \frac{1}{2}\boldsymbol{x}^T P\boldsymbol{x}$, $\boldsymbol{x} \in \mathbb{R}^2$, *where* $P \in \mathbb{R}^{2\times 2}$ *is positive definite. Let each (ith) vehicle be capable of measuring the local gradient,* $\nabla T(\boldsymbol{x}_i) = P\boldsymbol{x}_i, i = 1, 2, 3,$ *at its location given by* $\boldsymbol{x}_i \in \mathbb{R}^2$ *with respect to a fixed inertial frame. Let* $\boldsymbol{r} \in \mathbb{R}^2$ *be the position vector of the virtual leader which is contained within the convex hull of the three vehicle formation. Define* $\boldsymbol{p}_i = \boldsymbol{x}_i - \boldsymbol{r}$*. For each of the three vehicles, define* a_i *to be the area of the triangle with vertices coincident with the other two vehicles and virtual leader, i.e.* $a_i = \frac{1}{2}||\boldsymbol{p}_j \times \boldsymbol{p}_k||$ *for* $i, j, k \in \{1, 2, 3\}$ *and* $i \neq j, i \neq k, j \neq k$*. Additionally, let* $a = \sum_{i=1}^{3} a_i$*. Suppose that the virtual leader is given dynamics*

$$\dot{r} = \frac{d\boldsymbol{r}}{ds}\dot{s}$$

with

$$\frac{d\boldsymbol{r}}{ds} = -\sum_{i=1}^{3} \frac{a_i}{a} \nabla T(\boldsymbol{x}_i)$$

and $\dot{s}$ given by equation (3.2.1) where $\Phi(\boldsymbol{x}_1, \boldsymbol{x}_2, \boldsymbol{x}_3, s)$ is given by equation (2.5.1) with global minimum at zero. Then the formation will asymptotically converge to the minimum of T, i.e., $\boldsymbol{r}$ will converge to the origin and the formation will converge to the equilibrium at $s = s_f$. Further, $\Phi(\boldsymbol{x}_1, \boldsymbol{x}_2, \boldsymbol{x}_3, s) \leq V_U$ throughout.

Proof: Convergence of the virtual leader to the minimum of T can be proven with the Lyapunov function Ψ given by

$$\Psi(\boldsymbol{r}) = T(\boldsymbol{r}) = \frac{1}{2}\boldsymbol{r}^T P \boldsymbol{r}.$$

We compute

$$\begin{aligned}
\dot{\Psi} \;=\; \nabla T(\boldsymbol{r}) \cdot \dot{\boldsymbol{r}} \;&=\; -\frac{\dot{s}}{a} \nabla T(\boldsymbol{r}) \cdot \sum_{i=1}^{3} a_i \nabla T(\boldsymbol{x}_i) \\
&=\; -\frac{\dot{s}}{a} P\boldsymbol{r} \cdot \sum_{i=1}^{3} a_i P\boldsymbol{x}_i \\
&=\; -\frac{\dot{s}}{a} P\boldsymbol{r} \cdot \sum_{i=1}^{3} a_i P(\boldsymbol{p}_i + \boldsymbol{r}) \;=\; -\dot{s}||P\boldsymbol{r}||^2 \leq 0
\end{aligned}$$

since $\sum_{i=1}^{3} a_i \boldsymbol{p}_i = 0$ and $\dot{s} \geq 0$. Since $\dot{s} = 0$ only at $s = s_f$ and $P\boldsymbol{r} = 0$ only at $\boldsymbol{r} = 0$, $\dot{\Psi} = 0$ only at $r = 0$ in which case $T = 0$. Here we assume that s_f is chosen large enough that the formation reaches its goal. Boundedness of the formation Lyapunov function ($\Phi(\boldsymbol{x}, s) \leq V_U$) follows from Theorem 3.2.1. ∎

Remark 4.1.1. *The quantity $\sum_{i=1}^{3} \frac{a_i}{a} \nabla T(\boldsymbol{p}_i)$ is essentially a first-order (linear) approximation of the gradient field at $\boldsymbol{r}$, $\nabla T(\boldsymbol{r})$. Thus, for a quadratic field T the approximation is exact.*

Remark 4.1.2. *The result in Lemma 4.1.1 holds locally near the minimum of a more general gradient field when, near the minimum, the field can be approximated by a quadratic.*

If each vehicle can individually sense the gradient, we have illustrated a simple method for averaging these measurements which guarantees for the quadratic field that the vehicles will remain in formation while the vehicle fleet descends the gradient. In practice the individual gradient measurements can be obtained from multiple sensors on each vehicle. Of course, the practical value of the gradient measured at the scale of the vehicle size may be quite limited when the ultimate goal is to estimate the gradient at the center of the vehicle array. The practicality relies on the spatial scales of interest of the scalar field which dictate the array size (along with noise statistics if noise is present). In fact, in Section 4.2 we derive optimal vehicle spacings for estimating derivatives and show that the optimal measurement separation is proportional to higher-order derivatives and the noise variance. In this chapter we rely only on the scalar measurements obtained by each vehicle (and *not* a gradient measurement by each) and make use of the spatial distribution of measurements that a formation of vehicles affords. In [59, 7, 8] gradient ascent or descent is demonstrated (and proven) in the absence of noise, where given a single sensor per vehicle, each vehicle computes the gradient of T projected in its direction of motion.

4.1.1 Sampling Objectives

We are now poised to present the sampling objectives we will address. These objectives are

- to locate extrema, i.e. local minima and maxima, in the measured field and,
- to track frontal boundaries, such as temperature or salinity fronts.

To direct the vehicle fleet towards extrema we perform adaptive gradient climbing (or descent) in the sampled field. For example, gradient climbing could be used to steer a fleet towards (and therefore locate) a pollutant source by tracking the gradient of pollutant concentration. Alternatively, it may be desirable to direct the fleet to sample particularly

cold or warm water; in this case the group would be made to track the thermal gradient. We also present a *projected gradient* method which is designed to perturb a trajectory selected *a priori* in the direction of the estimated gradient.

Fronts are distinctive oceanographic features that mark the boundaries between water bodies with differences in temperature, salinity, density, or other characteristics [33]. They are characterized by large spatial gradients in these variables relative to the surrounding water.

The aggregation of marine organisms at frontal systems is well documented [47]. For example, during the spring and summer months in Monterey Bay frontal systems are observed to form as a result of upwelling. Upwelling events are caused by favorable cross shore winds which draw water away from the coastline which is then replaced by colder and nutrient rich water from below. Organisms such as phytoplankton thrive on this nutrient rich water and, in particular, they do so at the frontal boundaries [33]. The abundance of organisms at the lower levels of the food chain attract animals at higher levels. Even sea birds (and fisherman) have been known to aggregate at these frontal boundaries [13].

The study of fronts was a research focus of the AOSN II project in Monterey Bay, CA. During AOSN II, data collected by various sensors, such as autonomous vehicles, drifters, ships, etc, was assimilated into ocean models for the purpose of improving their predictive capabilities. One goal of the experiment was to forecast position and characteristics of discovered small-scale dynamical features like fronts and upwelling plumes [22]. A sensor array capable of directing itself towards and sampling along these frontal features or directing itself towards extrema and sampling within an upwelling plume may provide valuable data that, when assimilated, could in principle reduce the model error associated with predicting the location of these features. Thus, frontal regions are areas of much interest to

the oceanographic community, and sensor arrays capable of directing themselves towards and along these fronts are of potentially great value.

Another potential application for both gradient climbing and front tracking is in studying harmful algae blooms such as *red tides*. A red tide occurs when certain varieties of toxin-releasing algae experience population blooms and accumulate on the surface of the water and form dense patches. These blooms can have a great impact on the local ecosystem as the released toxins are distributed through the food chain affecting zooplankton, shellfish, fish, birds, marine mammals, and even humans [4]. Given the ecological and economical effects of these blooms, it is not surprising that research is underway to understand their dynamics and constituency. In fact, the use of multiple autonomous underwater gliders has already been proposed to monitor for the onset of red tides [17]. Front tracking algorithms provide a means for tracing the boundaries of these blooms and collecting data in and around these boundaries.

Fronts are ridges of high spatial variation in the sampled field. Not surprisingly, the indicator to detect and localize fronts involves the spatial gradients and high-order derivatives of the scalar field of interest. However, one is hard pressed to find a precise mathematical definition of a front in the oceanographic literature. Such a definition does exist in the meteorological literature. It is called the Thermal Front Parameter (TFP), denoted by ν [81]. The TFP is often used to produce frontal structures in atmospheric maps and it is a scalar function of the gradient and Hessian of the sampled field. To be precise it is the directional derivative of the magnitude of the gradient in the gradient direction (along with a normalization factor), i.e.,

$$\nu = -\nabla||\nabla T|| \cdot \frac{\nabla T}{||\nabla T||} = -\frac{\nabla T^T}{||\nabla T||} H \frac{\nabla T}{||\nabla T||}$$

where H is the Hessian of T. The *center line of the front* is defined at the contour where $\nu(T) = 0$. A *warm front* corresponds to contours or ridges where $\nu(T)$ is maximum and a *cold front* corresponds to contours or ridges where $-\nu(T)$ is maximum. These warm or cold fronts are located by taking the directional derivative of ν in the gradient direction and setting it equal to zero. The TFP front definition is illustrated in Figure 4.1.1. For example, in Figure 4.1.1a a warm front identified as a maximum of ν (along the gradient direction of T) is located at (1) whereas a front defined at $\nu = 0$ or where $\|\nabla T\|$ is maximum is located at (2). In Figure 4.1.1b, the fronts associated with a two-dimensional temperature field are illustrated.

An alternative definition of a front corresponds to regions where $\|\nabla T\|$ is maximum (note $\nu = 0$ in this case). In practice thresholding is performed where the constant ϵ_F, selected *a priori* , is used to define points belonging to a front as $\boldsymbol{X}_F = \{\boldsymbol{p} \in \mathbb{R}^l, l = 2, 3 \mid \|\nabla T(\boldsymbol{p})\| > \epsilon_F\}$. ϵ_F is a constant parameter which sets the threshold.

Whichever definition is used, estimates of the spatial variation of the field will need to be made in order to determine front locations. In Sections 4.2 and 4.3 we discuss how vehicle arrays can be used to obtain the required derivatives and in Section 4.4 we present a control strategy to direct the vehicle towards a perceived front and travel along it.

4.1.2 Problem Domain

For our investigations we model the ocean as a noisy and static environment. In ignoring the temporal dynamics of the field, we are focusing on phenomena with features, either critical points or frontal boundaries, that persist in time or evolve on time scales that are large relative to the ratio of spatial scale to vehicle speed. That is, we assume that the ratio

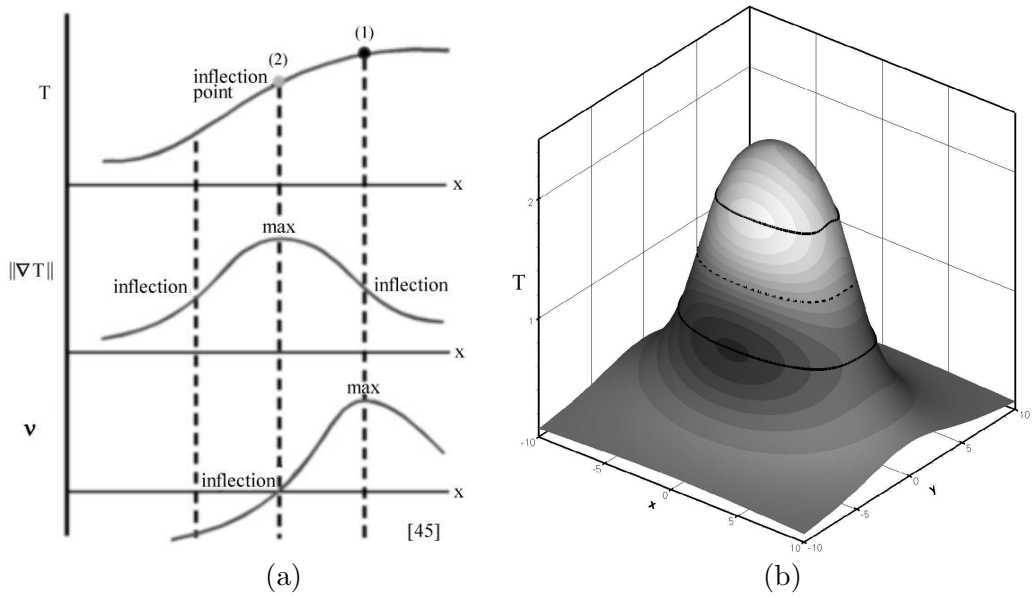

(a) (b)

Figure 4.1.1: **Front Definition.** (a) [45] From top to bottom, the scalar field, T, magnitude of its gradient, and thermal front parameter, ν, are plotted as a function of x where x parameterizes the curve tangent to the gradient of T. The black dot at (1) indicates a *warm front* corresponding to a maximum in ν (in the direction of the gradient). The gray dot at (2) indicates the *center line of the front* where $\nu = 0$. (b) Surface plot of $T = \arctan(5 - \frac{x^2}{10} - \frac{y^2}{2}), (x, y) \in \mathbb{R}^2$, with grayscale contours of ν. Dotted line indicates *center line of the front* where $\nu = 0$. Solid lines indicate *warm* and *cold fronts* where ν is maximum and minimum in the direction of the gradient of T, respectively.

of

$$\frac{v\triangle t}{\sigma_f} \gg \frac{\triangle t}{\tau_f},$$

where

$$\begin{aligned} \sigma_f &\triangleq \text{feature spatial scale,} \\ \tau_f &\triangleq \text{feature temporal scale,} \\ v &\triangleq \text{vehicle speed,} \\ \triangle t &\triangleq \text{duration of sampling mission.} \end{aligned}$$

This comparison asserts that the ratio of the distance the vehicles can travel to the spatial scale of the feature is much larger than the ratio of the duration of the sampling mission to the time scale at which the field changes. The assumption is that we can adequately sample

the field in space before the field changes significantly in time.

To make things concrete let us denote our environmental scalar $T(\boldsymbol{x}) : \mathbb{R}^l \to \mathbb{R}$, e.g. temperature, where $\boldsymbol{x} \in \mathbb{R}^l, l = 2, 3$. We assume this scalar field is a realization of a stochastic process that can be decomposed into the sum

$$T(\boldsymbol{x}) = \bar{T}(\boldsymbol{x}) + w(\boldsymbol{x})$$

of a deterministic mean field, $\bar{T}(\boldsymbol{x}) : \mathbb{R}^l \to \mathbb{R}$, where $\bar{T}$ is smooth, and $w(\boldsymbol{x}) \in \mathbb{R}$, a Gaussian noise process at $\boldsymbol{x}$[1] . The mean field can be thought as the value of the scalar field, T, averaged over the duration of the sampling experiment ($\triangle t$). We assume the noise is zero mean. Given a sequence of $w_i = w(\boldsymbol{x}_i)$ at N locations $\boldsymbol{x}_i \in \mathbb{R}^l$ for $i = 1, \ldots, N$, the covariance matrix is given by

$$E[\boldsymbol{w}\boldsymbol{w}^T] = \sigma_w^2 I + W$$

where $\boldsymbol{w} = (w_1, w_2, \ldots, w_N)^T \in \mathbb{R}^N$, $E[w_i^2] = \sigma_w^2$ for any i, I is the $N \times N$ identity matrix and W is the symmetric matrix with zeros along the diagonal given by

$$W = \begin{pmatrix} 0 & E[w_1 w_2] & \ldots & E[w_1 w_N] \\ E[w_1 w_2] & 0 & & E[w_2 w_N] \\ \vdots & & \ddots & \\ E[w_1 w_N] & E[w_2 w_N] & & 0 \end{pmatrix}.$$

If we assume the random component of the field T is completely uncorrelated then W is the zero matrix.

A measurement of this field, T_M, taken at a point $\boldsymbol{x}_i(t) \in \mathbb{R}^l$ (i.e. by the ith vehicle at time t) is given by

$$T_M(\boldsymbol{x}_i, t) = T(\boldsymbol{x}_i) + \epsilon_{Mi}, \tag{4.1.1}$$

[1] In the language of random field theory, $w(\boldsymbol{x})$, is a random field which is defined as a family of random variables indexed by $\boldsymbol{x}$. [95]

where $\epsilon_{Mi} = \epsilon_{Mi}(t)$ is the sensor noise associated with the measurement taken taken by the ith vehicle at $\boldsymbol{x}_i(t)$. $\epsilon_{Mi}(t)$ is a zero mean Gaussian distribution with variance σ_M^2. Given N vehicles and a set of measurements at locations $\boldsymbol{x}_i(t), i = \ldots, N$, we define the vector of sensor noise as $\boldsymbol{\epsilon_M}(t) = (\epsilon_{M1}(t), \epsilon_{M2}(t), \ldots, \epsilon_{MN}(t))^T$.

4.2 Derivative Estimation from Distributed Measurements

In this section we present techniques for estimating the derivatives of our field using measurements obtained from each vehicle in a sensor array.

4.2.1 Finite Differencing

Finite differencing formulas are very well known for numerical computation of derivatives, see for example [71]. In this section we present some simple formations to accurately estimate derivatives and investigate the error associated with each formation.

Consider the simple problem of estimating the derivative of the mean field, $\bar{T}$, in the plane at a point (u, v) in some coordinate frame in the direction of $\boldsymbol{n}$ given only two vehicles. As usual denote the x axis the abscissa and y axis as the ordinate. Furthermore, assume the frame is oriented such that $\boldsymbol{n}$ lies along the x axis. Aligning the vehicles along $\boldsymbol{n}$ at $\boldsymbol{x}_1 = (u + \triangle x, v)$ and $\boldsymbol{x}_2 = (u - \triangle x, v)$ where $\triangle x > 0$, and expanding $\bar{T}$ in a Taylor series about (u, v) we have

$$\begin{aligned}
\bar{T}(\boldsymbol{x}_1) &= \bar{T}(u,v) + \frac{d\bar{T}}{dx}(u,v)\triangle x + \frac{1}{2}\frac{d^2\bar{T}}{dx^2}(u,v)\triangle x^2 + \frac{1}{6}\frac{d^3\bar{T}}{dx^3}(u,v)\triangle x^3 + \mathcal{O}(\triangle x^4) \\
\bar{T}(\boldsymbol{x}_2) &= \bar{T}(u,v) - \frac{d\bar{T}}{dx}(u,v)\triangle x + \frac{1}{2}\frac{d^2\bar{T}}{dx^2}(u,v)\triangle x^2 - \frac{1}{6}\frac{d^3\bar{T}}{dx^3}(u,v)\triangle x^3 + \mathcal{O}(\triangle x^4).
\end{aligned}$$

By subtraction we find

$$\frac{d\bar{T}}{dx}(u,v) = \frac{\bar{T}(\boldsymbol{x}_1) - \bar{T}(\boldsymbol{x}_2)}{2\triangle x} - \frac{1}{6}\frac{d^3T}{dx^3}(u,v)\triangle x^2 + \mathcal{O}(\triangle x^4). \tag{4.2.1}$$

Ignoring the higher-order terms in (4.2.1), a second-order accurate estimate for the derivative along $\boldsymbol{n}$ at (u, v) is given by

$$\frac{d\bar{T}'}{dx}_{\text{est}} = \frac{\bar{T}(\boldsymbol{x}_1) - \bar{T}(\boldsymbol{x}_2)}{2\triangle x}. \tag{4.2.2}$$

This is the well known central differencing formula.

Now, we do not have $\bar{T}$ at $\boldsymbol{x}_1$ and $\boldsymbol{x}_2$ but rather T_M (at some time t) from (4.1.1). Substituting T_M for $\bar{T}$ on the right hand side of (4.2.1) and taking the expected value of the resulting expression yields

$$\begin{aligned} E\left[\frac{T_M(\boldsymbol{x}_1, t) - T_M(\boldsymbol{x}_2, t)}{2\triangle x}\right] &= E\left[\frac{\bar{T}(\boldsymbol{x}_1) - \bar{T}(\boldsymbol{x}_2) + w_1 + \epsilon_{M1} - w_2 - \epsilon_{M2}}{2\triangle x}\right] \\ &= \frac{\bar{T}(\boldsymbol{x}_1) - \bar{T}(\boldsymbol{x}_2)}{2\triangle x} \\ &= \frac{d\bar{T}'}{dx}_{\text{est}}. \end{aligned}$$

Therefore an expression for the estimated mean field derivative along $\boldsymbol{n}$, given our measurements, is given by

$$\frac{d\bar{T}}{dx}_{\text{est}} = \frac{T_M(\boldsymbol{x}_1, t) - T_M(\boldsymbol{x}_2, t)}{2\triangle x}. \tag{4.2.3}$$

This estimate is appropriate because its expected value is equal to the derivative estimate obtained by central differencing the mean field itself.

Expanding the measurement at $\boldsymbol{x}_1$ and $\boldsymbol{x}_2$ in a Taylor series about (u, v), we have

$$\begin{aligned} T_M(\boldsymbol{x}_1, t) &= \bar{T} + \frac{d\bar{T}}{dx}\triangle x + \frac{1}{2}\frac{d^2\bar{T}}{dx^2}\triangle x^2 + \frac{1}{6}\frac{d^3\bar{T}}{dx^3}\triangle x^3 + \frac{1}{24}\frac{d^4\bar{T}}{dx^4}\triangle x^4 + \mathcal{O}(\triangle x^5) + w_1 + \epsilon_{M1}, \\ T_M(\boldsymbol{x}_2, t) &= \bar{T} - \frac{d\bar{T}}{dx}\triangle x + \frac{1}{2}\frac{d^2\bar{T}}{dx^2}\triangle x^2 - \frac{1}{6}\frac{d^3\bar{T}}{dx^3}\triangle x^3 + \frac{1}{24}\frac{d^4\bar{T}}{dx^4}\triangle x^4 + \mathcal{O}(\triangle x^5) + w_2 + \epsilon_{M2}, \end{aligned}$$

where $\bar{T} = \bar{T}(u, v)$, $\frac{d\bar{T}}{dx} = \frac{d\bar{T}}{dx}(u, v)$, etc. Subtracting these expressions from one another and dropping the higher-order terms yields

$$\frac{T_M(\boldsymbol{x}_1, t) - T_M(\boldsymbol{x}_2, t)}{2\triangle x} = \frac{d\bar{T}}{dx} + \frac{1}{6}\frac{d^3\bar{T}}{dx^3}\triangle x^2 + \frac{w_1 + \epsilon_{M1} - w_2 - \epsilon_{M2}}{2\triangle x} + \mathcal{O}(\triangle x^4). \tag{4.2.4}$$

We now formulate an expression for the error in our estimate in terms of the expected value of the squared error,

$$E\left[\left(\frac{d\bar{T}}{dx}-\frac{d\bar{T}}{dx}_{\text{est}}\right)^2\right] = E\left[\left(\frac{1}{6}\frac{d^3\bar{T}}{dx^3}\triangle x^2+\frac{w_1+\epsilon_{M1}-w_2-\epsilon_{M2}}{2\triangle x}+\mathcal{O}(\triangle x^4)\right)^2\right] \quad (4.2.5)$$
$$= \frac{1}{36}\left(\frac{d^3\bar{T}}{dx^3}\right)^2\triangle x^4+\frac{1}{2\triangle x^2}(\sigma_w^2+\sigma_M^2-E[w_1w_2]),$$

where we have dropped all terms $\mathcal{O}(\triangle x^6)$ and above[2] .

We now optimize the vehicle spacing, $2\triangle x$, to minimize this error. Suppose that $\frac{E[w_1w_2]}{\triangle x^2}$ is either zero or not a function of $\triangle x$, then differentiating (4.2.5) with respect to $\triangle x$ and equating the result to zero we find

$$\frac{1}{9}\frac{d^3\bar{T}}{dx^3}^2\triangle x^3-\frac{\sigma_w^2+\sigma_M^2}{\triangle x^3}=0,$$

and thus the optimal $\triangle x \equiv \triangle x^*$ is given by,

$$\triangle x^{*6}=\frac{9(\sigma_w^2+\sigma_M^2)}{\left(\frac{d^3\bar{T}}{dx^3}\right)^2}. \quad (4.2.6)$$

Clearly the practicality of this formula is limited as it requires the knowledge of third-order derivatives. However, as stated in [64] where a similar error is used to derive an optimal spacing based on second-order derivatives, this formulation can serve as a *rule of thumb.* As noise increases it is desirable to spread the vehicles out, and as the field variation increases (manifested as increased higher-order terms), the inter-vehicle spacing should decrease.

To examine the effect of non-zero correlation in the process noise field, w, suppose that $E[w_1w_2]\neq 0$ but rather has the form of a Gaussian, e.g $E[w_1w_2]=\sigma_w^2e^{-4\frac{\triangle x^2}{\sigma_d^2}}$. σ_d is the

[2]Note that the $\mathcal{O}(\triangle x^4)$ produced by the $\mathcal{O}(\triangle x^{-1})$ and $\mathcal{O}(\triangle x^5)$ terms combining are zero after the expectation is taken since the noise is zero mean.

$\frac{1}{e}$ decorrelation length scale of the noise process. Returning to (4.2.5) and differentiating with respect to $\triangle x$ and equating the result to zero we find,

$$\frac{1}{9}\left(\frac{d^3\bar{T}}{dx^3}\right)^2 \triangle x^6 + \left(1 + 4\frac{\triangle x^2}{\sigma_d^2}\right)\sigma_w^2 e^{-4\frac{\triangle x^2}{\sigma_d^2}} - \sigma_w^2 - \sigma_M^2 = 0. \tag{4.2.7}$$

Dividing through by σ_w^2 we obtain an expression for the optimal $\triangle x$ in terms of three dimensionless parameters, $s_1 = \frac{\left(\frac{d^3\bar{T}}{dx^3}\right)^2}{\sigma_w^2}\sigma_d^6$, $s_2 = \frac{\sigma_M^2}{\sigma_w^2}$, and $\triangle\tilde{x} = \frac{\triangle x}{\sigma_d}$, i.e.

$$\frac{1}{9}s_1\triangle\tilde{x}^6 + \left(1 + 4\triangle\tilde{x}^2\right)e^{-4\triangle\tilde{x}^2} - 1 - s_2 = 0. \tag{4.2.8}$$

In Figure 4.2.1 we present a parameter study where we have varied s_2 and plotted the solution sets of (4.2.8) as a function of s_1 and $\triangle\tilde{x}$. Note that since we expect the sensor noise variance, σ_M^2, always to be less than the ocean (process) noise variance, σ_w^2, we only look at cases with $s_2 \leq 1$.

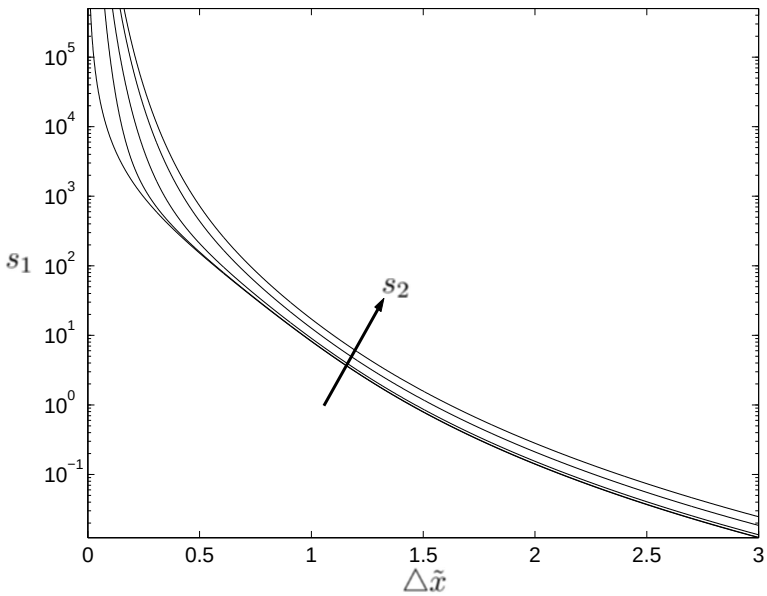

Figure 4.2.1: **Effects of Nonzero Covariance on Optimal Vehicle Separation.** The solid lines indicate solution contours of (4.2.8) for values of s_2 equal to $0, 0.01, 0.1, 0.5$, and 1. The arrow indicates the direction of increasing s_2.

Examining Figure 4.2.1 we see that for increasing values of s_1, $\triangle\tilde{x}$ decreases. Increasing

s_1 can occur by increasing σ_d, increasing the third-order derivative of T, or decreasing the ocean noise variance. Holding σ_d fixed, the effect of increasing the ratio of the third-order derivative to the ocean noise variance is to cause $\triangle x^*$ to decrease. This is analogous to the discussion above for the zero covariance case solution given by (4.2.6). The effect of increasing s_2, the ratio of sensor noise to ocean noise, while holding s_1 fixed, is to cause $\triangle \tilde{x}$ to increase. Thus, the effect of increasing sensor noise is to increase the optimal vehicle spacing.

We can get an approximate analytical solution for $\triangle x^*$ by expanding $e^{-4\frac{\triangle x^2}{\sigma_d^2}}$ up to $6th$ order terms, i.e. $e^{-4\frac{\triangle x^2}{\sigma_d^2}} \approx 1 - 4\frac{\triangle x^2}{\sigma_d^2} + 8\frac{\triangle x^4}{\sigma_d^4} - \frac{32}{3}\frac{\triangle x^6}{\sigma_d^6}$, and substituting it into (4.2.7) to yield,

$$\left(\frac{1}{9}\frac{d^3\bar{T}}{dx^3}^2 + \frac{64}{3}\frac{\sigma_w^2}{\sigma_d^6}\right)\triangle x^6 - 8\frac{\sigma_w^2}{\sigma_d^2}\triangle x^2 - \sigma_M^2 = 0. \tag{4.2.9}$$

where we have dropped the $\mathcal{O}(\triangle x^8)$ terms. Dividing through by σ_w^2 and defining

$$a_3 = \left(\frac{1}{9\sigma_w^2}\frac{d^3\bar{T}}{dx^3}^2 + \frac{64}{3}\frac{1}{\sigma_d^6}\right) \neq 0, \qquad a_2 = -8\frac{1}{a_3\sigma_d^2}, \qquad a_0 = -\frac{1}{a_3}\frac{\sigma_M^2}{\sigma_w^2},$$

and $\gamma = \triangle x^2$, we can write

$$\gamma^3 + a_2\gamma^2 + a_0 = 0.$$

The general solution to the cubic equation is given by Cardano's formula.

If we wish to compute the derivative in the y direction, we use two vehicles aligned in that direction and analogously derive

$$\frac{d\bar{T}}{dy}_{\text{est}}(u, v, t) = \frac{T_M(u, v + \triangle y, t) - T_M(u, v - \triangle y, t)}{2\triangle y}. \tag{4.2.10}$$

This suggests that four vehicles in a cross formation are sufficient to estimate the gradient of the mean field to second-order accuracy. Using this same formation, in [102] an error metric is based on second-order derivatives which are estimated through introduction of a procedure to estimate the curvature of level sets.

In the plane, if we wish to estimate the Hessian there are three second-order derivatives we will need to estimate, namely $\frac{d^2\bar{T}}{dx^2}$, $\frac{d^2\bar{T}}{dy^2}$, and $\frac{d^2\bar{T}}{dxdy}$ which can be estimated by classical finite difference equations. In the next section we present how to estimate second-order derivatives (or ever higher-order given a sufficient number of measurements) by taking a least squares error approach. The classical finite difference equations are particular solutions of the posed least squares problem. Furthermore, a least squares error formulation can provide a first-order accurate gradient estimate using only three vehicles.

4.2.2 Least-Squares Approximation

In [64] a procedure was presented to estimate the gradient by finding the best linear fit to measured data in a least squares sense. Given N noisy measurements, T_M, each taken by the ith vehicle at its current position $\boldsymbol{x}_i$ at time t, an estimate of $\bar{\boldsymbol{z}} = (\nabla\bar{T}(\boldsymbol{r})^T, \bar{T}(\boldsymbol{r}))^T$, i.e. the gradient and value of the mean field at $\boldsymbol{r} \in \mathbb{R}^l, l = 2, 3$, is sought. Recall from Chapter 2 and Chapter 3 that $\boldsymbol{r}$ is the position of the virtual body with respect to an inertial frame. Define $\boldsymbol{p}_i = \boldsymbol{x}_i - \boldsymbol{r}, i = 1, \ldots, N$ and given any $\boldsymbol{x}$, define $\boldsymbol{p} = \boldsymbol{x} - \boldsymbol{r}$. The following lemma is very similar to that presented in [64] but modified for our model selection, see Section 4.1.2.

Lemma 4.2.1 (Least Squares Estimate)**.** *The best, in a Least Squares sense, approximation $\boldsymbol{a}^T\boldsymbol{p}+\boldsymbol{b}$ of a continuously differentiable scalar field $T(\boldsymbol{x})$ about $\boldsymbol{r}$ from a set of measurements $\boldsymbol{y} = \{T_M(\boldsymbol{x}_1, t) \ldots T_M(\boldsymbol{x}_N, t)\}$ at positions $\boldsymbol{x}_i \in \mathbb{R}^l,\ N \geq l + 1$ is given by*

$$\bar{\boldsymbol{z}}_{\mathbf{LS}} = (C^TC)^{-1}C^T\boldsymbol{y}, \quad C = \begin{pmatrix} \boldsymbol{p}_1^T & 1 \\ \vdots & \vdots \\ \boldsymbol{p}_N^T & 1 \end{pmatrix}. \tag{4.2.11}$$

It is assumed that the $\boldsymbol{p}_i$'s are such that C above has full rank. Furthermore, the error

due to second-order terms and measurement noise can be written

$$(\bar{\boldsymbol{z}} - \bar{\boldsymbol{z}}_{\mathbf{LS}}) = -(C^T C)^{-1} C^T \boldsymbol{\epsilon}_{\boldsymbol{E}},$$

$$\textit{where} \quad \boldsymbol{\epsilon}_{\boldsymbol{E}} = \begin{pmatrix} \vdots \\ \frac{1}{2}\boldsymbol{p}_i^T \bar{H}(\boldsymbol{r})\boldsymbol{p}_i \\ \vdots \end{pmatrix} + \boldsymbol{\epsilon}_{\boldsymbol{M}} + \boldsymbol{w},$$

$\bar{H}(\boldsymbol{r})$ *is the Hessian of the mean field.*

Proof:

A Taylor expansion of the mean field around $\boldsymbol{r}$ together with assumed noises ϵ_{Mi} and w_i at each $\boldsymbol{x}_i$ gives the measurement

$$T_M(\boldsymbol{x}_i, t) = \bar{T}(\boldsymbol{r}) + \boldsymbol{p}_i^T \nabla \bar{T}(\boldsymbol{r}) + \frac{1}{2}\boldsymbol{p}_i^T \bar{H}(\boldsymbol{r})\boldsymbol{p}_i + \mathcal{O}(||\boldsymbol{p}_i||^3) + \epsilon_{Mi} + w_i.$$

Ignoring the higher-order terms and writing the equations in matrix form we get $\boldsymbol{y} = C\bar{\boldsymbol{z}} + \boldsymbol{\epsilon}_{\boldsymbol{E}}$. Applying the least squares estimate, [87], minimizing $\|C\bar{\boldsymbol{z}}_{\mathbf{LS}} - \boldsymbol{y}\|^2$, we get $\bar{\boldsymbol{z}}_{\mathbf{LS}} = (C^T C)^{-1} C^T \boldsymbol{y}$ yielding the estimation error

$$\begin{aligned} (\bar{\boldsymbol{z}} - \bar{\boldsymbol{z}}_{\mathbf{LS}}) &= \bar{\boldsymbol{z}} - (C^T C)^{-1} C^T (C\bar{\boldsymbol{z}} + \boldsymbol{\epsilon}_{\boldsymbol{E}}) \\ &= -(C^T C)^{-1} C^T \boldsymbol{\epsilon}_{\boldsymbol{E}}. \end{aligned}$$ ∎

Remark 4.2.1. *[64] Note that if the measurements $T_M(\boldsymbol{x}_i, t)$ are to be useful for estimating $\nabla T(\boldsymbol{r})$, then the distances $\|\boldsymbol{p}_i\|$ must be small enough to make the lower-order terms in the Taylor expansion above dominate.*

Remark 4.2.2. *Reassuringly the finite difference estimates of the gradient computed with the vehicles in rectangular formation given in (4.2.3) and (4.2.10) are identical to the least squares estimate computed by (4.2.11).*

The optimal formation problem is also addressed in [64] by minimizing

$$E[(\bar{\boldsymbol{z}} - \bar{\boldsymbol{z}}_{\mathbf{LS}})^T(\bar{\boldsymbol{z}} - \bar{\boldsymbol{z}}_{\mathbf{LS}})]$$

with respect to the set of $\boldsymbol{p}_i$. Expanding this expression we find that

$$E[(\bar{\boldsymbol{z}} - \bar{\boldsymbol{z}}_{\mathbf{LS}})^T(\bar{\boldsymbol{z}} - \bar{\boldsymbol{z}}_{\mathbf{LS}})] = E[(\bar{T} - \bar{T}_{\mathrm{LS}})^2 + \|\nabla\bar{T} - \nabla\bar{T}_{\mathrm{LS}}\|^2] \tag{4.2.12}$$

where $\bar{\boldsymbol{z}}_{\mathbf{LS}} = (\bar{T}_{\mathrm{LS}}, \nabla\bar{T}_{\mathrm{LS}}^T)^T = (C^TC)^{-1}C^T\boldsymbol{y}$. Notice that we have assumed that there is a unit weight conversion coefficient to assure that the sum in the right hand side of (4.2.12) is indeed summable.

Given our model (4.1.2) we use an identical metric to (4.2.12) but formulate it is as the trace of an error covariance matrix, i.e.

$$\mathrm{Tr}(E[(\bar{\boldsymbol{z}} - \bar{\boldsymbol{z}}_{\mathbf{LS}})(\bar{\boldsymbol{z}} - \bar{\boldsymbol{z}}_{\mathbf{LS}})^T].$$

This error metric is widely used in the oceanographic community when addressing *optimal interpolation* problems. One example of such a problem is how to best map a collection of measurements onto a uniform grid [39]. For ease of notation we introduce the following definition

$$\boldsymbol{\rho} = \begin{pmatrix} \vdots \\ \frac{1}{2}\boldsymbol{p}_i^T\bar{H}(\boldsymbol{r})\boldsymbol{p}_i \\ \vdots \end{pmatrix}, \tag{4.2.13}$$

and thus $\boldsymbol{\epsilon_E} = \boldsymbol{\rho} + \boldsymbol{\epsilon_M} + \boldsymbol{w}$.

Lemma 4.2.2 (Optimal Formation Problem)**.** [3]

Let $M(\boldsymbol{p}_1, \ldots, \boldsymbol{p}_N) = (C^TC)^{-1}C^T$, where C depends on $\boldsymbol{p}_i$ as in Lemma 4.2.1 above.

[3]Lemma 4.2.2 closely follows Lemma 5.2 in [64]. The only difference is the form of error metric (4.2.14).

The trace of the error covariance matrix is

$$\mathrm{Tr}(E[(\bar{\boldsymbol{z}} - \bar{\boldsymbol{z}}_{\mathbf{LS}})(\bar{\boldsymbol{z}} - \bar{\boldsymbol{z}}_{\mathbf{LS}})^T]) = \mathrm{Tr}(M\boldsymbol{\rho}\boldsymbol{\rho}^T M^T) + (\sigma_M^2 + \sigma_w^2)\mathrm{Tr}((C^T C)^{-1}) + \mathrm{Tr}(MWM^T) \tag{4.2.14}$$

An optimal formation geometry problem can now be formulated as

$$\min_{\boldsymbol{p}_1,\ldots,\boldsymbol{p}_N} g(\boldsymbol{p}_1,\ldots,\boldsymbol{p}_N) := \min_{\boldsymbol{p}_1,\ldots,\boldsymbol{p}_N} \mathrm{Tr}(E[(\bar{\boldsymbol{z}} - \bar{\boldsymbol{z}}_{\mathbf{LS}})(\bar{\boldsymbol{z}} - \bar{\boldsymbol{z}}_{\mathbf{LS}})^T]). \tag{4.2.15}$$

Proof: From Lemma 4.2.1 we directly have

$$(\bar{\boldsymbol{z}} - \bar{\boldsymbol{z}}_{\mathbf{LS}})(\bar{\boldsymbol{z}} - \bar{\boldsymbol{z}}_{\mathbf{LS}})^T = M\boldsymbol{\epsilon}_{\boldsymbol{E}}\boldsymbol{\epsilon}_{\boldsymbol{E}}{}^T M^T$$

Taking the expected value and expanding $\boldsymbol{\epsilon}_{\boldsymbol{E}}$ we get

$$\begin{aligned}
E[(\bar{\boldsymbol{z}} - \bar{\boldsymbol{z}}_{\mathbf{LS}})(\bar{\boldsymbol{z}} - \bar{\boldsymbol{z}}_{\mathbf{LS}})^T] &= ME[(\boldsymbol{\rho} + \boldsymbol{\epsilon}_{\boldsymbol{M}} + \boldsymbol{w})(\boldsymbol{\rho}^T + \boldsymbol{\epsilon}_{\boldsymbol{M}}{}^T + \boldsymbol{w}^T)]M^T \\
&= M\left(E[\boldsymbol{\rho}\boldsymbol{\rho}^T] + E[\boldsymbol{\epsilon}_{\boldsymbol{M}}\boldsymbol{\epsilon}_{\boldsymbol{M}}{}^T] + E[\boldsymbol{w}\boldsymbol{w}^T]\right)M^T \\
&= M\boldsymbol{\rho}\boldsymbol{\rho}^T M^T + \sigma_M^2 MM^T + \sigma_w^2 MM^T + MWM^T \\
&= M\boldsymbol{\rho}\boldsymbol{\rho}^T M^T + (\sigma_M^2 + \sigma_w^2)(C^T C)^{-1} + MWM^T,
\end{aligned}$$

where we utilized the fact that $E[\boldsymbol{\rho}\boldsymbol{\epsilon}_{\boldsymbol{M}}{}^T] = E[\boldsymbol{\rho}\boldsymbol{w}^T] = E[\boldsymbol{\epsilon}_{\boldsymbol{M}}\boldsymbol{w}^T] = 0$ and $MM^T = (C^T C)^{-1}$.

Finally,

$$\mathrm{Tr}(E[(\bar{\boldsymbol{z}} - \bar{\boldsymbol{z}}_{\mathbf{LS}})(\bar{\boldsymbol{z}} - \bar{\boldsymbol{z}}_{\mathbf{LS}})^T]) = \mathrm{Tr}(M\boldsymbol{\rho}\boldsymbol{\rho}^T M^T) + (\sigma_M^2 + \sigma_w^2)\mathrm{Tr}((C^T C)^{-1}) + \mathrm{Tr}(MWM^T).$$

■

Remark 4.2.3. *Clearly as before this optimization relies on an estimate of the Hessian. In [64] the Hessian is modelled as an additional noise term, e.g.* $\bar{H}(\boldsymbol{r}) \approx \epsilon_H H$ *where* ϵ_H *is zero mean with a Gaussian distribution and* H *is a rough estimate of the Hessian. The framework presented above allows for this same substitution.*

Remark 4.2.4. *It can be shown that the optimal formation metric given in (4.2.14) is invariant under formation rotation for 3 vehicles estimating the gradient.*

We can get a sense of the role each term in (4.2.14) by noting that if d is some average over all $\|\boldsymbol{p}_i\|$ then

$$\mathrm{Tr}(M\boldsymbol{\rho}\boldsymbol{\rho}^T M^T) \propto d^2,$$

$$\mathrm{Tr}((C^T C)^{-1}) \propto \frac{1}{d^2},$$

and if the covariance of the process field is taken as $E[w_i w_j] = e^{\frac{-\|\boldsymbol{p}_i - \boldsymbol{p}_j\|^2}{\sigma_d^2}}$ where σ_d is the $1/e$ decorrelation length scale,

$$\mathrm{Tr}(MWM^T) \propto \frac{e^{-d^2/\sigma_d^2}}{d^2}$$

and thus $\mathrm{Tr}(MWM^T) \propto 1/d^2$ for small $\|\boldsymbol{p}_i\|$ and $\mathrm{Tr}(MWM^T) \to 0$ for large $\|\boldsymbol{p}_i\|$, relative to σ_d.

When the covariance of the noise field, $w(\boldsymbol{x})$, is small enough or the vehicles are far enough away from each other such that we may model $E[\boldsymbol{w}\boldsymbol{w}^T] \approx \sigma_w I$, then the optimization problem is identical to that found in [64] with the substitution noted in Remark 4.2.3. In [64] it is discussed how the optimization problem is non-convex and therefore only local results are achievable using standard methods. It was found that for $\bar{H}(\boldsymbol{r}) \approx \sigma_H I$ formations consisting of vehicles at the vertices of regular polyhedra were locally optimal in $\mathbb{R}^2$ and vehicles at the vertices of a equilateral tetrahedron for four vehicles in $\mathbb{R}^3$.

The least squares method can also be used to estimate higher-order derivatives. For example in the plane, given $N \geq 6$ measurements $T_M(\boldsymbol{x}_i)$ taken at $\boldsymbol{p}_i = (p_i^x, p_i^y) \in \mathbb{R}^2, i =$

$1, \ldots, N$ (recall $\boldsymbol{p}_i = \boldsymbol{x}_i - \boldsymbol{r}$), we define

$$C = \begin{pmatrix} \frac{1}{2}(p_1^x)^2 & p_1^x p_1^y & \frac{1}{2}(p_1^y)^2 & p_1^x & p_1^y & 1 \\ \frac{1}{2}(p_2^x)^2 & p_2^x p_2^y & \frac{1}{2}(p_2^y)^2 & p_2^x & p_2^y & 1 \\ \vdots & \vdots & \vdots & \vdots & \vdots & \vdots \\ \frac{1}{2}(p_N^x)^2 & p_N^x p_N^y & \frac{1}{2}(p_N^y)^2 & p_N^x & p_N^y & 1 \end{pmatrix}, \text{ and } \boldsymbol{y} = \begin{pmatrix} T_M(\boldsymbol{x}_1, t) \\ T_M(\boldsymbol{x}_2, t) \\ \vdots \\ T_M(\boldsymbol{x}_N, t) \end{pmatrix}. \tag{4.2.16}$$

The least squares estimate of $\bar{\boldsymbol{z}}_{\boldsymbol{T}} = (\frac{\partial^2 \bar{T}}{\partial x^2}, \frac{\partial^2 \bar{T}}{\partial x \partial y}, \frac{\partial^2 \bar{T}}{\partial y^2}, \frac{\partial \bar{T}}{\partial x}, \frac{\partial \bar{T}}{\partial y}, \bar{T})^T$ is given as before by

$$\bar{\boldsymbol{z}}_{\mathbf{LS}} = (C^T C)^{-1} C^T \boldsymbol{y}.$$

4.2.3 Gradient-of-the-Average Approximation

In this subsection we present an alternative approach to gradient estimation: we compute the gradient of an average of the scalar environmental field values (measurements) over a closed region. This gradient is formulated as an integral over a continuous set of measurements and is approximated using the finite set of measurements provided by the vehicle group. We show that for a particular choice of discretization, i.e. numerical quadrature, and for certain distributions of vehicles over a circle in $\mathbb{R}^2$ and a sphere in $\mathbb{R}^3$, this gradient-of-the-average estimate is equivalent to the least-squares estimate presented in §4.2.2. The class of vehicle formations for which this equivalence holds includes the optimal formations mentioned in §4.2.2 and found in [64].

Suppose we had noisy measurements (at time t) inside a disc Ω of radius h_0, i.e. $\Omega = \{\boldsymbol{x} |\ \|\boldsymbol{x} - \boldsymbol{r}\| \leq h_0\}$ (see Figure 4.2.2). To mitigate noise we are motivated to average these measurements over Ω,

$$T_{avg}(\boldsymbol{r}, t) \quad = \quad \frac{1}{\pi h_0^2} \int_\Omega T_M(\boldsymbol{x}, t) d\boldsymbol{x}.$$

For a gradient climbing (or descent) problem, we seek the gradient of $T_{avg}(\boldsymbol{r}, t)$ with respect to $\boldsymbol{r}$. In light of our disc example, we can view $\nabla_r T_{avg}(\boldsymbol{r}, t)$ as specifying the best

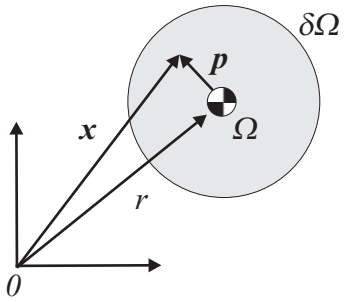

Figure 4.2.2: **The Ω Disc.**

direction to move the center of the disc so as to maximize (minimize) the average of T_M over Ω. As shown by Uryasev [94], this gradient can be written as

$$\nabla_r T_{avg}(\boldsymbol{r},t) = \frac{\nabla_r \int_\Omega T_M(\boldsymbol{x},t)d\boldsymbol{x}}{\pi h_0^2} = \frac{1}{\pi h_0^3}\int_{\partial\Omega} T_M(\boldsymbol{x},t)(\boldsymbol{x}-\boldsymbol{r})\, dS$$

where $\partial\Omega$ is the boundary of Ω and dS is a surface area element in $\mathbb{R}^3$ or line element in $\mathbb{R}^2$.

Suppose we are given only N measurements T_M at points $\boldsymbol{x}_i,\ i = 1,\ldots,N$, i.e., one from each vehicle, at time t. We can approximate the above integral using numerical quadrature. Consider the case in which the N vehicles are uniformly distributed over the boundary. Using the *composite trapezoidal rule,* we obtain

$$\frac{1}{\pi h_0^3}\int_{\partial\Omega} T_M(\boldsymbol{x},t)\ \boldsymbol{p}\ dS \approx \frac{1}{\pi h_0^3}\sum_{i=1}^{N} T_M(\boldsymbol{x}_i,t)\ \boldsymbol{p}_i\ \triangle s$$

where again $\boldsymbol{p}_i = \boldsymbol{x}_i - \boldsymbol{r}$, i.e. the measurement location relative to $\boldsymbol{r}$, and $\triangle s = \frac{2\pi h_0}{N}$. Thus,

$$\nabla_r T_{avg}(\boldsymbol{r},t) \approx \frac{2}{N h_0^2}\sum_{i=1}^{N} T_M(\boldsymbol{x}_i,t)\ \boldsymbol{p}_i. \tag{4.2.17}$$

Similarly, to compute the gradient of the average within a ball of radius h_0 in $\mathbb{R}^3$, we obtain:

$$\begin{aligned}\nabla_r T_{avg}(\boldsymbol{r},t) &= \frac{3}{4\pi h_0^4}\int_{\partial\Omega} T_M(\boldsymbol{x},t)(\boldsymbol{x}-\boldsymbol{r})dS \\ &\approx \frac{3}{N h_0^2}\sum_{i=1}^{N} T_M(\boldsymbol{x}_i,t)\boldsymbol{p}_i \end{aligned}\tag{4.2.18}$$

for vehicle distributions that permit N equal area partitions of the sphere with each vehicle located at a centroid of a partition, and where all vehicles do not lie on the same great circle.

Lemma 4.2.3 (Least Squares Equivalence)**.** *Consider N vehicles in $\mathbb{R}^l, l = 2, 3$. Suppose for $l = 2$ that the vehicles are uniformly distributed around a circle of radius h_0. Suppose in the case $l = 3$ that the vehicles are distributed over a sphere of radius h_0 such that the formation partitions the sphere into equal-area spherical polygons, where each vehicle is located at a centroid, and all vehicles do not lie on the same great circle. Denote $\boldsymbol{p}_i$, $i = 1, \ldots, N$, the position vector of the ith vehicle relative to the center of the circle or sphere. Each vehicle takes a noisy measurement $T_M(\boldsymbol{x}_i, t)$. Define $\boldsymbol{p}^j \equiv (p_1^j, \ldots, p_N^j)^T$ where p_i^j is the jth coordinate of $\boldsymbol{p}_i$.*

Assume that the group geometry satisfies

$$\sum_{k=1}^{N} p_k^j = 0 \qquad \textit{and} \qquad \langle \boldsymbol{p}^i, \boldsymbol{p}^j \rangle = \delta_{ij} \frac{N h_0^2}{l},$$

where $i, j = 1, \ldots, l$ and $\delta_{ij} = \begin{cases} 0 & \text{for } i \neq j \\ 1 & \text{for } i = j \end{cases}$, and $\langle \cdot, \cdot \rangle$ is the standard inner product on $\mathbb{R}^l$. Then, the least squares gradient estimate is equivalent to the gradient-of-the-average estimate as given above (4.2.17), (4.2.18).

Proof. A proof is only presented for formations in $\mathbb{R}^2$; the result in $\mathbb{R}^3$ follows analogously.

In terms of $\boldsymbol{p}^j$, $j = 1, 2$,

$$C^T C = \begin{pmatrix} \langle \boldsymbol{p}^1, \boldsymbol{p}^1 \rangle & \langle \boldsymbol{p}^1, \boldsymbol{p}^2 \rangle & \sum_{i=1}^{N} p_i^1 \\ \langle \boldsymbol{p}^2, \boldsymbol{p}^1 \rangle & \langle \boldsymbol{p}^2, \boldsymbol{p}^2 \rangle & \sum_{i=1}^{N} p_i^2 \\ \sum_{i=1}^{N} p_i^1 & \sum_{i=1}^{N} p_i^2 & N \end{pmatrix}$$

It follows from the hypotheses on group geometry that $(C^T C)^{-1} = diag(2/Nh_0^2,\ 2/Nh_0^2,\ 1/N)$.

Furthermore,

$$C^T \begin{pmatrix} \vdots \\ T_M(\boldsymbol{x}_i, t) \\ \vdots \end{pmatrix} = \begin{pmatrix} \sum_{i=1}^{N} T_M(\boldsymbol{x}_i, t)\, \boldsymbol{p}_i \\ \sum_{i=1}^{N} T_M(\boldsymbol{x}_i, t) \end{pmatrix}.$$

Thus the least squares estimate, $\bar{\boldsymbol{z}}_{\mathbf{LS}}$ *is given by,*

$$\bar{\boldsymbol{z}}_{\mathbf{LS}} = \begin{pmatrix} \frac{2}{Nh_0^2} \sum_{i=1}^{N} T_M(\boldsymbol{x}_i, t)\, \boldsymbol{p}_i \\ \frac{1}{N} \sum_{i=1}^{N} T_M(\boldsymbol{x}_i, t) \end{pmatrix}$$

which is equivalent to $\nabla_r T_{avg}(\boldsymbol{r}, t)$ *given in (4.2.17).* ∎

Remark 4.2.5. *For* N *vehicles in* $\mathbb{R}^2$*, the assumptions on the group geometry are satisfied for equally-spaced vehicles on the circle. These formations are* N*-sided, regular polyhedra that coincide with the optimal formations for* $H = \epsilon_{Hi} I$*.*

Remark 4.2.6. *For vehicles in* $\mathbb{R}^3$*, the group geometry assumptions are not so easily satisfied; indeed, the specifications may not be achievable for arbitrary* N*. Examples of formations meeting the assumptions include vehicles placed at the vertices of one of the five Platonic solids, i.e. tetrahedron (*$N = 4$*), octahedron (*$N = 6$*), cube (*$N = 8$*), icosahedron (*$N = 12$*), and dodecahedron (*$N = 20$*). The tetrahedron was found to be an optimal formation* $H = \epsilon_{Hi} I$ *in [64].*

Remark 4.2.7. *When numerically integrating periodic functions, composite trapezoidal quadrature typically outperforms other methods such as the standard Simpson's Rule, high-order Newton-Cotes, and Gaussian quadratures ([21]). In our numerical experiments with gradient estimation in quadratic and Gaussian temperature fields, the trapezoidal rule consistently outperformed the high-order Newton-Cotes methods by exhibiting smaller gradient estimation error. When equivalency holds, the averaging method may provide insight into when the least-squares linear approximation is appropriate for these kinds of fields.*

4.3 Discrete-Time Kalman Filter for Mean Field Estimation

So far we have focused on how to estimate the value and derivatives of the mean field, $\bar{T}$, given a set of measurements, one taken by each vehicle in the formation. We now address how to use previous measurements to improve these estimates and to do so we construct a Kalman filter. We derive a discrete-time filter, not only for ease of construction, but also because a discrete-time filter may be more appropriate to use with data from underwater gliders which only yield data at a given depth level every 100 m or more. In what follows we specialize to the plane but in principle the concepts can be extended to $\mathbb{R}^3$.

At the *kth* instant we have a measurement vector given by

$$\begin{aligned} \boldsymbol{y}_k &= C_k \bar{\boldsymbol{z}}_k + \boldsymbol{w}_k + \boldsymbol{\rho}_k + \boldsymbol{\epsilon}_{\boldsymbol{M}k}, \\ &= C_k \bar{\boldsymbol{z}}_k + \boldsymbol{w}_k + \boldsymbol{\epsilon}_k \end{aligned}$$

where

$$C_k = \begin{pmatrix} \boldsymbol{p}_{1k}^T & 1 \\ \boldsymbol{p}_{2k}^T & 1 \\ \vdots & \vdots \\ \boldsymbol{p}_{Nk}^T & 1 \end{pmatrix},$$

$\boldsymbol{\epsilon}_k = \boldsymbol{\rho}_k + \boldsymbol{\epsilon}_{\boldsymbol{M}k}$, and as before $\bar{\boldsymbol{z}}_k = (\nabla \bar{T}(\boldsymbol{r}_k), \bar{T}(\boldsymbol{r}_k))^T$. Note that the subscript k serves as a discrete-time index. We have assumed that $\boldsymbol{\rho}$ only contains second-order terms as in

(4.2.13) and that third-order and above terms can be discarded. Furthermore,

$$\begin{aligned} E[\boldsymbol{w}_k] &= 0, \\ E[\boldsymbol{\epsilon}_k] &= 0, \\ E[\boldsymbol{w}_k \boldsymbol{w}_k^T] &= \sigma_w^2 I + W_k, \\ E[\boldsymbol{w}_k \boldsymbol{w}_{k-1}^T] &= V_k, \\ E[\boldsymbol{\epsilon}_k \boldsymbol{\epsilon}_k^T] &= \tilde{R}_k = S_k + R_k, \\ E[\boldsymbol{\epsilon}_k \boldsymbol{\epsilon}_{k-1}^T] &= 0, \end{aligned}$$

given $E[\boldsymbol{\epsilon_M}_k] = 0, E[\boldsymbol{\rho}_k] = 0, E[\boldsymbol{\epsilon_M}_k \boldsymbol{\epsilon_M}_k^T] = R_k$ and $E[\boldsymbol{\rho}_k \boldsymbol{\rho}_k^T] = S_k$. Notice here we are interpreting $\boldsymbol{\rho}_k$ as a Gaussian white noise.

We wish to filter the estimate of $\bar{\boldsymbol{z}}_k$ given $\bar{\boldsymbol{z}}_{k-1}$. To derive the relation between these quantities we assume that the formation center of mass moves by $\boldsymbol{\delta}_k \in \mathbb{R}^2$ from the $k-1$ instant to the kth instant, see Figure 4.3.1. Define $\boldsymbol{p'}_{ik} = \boldsymbol{p}_{ik} + \boldsymbol{\delta}_k$, i.e. the position of the ith measurement at the kth instant with respect to the formation center of mass at the $k-1$ instant.

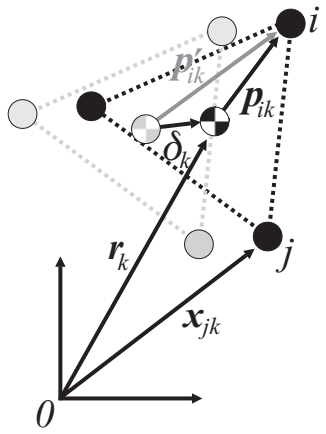

Figure 4.3.1: **Past and Previous Formations.**

Expanding the mean field, $\bar{T}$, with respect to the center of mass at the kth instant and

$k-1$ instant to express $\bar{T}$ at $\boldsymbol{x}_{ik}$ we get

$$\begin{aligned}
\bar{T}(\boldsymbol{x}_{ik}) &= \begin{pmatrix} \boldsymbol{p}_{ik}^T & 1 \end{pmatrix} \bar{\boldsymbol{z}}_k + \frac{1}{2}\boldsymbol{p}_{ik}^T \bar{H}_k \boldsymbol{p}_{ik} + \mathcal{O}(\|\boldsymbol{p}_{ik}\|^3) \\
\bar{T}(\boldsymbol{x}_{ik}) &= \begin{pmatrix} \boldsymbol{p'}_{ik}^T & 1 \end{pmatrix} \bar{\boldsymbol{z}}_{k-1} + \frac{1}{2}\boldsymbol{p'}_{ik}^T \bar{H}_{k-1} \boldsymbol{p'}_{ik} + \mathcal{O}(\|\boldsymbol{p'}_{ik}\|^3), \\
&= \begin{pmatrix} \boldsymbol{p'}_{ik}^T & 1 \end{pmatrix} \bar{\boldsymbol{z}}_{k-1} + \frac{1}{2}(\boldsymbol{p}_{ik} + \boldsymbol{\delta}_k)^T \bar{H}_{k-1} (\boldsymbol{p}_{ik} + \boldsymbol{\delta}_k) + \mathcal{O}(\|\boldsymbol{p'}_{ik}\|^3),
\end{aligned}$$

respectively.

Given measurements $i = 1, \ldots, N$ we can construct the matrix equations

$$\bar{\boldsymbol{y}}_{\boldsymbol{k}} = C_k \bar{\boldsymbol{z}}_k + \begin{pmatrix} \frac{1}{2}\boldsymbol{p}_{1k}^T \bar{H}_k \boldsymbol{p}_{1k} \\ \frac{1}{2}\boldsymbol{p}_{2k}^T \bar{H}_k \boldsymbol{p}_{2k} \\ \vdots \\ \frac{1}{2}\boldsymbol{p}_{Nk}^T \bar{H}_k \boldsymbol{p}_{Nk} \end{pmatrix}, \tag{4.3.1}$$

$$\bar{\boldsymbol{y}}_k = C'_k \bar{\boldsymbol{z}}_{k-1} + \begin{pmatrix} \frac{1}{2}(\boldsymbol{p}_{1k} + \boldsymbol{\delta}_k)^T \bar{H}_{k-1} (\boldsymbol{p}_{1k} + \boldsymbol{\delta}_k) \\ \frac{1}{2}(\boldsymbol{p}_{2k} + \boldsymbol{\delta}_k)^T \bar{H}_{k-1} (\boldsymbol{p}_{2k} + \boldsymbol{\delta}_k) \\ \vdots \\ \frac{1}{2}(\boldsymbol{p}_{Nk} + \boldsymbol{\delta}_k)^T \bar{H}_{k-1} (\boldsymbol{p}_{Nk} + \boldsymbol{\delta}_k) \end{pmatrix}, \tag{4.3.2}$$

where

$$C'_k = \begin{pmatrix} \boldsymbol{p'}_{1k}^T & 1 \\ \boldsymbol{p'}_{2k}^T & 1 \\ \vdots & \vdots \\ \boldsymbol{p'}_{Nk}^T & 1 \end{pmatrix},$$

and we have dropped the $\mathcal{O}(\|\boldsymbol{p}_{ik}\|^3)$ and $\mathcal{O}(\|\boldsymbol{p'}_{ik}\|^3)$ terms.

Expanding $\bar{H}_k$, we have

$$\bar{H}_k = (I \bigotimes \boldsymbol{\delta}_k)\bar{H}'_{k-1} + \bar{H}_{k-1}$$

where $\bar{H}_k = \begin{pmatrix} \bar{H}_{11k} & \bar{H}_{12k} \\ \bar{H}_{21k} & \bar{H}_{22k} \end{pmatrix} \in \mathbb{R}^{2\times 2}$,

$$(I \bigotimes \boldsymbol{\delta}_k) = \begin{pmatrix} \boldsymbol{\delta}_k^T & 0 \\ 0 & \boldsymbol{\delta}_k^T \end{pmatrix} \in \mathbb{R}^{2\times 4} \quad \text{and} \quad \bar{H}'_k = \begin{pmatrix} \nabla\bar{H}_{11k} & \nabla\bar{H}_{12k} \\ \nabla\bar{H}_{21k} & \nabla\bar{H}_{22k} \end{pmatrix} \in \mathbb{R}^{4\times 2}.$$

Subtracting (4.3.2) from (4.3.1) we have

$$C_k\bar{\boldsymbol{z}}_k = C'_k\bar{\boldsymbol{z}}_{k-1} - \frac{1}{2}\begin{pmatrix} \boldsymbol{p}_{1k}^T(I\bigotimes\boldsymbol{\delta}_k)\bar{H}'_{k-1}\boldsymbol{p}_{1k} \\ \boldsymbol{p}_{2k}^T(I\bigotimes\boldsymbol{\delta}_k)\bar{H}'_{k-1}\boldsymbol{p}_{2k} \\ \vdots \\ \boldsymbol{p}_{Nk}^T(I\bigotimes\boldsymbol{\delta}_k)\bar{H}'_{k-1}\boldsymbol{p}_{Nk} \end{pmatrix} + \begin{pmatrix} \boldsymbol{p}_{1k}^T\bar{H}_{k-1}\boldsymbol{\delta}_k \\ \boldsymbol{p}_{2k}^T\bar{H}_{k-1}\boldsymbol{\delta}_k \\ \vdots \\ \boldsymbol{p}_{Nk}^T\bar{H}_{k-1}\boldsymbol{\delta}_k \end{pmatrix},$$

where $\mathcal{O}(\|\boldsymbol{\delta}_k\|^2)$ terms have been dropped.

Rearranging we now have an expression for $\bar{\boldsymbol{z}}_k$ in terms of $\bar{\boldsymbol{z}}_{k-1}$,

$$\bar{\boldsymbol{z}}_k = (C_k^TC_k)^{-1}C_k^TC'_k\bar{\boldsymbol{z}}_{k-1} + (C_k^TC_k)^{-1}C_k^T\left(\begin{pmatrix} \boldsymbol{p}_{1k}^T\bar{H}_{k-1}\boldsymbol{\delta}_k \\ \boldsymbol{p}_{2k}^T\bar{H}_{k-1}\boldsymbol{\delta}_k \\ \vdots \\ \boldsymbol{p}_{Nk}^T\bar{H}_{k-1}\boldsymbol{\delta}_k \end{pmatrix} - \frac{1}{2}\begin{pmatrix} \boldsymbol{p}_{1k}^T(I\bigotimes\boldsymbol{\delta}_k)\bar{H}'_{k-1}\boldsymbol{p}_{1k} \\ \boldsymbol{p}_{2k}^T(I\bigotimes\boldsymbol{\delta}_k)\bar{H}'_{k-1}\boldsymbol{p}_{2k} \\ \vdots \\ \boldsymbol{p}_{Nk}^T(I\bigotimes\boldsymbol{\delta}_k)\bar{H}'_{k-1}\boldsymbol{p}_{Nk} \end{pmatrix}\right),$$

or

$$\bar{\boldsymbol{z}}_k = A_{k-1}\bar{\boldsymbol{z}}_{k-1} + \boldsymbol{q}_{k-1},$$

where

$$\begin{aligned} A_{k-1} &= (C_k^TC_k)^{-1}C_k^TC'_k, \\ \boldsymbol{q}_{k-1} &= (C_k^TC_k)^{-1}C_k^T\left(\begin{pmatrix} \boldsymbol{p}_{1k}^T\bar{H}_{k-1}\boldsymbol{\delta}_k \\ \boldsymbol{p}_{2k}^T\bar{H}_{k-1}\boldsymbol{\delta}_k \\ \vdots \\ \boldsymbol{p}_{Nk}^T\bar{H}_{k-1}\boldsymbol{\delta}_k \end{pmatrix} - \frac{1}{2}\begin{pmatrix} \boldsymbol{p}_{1k}^T(I\bigotimes\boldsymbol{\delta}_k)\bar{H}'_{k-1}\boldsymbol{p}_{1k} \\ \boldsymbol{p}_{2k}^T(I\bigotimes\boldsymbol{\delta}_k)\bar{H}'_{k-1}\boldsymbol{p}_{2k} \\ \vdots \\ \boldsymbol{p}_{Nk}^T(I\bigotimes\boldsymbol{\delta}_k)\bar{H}'_{k-1}\boldsymbol{p}_{Nk} \end{pmatrix}\right). \end{aligned}$$

Note that as in Lemma 4.2.1, we assume that at the kth instant the formation geometry is such that $C_k^T C_k$ is nonsingular.

In the absence of correlated field noise, i.e. when $E[\boldsymbol{w}_{k-1}\boldsymbol{w}_k^T] = 0$, the discrete-time linear system for which we wish to find filtered state estimates is given by

$$\begin{aligned} \bar{\boldsymbol{z}}_k &= A_{k-1}\bar{\boldsymbol{z}}_{k-1} + \boldsymbol{q}_{k-1} \\ \boldsymbol{y}_k &= C_k\bar{\boldsymbol{z}}_k + \boldsymbol{w}_k + \boldsymbol{\epsilon}_k. \end{aligned} \tag{4.3.3}$$

As in [64] we interpret $\boldsymbol{q}$ as a stochastic noise source and we define $Q_k = E[\boldsymbol{q}_k\boldsymbol{q}_k^T]$.

The model in (4.3.3) does not take into account that we have modelled our field so that the noise in the previous measurement, $\boldsymbol{w}_{k-1}$, will in general be correlated with the noise $\boldsymbol{w}_k$ in the current measurement, i.e. $E[\boldsymbol{w}_{k-1}\boldsymbol{w}_k^T] \neq 0$. Following the development in [86] we assume that the field noise can be modelled as a first-order Gauss Markov process

$$\boldsymbol{w}_k = G_{k-1}\boldsymbol{w}_{k-1} + \boldsymbol{\eta}_{k-1}, \tag{4.3.4}$$

where $\boldsymbol{\eta}_k$ is a white noise sequence with $E[\boldsymbol{\eta}_k] = 0$, $E[\boldsymbol{\eta}_k\boldsymbol{\eta}_k^T] = U_k$. Given the statistics $E[\boldsymbol{w}_k\boldsymbol{w}_k^T] = \sigma_w^2 I + W_k$ and $E[\boldsymbol{w}_k\boldsymbol{w}_{k-1}^T] = V_k$ the required model parameters are derived to be

$$\begin{aligned} G_{k-1} &= V_k(\sigma_w^2 I + W_{k-1})^{-1} \\ U_{k-1} &= \sigma_w^2 I + W_k - \sigma_w^2 G_{k-1}G_{k-1}^T - G_{k-1}W_{k-1}G_{k-1}^T. \end{aligned}$$

With noise model (4.3.4) in hand we now can define the complete model to be filtered as

$$\begin{pmatrix} \bar{\boldsymbol{z}}_k \\ \boldsymbol{w}_k \end{pmatrix} = \begin{pmatrix} A_{k-1} & 0 \\ 0 & G_{k-1} \end{pmatrix} \begin{pmatrix} \bar{\boldsymbol{z}}_{k-1} \\ \boldsymbol{w}_{k-1} \end{pmatrix} + \begin{pmatrix} \boldsymbol{q}_{k-1} \\ \boldsymbol{\eta}_{k-1} \end{pmatrix}$$

with output equation given by

$$\boldsymbol{y}_k = \begin{pmatrix} C_k & I \end{pmatrix} \begin{pmatrix} \bar{\boldsymbol{z}}_k \\ \boldsymbol{w}_k \end{pmatrix} + \boldsymbol{\epsilon}_k$$

Or defining

$$\boldsymbol{\xi}_k = \begin{pmatrix} \bar{\boldsymbol{z}}_k \\ \boldsymbol{w}_k \end{pmatrix}, \; \tilde{A}_{k-1} = \begin{pmatrix} A_{k-1} & 0 \\ 0 & G_{k-1} \end{pmatrix}, \; \tilde{H}_k = \begin{pmatrix} C_k & I \end{pmatrix}, \; \tilde{\boldsymbol{w}}_k = \begin{pmatrix} \boldsymbol{q}_{k-1} \\ \boldsymbol{\eta}_{k-1} \end{pmatrix}$$

we have

$$\begin{aligned} \boldsymbol{\xi}_k &= \tilde{A}_{k-1}\boldsymbol{\xi}_{k-1} + \tilde{\boldsymbol{w}}_{k-1} \\ \boldsymbol{y}_k &= \tilde{H}_k\boldsymbol{\xi}_k + \boldsymbol{\epsilon}_k \end{aligned} \tag{4.3.5}$$

with

$$\begin{aligned} E[\tilde{\boldsymbol{w}}_k\tilde{\boldsymbol{w}}_k^T] &= \begin{pmatrix} Q_k & 0 \\ 0 & U_k \end{pmatrix} = \Theta_k \\ E[\tilde{\boldsymbol{w}}_k\boldsymbol{\epsilon}_k^T] &= 0. \end{aligned}$$

Defining the estimate of $\boldsymbol{\xi}_k$ as $\boldsymbol{\xi}_{\mathbf{est}k}$ and the error covariance matrix $P_k = E[(\boldsymbol{\xi}_k - \boldsymbol{\xi}_{\mathbf{est}k})(\boldsymbol{\xi}_k - \boldsymbol{\xi}_{\mathbf{est}k})^T]$, the Kalman estimate is obtained by propagating the discrete state equation

$$\boldsymbol{\xi}_{\mathbf{est}k} = \tilde{A}_{k-1}\boldsymbol{\xi}_{\mathbf{est}k-1} + K_k^*(\boldsymbol{y}_k - \tilde{H}_k\tilde{A}_{k-1}\boldsymbol{\xi}_{\mathbf{est}k-1}),$$

where the optimal Kalman filter gain, K_k^*, is found by minimizing the cost function, $J_k = \mathrm{Tr}(P_k)$ [86], and is given by

$$K_k^* = (\tilde{A}_{k-1}P_{k-1}\tilde{A}_{k-1}^T + \Theta_{k-1})\tilde{H}_k^T \left(\tilde{H}_k(\tilde{A}_{k-1}P_{k-1}\tilde{A}_{k-1}^T + \Theta_{k-1})\tilde{H}_k^T + \tilde{R}_k\right)^{-1}$$

with error covariance

$$P_k = (I - K_k^*\tilde{H}_k)(\tilde{A}_{k-1}P_{k-1}\tilde{A}_{k-1}^T + \Theta_{k-1})(I - K_k^*\tilde{H}_k)^T + K_k^*\tilde{R}_kK_k^{*T}.$$

The derivation can be found in Appendix B.

Note that we have derived the Kalman filter associated with estimating the mean field and gradient. However, by defining the C matrix as in (4.2.16), we can also use this formulation to estimate filtered higher-order derivatives.

To demonstrate the Kalman filter we simulate three vehicles in a triangle formation traversing a region in which a noisy field is present and estimate the mean field and its gradient. The field consists of a Gaussian mean field given by $\bar{T} = e^{\frac{-y^2}{2\sigma^2}}$ with $\sigma = 5$ and superimposed Gaussian noise, see Figure 4.3.2. The noise field, w, is generated from an isotropic, zero mean Gaussian distribution with covariance function given by $E[w(\boldsymbol{x}_i)w(\boldsymbol{x}_j)] = \sigma_w^2 e^{-\frac{\|\boldsymbol{x}_i - \boldsymbol{x}_j\|^2}{\sigma_d^2}}$. The scale length of this noise $\sigma_d = 1$ and the variance $\sigma_w^2 = 0.005$. If the length scale is to be interpreted as km then this random field may be thought of as characteristic of a small scale feature such as a biological plume, a red tide or a pollutant plume. For simulation purposes we use the *sampling from the spectrum* technique for generating a realization of a homogenous and isotropic field given the spectral density function [15] which was also implemented in [100].

Each vehicle takes a measurement of the noisy field that is corrupted by white sensor noise with variance $\sigma_M^2 = 0.0001$. To evaluate how the filter can perform with potentially poor estimates of the higher-order terms in the mean field expansion, represented by Q_k and S_k in the filter, we assign fixed values of $Q_k = 2 \times 10^{-5} I$ and $S_k = 10^{-3} I$. The correct noise covariances, σ_w, W_k and V_k, and correct noise scale length, σ_d were used in the filter equations. The inter-vehicle distance is fixed at $2.5\sqrt{3}$. This size was found to be near a local minimum of the integrated least squares error (4.2.12) along the formation's trajectory (shown in Figure 4.3.2).

At each step the formation propagates 0.1 units. The initial conditions for the filter are

$\boldsymbol{\xi}_0 = 0$ and $P_0 = I$. In Figure 4.3.2 we present snap shots of the three vehicle formation as it moves across the region from bottom to top and the noise field.

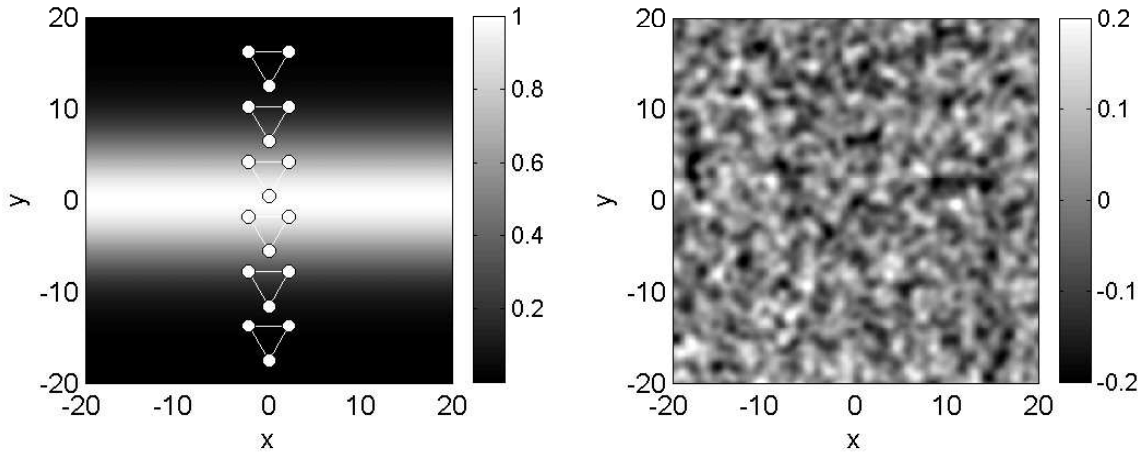

Figure 4.3.2: **Kalman Filtering for Mean Field Estimation Simulation.** Left pane shows the mean field with snap shots of the formation which traverses the region from bottom to top. Right pane shows the noise field which is superimposed onto the mean field.

In Figure 4.3.3 we present the filtering results. Clockwise from the top left pane we show $\frac{\partial \bar{T}}{\partial x}$, $\frac{\partial \bar{T}}{\partial y}$, Trace$(P), \bar{T}$, where Trace$(P)$ is the trace of the filter error covariance metric. We also present the actual mean field values, Kalman Filter estimates, and instantaneous Least Squares estimate, at the formation center of mass. The black solid line indicates the Kalman filter estimate, the grey solid line indicates the instantaneous least squares estimate, and the dashed black line indicates the actual mean field value. The bottom right figure demonstrates that our filter indeed converged.

The results shown in Figure 4.3.3 indicate that the Kalman filter estimate did not significantly improve the mean field estimate $\bar{T}$ but did yield an improved estimate of its gradient. Denoting the Kalman filter estimate of $\frac{\partial \bar{T}}{\partial x}$ at the formation center as $\frac{\partial \bar{T}}{\partial x}_{\text{KF}}$ and

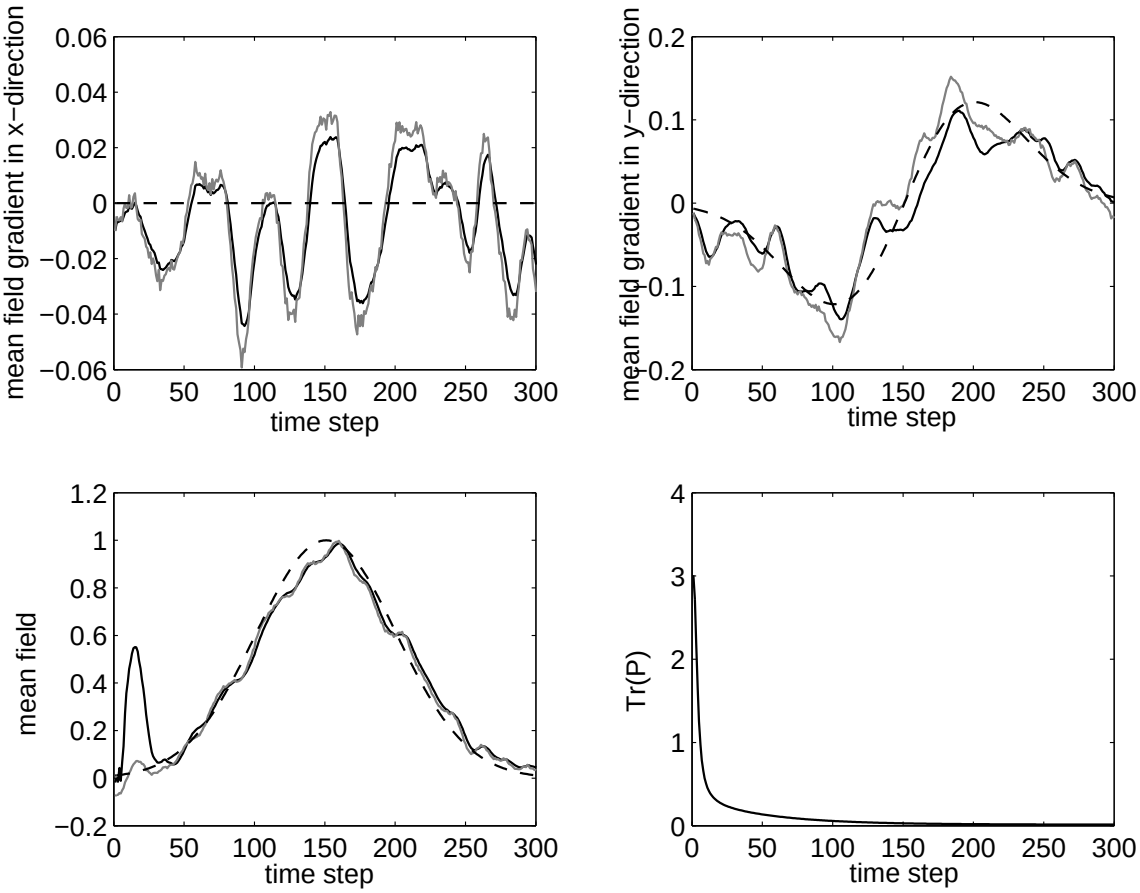

Figure 4.3.3: **Kalman Filtering Results.** Black solid lines indicate the Kalman filter estimates, the gray solid lines indicate the instantaneous least square estimates, and the black dashed lines indicate the actual mean field values.

the instantaneous least squares estimate as $\frac{\partial \bar{T}}{\partial x}_{\mathrm{LS}}$ we find

$$\frac{\|\frac{\partial \bar{T}}{\partial x}_{\mathrm{KF}} - \frac{\partial \bar{T}}{\partial x}\|}{\|\frac{\partial \bar{T}}{\partial x}_{\mathrm{LS}} - \frac{\partial \bar{T}}{\partial x}\|} = 0.80, \quad \frac{\|\frac{\partial \bar{T}}{\partial y}_{\mathrm{KF}} - \frac{\partial \bar{T}}{\partial y}\|}{\|\frac{\partial \bar{T}}{\partial y}_{\mathrm{LS}} - \frac{\partial \bar{T}}{\partial y}\|} = 0.93.$$

Here we are utilizing the L^2 norm defined as

$$\|z(t)\|^2 = \frac{1}{T}\int_0^T |z(t)|^2 \, dt$$

for square integrable functions $z(t), t \in [0, T]$. Recall that the sensor array diameter was chosen to minimize the least squares error. In simulations with non-optimal sensor diameters, the Kalman filter performed even better relative to the instantaneous least squares estimate.

4.4 Gradient Climbing and Feature Tracking

In this section we demonstrate how to use the derivative estimates computed by the vehicle array to perform gradient climbing and front tracking given a noisy scalar field. We specialize to the plane for the discussions but the concepts presented are applicable in $\mathbb{R}^3$.

4.4.1 Gradient Climbing

To enable gradient climbing we direct the virtual body to follow the estimate $\nabla \bar{T}_{\text{est}}$ (to descend we track the estimate $-\nabla \bar{T}_{\text{est}}$). Recall from Chapter 3 that the virtual body direction is given by $\widehat{\frac{d\boldsymbol{r}}{ds}}$. Thus, for gradient ascent we set

$$\widehat{\frac{d\boldsymbol{r}}{ds}} = \frac{\nabla \bar{T}_{\text{est}}}{\|\nabla \bar{T}_{\text{est}}\|}.$$

When the field is noisy it may be preferable to use the estimated gradient to define a desired virtual body heading angle and then use a simple controller to direct the virtual body heading to track the desired heading. For example, suppose we denote $\theta_d \in (-\pi, \pi]$ as the desired virtual body heading, i.e. for gradient ascent $\frac{\nabla \bar{T}_{\text{est}}}{\|\nabla \bar{T}_{\text{est}}\|} = (\cos\theta_d, \sin\theta_d)$ and define the virtual body heading as $\theta_v \in (-\pi, \pi]$ such that $\widehat{\frac{d\boldsymbol{r}}{ds}} = (\cos\theta_v, \sin\theta_v)$. We define the heading angle error $\theta_{ev} = \theta_v - \theta_d \in (-\pi, \pi]$. As a heading controller we may use

$$\dot{\theta}_v = -k_r \sin\theta_{ev} \tag{4.4.1}$$

where $k_r > 0$ adjusts the rate of the convergence. Implementation of this controller can help mitigate steering chatter when gradient estimates are noisy.

It may also be desirable for the adaptive path of the glider group to be computed as a modification of the path that one might otherwise select based on model forecasts, satellite imagery, aircraft or other data. To perturb the formation's path in the direction of the estimated positive or negative gradient, a *projected gradient* approach could be utilized [77],

see Figure 4.4.1. For example, to induce gradient descent, the negative of the estimated gradient is projected perpendicular to $\hat{\boldsymbol{r}}_{\boldsymbol{w}}$, the normalized vector from the virtual body center to a chosen final destination. This vector is denoted $\nabla \bar{T}_{\text{est}}^{\perp}$, and $\nabla \bar{T}_{\text{est}}^{\perp} \perp \hat{\boldsymbol{r}}_{w}$. The virtual body steering direction is given by

$$\widehat{\frac{d\boldsymbol{r}}{ds}} = \frac{\hat{\boldsymbol{r}}_{\boldsymbol{w}}(1 - w_{\perp}) - w_{\perp} \nabla \bar{T}_{\text{est}}^{\perp}}{\| \hat{\boldsymbol{r}}_{\boldsymbol{w}}(1 - w_{\perp}) - w_{\perp} \nabla \bar{T}_{\text{est}}^{\perp} \|}. \tag{4.4.2}$$

The scalar $w_{\perp} \in [0, 1]$ weights the influence of the gradient estimate on the virtual body path.

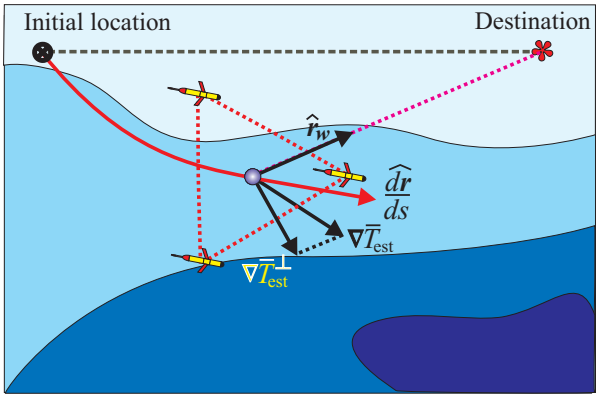

Figure 4.4.1: **Projected Gradient Descent.** The total virtual body heading vector $\widehat{\frac{d\boldsymbol{r}}{ds}}$ is composed of the unit-vector directed towards the desired destination, $\hat{\boldsymbol{r}}_{\boldsymbol{w}}$, less the normalized projected gradient, $\nabla \bar{T}_{\text{est}}^{\perp}$, weighted by $w_{\perp}$. The black-dashed line represents a fixed sampling path and the black solid line illustrates the path when directing the virtual body with the negative projected gradient for gradient descent.

Projecting the gradient perpendicular to the vector towards the desired destination ensures that the virtual body converges towards to the destination while traversing a path closer to minima or maxima in the field. Gradient ascent is achieved by adding rather than subtracting the weighted sum of the projected gradient in (4.4.2).

To demonstrate gradient ascent of a noisy scalar field we present a simulation with three vehicles in a triangle formation climbing a fabricated noisy field. In this simulation the vehicle center of mass (virtual leader) is directed by the Kalman filter gradient estimate. Note that the formation is rigid about the center of mass and we are not simulating vehicle

dynamics relative to the center of mass. The formation is made to rotate about the center of mass as is to be explained in what follows, but the formation is always a rigid triangle.

Consider the mean field, $\bar{T}$, shown in the left pane of Figure 4.4.2. The mean field is given by

$$\bar{T}(x,y) = (y+20)/10\; e^{-\frac{\left(x-\sin\left(\frac{2\pi y}{10}\right)\right)^2}{2\sigma^2}} \tag{4.4.3}$$

with $\sigma = 10$. The noise field, w, is the same as used in the Kalman Filter simulation found in Section 4.3 and Figure 4.3.2. An inter-vehicle spacing of $\sqrt{3}$ units was found to nearly minimize the least squares error (4.2.12) and was used in this simulation.

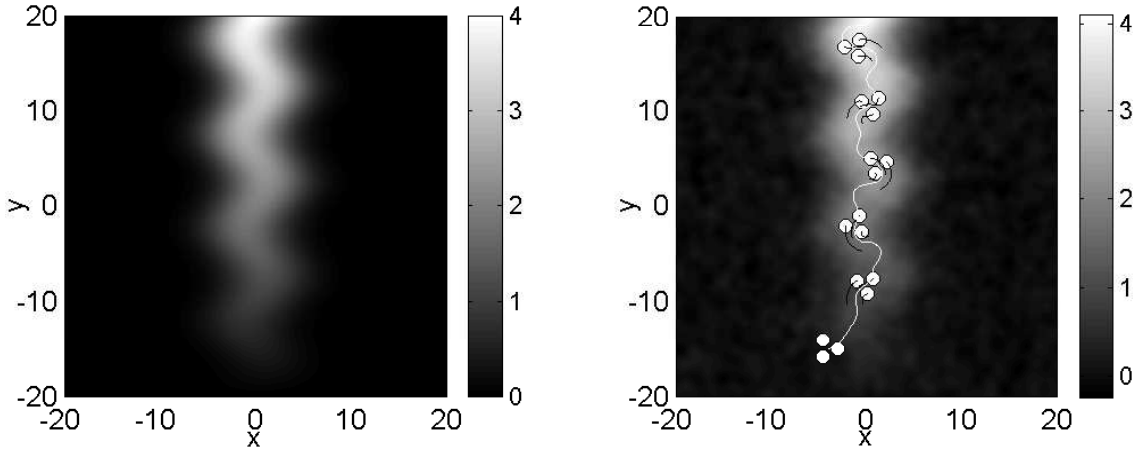

Figure 4.4.2: **Simulated Mean Field, Gaussian Noise and Formation Trajectories.** Left pane shows mean field given by (4.4.3). The right pane shows noisy field with formation snapshots (white dots) and center of mass trajectory (white line). Triangle moves from bottom of pane to top.

The Kalman filter presented in Section 4.3 is implemented with $Q_k = 4\times10^{-4}I$ and $S_k = 10^{-3}I$. As before, the noise statistics in the filter were chosen to match their actual values. To further smooth the formation motion we implement the virtual body heading control presented in (4.4.1) with $k_r = 1$. Additionally, in order to avoid redundant measurements while travelling in a straight line, we implement a simple control which rotates the formation such that there is always a line connecting two vehicles that is perpendicular to the direction

of travel. In this simulation the vehicles are rigidly attached to the virtual leader frame and orientation of the virtual leader frame (with respect to the inertial $x-y$ frame) is specified by a single angle, θ_f. To rotate the virtual leader frame so that the vehicles are oriented as desired we implemented the control law

$$\dot{\theta}_f = -k_{rf} \sin \theta_{ef} \tag{4.4.4}$$

with $k_{rf} = 10$ where $\theta_{ef} = \theta_f - \theta_v \in (-\pi, \pi]$. We choose the orientation of the virtual leader frame so that an edge of the triangle is perpendicular to the direction of travel when $\theta_{ef} = 0$.

As shown in the right pane of Figure 4.4.2 the group successfully navigates its way up the wiggling slope.

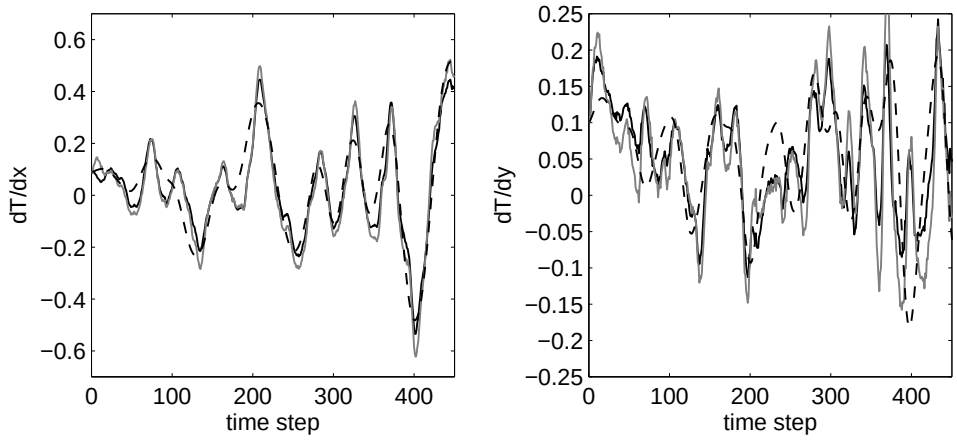

Figure 4.4.3: **Gradient Estimates.** Heavy black line indicates Kalman filter estimate, gray line indicates instantaneous least squares estimate, and dashed line indicates mean field value.

In Figure 4.4.3 we plot the components of the gradient estimates. Both instantaneous least squares and Kalman filter estimates are shown along with the derivatives of the mean field. As before the Kalman filter has the effect of reducing the excursions seen in the least squares estimate. We again evaluate the ratio of Kalman filter estimate error with the instantaneous least squares estimate error. Denoting the Kalman filter estimate of $\frac{\partial \bar{T}}{\partial x}$ at

the formation center as $\frac{\partial \bar{T}}{\partial x}_{\mathrm{KF}}$ and the instantaneous least squares estimate as $\frac{\partial \bar{T}}{\partial x}_{\mathrm{LS}}$ we find

$$\frac{\|\frac{\partial \bar{T}}{\partial x}_{\mathrm{KF}} - \frac{\partial \bar{T}}{\partial x}\|}{\|\frac{\partial \bar{T}}{\partial x}_{\mathrm{LS}} - \frac{\partial \bar{T}}{\partial x}\|} = 0.89, \quad \frac{\|\frac{\partial \bar{T}}{\partial y}_{\mathrm{KF}} - \frac{\partial \bar{T}}{\partial y}\|}{\|\frac{\partial \bar{T}}{\partial y}_{\mathrm{LS}} - \frac{\partial \bar{T}}{\partial y}\|} = 0.76.$$

4.4.2 Front Tracking

In this subsection we demonstrate how to use derivative estimates to track fronts. As described in Section 4.1.1, we define a front as the contour where the Thermal Front Parameter (TFP) given by $\nu = -\frac{\nabla \bar{T}^T}{\|\nabla \bar{T}\|} \bar{H} \frac{\nabla \bar{T}}{\|\nabla \bar{T}\|} = 0$ and $\|\nabla \bar{T}\| > 0$. A simple solution would be to track the gradient of the TFP as presented in [49]. However, given our framework this would require an estimation of third-order derivatives which would be very difficult to acquire in the presence of noise. Instead, we present a method which only relies on the estimation of first and second derivatives. It does not track the gradient of ν and thus does not require the third-order terms. However, it also does not take the most direct path to the front.

We propose that if we follow the local gradient we will eventually cross the center line of a front. The value of ν provides us with an indication of what side of the front we are on, for example for $\nu > 0$ we are on the "warm" side of the front and should descend the gradient to reach the front. If $\nu < 0$ we are on the "cold" side of the front and should climb the gradient to reach the front (see Figure 4.1.1). Thus assuming that $\nu = 0$ only at the front then we can reach the front by tracking $-\nu \nabla \bar{T}$. To travel along the front, we choose to move in the direction perpendicular to the gradient, $\nabla \bar{T}^{\perp}$, as $\nu \to 0$. The desired direction of travel is then given by the weighted sum of $\nabla \bar{T}$ and $\nabla \bar{T}^{\perp}$

$$\boldsymbol{r_d} = w_\nu(\nu) \nabla \bar{T} + |1 - w_\nu(\nu)| \nabla \bar{T}^{\perp}. \tag{4.4.5}$$

$w_\nu(\nu) : \mathbb{R} \to [0, 1]$ is a weight function defined by

$$w_\nu(\nu) = \begin{cases} 1 & \nu \leq -\nu_l \\ -\sin(\frac{\pi}{2}\frac{\nu}{\nu_l}) & -\nu_l < \nu \leq \nu_l \\ -1 & \nu > \nu_l \end{cases} \tag{4.4.6}$$

where ν_l is a positive constant thresholding parameter which is selected *a priori* . For $\nu \leq -\nu_l, \boldsymbol{r_d}$ steers the formation along the gradient since the formation is on the cold side of the front. Likewise for $\nu > \nu_l$ the formation is directed along the negative gradient since the formation is on the warm side of the front. At the front where $\nu = 0, w_\nu = 0$ and thus the formation is directed along a contour of the mean field. It should be understood that this is not the zero contour of ν and thus the formation will likely be steered away from the front. However, at some future instant $|\nu| \neq 0$ and it will be large enough such that the formation should be directed back towards the $\nu = 0$ contour.

To demonstrate front tracking on a noisy scalar field we present a simulation with six vehicles attempting to follow a contour of $\nu = 0$. The formation consists of five vehicles in a pentagon formation with a single vehicle in the center. The distance between the vehicle at the center of the formation and each of the other vehicles is 3.5 units. This formation size was found to minimize the integrated least squares error (4.2.12) along the formation trajectory. As in the gradient climbing simulation, the vehicle center of mass (virtual leader) is directed by the Kalman filter estimates. Furthermore, the formation is again rigid about the center of mass and there are no vehicle dynamics relative to the center of mass other than rigid body rotation.

The mean field is given by

$$\bar{T}(x, y) = e^{-\frac{x^2+y^2}{2\sigma^2}}$$

with $\sigma = 5$. The noise field, w, is identical to the one used in 4.4.1 except the variance, σ_w^2,

is chosen as 0.001.

The Kalman filter presented in Section 4.3 is implemented with the actual noise parameters and we chose $Q_k = 2 \times 10^{-5} I$ and $S_k = 10^{-3} I$. We again implement a discretized version of the virtual body heading control presented in (4.4.1) with $k_r = 1$ and a discretized version of the formation orientation control presented in (4.4.4) with $k_{rf} = 1$. The formation center of mass is propagated 0.1 units per time step in the direction specified by (4.4.5) and (4.4.6) with $\nu_l = 0.02$.

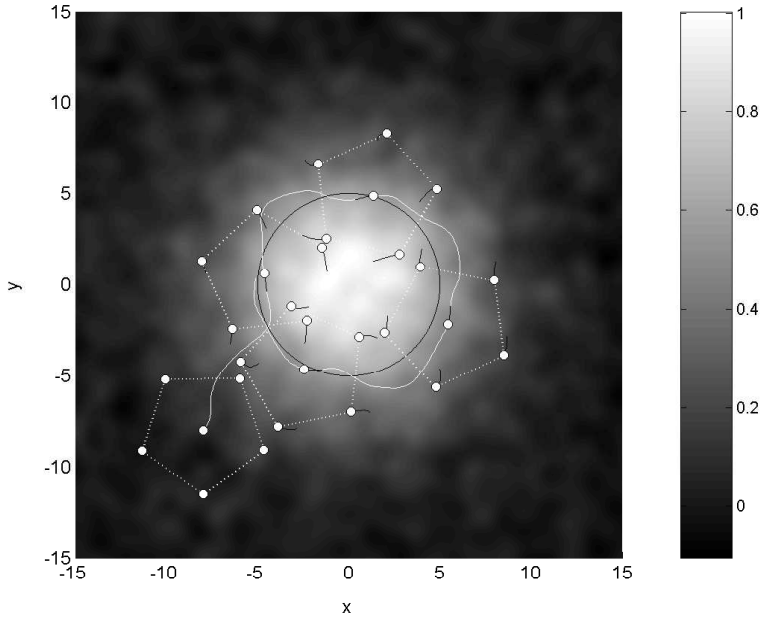

Figure 4.4.4: **Front Tracking Simulation.** Formation snap shots (white dots) and center of mass trajectory (white line) are plotted against the noisy field sampled by the vehicle array.

Figure 4.4.4 shows the front tracking performance. The solid white line is the trajectory of the formation center of mass. The solid black circle is the front where $\nu = 0$. The white dots denote vehicles at incremental instances. In general, the formation appears to stay relatively close the front while travelling around it. In the left pane of Figure 4.4.5 we plot the Kalman filter-estimated ν (solid black line), the instantaneous least squares estimate of ν (solid gray line), and the mean field ν (black dashed line) along the trajectory

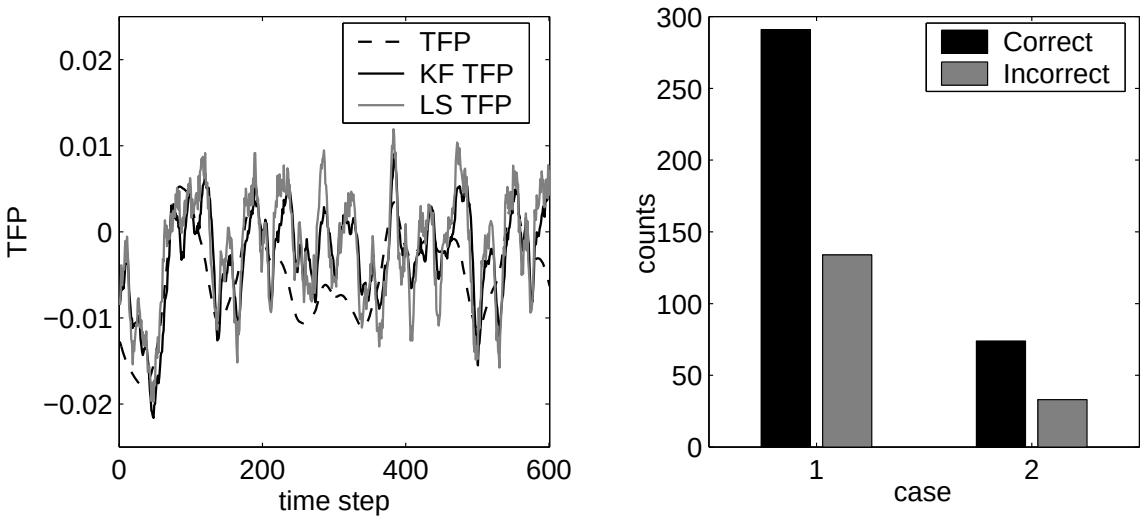

Figure 4.4.5: **Thermal Front Parameter Estimate and Correct Heading Histogram.** Left pane plots the actual, Kalman filter, and instantaneous least squares estimate of the thermal front parameter at the formation center. Right pane presents histograms of how often the TFP estimate correctly vs. incorrectly directs the formation (see text for description).

of the formation center of mass. The ratio of Kalman filter estimate error and least squares estimate error utilizing the L^2 norm is given by

$$\frac{\|\nu_{\mathrm{KF}} - \bar{\nu}\|}{\|\nu_{\mathrm{LS}} - \bar{\nu}\|} = 0.84$$

where $\bar{\nu}$ is the actual mean field value of the thermal front parameter at the formation center of mass.

Recall we wish to estimate ν so that when the formation is on the warm side of the front we are correctly directed down the gradient and vice versa when the formation is on the cold side of the front. In the right pane of Figure 4.4.5 we present histograms of how often the estimate of ν correctly directed the formation down the gradient when $\nu > 0$ and up the gradient when $\nu < 0$. Case 1 on the histogram is when the formation is on the cold side of the front, i.e. the formation center of mass is outside the circle of radius σ from the center. The black bar is the number of instances for which w_ν correctly directed the

formation to approach the front while the gray bar is the number of instances for which w_ν incorrectly directed the formation to drive away from the front. As shown, the algorithm correctly directed the formation towards the front twice as often as it incorrectly directed the formation. Likewise Case 2 on the histogram is when the formation is on the warm side of the front, i.e. the formation center of mass is inside the circle of radius σ. The black and gray bars have identical meaning to that of Case 1. As before, the algorithm correctly directed the formation towards the front twice as often as it incorrectly directed the formation.

Chapter 5

Cooperative Control of Autonomous Underwater Glider Fleets

In the preceding chapters we have presented methodologies for both coordinating vehicles and using the resulting formations to perform tasks that could be used in the ocean. However, the theory presented in these chapters does not directly address various operational constraints associated with coordinating real vehicles in a dynamic sea. In this chapter we address these issues in a presentation of our implementation of the VBAP methodology for a fleet of autonomous underwater gliders. This implementation was developed for use during the Autonomous Oceanographic Sampling Network II (AOSN II) experiment conducted in Monterey Bay, California, during the summer of 2003. In August of 2003 we implemented this specialization of VBAP on a fleet of Slocum underwater gliders. The results of the sea trials are presented in Chapter 6.

The contents of this chapter are as follows. In Section 5.1 we describe autonomous

underwater gliders and, in particular, the Slocum autonomous underwater glider. In Section 5.2 we give a detailed account of the operational constraints which impact coordinating multiple Slocum gliders in this setting and present the modification and extensions of VBAP we developed to account for these constraints. Some constraints are related in part to limitations of current underwater technologies; for example, the Slocum gliders do not communicate with each other while underwater. Other constraints are specific to design choices in AOSN II; for example, the gliders were operated at a constant speed relative to the flow (on average). In Section 5.3 we summarize the complete VBAP/Slocum glider system in place during AOSN II. After presenting the operational scenario and complete implementation, in Section 5.4 we present realistic simulations that were designed to test and demonstrate our methodology prior to the sea trials at AOSN II. In particular we describe a simulation of an autonomous glider fleet performing cooperative projected gradient descent in Monterey Bay using both available model and measured data in Monterey Bay from summer 2000.

5.1 The Autonomous Underwater Glider

Autonomous underwater gliders are a class of energy-efficient autonomous underwater vehicles (AUVs) designed for continuous, long-term deployment [78] and as a result are playing an increasingly critical role in autonomous, large-scale ocean surveys [2]. Additionally, gliders can be significantly less expensive and require less operational infrastructure as compared to conventional AUVs, so they are well-suited to be deployed in large numbers, particularly in multiple vehicle operations. Over the last few years underwater gliders have become a promising emerging technology for oceanographic sensing applications. In the United States three types of ocean-going underwater gliders have been developed for oceanographic ap-

plications: the Slocum [99], the Spray [82], and the Seaglider [28]. The Slocum glider manufactured by Webb Research Corporation is shown in Figure 5.1.1.

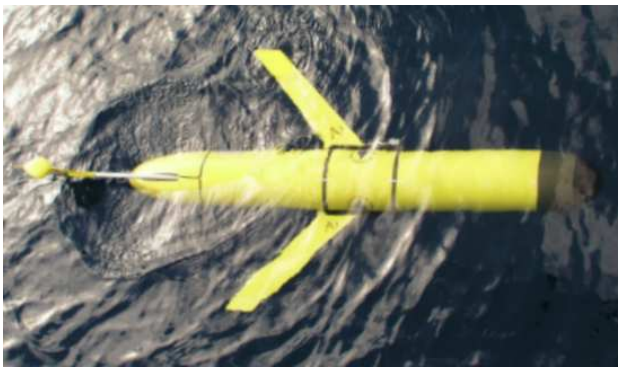

Figure 5.1.1: **Webb Research Corporation Slocum glider.**

Whereas a propeller driven vehicle can sustain operations for hours, glider endurance is measured in weeks. With long term deployments in mind, gliders are designed to require relatively little on-site operational infrastructure. The glider philosophy is "to throw it in the water and go", literally. For example in the spring of 2004 for a US Navy demonstration, a Slocum glider owned by Dr. David Fratantoni of the Woods Hole Oceanographic Institution (WHOI), was operating in the Sea of Japan while Dr. Fratantoni was prescribing missions from his lab in Massachusetts [34]. All communication with the glider occurred via satellite data links and internet traffic. Personnel from WHOI were locally on hand in the Sea of Japan just to deploy and retrieve the glider, and to monitor glider activities. In the future, other than for deployment and retrieval (which could be separated by weeks) no personnel will be required to be on hand.

The energy efficiency of the gliders is due in part to the use of a buoyancy engine. Gliders change their net buoyancy (e.g. using a piston-type ballast tank) to change their vertical direction of motion. Actively controlled redistribution of internal mass is used for fine tuning attitude. For example, the Slocum glider moves its battery pack fore to aft (and

vice versa); whereas the Spray and Seaglider move their battery packs to fine tune pitch and additionally, roll (for heading control). The Slocum uses a rudder for heading control. Underwater gliders use body surfaces, typically fixed wings, to provide lift which induces motion in the horizontal direction. The nominal motion of the glider in the longitudinal plane is along a sawtooth trajectory where one down-up cycle is called a yo. Being generally slow moving, gliders are very sensitive to external currents.

The Slocum glider is equipped with an Iridium-based, global communication system and a line-of-sight, high-bandwidth Freewave system for data communication. Both systems are RF-based and subsequently can only be used at the surface. While the glider is on the surface, data collected can be sent back to the shore station (wherever it may be) and new mission parameters can be downloaded onto the glider. The shore station will usually be running server software to retrieve the incoming data, log it, and send new commands to the gliders. For example, Dr. David Fratantoni has created the Glider Data System (GDS), a custom software suite which provides real-time monitoring and mission cueing services for multiple-Slocum glider operations. When a glider surfaces it acquires a Global Positioning System (GPS) fix and then establishes a connection with the GDS Server. This occurs either through Freewave when a receiver is in the local vicinity of the gliders, e.g. ship board, or through Iridium when Freewave coverage is insufficient. In the latter case, the gliders can be operating anywhere in the world wherever adequate Iridium coverage is present. In either case, the recently acquired GPS fix, sensor profile data, and estimated external currents are uploaded to the GDS server where they go through quality control and are subsequently logged. Then either a new mission is downloaded to the glider or the glider is directed to go about finishing its current mission.

During AOSN II operations, the gliders communicated solely by Iridium and at each

surfacing, gliders would relay their data to the GDS at WHOI. This data would then be available for retrieval via the internet by the operator stationed at the Monterey Bay Aquarium Research Institute (MBARI). Once new mission plans were generated they would be sent back to the GDS from MBARI (via the internet) to be uploaded at the next glider surfacing. A simple schematic of the data flow during AOSN II is shown in Figure 5.1.2.

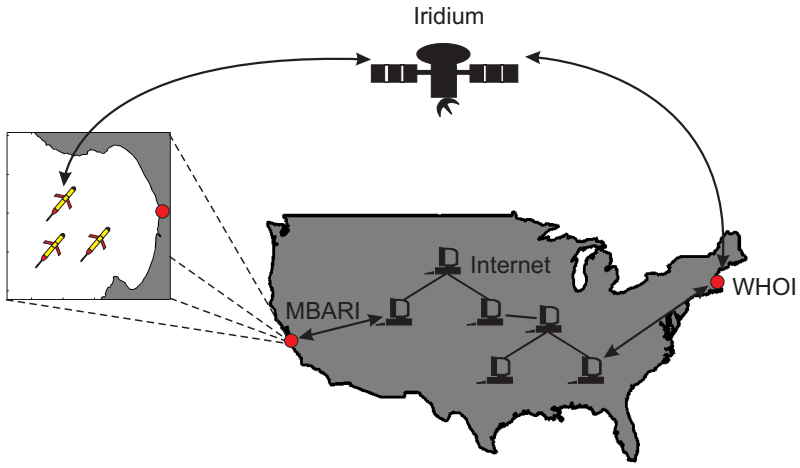

Figure 5.1.2: **AOSN II VBAP Communication Summary.** All communication links on this figure are bi-directional. At the surface the Slocum gliders transmit data to the GDS server at WHOI by Iridium satellite connection. This data is then retrieved from MBARI through the internet. New mission plans are sent to the GDS server via the internet where they are downloaded to the gliders during their next respective Iridium connection.

The Slocum glider operates autonomously, tracking waypoints in the horizontal plane. While underwater, the glider uses dead reckoning for navigation, computing its position using integration of its horizontal-plane velocity, estimated from its depth and attitude measurements. The GPS fix acquired at the surface is used to update its dead reckoning. Gliders are inherently sensitive to ocean currents and the Slocum addresses the effects of external currents in its dead reckoning algorithms and heading controller. However, during a dive cycle the glider does not have a local current measurement. Instead the glider uses a constant estimate computed at the last surfacing by comparing dead-reckoned position

with recently acquired GPS fixes. Any discrepancy between the two is attributed to an external current and is used to compute a new estimate of average current. This estimate of average current is also made available as science data.

Gliders can be equipped with a variety of sensors for gathering data useful for ocean scientists. The Slocum gliders used in Monterey Bay in 2003 housed sensors for temperature, salinity, depth, chlorophyll fluorescence, optical backscatter and photo-synthetic active radiation (PAR). Sensor measurements can be used to drive multi-vehicle feedback control algorithms with the goal of collecting data that is most useful to understanding and predicting dynamic fields in the environment. This application of feedback control to a sensor network is called *adaptive sampling* as described in Chapter 4.

5.2 VBAP and Coordinating Slocum Gliders at AOSN II

As part of the AOSN II experiment during August 2003, twelve Slocum gliders, operated by Dr. David Fratantoni of WHOI, were deployed in Monterey Bay, CA. These gliders were monitored from a central shore station located at the Monterey Bay Aquarium Research Institute (MBARI) at Moss Landing, CA. During the experiment we performed demonstrations of coordinated glider operations with a subfleet of these gliders. In this section we describe constraints associated with coordinating Slocum gliders during AOSN II and address how we modified VBAP to account for them. Constraints described here are as follows:

- **Constant-Speed Constraints.** Glider speed was held fixed throughout the experiment. This limits the range of feasible formations especially when currents which vary across the array are present.

- **External Currents.** The methodology presented in Chapters 2 and 3 assumes no external current. Given that the glider is particularly susceptible to external currents this needed to be addressed.

- **Intermittent Feedback.** Lack of underwater communication restricted coordinating feedback to occur only while gliders were on the surface. While underwater, the glider could only follow prescribed waypoints. Thus the effective feedback sampling period for coordinated control of the glider fleet was the interval between glider surfacings. During AOSN II, this interval was approximately two hours, i.e. each glider surfaced every two hours.

- **Data Latency.** In order to restrict the amount of time each glider would be at the surface, mission plans had to be immediately available at surfacing and no time was allotted for closing the feedback loop at the surface. Thus, the VBAP generated trajectories had to be computed with data from less recent glider surfacings.

- **Asynchronous Surfacings.** A further complication arose from the fact that gliders in a formation were not made to all surface at the same time. These asynchronous surfacings complicated mission planning because gliders could not communicate while underwater. Thus the gliders that have already surfaced that were give new plans would be on different mission plans than the gliders that have yet to.

We tested our procedures for accommodating these constraints prior to AOSN II through glider trials at sea and in simulation. During January 2003, prior to AOSN II, we participated in Slocum glider shakedown trials in the Caribbean. Dr. David Fratantoni was the principle investigator for this cruise. As part of the shakedown we ran tests on a single Slocum vehicle. We performed a two-vehicle coordination experiment with a single real ve-

hicle and a second virtual vehicle. We also conducted detailed simulations of three Slocum gliders in Monterey Bay. We used both model data and measured data to serve as the ocean environment. These simulations are discussed in Section 5.4.

5.2.1 VBAP with a Constant Speed Constraint

During AOSN II, glider speed was not a control variable, i.e. speed remained fixed (on average). A glider moves in a sawtooth motion with the forward speed of the glider slowing at the inflections from upwards to downwards dives or downwards to upwards dives. Therefore, the glider speed varies; however, when averaged over several yos, glider speeds are found to be approximately constant relative to the external current. Thus we model the glider in VBAP with fixed speed. Further we use a first-order vehicle model with constant magnitude control input.

VBAP with First-Order Dynamics

The control methodology presented in Chapters 2 and 3 was presented for a point mass model with second-order dynamics. In order to implement the constant speed constraint, a first-order model was utilized. Recall that the ith vehicle's position is given by $\boldsymbol{x}_i \in \mathbb{R}^2$. As before, **bold** font is reserved for vectors, and the same symbol in normal font indicates the magnitude, i.e. $h = \|\boldsymbol{h}\|$. The hat character indicates that a vector has been normalized, e.g. $\hat{\boldsymbol{h}} = \frac{\boldsymbol{h}}{h}$. The VBAP framework presented in the previous chapters varies slightly in that now we have

$$\dot{\boldsymbol{x}}_i = \boldsymbol{u}_i, \tag{5.2.1}$$

and

$$\boldsymbol{u}_i = -\nabla_{x_i} V_i. \tag{5.2.2}$$

Notice that the term $\boldsymbol{f}_{\boldsymbol{v}i}$ (see (2.1.2)) goes away in the kinematic model.

Define $\boldsymbol{\chi}_{\boldsymbol{\kappa}} = (\boldsymbol{x}_1^T, \ldots, \boldsymbol{x}_N^T)^T$ and note that equilibrium of the kinematic model are obtained by setting $\dot{\boldsymbol{\chi}}_{\boldsymbol{\kappa}} = 0$. Recall from Chapter 2 and Chapter 3 that vehicle-to-vehicle and vehicle-to-virtual leader interactions are defined by artificial potentials. The potentials are designed such that the desired formation is the global minimum of the sum of all artificial potentials.

Recall that in Section 3.2 a vehicle control law requirement when introducing virtual body dynamics was that we had a Lyapunov function to prove asymptotic stability to the desired equilibrium when $\dot{s} = 0$. That is, we required the existence of a function $\Phi(\boldsymbol{\chi}_{\boldsymbol{\kappa}}, s) \geq 0$ with $\frac{d\Phi}{d\boldsymbol{\chi}_{\boldsymbol{\kappa}}}^T \dot{\boldsymbol{\chi}}_{\boldsymbol{\kappa}} \leq 0$ within some ball about $\boldsymbol{\chi}^*_{\boldsymbol{\kappa}}$ where $\frac{d\Phi}{d\boldsymbol{\chi}_{\boldsymbol{\kappa}}}^T \dot{\boldsymbol{\chi}}_{\boldsymbol{\kappa}} = 0$ only at $\boldsymbol{\chi}_{\boldsymbol{\kappa}} = \boldsymbol{\chi}^*_{\boldsymbol{\kappa}}$. With first-order dynamics, a suitable Lyapunov function (for the s-frozen dynamics, $\dot{s} = 0$) is the sum of all artificial potentials (c.f. for second-order dynamics, the total energy including the kinetic energy of the vehicle point masses was used), i.e.

$$\begin{aligned}
\Phi(\boldsymbol{\chi}_{\boldsymbol{\kappa}}, s) &= \sum_{i=1}^{N} V_i \geq 0, \\
\frac{d\Phi}{d\boldsymbol{\chi}_{\boldsymbol{\kappa}}}^T \dot{\boldsymbol{\chi}}_{\boldsymbol{\kappa}} &= \sum_{i=1}^{N} \nabla_{x_i} V_i \cdot \dot{\boldsymbol{x}}_i, \\
&= -\sum_{i=1}^{N} ||\nabla_{x_i} V_i||^2 \leq 0.
\end{aligned}$$

If $\nabla_{x_i} V_i = 0$ only at $\boldsymbol{\chi}_{\boldsymbol{\kappa}} = \boldsymbol{\chi}^*_{\boldsymbol{\kappa}}$ in some region around $\boldsymbol{\chi}^*_{\boldsymbol{\kappa}}$ then $\boldsymbol{\chi}^*_{\boldsymbol{\kappa}}$ is an asymptotically stable equilibrium.

Kinematic speed constraint

We now impose a constant speed constraint on the vehicle point mass model. To this effect we make the following modification to the control vector for each glider:

$$\begin{aligned} \dot{\boldsymbol{x}}_i &= \boldsymbol{u}_i{}' \\ \boldsymbol{u}_i{}' &= \alpha_i \left(\boldsymbol{u}_i - \zeta_i \, \hat{\boldsymbol{u}}_i{}^{\mathbf{c}} \right) \end{aligned} \tag{5.2.3}$$

where $\boldsymbol{u}_i$ is defined by 5.2.2, $\hat{\boldsymbol{u}}_i{}^{\mathbf{c}}$ is a unit vector given by $-\frac{\widehat{d\boldsymbol{r}}}{ds}, -\widehat{\boldsymbol{h}}_{il}$, or $-\widehat{\boldsymbol{h}}_{il}^{\perp}$, for virtual body translation, expansion, or rotation, respectively, and,

$$\begin{aligned} \zeta_i(t) &= \begin{cases} \epsilon_\kappa, & ||\boldsymbol{u}_i(t)|| \leq \epsilon_\kappa^2 \\ 0, & ||\boldsymbol{u}_i(t)|| > \epsilon_\kappa^2 \end{cases}, \\ \alpha_i(t) &= \frac{u_g}{||\boldsymbol{u}_i - \zeta_i \, \hat{\boldsymbol{u}}_i{}^{\mathbf{c}}||}, \end{aligned} \tag{5.2.4}$$

ϵ_κ is fixed with $0 < \epsilon_\kappa \ll 1$ and $u_g > 0$ is the constant glider speed in the horizontal plane. The term $\zeta_i \hat{\boldsymbol{u}}_i{}^{\mathbf{c}}$ is necessary to avoid singularities when $\boldsymbol{u}_i \to 0$.

In the presence of this kinematic constraint, we present a condition sufficient to guarantee bounded formation error since it will be shown to permit a Lyapunov Function for the s-frozen, i.e. $\dot{s} = 0$, closed-loop dynamics. By Theorem 3.2.1, with $\dot{s}$ dynamics given in (3.2.1), bounded formation error remains guaranteed.

Lemma 5.2.1 (Control Req. for Boundedness)**.** *Consider $\Phi(\boldsymbol{\chi_\kappa}, s)$ that is used as a Lyapunov function for proving asymptotic stability of $\boldsymbol{\chi}_{\boldsymbol{\kappa}}^*$ when $\dot{s} = 0$, i.e. for the s-fixed system, and is given by*

$$\Phi(\boldsymbol{\chi_\kappa}, s) = \sum_{i=1}^{N} V_i \geq 0$$

where $\Phi = 0$ only when $\boldsymbol{\chi_\kappa} = \boldsymbol{\chi}_{\boldsymbol{\kappa}}^*$. Suppose we constrain the vehicle kinematics such that

$$\dot{\boldsymbol{x}}_i = \boldsymbol{u}_i{}' = \alpha_i \left(\boldsymbol{u}_i - \zeta_i \, \hat{\boldsymbol{u}}_i{}^{\mathbf{c}} \right),$$

where $\alpha_i, \zeta_i, \boldsymbol{u}_i$, *and* $\boldsymbol{u}_i{}^c$ *are defined in (5.2.3) and (5.2.4). Suppose at time* $t \geq 0$, $||\boldsymbol{u}_i(t)|| > \epsilon_\kappa^2$, *for* $i = 1, \ldots p \leq N$, *and* $||\boldsymbol{u}_j(t)|| \leq \epsilon_\kappa^2$ *for* $j = p+1, \ldots, N$ *where* $0 < \epsilon_\kappa \ll 1$

If at time $t \geq 0$,

$$\sum_{i=1}^{p} ||\boldsymbol{u}_i|| > \sum_{j=p+1}^{N} \frac{-\|\boldsymbol{u}_j\|^2 + \langle \boldsymbol{u}_j, \epsilon_\kappa\ \hat{\boldsymbol{u}}_j{}^{\mathbf{c}} \rangle}{||\boldsymbol{u}_j - \epsilon_\kappa \hat{\boldsymbol{u}}_j{}^{\mathbf{c}}||}, \tag{5.2.5}$$

then,

$$\frac{d\Phi}{d\boldsymbol{\chi}_{\boldsymbol{\kappa}}}^T \dot{\boldsymbol{\chi}}_{\boldsymbol{\kappa}} = \sum_{i=1}^{N} \nabla_{x_i} V_i \cdot \dot{\boldsymbol{x}}_i \leq 0.$$

Furthermore, if

$$\sum_{i=1}^{p} ||\boldsymbol{u_i}|| > (N-p) \frac{\epsilon_\kappa^2}{1-\epsilon_\kappa}, \tag{5.2.6}$$

then,

$$\frac{d\Phi}{d\boldsymbol{\chi}_{\boldsymbol{\kappa}}}^T \dot{\boldsymbol{\chi}}_{\boldsymbol{\kappa}} < 0.$$

Proof: Since $\Phi(\boldsymbol{\chi}_{\boldsymbol{\kappa}}, s) = \sum_{i=1}^{N} V_i$,

$$\begin{aligned}
\frac{d\Phi}{d\boldsymbol{\chi}_{\boldsymbol{\kappa}}}^T \dot{\boldsymbol{\chi}}_{\boldsymbol{\kappa}} &= \sum_{i=1}^{N} -\boldsymbol{u}_i \cdot \boldsymbol{u}_i{}', \\
&= \sum_{i=1}^{N} -\boldsymbol{u}_i \cdot \alpha_i \left(\boldsymbol{u}_i - \zeta_i\ \hat{\boldsymbol{u}}_i{}^{\mathbf{c}} \right), \\
&= \sum_{i=1}^{N} -\alpha_i ||\boldsymbol{u}_i||^2 + \alpha_i \langle \boldsymbol{u}_i, \zeta_i\ \hat{\boldsymbol{u}}_i{}^{\mathbf{c}} \rangle.
\end{aligned}$$

Since $||\boldsymbol{u}_i(t)|| > \epsilon_\kappa^2,\ \zeta_i = 0$ *for* $i = 1, \ldots, p \leq N$.

Similarly since $||\boldsymbol{u}_j(t)|| \leq \epsilon_\kappa^2,\ \zeta_j = \epsilon_\kappa$ *for* $j = p+1, \ldots, N$.

Therefore, using the hypotheses in (5.2.5)

$$\begin{aligned}
\frac{d\Phi}{d\boldsymbol{\chi}_{\boldsymbol{\kappa}}}^T \dot{\boldsymbol{\chi}}_{\boldsymbol{\kappa}} &= -\sum_{i=1}^{p} \alpha_i ||\boldsymbol{u}_i||^2 + \sum_{j=p+1}^{N} \alpha_j (-||\boldsymbol{u}_j||^2 + \langle \boldsymbol{u}_j, \epsilon_\kappa\ \hat{\boldsymbol{u}}_j{}^{\mathbf{c}} \rangle), \\
&= u_g \left(-\sum_{i=1}^{p} ||\boldsymbol{u}_i|| + \sum_{j=p+1}^{N} \frac{-||\boldsymbol{u}_j||^2 + \langle \boldsymbol{u}_j, \epsilon_\kappa\ \hat{\boldsymbol{u}}_j{}^{\mathbf{c}} \rangle}{||\boldsymbol{u}_j - \epsilon_\kappa \hat{\boldsymbol{u}}_j{}^{\mathbf{c}}||} \right), \\
&< 0.
\end{aligned}$$

Furthermore, since $\|\boldsymbol{u}_j(t)\| \leq \epsilon_\kappa^2, j = p+1, \ldots, N$,

$$\begin{aligned} ||\boldsymbol{u}_j - \epsilon_\kappa \hat{\boldsymbol{u}}_j{}^{\mathbf{c}}|| &= ||\epsilon_\kappa \hat{\boldsymbol{u}}_j{}^{\mathbf{c}} - \boldsymbol{u}_j||, \\ &\geq \epsilon_\kappa - ||\boldsymbol{u}_j||, \\ &\geq \epsilon_\kappa - \epsilon_\kappa^2, \end{aligned}$$

and thus,

$$\begin{aligned} \sum_{j=p+1}^{N} \frac{-\|\boldsymbol{u}_j\|^2 + \langle \boldsymbol{u}_j, \epsilon_\kappa\, \hat{\boldsymbol{u}}_j{}^{\mathbf{c}} \rangle}{||\boldsymbol{u}_j - \epsilon_\kappa \hat{\boldsymbol{u}}_j{}^{\mathbf{c}}||} &\leq \sum_{j=p+1}^{N} \frac{\langle \boldsymbol{u}_j, \epsilon_\kappa\, \hat{\boldsymbol{u}}_j{}^{\mathbf{c}} \rangle}{\epsilon_\kappa - \epsilon_\kappa^2}, \\ &\leq \sum_{j=p+1}^{N} \frac{\|\boldsymbol{u}_j\|\, \epsilon_\kappa}{\epsilon_\kappa - \epsilon_\kappa^2}, \\ &\leq (N-p)\frac{\epsilon_\kappa^3}{\epsilon_\kappa - \epsilon_\kappa^2}, \\ &\leq (N-p)\frac{\epsilon_\kappa^2}{1-\epsilon_\kappa}. \end{aligned}$$

Thus, if the inequalities in (5.2.5) and (5.2.6) hold,

$$\begin{aligned} \frac{d\Phi}{d\boldsymbol{\chi}_{\boldsymbol{\kappa}}}^T \dot{\boldsymbol{\chi}}_{\boldsymbol{\kappa}}(t) &= u_g \left(-\sum_{i=1}^{p} ||\boldsymbol{u}_i|| + \sum_{j=p+1}^{N} \frac{-||\boldsymbol{u}_j||^2 + \langle \boldsymbol{u}_j, \epsilon_\kappa\, \hat{\boldsymbol{u}}_j{}^{\mathbf{c}} \rangle}{||\boldsymbol{u}_j - \epsilon_\kappa \hat{\boldsymbol{u}}_j{}^{\mathbf{c}}||} \right), \\ &\leq u_g \left(-\sum_{i=1}^{p} ||\boldsymbol{u}_i|| + (N-p)\frac{\epsilon_\kappa^2}{1-\epsilon_\kappa} \right), \\ &< 0. \end{aligned}$$

■

The constant-speed equality constraint will ultimately restrict what formations are feasible using our potential function methods. Numerical simulations have shown that formations that are not *kinematically consistent* with the speed constraint will not converge properly. For example, a "rolling" formation defined by a virtual body that is simultaneously translating and rotating is not kinematically consistent with the constant speed constraint. This is because each vehicle must slow down at some point to be "overtaken" by its neighbor.

Recall we define our artificial potentials such that the desired formation about the virtual body is a global minimum of the sum of all potentials Φ. Consider a virtual body translation, as the virtual body translates so do the desired vehicle positions which minimize Φ since these desired vehicle positions are fixed in a frame attached to the virtual body. We call the trajectories of these desired vehicle positions the *desired vehicle trajectories.* A VBAP simulation in which $\Phi(\boldsymbol{\chi}_{\boldsymbol{\kappa}}(t), s(t)) = 0$ for all $t \geq 0$, yields vehicle trajectories which coincide with the desired vehicle trajectories throughout the simulation. However, the VBAP methodology does not ensure $\Phi = 0$ throughout, rather $\Phi(\boldsymbol{\chi}_{\boldsymbol{\kappa}}(t), s(t)) \leq \Phi_U, \forall t \geq 0$ given $(\boldsymbol{\chi}_{\boldsymbol{\kappa}}(0), s(0)) \leq \Phi_U$. Φ_U is the upper bound on the permissable formation error for which Φ is the metric. As we increase Φ_U, we increase the permitted error from the desired formation. We can visualize the effects of increasing Φ_U on the vehicle trajectories by imagining a set of tubes around each desired formation trajectory which contains all possible vehicle trajectories for which $\Phi \leq \Phi_U$. By increasing Φ_U we increase the size of these tubes since increasing Φ_U corresponds to increasing the allowable vehicle trajectory error from the desired vehicle trajectories. In most simulations of *infeasible* desired trajectories, i.e. desired trajectories that are inconsistent with the uniform constant speed constraint, numerical convergence during simulation could not be obtained for small values of Φ_U. Feasible formations include pure translation, rotation, *or* expansion/contraction, combined rotation and expansion/contraction, and other basic maneuvers. Throughout the AOSN II demonstration, during each VBAP simulation, the virtual body was made to translate while the orientation and size of the desired formation was held fixed.

Trajectory Discretization into Waypoints

Trajectories generated by VBAP are continuous curves that must be discretized into glider waypoints. We propose discretizing via the constrained minimization of an appropriate cost function. We assume the number of waypoints, q, has been pre-selected. Denote a continuous VBAP trajectory for the ith glider as $\boldsymbol{s}_i{}^{\mathbf{V}}(t) \in \mathbb{R}^2, t \in [t_s, t_f]$ and define the waypoint set as $\boldsymbol{w}_i = \{\boldsymbol{w}_i^1, \boldsymbol{w}_i^2, \ldots, \boldsymbol{w}_i^q\}$ where $\boldsymbol{w}_i^j = \boldsymbol{s}_i{}^{\mathbf{V}}(t_j)$ for $j = 1, \ldots, q$ such that $t_s < t_1 < t_2 < \ldots < t_q = t_f$. Denote the trajectory composed of connecting these waypoints with straight line segments and endpoints at the glider's starting location and last waypoint as $\boldsymbol{s}_i{}^{\boldsymbol{w}}$. Having a time parametrization of $\boldsymbol{s}_i{}^{\boldsymbol{w}}$ implicitly defined by the constant speed u_g of the glider, a constrained minimization problem is specified by,

$$\min_{t_i} J(t_i) = \int_{t_s}^{t_f} ||\boldsymbol{s}_i{}^{\mathbf{V}}(t) - \boldsymbol{s}_i{}^{\boldsymbol{w}}(t)||^2 \, dt$$

subject to $||\boldsymbol{w}_i^{m+1} - \boldsymbol{w}_i^m|| > d_{\min}$ for $m = 0, 1, \ldots, q-1,$ and $\boldsymbol{w}_i^0 = \boldsymbol{s}_i{}^{\boldsymbol{V}}(t_s)$. The scalar parameter $d_{\min}$ specifies the minimum acceptable spacing between two adjacent waypoints.

For the AOSN II implementation we chose $q = 2\frac{\text{waypoints}}{\text{hr}}(t_f - t_s)$ and manually selected the initial guess. Numerical optimizations suggest that the cost function may be non-convex resulting in only locally optimal waypoint lists. Thus, there is some degree of sensitivity to initial guesses.

5.2.2 External Currents

Gliders are inherently sensitive to ocean currents and it is important to include estimated and forecast currents in the motion planning. For AOSN II we chose to focus on meso-scale currents which are assumed to be adequately modelled as fairly uniform in an area of interest. Accordingly, we used a simple average of the glider estimated currents $\boldsymbol{u}_{\mathbf{avg}}^{\boldsymbol{f}}$ in our

planning that was computed as

$$\boldsymbol{u}^{\boldsymbol{f}}_{\mathbf{avg}} = \frac{1}{N}\sum_{i=1}^{N} \boldsymbol{u}_i{}^{\boldsymbol{f}},$$

where $\boldsymbol{u}_i{}^{\boldsymbol{f}}$ is the ith vehicle's estimate of the (constant) local advecting current. These current estimates are constant throughout each planning stage. For use in simulation and control design, the virtual body and vehicle velocity are then computed to be

$$\begin{aligned} \dot{\boldsymbol{r}} &= \widehat{\frac{d\boldsymbol{r}}{ds}}\dot{s} + \boldsymbol{u}^{\boldsymbol{f}}_{\mathbf{avg}}, \\ \dot{\boldsymbol{x}}_i &= \boldsymbol{u}_i{}' + \boldsymbol{u}^{\boldsymbol{f}}_{\mathbf{avg}}. \end{aligned}$$

This approximation assumes the flow average and ith glider's flow estimate will not differ significantly. By assuming identical advecting flow to each vehicle and the virtual body, the bounded formation error results of Section 3.2 and Section 5.2.1 remain valid. That is, you can think of the previous analysis as being done with respect to a frame that moves with velocity, $\boldsymbol{u}^{\boldsymbol{f}}_{\mathbf{avg}}$.

As discussed in Section 3.1 the motion of the virtual body is responsible for directing the motion of the glider fleet in addition to maintaining formation. To compensate for the imposed advecting flow during translation, we direct the virtual body ($\widehat{\frac{d\boldsymbol{r}}{ds}}$) in a direction to cancel the current perpendicular to the desired direction of travel as $\dot{s}$ converges to u_g.

The desired direction of travel of the virtual body at s is denoted by the unit-vector $\hat{\boldsymbol{r}}_{\boldsymbol{d}}(s)$ (see Figure 5.2.1). We then write $\boldsymbol{u}^{\boldsymbol{f}}_{\mathbf{avg}}$ in terms of the orthonormal basis established by $\hat{\boldsymbol{r}}_{\boldsymbol{d}}$ and $\hat{\boldsymbol{r}}_{\boldsymbol{d}}{}^{\perp}$,

$$\begin{aligned} \boldsymbol{u}^{\boldsymbol{f}}_{\mathbf{avg}} &= \langle \boldsymbol{u}^{\boldsymbol{f}}_{\mathbf{avg}}, \hat{\boldsymbol{r}}_{\boldsymbol{d}} \rangle \, \hat{\boldsymbol{r}}_{\boldsymbol{d}} + \langle \boldsymbol{u}^{\boldsymbol{f}}_{\mathbf{avg}}, \hat{\boldsymbol{r}}_{\boldsymbol{d}}{}^{\perp} \rangle \, \hat{\boldsymbol{r}}_{\boldsymbol{d}}{}^{\perp}, \\ &= u^{f||}_{\mathrm{avg}} \, \hat{\boldsymbol{r}}_{\boldsymbol{d}} + u^{f\perp}_{\mathrm{avg}} \, \hat{\boldsymbol{r}}_{\boldsymbol{d}}{}^{\perp}, \end{aligned}$$

where $u^{f||}_{\mathrm{avg}} = \langle \boldsymbol{u}^{\boldsymbol{f}}_{\mathbf{avg}}, \hat{\boldsymbol{r}}_{\boldsymbol{d}} \rangle$ and $u^{f\perp}_{\mathrm{avg}} = \langle \boldsymbol{u}^{\boldsymbol{f}}_{\mathbf{avg}}, \hat{\boldsymbol{r}}_{\boldsymbol{d}}{}^{\perp} \rangle$.

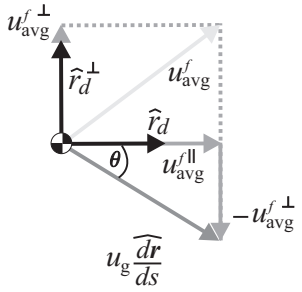

Figure 5.2.1: **Virtual Body Direction in Response to Current.** Origin of frame is virtual body center of mass.

Recall that the virtual body dynamics are given by $\dot{\boldsymbol{r}} = \widehat{\frac{d\boldsymbol{r}}{ds}}\dot{s} + \boldsymbol{u^f_{\text{avg}}}$. Let

$$\widehat{\frac{d\boldsymbol{r}}{ds}} = (\cos\theta, \sin\theta),$$

θ is defined as in Figure 5.2.1, i.e. to cancel the flow component perpendicular to $\hat{\boldsymbol{r}}_{\boldsymbol{d}}$ we choose θ such that

$$u_g \sin\theta = -u^{f\perp}_{\text{avg}}. \tag{5.2.7}$$

Clearly a real solution, θ^*, exists only when $u^{f\perp}_{\text{avg}} \leq u_g$. Even when a real solution exists it may be possible that $u^{f\parallel}_{\text{avg}} > u_g \cos\theta^*$ in which case no progress in the direction of $\hat{\boldsymbol{r}}_{\boldsymbol{d}}$ will be made. When $u_g > ||\boldsymbol{u^f_{\text{avg}}}||$, equation (5.2.7) is guaranteed to have a real solution, $u^{f\parallel}_{\text{avg}} < u_g \cos\theta^*$ and the formation will move in the direction of $\hat{\boldsymbol{r}}_{\boldsymbol{d}}$.

In the instances when $u_g < ||\boldsymbol{u^f_{\text{avg}}}||$, the formation may or may not be able to make headway in the direction of $\hat{\boldsymbol{r}}_{\boldsymbol{d}}$. For example, if $u_g > u^{f\perp}_{\text{avg}}$ then the perpendicular flow component can be completely cancelled. Furthermore when $u_g < ||\boldsymbol{u^f_{\text{avg}}}||$ and $u_g > u^{f\perp}_{\text{avg}}$ then $u_g < u^{f\parallel}_{\text{avg}}$. So if $u^{f\parallel}_{\text{avg}} > 0$ then the formation will move in the direction of $\hat{\boldsymbol{r}}_{\boldsymbol{d}}$. However if $u^{f\parallel}_{\text{avg}} < 0$ progress will not be possible in the direction of $\hat{\boldsymbol{r}}_{\boldsymbol{d}}$.

5.2.3 Intermittent Feedback

The VBAP methodology presented in Chapters 2 and 3 provides a nonlinear state-feedback controller implemented in continuous time. However, the feedback control implemented on the Slocum glider used during AOSN II is capable of only following predefined waypoint lists while underwater. Higher level feedback for formation control is only performed while on the surface where inputs required for VBAP are relayed and new waypoint plans are received. This feedback is intermittent, occurring at the rate of glider surfacing. During AOSN II the minimum surfacing interval for the Slocum glider was dictated to be two hours. This interval was the smallest interval agreed upon by the AOSN II participants. It was chosen to balance the effects of surface drift due to winds or threats while on the surface which increase with more frequent surfacing and the degradation in coordination performance that comes with less frequent surfacing.

Because of the long periods between coordinating feedback, we developed an approach whereby motion plans are computed using the VBAP methodology applied to the gliders in simulation with initial conditions given by the measurement or estimation based on measurements. Motion plans are re-computed only as frequently as new measurements are available. In between measurement updates for coordination (i.e. in between surfacings) each glider uses its low-level control to follow waypoints prescribed by the coordinated motion plans.

5.2.4 Latency

At each glider surfacing new waypoint lists will be uploaded to the glider after data obtained during the last mission has been downloaded. During AOSN II it was decided that the loop could not be closed on the surface, i.e. the new waypoints should be ready for upload even

before the data from the glider (including GPS and average current estimate) is downloaded. The uploaded mission therefore does not use the latest GPS fix, local current estimate and sensor measurements, but uses information gathered during the previous surfacing of the glider. This introduces a degree of latency in the VBAP implementation. Simulations indicate that with two-hourly feedback the formation is reasonably robust to these latencies.

5.2.5 Surfacing Asynchronicity

In addition to intermittent feedback and latency, there is also no guarantee of synchronized glider surfacings since these are improbable and impractical to enforce. Variabilities across the glider fleet, such as w-component (vertical) currents and the local bathymetry, decrease the probability of synchronous surfacings. Furthermore, substantial winds and surface traffic (like fishing boats, etc.) render waiting on the surface to impose synchronicity impractical. When surfacing asynchronicity is present, gliders will be communicating new information and receiving new missions at different times.

Before AOSN II we experimented with two strategies for implementing VBAP in the presence of this asynchronicity. The strategies differed in the number of VBAP plans generated per formation cycle. A VBAP *plan* is the set of trajectories generated for all the gliders in the formation given a set of initial conditions. A *formation cycle* is defined as the interval between the *lead* glider's surfacings. The *lead* glider is the glider to surface first and thus the first glider in need of new waypoints during the first formation cycle. In the following we assume that the time interval between each glider's consecutive surfacings is uniform across the group.

The two strategies proposed involve either a single plan per formation cycle or multiple plans per formation cycle:

A. Single plan per formation cycle. In this strategy, waypoint plans are generated once per formation cycle. The starting time t_{FC} for a new formation cycle is the estimated time of the lead glider's next surfacing. The waypoint plans remain fixed during the formation cycle even if new information becomes available. VBAP is initialized with estimated glider locations and local currents at t_{FC}. Glider locations are estimated using their active waypoint plans and last reported GPS fixes and local current estimates. Waypoint lists for each glider are generated all at once and passed to each glider as they surface. This scenario is illustrated in Figure 5.2.2.

The lead glider's estimated location for planning (the location which initializes VBAP) and its estimated surfacing location (where it is expected to acquire these waypoints) will coincide. However, for an asynchronous group, the other gliders' estimated locations for planning may be behind their estimated surfacing locations. To avoid backtracking, the waypoint plans generated for these gliders are edited to remove waypoints between the estimated planning location and the estimated surfacing location.

B. Multiple plans per formation cycle. In this scenario new waypoint lists are generated during a formation cycle whenever new information is available. New information becomes available every time a glider surfaces. The actual surfacing location (last reported GPS) and sensor measurements of the last glider to surface are used to immediately plan waypoints for the glider to surface next. The location of each glider at the *estimated* surfacing of the glider to surface next are used as initial conditions. This scenario is also illustrated in Figure 5.2.2. During the VBAP simulation we did not have the capability of constraining the trajectories of gliders currently underway. Thus, waypoint plans among gliders will not, in general, be consistent because they will be computed with different information sets. Furthermore, there must be sufficient time between glider surfacings to ensure that a plan

can be available for download immediately when the next glider surfaces. So a large degree of surfacing asynchronicity is favorable for this implementation. Simulations demonstrated however, that with a two hourly surfacing interval (the interval to be used during AOSN II) and asynchronous surfacings, cohesive formations were obtainable.

5.3 AOSN II VBAP Operational Summary

In this section we summarize the AOSN II VBAP operational scenario. Figure 5.3.1 presents a detailed schematic view of the coupled VBAP-Glider system implemented during AOSN II.

Starting from the top of Figure 5.3.1, gliders surfaced on a two-hourly interval, acquired a GPS fix and then established an Iridium connection with the GDS server located at WHOI. Data such as science measurements, the on-board average current estimate, and the glider's current location were transmitted. As discussed, no attempt was made to synchronize glider dives or surfacings. The GDS then performed quality control, logged the data, and made it available for download. At MBARI a standard Pentium IV laptop downloaded the glider data via the internet, performed the necessary computations, and uploaded mission files back to the GDS server.

In the following, we describe the computations used during operations in terms of three modules: *Glider Simulator, VBAP, and Waypoint Generator.*

The *Glider Simulator* performs a dynamic simulation of a Slocum glider. It utilizes a "black-box" model of the Slocum glider with parameters obtained by fitting model data from the Slocum shakedown trials performed in the Caribbean during January 2003. As its inputs, the simulator utilizes the current mission plan, consisting of waypoints, mission duration, and yo depth bounds, the last known position before diving, and the currents

Single plan per formation cycle:

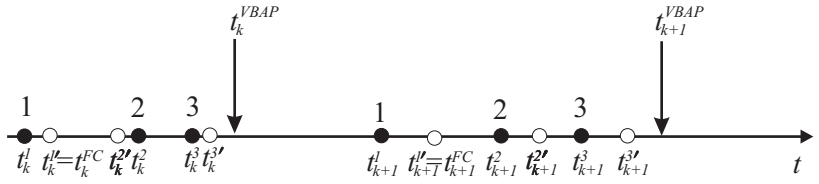

Multiple plans per formation cycle:

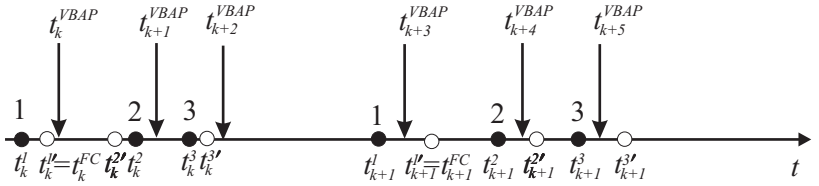

Figure 5.2.2: **Planning Scenarios.** Horizontal axis is time axis and solid circles indicate the time of actual surfacing for three fictitious gliders 1, 2, and 3. Adjacent (hollow) circles indicate the estimated surfacing time. t_k^i indicates the kth surfacing of the ith glider. $t_k^{i'}$ indicates the *estimated* kth surfacing of the ith glider. Glider 1 is the *lead* glider. The arrows labelled t_k^{VBAP} indicate the moments when the kth VBAP simulation is performed. *VBAP* is initialized with the *estimated* glider positions at their next surfacings and the average of the current estimates reported by each glider. *Single plan per formation cycle*: in this strategy the kth *VBAP* computation is performed at t_k^{VBAP} after all gliders have surfaced and utilizes the GPS fixes and estimated currents reported at each t_k^i, $\forall i = 1, 2, 3$. *VBAP* is initialized with the *estimated* positions of *all* gliders at $t_{k+1}^{1'}$, i.e. the *lead* glider's next estimated surfacing. The waypoint lists generated for each glider are downloaded at each glider's surfacing at t_{k+1}^i. *Multiple plans per formation cycle*: in this strategy *VBAP* is performed each time a glider surfaces, i.e. each time new information is available. The VBAP plan generated after the ith glider surfaces at t_k^i is for the glider that is estimated to surface next. For example, in the figure, the *VBAP* plan generated at t_k^{VBAP} after glider 1 surfaces uses the *estimated* positions of all gliders at $t_k^{2'}$ and the last reported estimated currents for each glider as initial conditions. The waypoints from this plan are expected to be uploaded to glider 2 at $t_k^{2'}$. Note there must be sufficient time between glider surfacings to ensure that the plan will be available for download immediately when gliders surface. For example, the *VBAP* plan computed at t_k^{VBAP} must be available for upload to glider 2 at t_k^2. In the event that the plan computed at t_k^{VBAP} is not available for glider 2 at t_k^2, the waypoint plan computed at t_{k-1}^{VBAP} is issued to glider 2 at t_k^2.

reported during the last mission. The simulator is fairly detailed; an in-depth presentation can be found in Appendix C. The simulator generates required information for both the *VBAP* module and the *Waypoint Generator.*

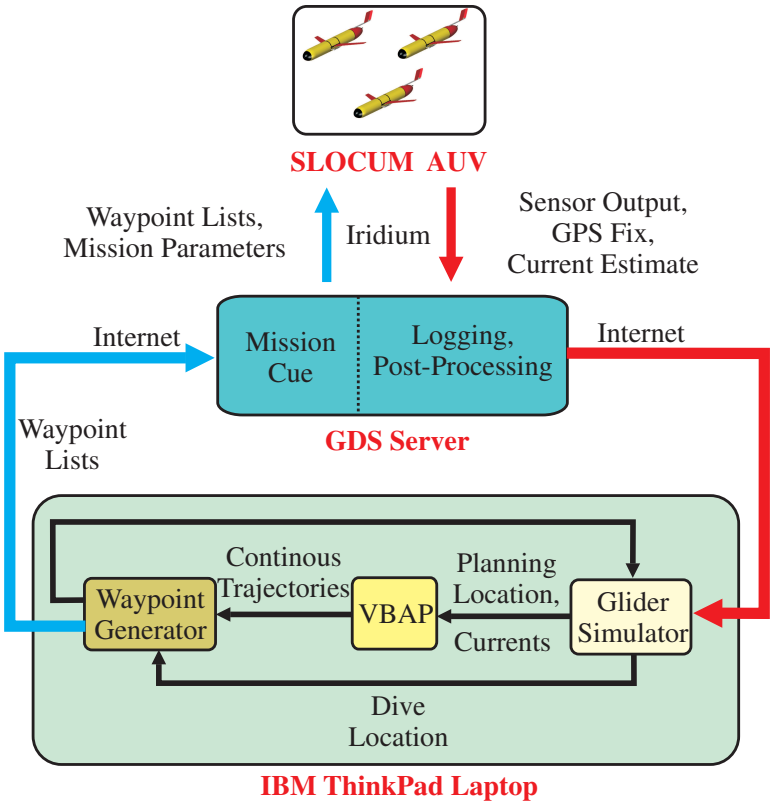

Figure 5.3.1: **AOSN II VBAP Operational Scenario.**

The VBAP implementation used during AOSN II was the *single plan per formation cycle* strategy described in Section 5.2.5. So that mission plans are immediately available at surfacing, an estimate is needed of the dive location of each glider at the start of its *next* mission, denoted *dive location.* Also needed for each glider is its location when the *lead* glider dives, denoted *planning location.* Both sets of locations are introduced to accommodate the possibility of surfacing asynchronicity. The planning locations are used as initial positions for each glider included in *VBAP.* The dive locations are used to adjust the generated waypoint lists so that they are consistent with the locations of the gliders when they actually start the mission. Both planning and diving locations are generated by the *Glider Simulator.*

Using the average of the last reported estimated currents, *VBAP* generates a continuous trajectory for each glider which is then discretized into waypoints in the *Waypoint*

Generator. In the process of generating waypoints, given the dive locations, we have the option of removing waypoints for any glider if the output of the waypoint generator is expected to yield backtracking. During the sea-trials described in Chapter 6 this was never required. The waypoint lists are then uploaded to the GDS and enter the mission queue to be transmitted to each glider during the next Iridium connection along with mission parameters such as glider max yo depth and time for next surface. The waypoint plans are also fed-back to the *Glider Simulator.*

5.4 Simulations

Prior to the AOSN II demonstrations we ran detailed simulations of an autonomous glider fleet in order to dry-run our methodologies and tune control parameters. In this section we describe simulations of the fleet performing cooperative projected gradient descent (see Chapter 4.4.1). During AOSN II, model-generated ocean forecasts were to be available to guide glider mission planning. We simulated an adaptive sampling procedure that uses a forecast to prescribe a coarse direction for sampling and gradient climbing to refine sampling paths in response to on-board glider temperature measurements. For example, the forecast might direct the gliders to the north to the cold water while the gradient climbing will redirect the gliders according to the gliders' estimate of the temperature gradient. For these tests we use two sets of temperature data from the MOOS Upper-Water-Column Science Experiment (MUSE) performed in Monterey Bay, California in August 2000. Innovative Coastal-Ocean Observation Network (ICON) model data [83] is used as the forecast model data set and the aircraft-observed sea-surface temperature (SST) data is used as the "truth" data set. We use both datasets to demonstrate a principal advantage of adaptive sampling, that is, the ability to correct for errors in the plans generated a priori. In addition to

temperature data, ICON also supplies the flow field truth data set in which the simulated gliders are advected.

Both the ICON data and airborne measured SST data is for August 17, 2000. During this time, there is a temperature front near the 36.8-degree N parallel in the ICON data (forecast set). However the aircraft-observed SST data (truth set) indicates the front is southwest of the front predicted by the ICON data. We describe a simulation of a glider fleet that is initially directed along the temperature front identified in the ICON model data. By using the feedback temperature measurements and generating in-situ gradient estimates, the fleet tries to redirect itself towards what it perceives to be the actual temperature front.

5.4.1 Truth and Model fields

Aircraft SST Data

The aircraft SST data, which provides the truth temperature field for our simulation, was generated during MBARI's MOOS Upper-Water-Column Science Experiment (MUSE) in August 2000 by the Naval Postgraduate School in collaboration with Navy's SPAWAR System Center-San Diego and Gibbs Flying Services, Inc., San Diego, CA. The data was collected on the afternoon of August 17, 2000 using a twin engine Navajo aircraft, which was flown along a regular grid over Monterey Bay at an altitude of less than 1000 feet. The aircraft measured sea surface temperature immediately below its location. More details about the data collection and the MUSE experiment can be obtained from Monterey Bay Aquarium Research Institute (MBARI)'s website [92].

Figure 5.4.1a presents the aircraft SST data. The black box illustrates a region of particular interest which corresponds to a cold tongue of water entering the bay from the north. This is characteristic of an upwelling event. In this section we present simulation

results of a glider fleet exploring this region.

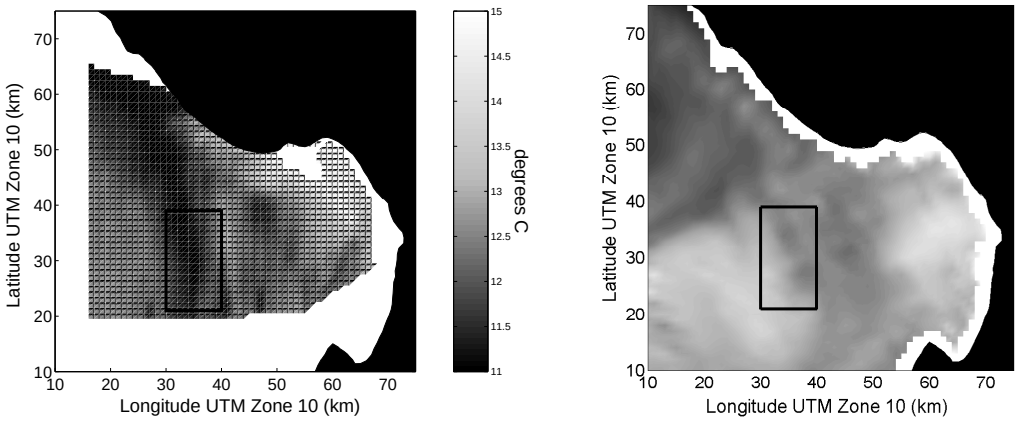

Figure 5.4.1: **Sea Surface Temperature (SST) in Monterey Bay.** (a) NPS Aircraft SST, Monterey Bay, August 17, 2000 (b) ICON SST, Monterey Bay, August 17, 2000 16:00 local time

Innovative Coastal-Ocean Observing Network (ICON)

The fine-resolution numerical ocean model of the Monterey Bay Area (ICON model) was developed in the "Innovative Coastal-Ocean Observing Network" (ICON) project [83]. The ICON model is a three-dimensional, free surface model based on the Princeton Ocean Model (POM) [14]. The model has an orthogonal, curvilinear grid, extending 110 km offshore and 165 km in the alongshore direction. The horizontal resolution is 1-4 km with the maximum resolution in the vicinity of Monterey Bay. Vertically, the model is characterized by a realistic bottom topography with 30 vertical levels. On the open boundaries the model is coupled to a larger-scale Naval Research Laboratory (NRL) Pacific West Coast ocean model. The ICON model was run with atmospheric forcings from COAMPS (Navy Coupled Ocean and Atmospheric Mesoscale Prediction System) model predictions [44]. HF radar (CODAR)-derived surface currents are assimilated into the model [84].

In our simulations we use the ICON data from August 17, 2000 fixed at 16:00 hours local

time. The ICON sea surface temperature serves as a representative model field that we will use to motivate a glider fleet mission. The ICON SST data is presented in Figure 5.4.1b. The black rectangle illustrates the area of the interest as it appears in the ICON data. ICON also supplies the quasi three-dimensional flow field truth set in which the simulated gliders are advected. By quasi three-dimensional we mean horizontal currents are available at various depth levels. The depth-averaged ICON model currents are shown in Figure 5.4.2. In the region where the simulations were conducted the flow is predominately flowing to the south and southwest.

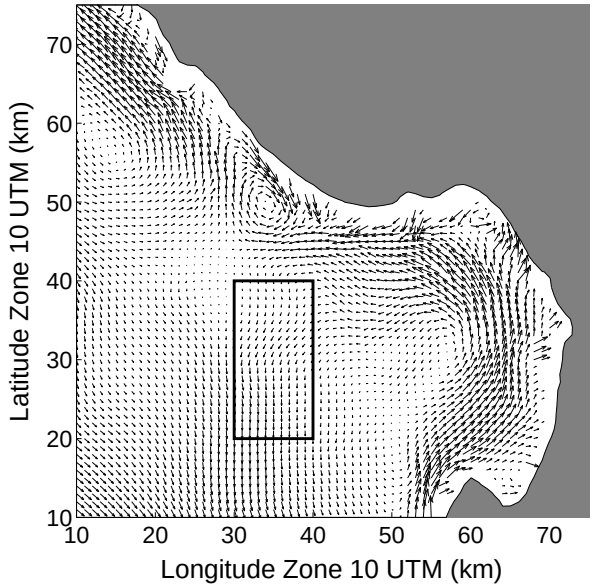

Figure 5.4.2: **ICON Depth Averaged Current Vector Field, Monterey Bay, August. 17, 2000 16:00 local time.** The average current magnitude is 7 cm/s within the black rectangle.

5.4.2 Setup and Results

For our simulations we propose the following scenario: a perceived frontal boundary in the model data (see box in Figure 5.4.1b) motivates us to drive a fleet of gliders through this region while performing a projected gradient descent to steer the formation towards the

colder regions. We assume we have a fleet of three gliders and choose an equilateral triangle formation with an inter-vehicle spacing of 3 km.

While underwater the gliders are simulated to move at a horizontal speed of 40 cm/s and a nominal vertical speed of 20 cm/s relative to water, consistent with the assumptions made in Section 5.1. The horizontal velocity of each glider is added to the "truth" local horizontal flow velocity, which is provided by the ICON data set, to compute the total absolute horizontal velocity of the glider. Vertical velocity from ICON model predictions were unavailable and not used in this study. Instead a zero-mean white noise is added to the nominal vertical velocity of the glider to account for the vertical component of the true local flow field.

The gliders are simulated to dive until 25 m above the sea floor, up to a maximum depth of 200 m. Then they glide upward until they are 5 m from the surface before going downward again, unless they are surfacing in which case they rise all the way to the surface. The gliders are commanded to start surfacing 2 hours after they dive into the water. Since the glider could be at any depth between 0 and 200 m when it starts surfacing, the total time of implementation of the 'glider in water' module will in general be a little over 2 hours during every cycle.

The glider is set to drift with the flow when it is on the surface. The amount of time spent on the surface is the sum of a static term (estimated from historical data for time required for GPS fixes and Iridium connections) and a random component. The random component is simple white noise to model uncertainties associated with dropped Iridium connections or lost GPS links due to wash over the glider's antenna.

During the mission, surface temperature measurements for each glider are stored along with their corresponding location. Whenever new waypoints are generated with VBAP, the

last reported surface temperature measurements and corresponding locations are used to compute a least-squares gradient estimate. The gradient estimate is then used to redirect the group as described in Section 4.2.2.

The virtual body is composed of a single virtual leader. We suppose that it has been decided to direct the group to head predominately south. So we choose the destination, $\boldsymbol{r_w}$, to be approximately 70 km due south from the virtual leader's initial location (see Section 4.4.1). We design our artificial potentials such that the desired triangle formation about the virtual leader will be oriented such that a triangle edge spans from east to west with the inside-directed normal to that edge pointing northward.

The formation error function used in the control law for the virtual body speed $\dot{s}$ given in (3.2.1), is

$$\Phi(\boldsymbol{\chi}, s) = \sum_{i=1}^{3} \left(V_h^c(h_{i1}) + V_h^o(\theta_{i1}) + \frac{1}{2} \sum_{j \neq i}^{3} V_I(x_{ij}) \right) \tag{5.4.1}$$

where $V_I(x_{ij})$ is given in (2.2.1) with $\alpha_I = 10$ /km/hr, $d_0 = 3$ km, and $d_1 = 100$ km. $V_h(h_{i1})$ is analogous to that found in (2.2.1) where x_{ij}, α_I, d_0, and d_1 are replaced by $h_{il}, \alpha_h^c = 2$ /km/hr, $h_0 = \sqrt{3}$ km, and $h_1 = 100$ km, respectively. V_h^o is given in (2.3.2) with $\alpha_h^o = 10$ km/hr, $r = 3$ and $\phi^d = \pi/2$. Φ_U was set at 0.2. The virtual leader heading direction, $\widehat{\frac{d\boldsymbol{r}}{ds}}$, is computed using (4.4.2) with the weight $w_\perp = 0.5$. An approximately 12 hour experiment was simulated.

Initially we assume the fleet is synchronized and compute a VBAP plan based on each glider's initial location. Initial local current estimates are taken to be the depth-averaged current at each glider's location. To induce asynchronous surfacings, we artificially stagger the next surfacing time of each glider by 40 minutes (recall each glider surfaces approximately every 2 hours). Thus, the first glider (glider 1) will begin surfacing after 40 minutes, the second (glider 2) after 80 minutes, and the third after 120 minutes (glider 3). We

simulate both asynchronous implementations presented in Section 5.2.5. In both cases, the virtual leader is relocated to the glider formation center of mass at the start of each VBAP implementation.

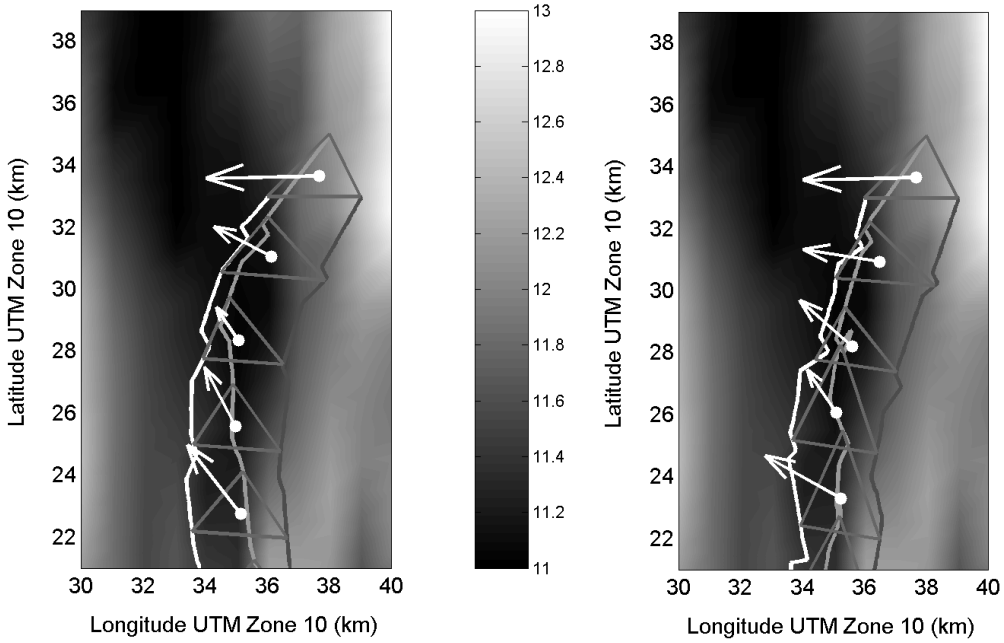

(a) (b)

Figure 5.4.3: **Coordinated Glider Simulations.** Circle indicates initial formation center of mass (virtual leader position). Tracklines denote glider trajectories, glider 1, 2, and 3 are shaded white, dark gray, and light gray, respectively. Triangles illustrate glider relative locations at two hour intervals. Grayscale contour shows "truth" sea surface temperature in degrees Celsius. Arrows are (the negative) instantaneous least square gradient estimate. (a) Strategy A: Single plan per formation cycle. (b) Strategy B: Multiple plans per formation cycle.

Multiple simulations were performed to tune and converge upon the parameters in (5.4.1). We now present the trajectories and brief discussion of two simulations. Figure 5.4.3a presents the glider trajectories when implementing a single plan per formation cycle (strategy A of Section 5.2.5). As shown, the fleet maintains the desired formation and detects the cold water tongue in the truth field (aircraft SST data), redirecting the fleet towards it while heading towards the destination. Figure 5.4.3b presents the glider trajectories when planning multiple times per formation cycle (strategy B of Section 5.2.5).

The glider fleet detects the cold water tongue but does not maintain formation as well and exhibits noticeable stretching. Examining the individual glider trajectories indicates that back-tracking for glider 3 is the cause. This illustrates a shortcoming in this planning method. Distortion is likely to result from inconsistent trajectories since mission plans cannot be sent to gliders currently underway. Thus the trajectory for a particular glider is generated on the incorrect assumption that gliders 1 and 2 will follow corresponding trajectories that are generated simultaneously.

We also illustrate with arrows in Figure 5.4.3, the negative of the least squares estimated temperature gradients. These gradients are estimated using the temperature measurements taken by the gliders from the truth data set. Qualitatively, it can be seen that these vectors do point in the direction of the coldest water. This demonstrates the formation's ability (at 3 km inter-vehicle spacing) to serve as a sensor array and correctly identify the path to the coldest part of this feature. The temperature profiles recorded by each glider is shown in Figure 5.4.4.

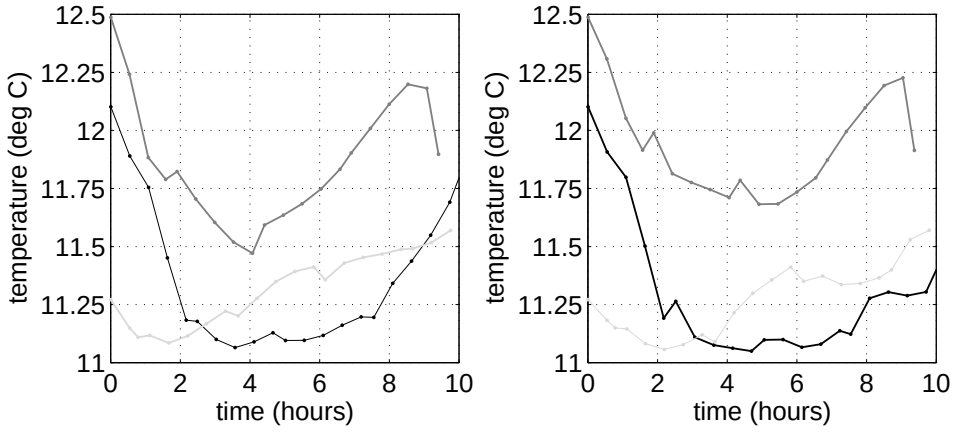

Figure 5.4.4: **Simulated Glider SST Profiles.** SST measurements recorded by each glider implementing the (a) *single plan per formation cycle* strategy and (b) *multiple plans per formation cycle* strategy. Measurements from gliders 1, 2, and 3 are shown in light gray, dark gray, and black, respectively.

In Figure 5.4.5 we qualitatively compare the performance of each planning method in

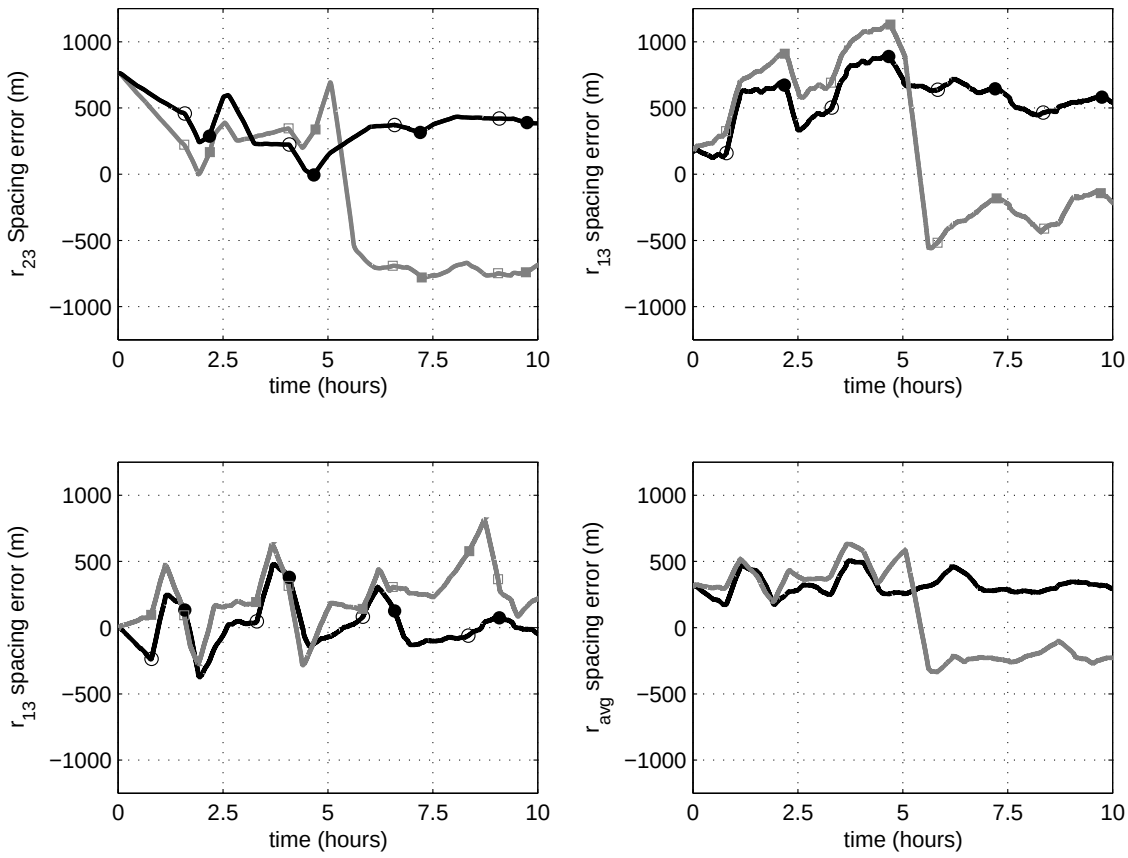

Figure 5.4.5: **Inter-Vehicle Spacing Error.** Black lines correspond to single plan per formation cycle and gray lines correspond to multiple plans per formation cycle. Three of the plots show r_{ij} spacing error, $i, j \in \{1, 2, 3\}, i \neq j$. The solid circles or squares refer to the surfacing of the ith vehicle and the hollow circles or squares refer to the surfacing of the jth vehicle. The bottom right shows the average spacing error, r_{avg}, as a function of time.

terms of the formation's ability to achieve and maintain the desired inter-vehicle spacing of 3 km. In the top left pane, the inter-vehicle distance error between glider 1 and glider 2 is plotted as a function of time. In the top right pane we plot the inter-vehicle distances between glider 1 and glider 3. In the lower left pane inter-vehicle distances are plotted for glider 2 and 3. The error is computed as 3 km $- r_{ij}$ where r_{ij} is the distance between vehicle i and j in km. Lastly, in the bottom right pane we plot the average inter-vehicle distance error which is given by 3 km $- r_{avg}$ where $r_{avg} = (|r_{12}| + |r_{13}| + |r_{23}|)/3$. Comparing the two planning methods using these qualitative plots we see that the inter-vehicle spacing seems

well correlated between both strategies for the first half of the experiment but becomes less correlated during the latter half after the back tracking of glider 3. Comparing the average inter-vehicle distance error we find that the two planning strategies performed similarly with respect to this metric.

A serious issue when generating multiple plans per formation cycle arises when the gliders surface so soon after each other that there is not enough time to have waypoint plans immediately available. The simulation presented here is structured so that the asynchronous surfacings are mostly uniform at 40 minute intervals. When surfacings occur at small intervals plans may not be ready on time, in which case the waypoint plans generated from the previous VBAP simulation are utilized. During AOSN II we utilized the *single plan per formation cycle* strategy. We did so because it appeared robust through simulation, it required less frequent VBAP planning (see Figure 5.2.2), and had a simpler implementation when the degree of glider asynchronicty was unknown.

Chapter 6

Sea Trials: AOSN II, Monterey Bay Summer 2003

In this chapter we present an account of sea trials performed with a fleet of autonomous underwater gliders in Monterey Bay during August 2003. These trials were performed as part of the Autonomous Ocean Sampling Network (AOSN) II project [2] and demonstrate our ability to coordinate autonomous underwater vehicles.

During these sea-trials, performed on August 6, 2003 and August 16, 2003, we coordinated a group of Slocum underwater gliders into triangle formations and explored various orientation schemes and inter-vehicle spacing sequences as the formation made its way through the bay. In both cases, we used our VBAP methodology modified for implementation on Slocum underwater gliders as described in Chapter 5. We remark that during AOSN II all virtual body parameters such as heading direction and formation size were pre-planned and not directed by vehicle sensor measurements. Due to logistical constraints, these trials focused strictly on demonstrating coordination. However, we do present gradient estimates that were computed offline that in principle could have been used to direct

the motion of the fleet.

6.1 Brief Review of Operations during AOSN II

In this section we briefly review the operational scenario described in detail in Chapter 5.

AOSN II was devised to build a coupled observation/prediction system where ocean models would assimilate observations made by AUVs. In August 2003 the first experimental component of AOSN II was performed in Monterey Bay, CA with the deployment of 12 Webb Slocum autonomous underwater gliders and 5 Spray underwater gliders designed and operated by the Scripps Institution of Oceanography.

During AOSN II fixed glider trajectories were chosen to provide sufficient sampling (or coverage) of the pertinent model domains[1] . The Slocum gliders were tasked with sampling inside and near Monterey Bay while the Spray gliders were tasked with sampling outside the bay and across model boundaries, see Figure 6.1.1. For the majority of the experiment the Slocum gliders were placed on closed loops or *race tracks.* These are clearly visible in the left pane of Figure 6.1.1. However, on two occasions we were given the opportunity to take control of a three glider subfleet to perform demonstrations of coordinated glider operations. The Spray gliders remained on fixed, cross-shore trajectories throughout the experiment.

Two coordinated control demonstrations with the three Slocum glider subfleets were performed, on August 6 and August 16 of 2003. The former involved directing the vehicle group towards a fixed destination. For the first half of the experiment the group was permitted to rotate freely about a single virtual leader which served as the virtual body.

[1]Alternatively, in the Adaptive Sampling and Prediction (ASAP) program the process will become more adaptable by recomputing vehicle trajectories that optimize sampling performance over large regions (20 km $\times$40 km) although not quite as large as the model domains used during AOSN II [52].

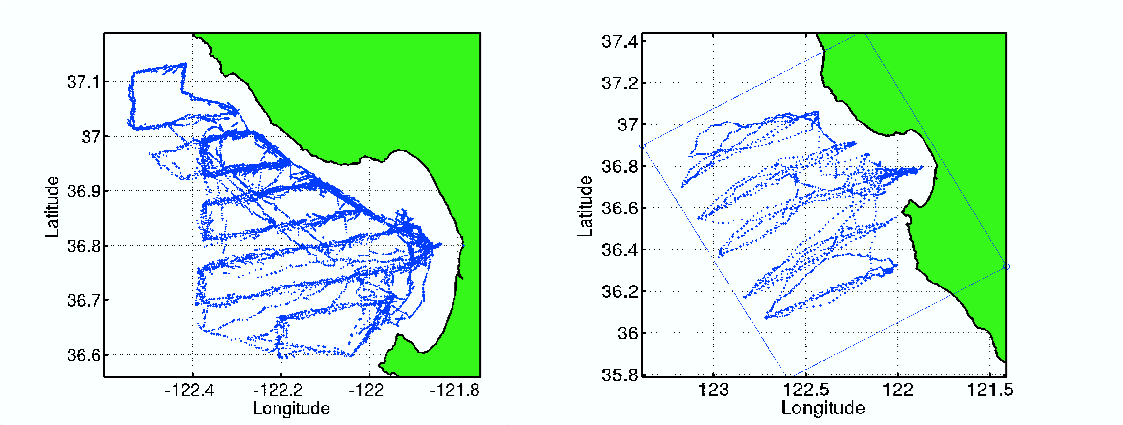

Figure 6.1.1: **Autonomous Glider Tracks in Monterey Bay During AOSN II.** The left pane shows Slocum glider tracks whereas as the right pane shows Spray glider tracks. Each point locates a glider at the center of its dive. [52]

During the latter half, we activated orientation control which acted to orient the triangle formation about the virtual leader at a desired angle. During the August 16 experiment we directed the vehicle group to follow a piecewise linear path consisting of multiple straight line segments. We also demonstrated group contraction as the formation was made to reduce its size by half. Throughout the entire course of this experiment we implemented orientation control about the single virtual leader (which again served as the virtual body).

During both sea trials new mission plans consisting of waypoint lists were uploaded every two hours when the gliders surfaced. A glider mission consisted of each glider tracking its waypoint list while diving to a maximum depth of 100 meters. After two hours the glider surfaced and established contact with the Glider Data System (GDS) at Woods Hole Oceanographic Institution (described in Section 5.1). Sensor data, the glider's GPS position, and the average estimated currents during the last mission were transmitted to the GDS and the next mission (having been pre-computed) was downloaded onto the glider. Mission generation was computed in the "war room" located at the Monterey Bay Aquarium and Research Institute (MBARI) in Moss Landing, CA. Data from the GDS was retrieved via

the internet using a portable windows-based laptop and Mathworks Matlab was utilized to implement the VBAP methodology for underwater gliders, as discussed in Chapter 5. When planning each mission the virtual leader was initialized at the predicted center of mass of the three glider formation at the lead glider's next surfacing (see Section 5.2). After VBAP generated continuous paths for each glider, we implemented the waypoint selection routine described in Section 5.2.1. Mission plans (waypoint lists) were generated after all vehicles had surfaced and uploaded to GDS to be ready for download onto the corresponding glider at its next surfacing.

6.2 Discussion of Metrics

To quantify performance we compute and present graphically the following metrics:

- **Virtual Leader Tracking Error.**

  Let Λ denote the set of all points which comprise the desired virtual body path, i.e. the straight line or piecewise linear path, and $\boldsymbol{r}(t)$ denote the VBAP planned (continuous) trajectory for the body center. $\boldsymbol{r}(t)$ is the result of controlling the virtual body given the vehicle initial conditions, external currents, and desired virtual body path. Then we define the virtual leader tracking error, $\epsilon_v(t)$, as

  $$\epsilon_v(t) = \min_{\boldsymbol{\lambda} \in \Lambda} \|\boldsymbol{r}(t) - \boldsymbol{\lambda}\|. \tag{6.2.1}$$

  which is a measure (as a function of time) of how far the virtual leader strays from the desired path.

- **Formation Center of Mass Tracking Error.**

  Since the virtual body consisted of only one virtual leader, its trajectory, $\boldsymbol{r}(t)$, was *the trajectory of the desired center of mass (centroid) of the formation.* Each mission

defined a two-hour segment of the demonstration and the start of each mission was defined by the time at which the lead glider dives after having surfaced. Thus, for a demonstration lasting $2K$ hours, VBAP generated K missions.

The glider dead reckoning and current estimate histories were post-processed to estimate each glider's trajectory during the course of each demonstration. Denote the i^{th} glider's position at time t in the horizontal plane as $\boldsymbol{g}_i(t)$. (Note: $\boldsymbol{g}_i(t)$ is distinguished from $\boldsymbol{x}_i(t)$ which refers to the position of the i^{th} glider at time t as planned by VBAP). The instantaneous formation center of mass is defined as

$$\bar{\boldsymbol{g}}(t) = \frac{1}{N}\sum_{i=1}^{N} \boldsymbol{g}_i(t)$$

where N is the number of vehicles in the formation. The *formation centroid error* at time t is defined as

$$\epsilon(t) = \|\bar{\boldsymbol{g}}(t) - \boldsymbol{r}(t)\|$$

i.e. it is the magnitude of the error between the formation centroid and the virtual leader position generated by VBAP at time t. We note that this error defines a rather conservative performance metric because it requires, for good performance, that the formation tracks the virtual body both in space and in time.

In case centroid tracking in space without regard to time is of central importance, then a more suitable (and less conservative) metric can be defined by

$$\varepsilon'(t) = \min_{\boldsymbol{\lambda}\in\Gamma} \|\bar{\boldsymbol{g}}(t) - \boldsymbol{\lambda}\|$$

where $\Gamma = \{\boldsymbol{r}(t) \mid \forall\, t\}$ is the set of all points along the path of the virtual leader.

- **Inter-vehicle Distance Error.**

The inter-vehicle distance between gliders is given by

$$\boldsymbol{d}_{ij}(t) = \|\boldsymbol{g}_i(t) - \boldsymbol{g}_j(t)\|$$

where $i, j = 1, \ldots, N, i \neq j$.

- **Formation Orientation Error.**

  During portions of the Monterey Bay sea trials, we let the orientation of the formation about the virtual leader remain unconstrained. In principle, this means that the formation can take any orientation around the virtual leader as it moves with the virtual leader. In the case of significant currents and limited control authority, this approach allows us to dedicate all the control authority to maintaining the desired shape and size of the formation. Sometimes, however, it is of interest to devote some control authority to control over the orientation. For instance, to maximize trackline separation for improved sampling, we ran portions of the sea trials with one edge of the formation triangle perpendicular to the path directed from the initial virtual leader location to the desired destination. In order to effect this, we defined the desired orientation of the formation by constraining the direction of the relative position vectors ($\boldsymbol{x}_i - \boldsymbol{r}$) (the vector from virtual leader to i^{th} vehicle). Potential functions V_r as described in Section 2.3 were used to impose this constraint. The orientation error for a given glider is defined as the absolute value of the difference between the desired angle of the ideal glider position relative to the virtual leader position (θ_{ik} in Figure 2.3.1) and the measured angle of the measured glider position relative to the measured formation centroid.

All results pertaining to these metrics are subject to additional error in the estimate of each glider's trajectory from the dead reckoning and estimates of the current histories. All

quantitative discussion of errors herein are relative to the estimated glider trajectories only.

6.3 August 6, 2003: Glider Formation at Upwelling Event

On August 6, 2003 three Slocum gliders were coordinated into a triangle formation and directed towards the northwest part of Monterey Bay in response to the anticipated onset of an upwelling event (see Figure 6.3.1). The WHOI gliders, numbered WE07, WE12, and WE13, were initially holding station at the mouth of the bay and the overall objective was to transit the gliders to the northwest in an equilateral triangle formation with an inter-vehicle spacing of 3 km. The entire demonstration spanned sixteen hours, i.e. eight two-hour missions. Each glider surfaced every two hours for a GPS fix and an updated mission plan. During the first four missions the triangle formation was free to rotate about the virtual leader. The virtual leader (body) was directed towards a single, fixed waypoint as indicated by the solid diamond in Figure 6.3.1. The procedure for addressing external currents as discussed in Section 5.2.2 was implemented. During the last four missions, the orientation of the group about the virtual leader was controlled so that an edge of the triangle formation would be perpendicular to the line connecting the initial virtual leader location at the start of each mission and the virtual leader destination waypoint.

In the left pane of Figure 6.3.2 we present the glider trajectories and instantaneous glider formations. Starting from their initial distribution, the gliders expanded to the desired configuration while the formation centroid tracked the desired reference trajectory, i.e. the virtual leader. As shown, the group did maintain formation while transiting. At 02:36 UTC orientation control was activated and by 06:55 the group had noticeably reoriented itself. As a result of generating waypoint plans that respect a glider with constant speed, some degree of backtracking is seen to occur during the initial creation of the desired formation

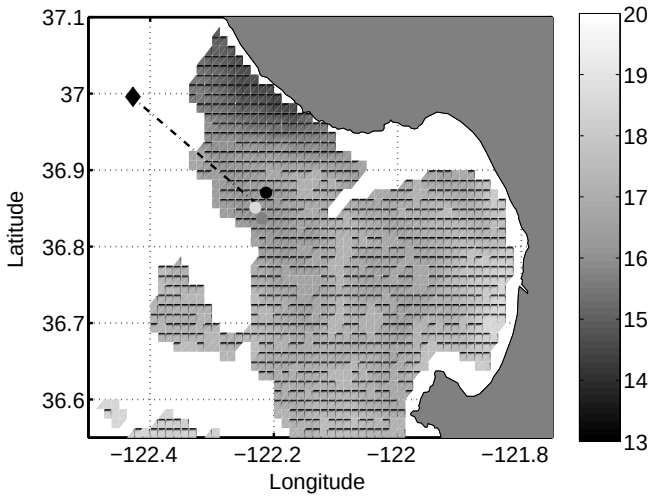

Figure 6.3.1: **Satellite Sea Surface Temperature (degrees Celsius) in Monterey Bay for August 6, 2003 19:02 UTC.** Cold water region near the northwest entrance of the bay indicates possible onset of upwelling event. The three solid dots indicate the starting locations of the Slocum gliders at approximately 18:00 UTC. The solid diamond is the desired destination of the glider group. AVHRR HRPT data provided courtesy of NOAA NWS Monterey Office and NOAA NESDIS CoastWatch program.

and during the missions when orientation control was active. In the right pane of Figure 6.3.2 we present the trajectory of the virtual leader for all eight missions. Alternating black and gray color is used to differentiate between subsequent missions. Note that no control was utilized to direct the virtual leader to stay close to the line from the initial virtual leader location at the start of mission 1 to the destination (dash-dot line in Figure 6.3.2). The virtual leader is only trying to steer directly towards the destination. However, it is clear from Figure 6.3.2 that the virtual leader in general did not stray far from this line as it progressed towards the desired destination.

In Figure 6.3.3 we present the glider trajectories and the corresponding VBAP planned trajectories for each mission. As shown, the demonstration got off to a rocky start with each vehicle surfacing early during the first mission. At this surfacing the gliders did not receive updated plans and continued with the first mission surfacing again at approximately 2 hours from the start of the mission. The time spent on the surface (approximately 17

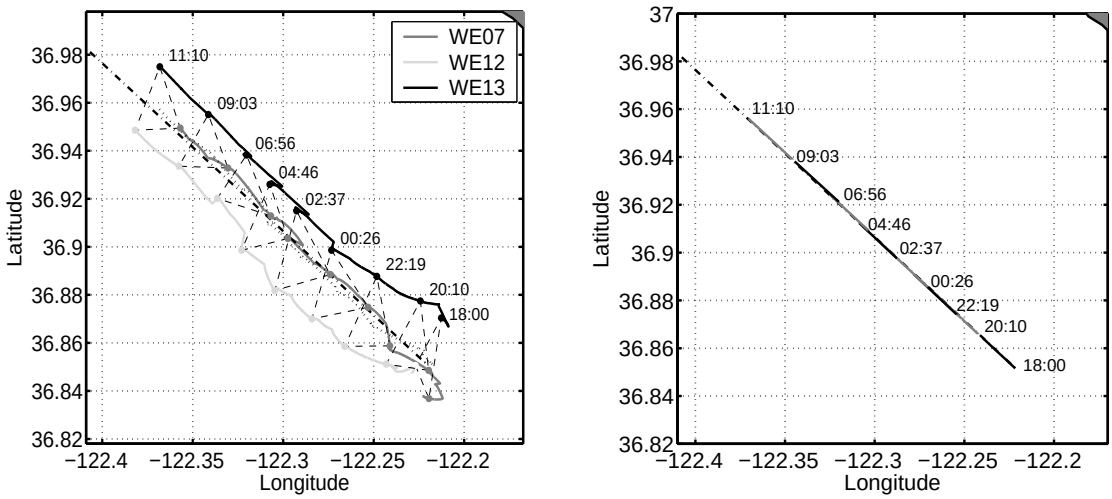

Figure 6.3.2: **Glider Trajectories, Formation Snapshots, and Virtual Body Trajectory for August 6 Demonstration.** Left pane: solid lines are glider trajectories. Black dashed lines illustrate instantaneous formations at 2-hour intervals. Dotted line is formation centroid. Black dash-dot line is virtual leader's trajectory (desired trajectory of formation centroid). Right pane: Virtual leader trajectory is plotted in alternating black and gray. Time is UTC from midnight August 5, 2003.

minutes) and not travelling resulted in poor planning and execution of the second mission. However, this bug did not materialize in any subsequent mission and as indicated in Figure 6.3.3 planning performance improved thereafter.

We now look at our coordination metrics. In Figure 6.3.4 we plot the virtual leader tracking error for each mission as defined in (6.2.1). Throughout the course of the demonstration the virtual leader tracking error did not exceed 60 meters. The integrated time average of the virtual leader tracking error over all eight missions is 22.0 meters with a standard deviation of 12.5 meters. The increasing error during the first mission was due to the virtual leader slowing in response to large initial formation error while being advected in an averaged external current whose speed exceeded that of the virtual leader.

The formation centroid error ϵ is plotted over all eight missions as a function of time t in Figure 6.3.5. The mean value of ϵ averaged over all eight missions is 623 meters with a standard deviation of 500 meters. The average error over the last four missions is 255

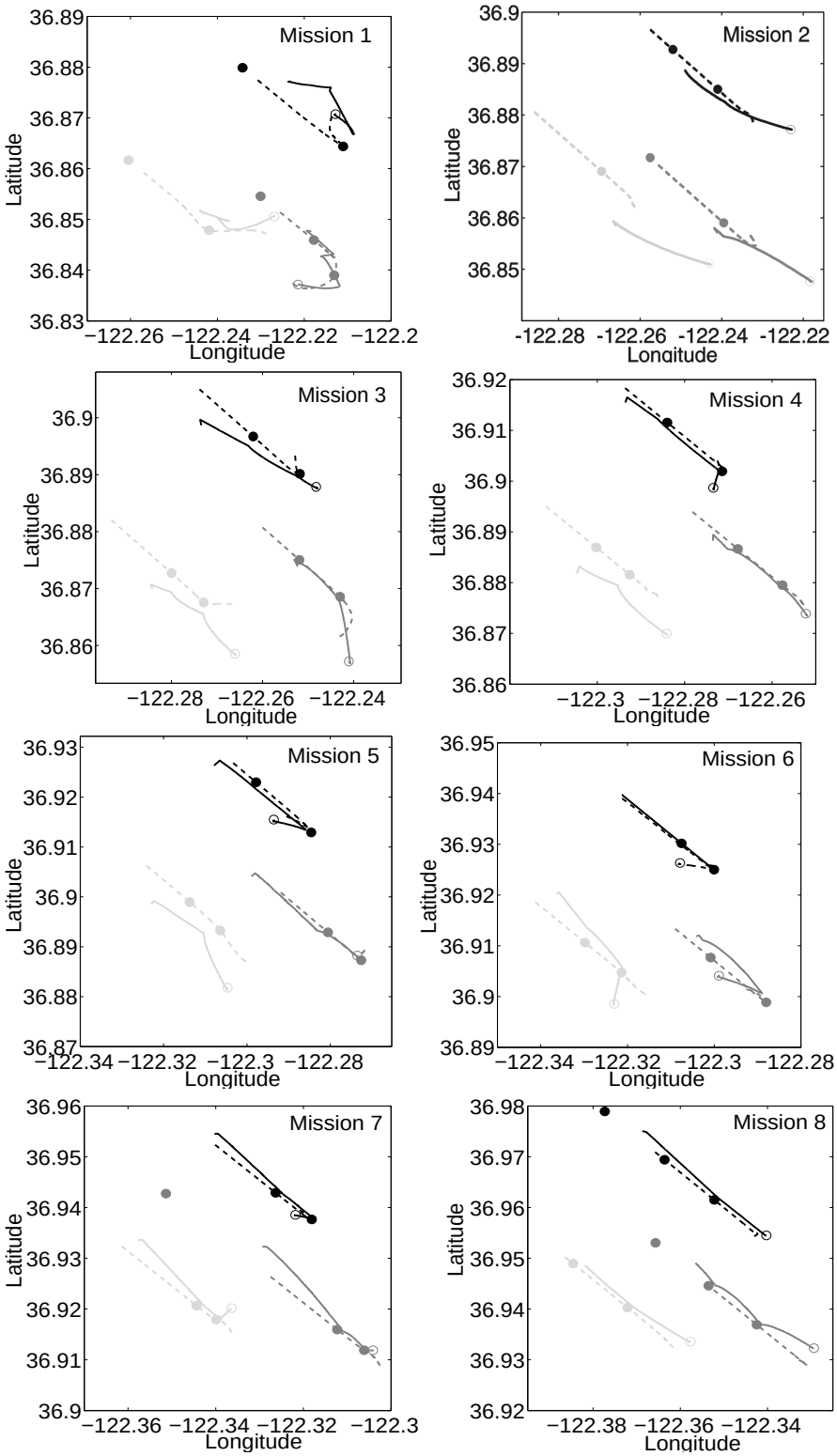

Figure 6.3.3: **VBAP and Glider Trajectories for August 6 Demonstration.** Solid lines are glider trajectories, dashed lines are VBAP plans. Dark gray, light gray, and black identify gliders WE07, WE12, and WE13, respectively. Solid dots indicate waypoints. Outlined circles indicate glider surfacing location at the beginning of the mission.

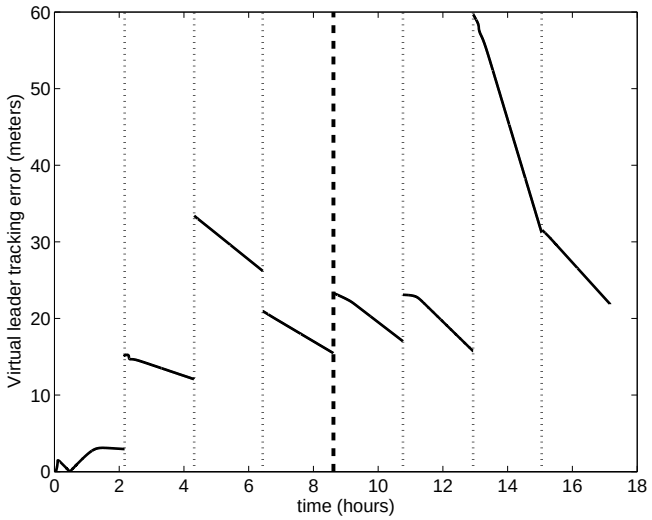

Figure 6.3.4: **Virtual Leader Tracking Error for August 6 Demonstration.** Dotted vertical lines indicate the beginning of each mission. Heavier dashed vertical line indicates when orientation control was activated (time = 8.6 hours).

meters with a standard deviation of 67 meters. The discontinuity at each mission replan is a result of re-initializing the virtual leader at the expected centroid of the group. The error across the discontinuity gives insight into how well we predicted the initial location of the group centroid at the start of each mission. During mission 2 we performed worse at predicting initial centroid location and maintaining the distance between the actual and desired centroid location. It is likely that the fact that each glider surfaced twice during the previous mission contributed to this error. Furthermore, this error also corresponds to the largest error between the estimates of current fed-forward into the glider simulator and VBAP (see Figure 5.3.1), and the estimated current measured by the gliders at the end of that mission.

We performed best with respect to this metric during the last four missions. It is possible that the difference in performance is related to our observations that during the latter part of the demonstration each glider travelled fastest relative to ground due to more favorable currents in the glider's direction of travel.

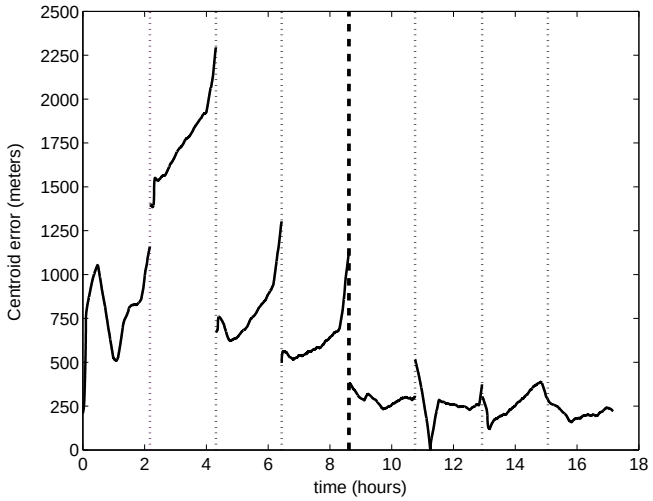

Figure 6.3.5: **Formation Centroid Error ϵ vs. Time for August 6 Demonstration.** Black dotted vertical lines indicate the beginning of each mission. Heavier black dashed vertical line indicates when orientation control was activated (time = 8.6 hours).

Figure 6.3.6 portrays the magnitude of the error in inter-vehicle distance $d_{ij}(t)$ versus time for the three glider pairings WE07-WE12, WE07-WE13, and WE12-WE13. The mean error of all three pairings is 423 meters, roughly 14% of the desired spacing of 3km, with a standard deviation of 159 meters. The mean inter-vehicle spacing error was largest during missions 2 and 5.

Formation orientation error versus time is portrayed in Figure 6.3.7. The desired orientation was chosen to have an edge of the formation perpendicular to the line from the initial virtual leader location at the start of each mission to the final destination, with two vehicles in the front, side-by-side, and one vehicle trailing. The control is designed so that any of the vehicles can play any of the roles, i.e. we do not assign a particular vehicle to a particular place in the oriented triangle. As shown in Figure 6.3.2, WE07 was the trailing glider and WE12 and WE13 the leading gliders in the triangle formation.

For comparison purposes, we plot the error during the first four missions, when the orientation of the group was not controlled, and during the last four missions when the

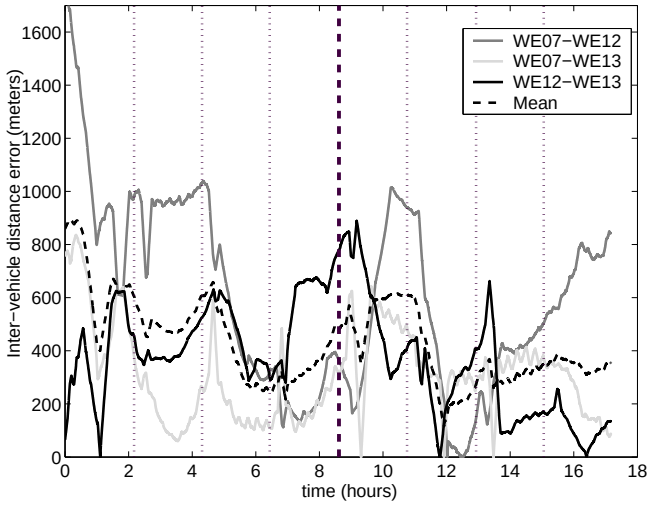

Figure 6.3.6: **Magnitude of Inter-Glider Distance Error vs. Time for August 6 Demonstration.** Black dotted vertical lines indicate the beginning of each mission. Heavier black dashed vertical line indicates when orientation control was activated (time = 8.6 hours).

orientation was controlled. During missions 3 and 4, the mean orientation error was 18.2 degrees with a standard deviation of 7.8 degrees. We do not concern ourselves with the first two missions since the orientation is in a state of flux while the formation is expanding or contracting to achieve the desired inter-vehicle and vehicle-to-virtual-leader spacings. During missions 5-8 the mean orientation error was reduced to 8.1 degrees with a standard deviation of 8.1 degrees.

To examine the ability of the formation to serve as a sensor array and detect regions of minimum (or maximum) temperature, we computed least-square gradient estimates of temperature given each glider's temperature measurements. The negative of these least squares gradient estimates, $-\nabla T_{\text{est}}$ (to point to cold regions), are shown as vectors in Figure 6.3.8. These gradients are computed using data measured along the 10 m isobath for comparison with the available AVHRR SST data (satellite sea surface temperature data). All glider temperature measurements and their respective locations which fall within a 0.5 m bin around the 10 m isobath are extracted from the post-processed glider data. Values

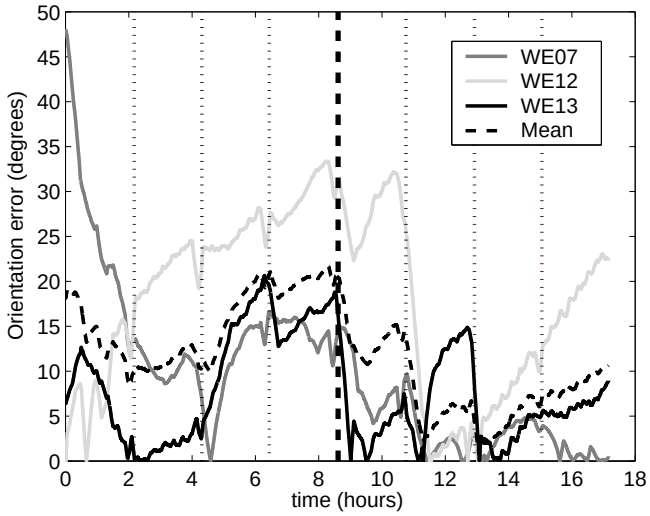

Figure 6.3.7: **Magnitude of Orientation Error vs Time for August 6 Demonstration.** Black dotted vertical lines indicate the beginning of each mission. Heavier black dashed vertical line indicates when orientation control was activated (time = 8.6 hours).

within each bin are then averaged. Since the gliders travel asynchronously through depth we interpolated the data as a function of time. For simplicity, we chose to compute the gradients at the times associated with the lead (WE12) glider's binned measurements. Comparison with Figure 6.3.1 illustrates that the formation points correctly to the cold water near the coast at the northwest entrance of the bay.

6.4 August 16, 2003: Multi-Asset Demonstration

On August 16, 2003 a formation of three Slocum gliders was directed to travel in a region simultaneously sampled by a ship dragging a towfish sensor array and the MBARI propeller-driven AUV Dorado. The towfish and Dorado measurements provide an independent data set by which to corroborate the glider formation's sampling abilities [32].

The mobile observation platforms should be used so that their capabilities are compatible with the spatial and temporal scales of interest. The towfish, Dorado and gliders can be used to resolve different length and time scales. For example, the towfish is much faster

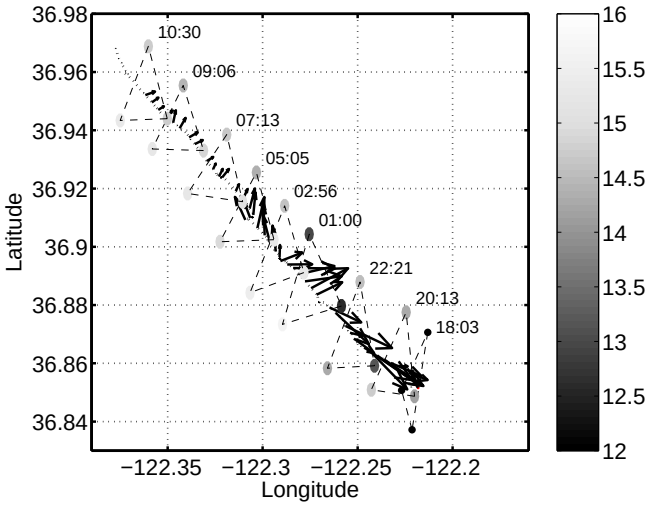

Figure 6.3.8: **Glider Formation and Negative of the Least-Square Gradient Estimates for August 6 Demonstration.** Estimates are computed at the instantaneous formation centroid. Each glider is colored to indicate its temperature measurement in degrees Celsius.

than the Dorado and the gliders, whereas the Dorado is up to three times faster than the gliders. Some analysis of sampling capabilities based on a metric computed from estimation error of the sampled process of interest is presented in [32, 52].

Figure 6.4.1 illustrates the towfish and Dorado trajectories, the initial positions of the three gliders and the desired trackline of the glider formation centroid. The WHOI gliders WE05, WE09, and WE10, were initially holding station near the center of the bay, and the overall objective was to criss-cross a region to the southeast while in an equilateral triangle formation. The entire trial spanned seven two-hour missions. The desired inter-vehicle distance was set to 6 km for the first three missions and reduced to 3 km thereafter. The orientation of the desired triangle formation was controlled in the same manner as the August 6 demonstration except the control was active during the entire experiment. The virtual leader followed the piece-wise linear path shown as the black dash-dot line in Figure 6.4.1. The endpoints of each line segment comprising the path were the waypoints the virtual body was to track. In addition, to keep the virtual body near the path we

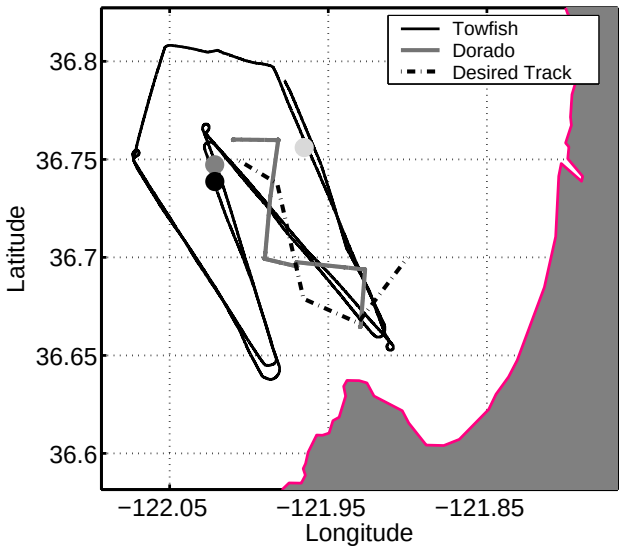

Figure 6.4.1: **August 16 Demonstration.** Black line is Towfish trajectory. Gray line is Dorado trajectory. Shaded dots denote initial locations of gliders WE05, WE09, and WE10, respectively. Black dash-dot line is desired formation centroid trackline. The towfish begins at 15:07 UTC and finishes two transects of the "W" pattern by 03:20 August 17 UTC. The Dorado vehicle begins its single transect at 14:19 August 16 UTC and finishes at 17:58 UTC. The gliders start at 14:11 August 16 UTC and finish at 06:17 August 17 UTC. Special thanks goes to Steve Haddock and John Ryan from MBARI for cooperating with us on this sea-trial.

chose the desired virtual body steering direction as a weighted sum of a vector directing the formation towards the virtual body waypoint and a vector normal to the desired the path. This steering direction was then adjusted to account for the effects of the local advecting current as described in Section 5.2.2. The methodology for deriving the desired virtual body steering direction to counter this *cross track error* is presented in Appendix D.

Figures 6.4.2 and 6.4.3 present the instantaneous glider formations and glider trajectories during the demonstration, respectively. Starting from their initial distribution, the gliders expand to the desired spacing and orientation while the group centroid attempts to track the desired reference trajectory. In Figure 6.4.4 we present the trajectory of the virtual leader for all seven missions. Alternating black and gray color is used to differentiate between subsequent missions. In these figures we see that the group centroid had a difficult time

staying near the reference trajectory in space for the first few missions.

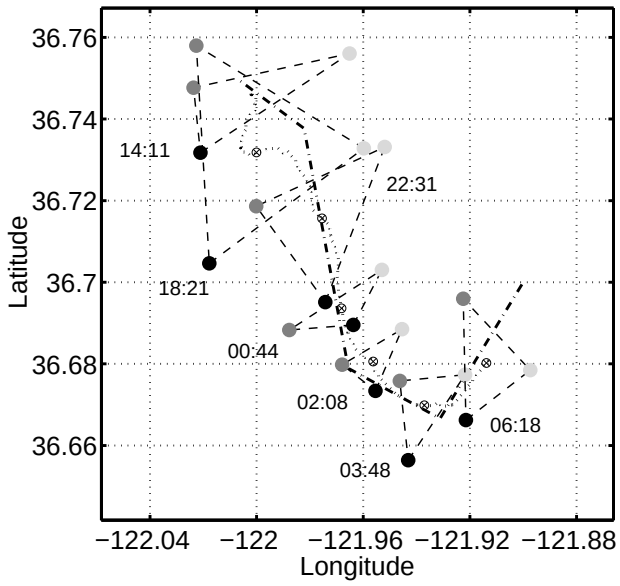

Figure 6.4.2: **Glider formation Snapshots for August 16 Demonstration.** Black dashed lines illustrate instantaneous formations. Dotted line is formation centroid. Dash-dot line is desired virtual leader path, i.e. desired centroid trajectory. Time is UTC from midnight August 15, 2003.

In Figure 6.4.5 we present VBAP planned trajectories and corresponding glider trajectories for each mission.

In Figure 6.4.6 we plot the virtual leader tracking error for each mission as defined in (6.2.1). In general the tracking error was greater throughout the August 16 demonstration than what we observed during the August 6 demonstration. We attribute this to both the increased complexity of the maneuver and the presence of much more aggressive external currents in the local vicinity. For example, the large error during the second mission was caused by a large discrepancy between the currents used in the VBAP mission plan and the currents in the region when the plan was executed. Due to moderate southward currents during mission 1 we observed that glider WE10 (colored dark gray in Figure 6.4.5) makes little progress northward. This strong current was not detected during planning for this mission but was detected when the gliders surfaced to accept the mission. Thus, VBAP

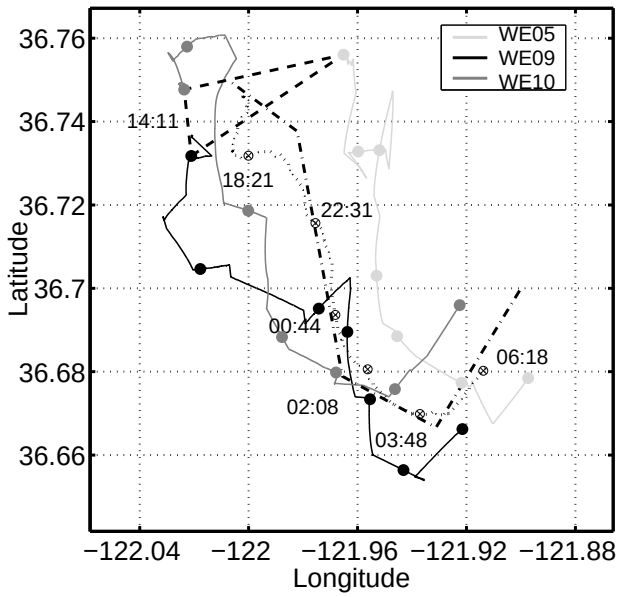

Figure 6.4.3: **Glider Trajectories for August 16 Demonstration.** Solid lines are glider trajectories. Dotted line is formation centroid. Dash-dot line is virtual leader path, i.e. desired centroid trajectory. Time is UTC from midnight August 15, 2003.

correctly provided a plan for the second mission that took into account that the formation would initially be displaced to the south. The large initial error during mission 2 as seen in Figure 6.4.6 is an artifact of the poor plans issued during mission 1. In general the cross track error control did aggressively reduce the cross track error; however, we do observe that the virtual leader tended to overshoot and cross over the desired path while traversing along it. Throughout the course of the entire demonstration the integrated time average of the virtual leader tracking error over all seven missions is 158.7 meters with a standard deviation of 340.1 meters. The average error and standard deviation with the second mission removed is 42.0 meters and 39.8 meters, respectively.

The formation centroid error ϵ is plotted in Figure 6.4.7 as a function of time t. The mean value of ϵ averaged over all 7 missions is 732 meters with a standard deviation of 426 meters. The worst performance was observed to occur during mission 5. As on August 6, this error corresponds to the largest error between the current estimates fed forward

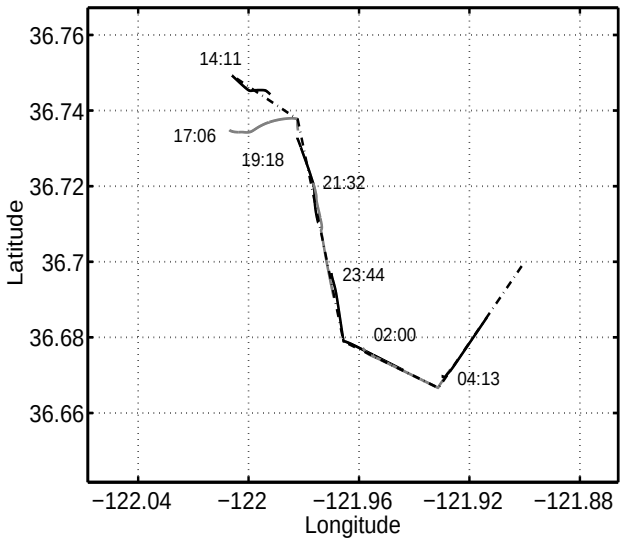

Figure 6.4.4: **Virtual Leader Trajectories for August 16 Demonstration.** Dash-dot line is desired virtual leader path, i.e. desired centroid trajectory. Solid lines are planned virtual leader trajectories colored alternating black and gray. Time is UTC from midnight August 15, 2003.

into the glider simulator and VBAP, and those estimated by the gliders at the end of that mission. In general, the methodology did not perform as well with respect to this metric as it did on August 6. One difference of note is the significantly stronger currents experienced on August 16, exceeding 30 cm/s on more than one occasion (c.f. the average glider speed relative to the surrounding water is 40 cm/s).

Figure 6.4.8 presents the less conservative formation centroid error ε' for this demonstration as a function of time t. When utilizing the formation centroid metric that the methodology performs quite well for the latter part of the experiment which is consistent with what is observed in Figures 6.4.2 and 6.4.3. In particular, the mean error overall is 471 meters with a standard deviation of 460 meters. For missions 4 through 7 the mean error is 210 meters with a standard deviation of 118 meters.

The magnitude of the inter-vehicle distance error versus time for the three glider pairings WE05-WE09, WE05-WE10, and WE09-WE10, are presented in Figure 6.4.9. For missions 2 and 3, the mean error over all three pairings was 394 meters, roughly 7% of the desired

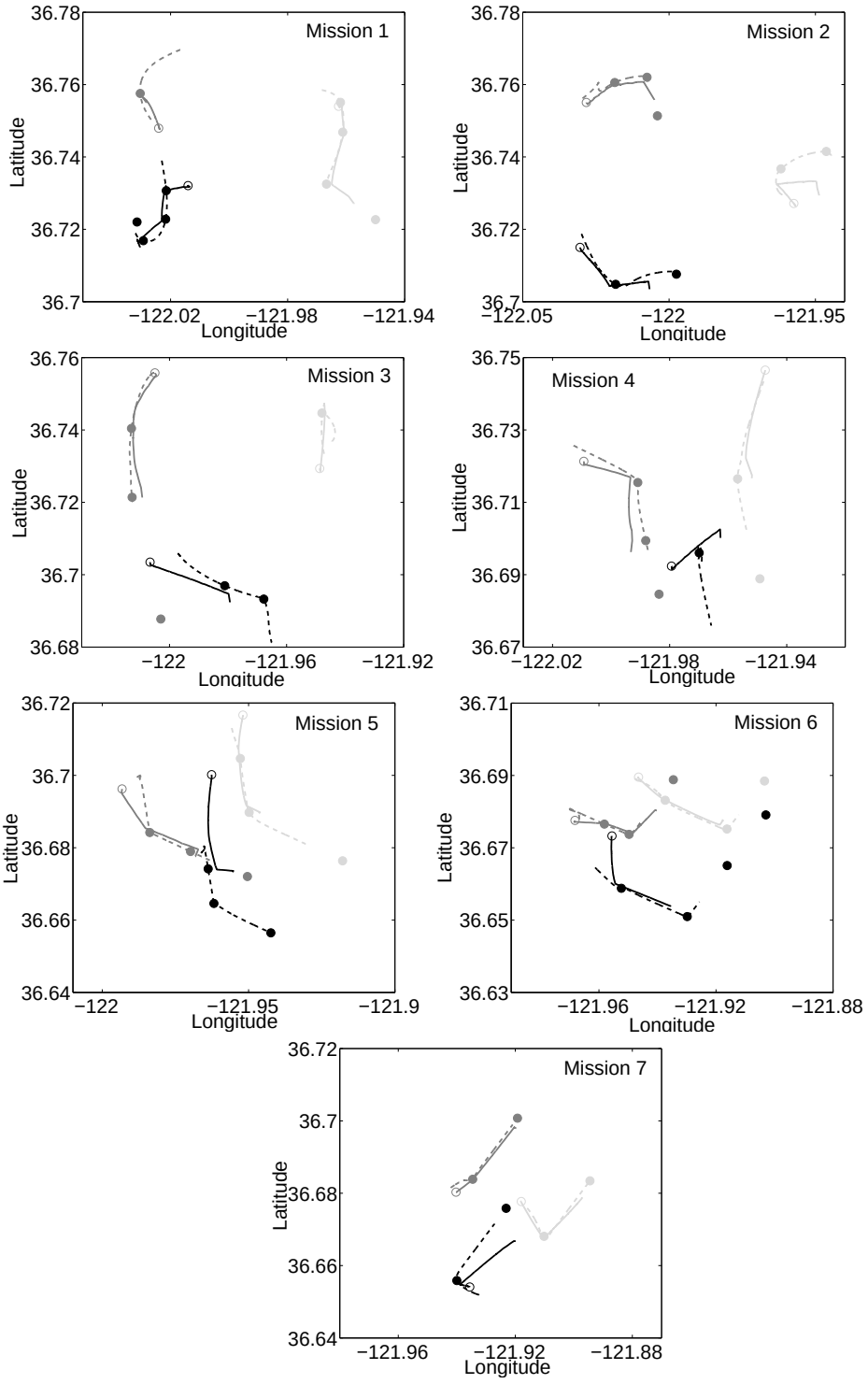

Figure 6.4.5: **VBAP and Glider Trajectories for August 16 Demonstration.** Solid lines are glider trajectories, dashed lines are VBAP plans. Light gray, black, and dark gray identify gliders WE05, WE09, and WE10, respectively. Solid dots indicate waypoints. Outlined circles indicate glider surfacing location at the beginning of the mission.

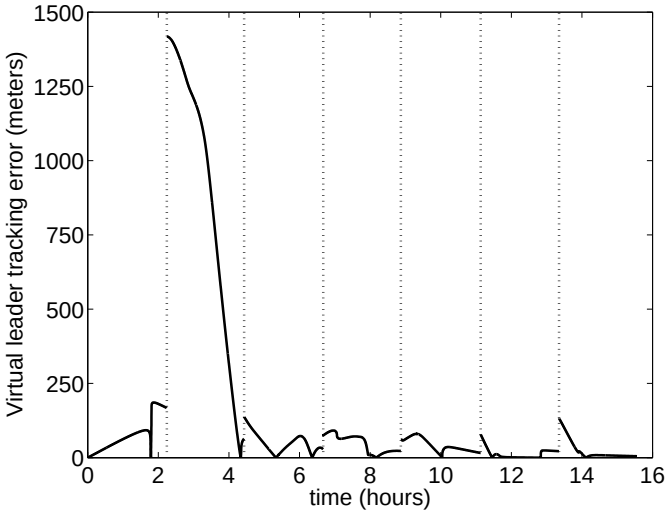

Figure 6.4.6: **Virtual Leader Tracking Error for August 16 Demonstration.** Black dotted vertical lines indicate the beginning of each mission.

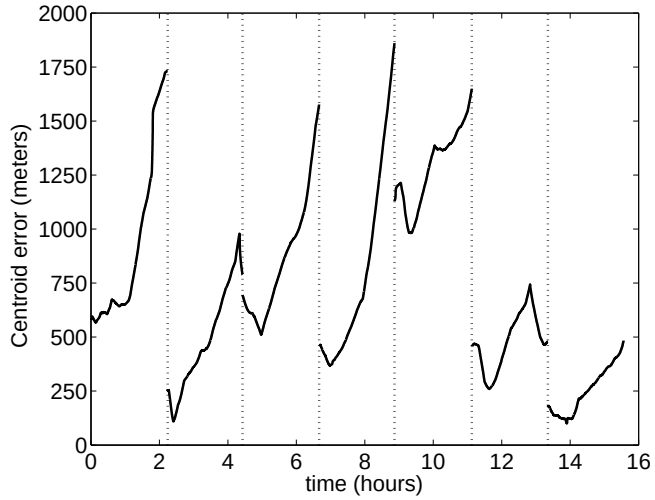

Figure 6.4.7: **Formation Centroid Error ϵ vs. Time for August 16 Demonstration.** Black dotted vertical lines indicate the beginning of each mission.

spacing of 6km, with a standard deviation of 270 meters. For missions 5 through 7, the mean error over all three pairings was 651 meters, roughly 22% of the desired 3 km spacing, with a standard deviation of 312 meters. During this period the average inter-vehicle distance was less than the desired 3 km.

The orientation error is plotted in Figure 6.4.10. The discontinuities reflect changes in the desired orientation of the reference formation which were allowed to occur only at the

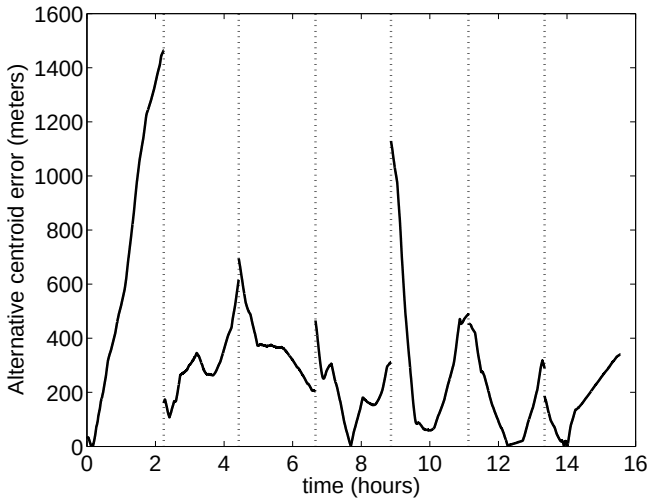

Figure 6.4.8: **Alternate Formation Centroid Error ε' vs. Time for August 16 Demonstration.** Black dotted vertical lines indicate the beginning of each mission.

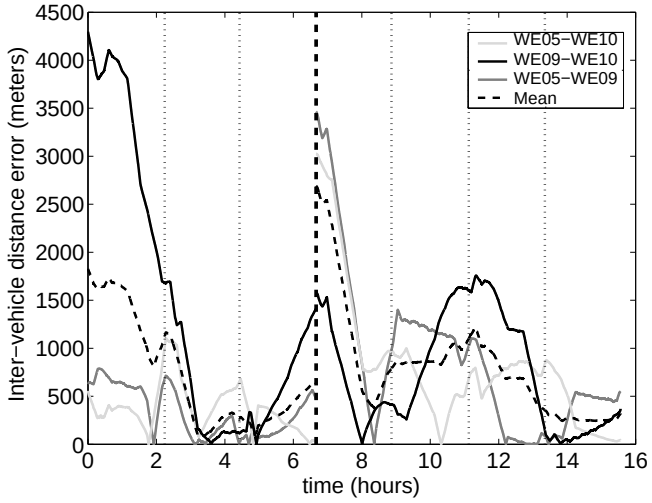

Figure 6.4.9: **Magnitude of Inter-Glider Distance Error vs. Time for August 16 Demonstration.** Dotted vertical lines indicate the beginning of each mission. Heavier dashed vertical line indicates when desired inter-vehicle spacing was decreased from 6km to 3km (time = 6.7 hours).

beginning of a mission. The mean orientation error for mission 2 was 31 degrees with a standard deviation of 3 degrees. This corresponds to the period when the formation centroid was having difficulty staying on the desired trackline. At mission 3 the first significant change in desired reference formation orientation occurred. The mean orientation error during missions 3 through 5 was 18 degrees with a standard deviation of 11 degrees. The

large standard deviation reflects the relatively lower orientation error during missions 3 and 4 as compared with mission 5. The next significant desired reference formation orientation change occurred at mission 6 and the final change occurred at mission 7. For mission 6 the mean orientation error was 13 degrees with a standard deviation of 2 degrees. For mission 7 the mean orientation error was 9 degrees with standard deviation of 7 degrees. Both the mean inter-vehicle distance error and the mean orientation error exhibit similar trends during missions 5 and 6. Recall that the formation centroid error was also largest during mission 5 which corresponds to the largest variation between fed-forward currents and those actually experienced.

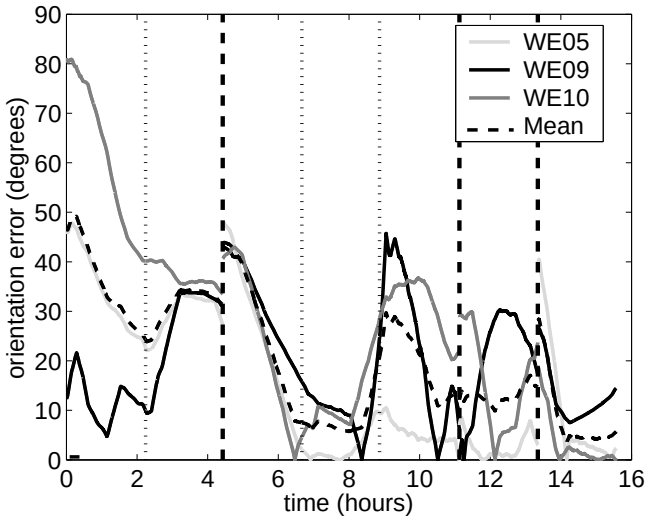

Figure 6.4.10: **Magnitude of Orientation Error vs Time for August 16 Demonstration.** Dotted vertical lines indicate the beginning of each mission. Heavier dashed vertical line indicates when desired orientation changed to reflect change in virtual body direction (time = 4.4, 11.2, and 13.4 hours).

In conclusion we have illustrated that our methods were successful in coordinating sub-fleets of gliders. The results show that groups of AUVs, namely gliders, can be controlled as formations which move around as required, maintaining prescribed formation orientation and inter-vehicle spacing with decent accuracy despite periods of strong currents and numerous operational constraints.

Chapter 7

Summary and Future Work

The principle theme of this work was the development and application of a coordinated control framework for multiple autonomous vehicles to perform adaptive sampling, both in theory for simple point mass models and in practice, as was demonstrated with a group of autonomous underwater vehicles at sea. Coordinating vehicle groups, an interesting problem in its own right, was not the sole aim, but rather we also sought to illustrate how these vehicle groups could be used to perform adaptive sampling. In this thesis, we have provided some tools that use the individual measurements of each vehicle in a formation to dictate the actions for the whole to achieve the sampling objective of autonomous gradient climbing and front tracking.

7.1 Summary

In Chapter 2 we presented the framework for the Virtual Body and Artificial Potential (VBAP) multi-vehicle control methodology. Formations were constructed using artificial potentials, the gradient of which serve in each vehicle's control laws. The design principles for VBAP include the introduction of virtual leaders and virtual bodies along with artificial

potentials which define their interactions with the vehicles. A major theme of Chapter 2 was the utilization of virtual leaders and the virtual body for symmetry breaking. Additionally, interactions between vehicles were introduced to regulate inter-vehicle distance to further the possibilities of formation design and prevent vehicle-to-vehicle collisions. An advantage of utilizing artificial potentials in control design is a readily available Lyapunov function for proving local stability of a desired formation configuration.

At the end of Chapter 2 we provided a control law to stabilize a formation to a virtual body that is strictly translating. In Chapter 3 we introduced a methodology[1] that eases the restrictions on virtual body maneuvers and permits any combination of translation, rotation, expansions/contractions, and formation deformation. Each maneuver was defined as a trajectory in the virtual body configuration space. Parametrization of these trajectories by the time-like variable s provided a mechanism to introduce dynamics to the virtual body. As illustrated, a key feature of designing formation maneuvers in this fashion is the inherent decoupling of the formation stabilization and the formation maneuver/mission control subproblems. By appropriate choice of vehicle control law (2.1.2) and control law for $\dot{s}$ (3.2.1), it was shown that formation error remains bounded regardless of virtual body maneuver direction.

To summarize, the VBAP methodology has the following desirable features:

- No specific ordering or numbering of the vehicles is required.
- Vehicular control laws which rely only on local interactions are possible.
- Controller design for formation shape regulation is decoupled from the design of the controller that regulates formation maneuvers.

[1]This research was conducted jointly with Petter Ögren [65, 64] who now resides at the Swedish Defense Research Agency (FOI)

- Stability of the formation is automatic from the construction.

With a framework for coordinating vehicles into dynamic sensor arrays in place, in Chapter 4 we investigated how to use these arrays to achieve the scientific objective of adaptive ocean sampling in the context of gradient climbing and front tracking in the presence of both correlated and uncorrelated noise. A central ingredient to perform these tasks are gradients (first-order and higher) and we put to task various techniques for their estimation including finite differencing, least squares error minimization, averaging, and Kalman filtering.

In Chapter 5 we transitioned the theoretical developments in Chapters 2 and 3 to a *real-world* implementation on Slocum underwater gliders in Monterey Bay. The transition was complicated by the fact that our solution had to be a direct plug-in fit to a pre-existing glider command structure (see Section 5.3). Inherited constraints included speed constraints, glider commands that were limited to waypoint tracking, and glider communication only available at the surface and at two hour intervals. Furthermore, we had to cope with external currents. To test our methodology prior to sea trials, we performed a series of simulations in realistic settings implementing communication constraints, computational limitations, and constrained vehicle kinematics and dynamics.

Chapter 6 presented the coordination demonstrations performed during the AOSN II experiment at Monterey Bay in August 2003. We described two sea-trials, performed on August 6, 2003 and August 16, 2003, which demonstrated our ability to coordinate a group of three Slocum underwater gliders into triangle formations. The metrics we evaluated relate to virtual body trajectory tracking error, inter-vehicle spacing error, orientation error, and group center of mass tracking error. With limited reports of coordinated autonomous underwater vehicles in the field, the Monterey Bay demonstrations are especially meaningful.

7.2 Future Work

- **Centralization and VBAP.**

  The VBAP control methodology and its implementation during AOSN II is centralized. That is, during AOSN II, the evaluation of the control law for both vehicles and virtual body is performed at a single computational node. In general, centralization requires a high degree of communication as each vehicle's state information must be broadcast to a single location for evaluation of the control law. At each time step, each vehicle's absolute position (and velocity for vehicles with second-order dynamics) is used in the evaluation of the vehicle control law (2.1.2) and the virtual body dynamics (3.2.1). This centralized implementation was well suited for AOSN II as vehicles could not measure the state of other vehicles nor communicate with each other, neither underwater nor on the surface. However, underwater modems are currently under testing and are expected to be available in the near future. Furthermore, should one wish to implement VBAP on ground or aerial vehicles, vehicle-to-vehicle communications would then likely be available. In these cases, where inter-vehicle communication is possible, a distributed implementation of VBAP may be feasible.

- **Adaptive sampling strategies for time dependent, non-homogeneous fields.**

  The problem domain in which we presented our adaptive sampling methodologies in Chapter 4 is one in which the time scales of the phenomena of interest are much longer than the spatial scales the formation traverses during the course of the experiment. This assumption allowed us to consider a temporally static field and focus exclusively on exploiting the spatially distributed measurements acquired by the formation. Further, the assumption of homogeneous and isotropic noise facilitated the

use of least squares estimation and Kalman filtering. However, these assumptions may restrict application of our methods, for example, for phenomena where the time scales are rather short when compared with the spatial scales and when the noise is poorly modelled as homogeneous. Research on this topic is ongoing in preparation for the Adaptive Sampling and Predication (ASAP) [1] project, a followup to AOSN II in which a fleet of underwater gliders will be used to minimize an error metric associated with sampling a 20 km by 40 km region with time scales at roughly 1.5 days. An investigation into an optimal coverage metric in the presence of noise with non-homogenous statistics is discussed in [48].

- **AOSN II operational constraints.**

  In Chapter 5 we discussed operational constraints relating to coordinating fleets of underwater gliders during AOSN II. In this thesis, we have not quantitatively addressed the effects of the intermittent feedback and surfacing asynchronicity during AOSN II. Clearly studying the effects of these constraints could lead to improvements in coordination performance. In preparation for ASAP, research on the effects of intermittent feedback on sampling arrays is already being conducted [50].

- **Adaptation based on sensor measurements in the field.** At AOSN II in 2003 we demonstrated that Slocum gliders could be coordinated and perform various maneuvers at sea. However, technical constraints made it impossible to perform sensor-based feedback for adaptive sampling during the sea-trials. The ASAP project will demonstrate the use of sensory feedback for coordinated and autonomous adaptive sampling in Monterey Bay in the summer of 2006. The trajectories of approximately 9 autonomous underwater gliders will be recomputed to optimize sampling perfor-

mance. “Real life” demonstrations and experiments with coordinated autonomous vehicles performing practical and meaningful tasks, such as those planned for ASAP, are the next logical step for research to progress beyond the theoretical stage towards real-world implementations.

Appendix A

Proof of Theorem 3.2.1 [64]

The proof of Theorem 3.2.1 is presented in two parts: we first show that Φ bounded above by Φ_U and secondly we show that trajectories to converge to $(\boldsymbol{\chi}^*(s_f), s_f)$. This presentation is nearly identical to that found in [64].

Boundedness Given the Lyapunov function $\Phi(\boldsymbol{\chi}, s)$ for every fixed point of s with $\Phi(\boldsymbol{\chi}^*, s) = 0$. We directly have

$$\dot{\Phi} = \left(\frac{\partial \Phi}{\partial \boldsymbol{\chi}}\right)^T \dot{\boldsymbol{\chi}} + \frac{\partial \Phi}{\partial s}\dot{s}(\boldsymbol{\chi}, s)$$

If $\frac{\partial \Phi}{\partial s} \leq 0$ we get $\dot{\Phi} \leq \left(\frac{\partial \Phi}{\partial \boldsymbol{\chi}}\right)^T \dot{\boldsymbol{\chi}} \leq 0$. If, on the other hand, $\frac{\partial \Phi}{\partial s} > 0$, we get

$$\dot{\Phi} \leq \left(\frac{\partial \Phi}{\partial \boldsymbol{\chi}}\right)^T \dot{\boldsymbol{\chi}} + \frac{\partial \Phi}{\partial s}\left(\frac{-\left(\frac{\partial \Phi}{\partial \boldsymbol{\chi}}\right)^T \dot{\boldsymbol{\chi}}}{\delta + |\frac{\partial \Phi}{\partial s}|}\left(\frac{\delta + \Phi_U}{\delta + \Phi(\boldsymbol{\chi}, s)}\right) + h(\Phi(\boldsymbol{\chi}, s))\right).$$

Now, assume that $\Phi(\boldsymbol{\chi}(t_0), s(t_0)) \geq \Phi_U$. This gives

$$h(\Phi(\boldsymbol{\chi}, s)) = 0, \qquad \frac{\delta + \Phi_U}{\delta + \Phi(\boldsymbol{\chi}(t_0), s(t_0))} \leq 1,$$

$$\frac{\frac{\partial \Phi(\boldsymbol{\chi}(t_0), s(t_0))}{\partial s}}{\left(\delta + \left|\frac{\partial \Phi(\boldsymbol{\chi}(t_0), s(t_0))}{\partial s}\right|\right)} \leq 1,$$

and $((\partial \Phi / \partial \boldsymbol{\chi})^T \dot{\boldsymbol{\chi}})(t_0) \leq 0$. Thus

$$\dot{\Phi} \leq \left(\frac{\partial \Phi}{\partial \boldsymbol{\chi}}\right)^T \dot{\boldsymbol{\chi}} + \left(\frac{-\left(\frac{\partial \Phi}{\partial \boldsymbol{\chi}}\right)^T \dot{\boldsymbol{\chi}}}{1} 1 + 0\right) = 0.$$

Therefore, if $\Phi(\boldsymbol{\chi}, s) \geq \Phi_U$ then $\dot{\Phi}(\boldsymbol{\chi}, s) \leq 0$ along trajectories in both cases. Thus $\Phi(\boldsymbol{\chi}(t), s(t)) \leq \Phi_U$ for all $t \geq t_0$ if $\Phi(\boldsymbol{\chi}(t_0), s(t_0)) \leq \Phi_U$.

Asymptotic Stability Let the extended state of the system be $(\boldsymbol{\chi}, s) \in \mathbb{R}^n$, $n = 6N + 1$, and

$$\begin{aligned} \Omega_c &= \{(\boldsymbol{\chi}, s) \in \mathbb{R}^n : s \in [s_s, s_f], \Phi(\boldsymbol{\chi}, s) \leq \Phi_U\} \\ S &= \{(\boldsymbol{\chi}, s) \in \Omega_c : \dot{s} = 0\}. \end{aligned}$$

Since $\dot{s} \geq 0$ and $s \in [s_s, s_f]$, the limit $s_0 = \lim_{t\to\infty} s(t)$ exists. By the boundedness property of Φ above, Ω_c is invariant and bounded. Thus, on Ω_c the ω-limit set L exists, is invariant and $(\boldsymbol{\chi}, s) \to L \subset \Omega_c$. For $(\boldsymbol{\chi}_L, s_L) \in L$ we must have $s_L = s_0$ and therefore $L \subset S$. We will now show that $\{(\boldsymbol{\chi}_{eq}(s_f), s_f)\}$ is the largest invariant set in S and therefore $(\boldsymbol{\chi}, s) \to \{(\boldsymbol{\chi}_{eq}(s_f), s_f)\} = L$.

$\dot{s} = 0$ implies that $\Phi(\boldsymbol{\chi}, s)$ is a Lyapunov function with respect to $\boldsymbol{\chi}$ (since s is fixed). Thus, every trajectory candidate approaches $\boldsymbol{\chi}_{eq}(s)$, where $\Phi(\boldsymbol{\chi}_{eq}(s), s) = 0$. This implies (by the choice of $\dot{s}$ in (3.2.1) that $\dot{s} > 0$ (due to the h term, unless $s = s_f$ where the trajectory is completed and we let s halt). Therefore, $\{(\boldsymbol{\chi}_{eq}(s_f), s_f)\}$ is the only invariant set in S. Thus, $(\boldsymbol{\chi}, s) \to (\boldsymbol{\chi}_{eq}(s_f), s_f)$ and the system is asymptotically stable. ∎

Appendix B

Kalman Filter Derivation

The model for which we implement the Kalman filter is presented in (4.3.5) and reproduced here,

$$\begin{aligned} \boldsymbol{\xi}_k &= \tilde{A}_{k-1}\boldsymbol{\xi}_{k-1} + \boldsymbol{w}_{k-1} \\ \boldsymbol{y}_k &= \tilde{H}_k\boldsymbol{\xi}_k + \boldsymbol{\epsilon}_{\boldsymbol{M}k} \end{aligned}$$

with

$$\begin{aligned} E[\boldsymbol{w}_k\boldsymbol{w}_j^T] &= \begin{pmatrix} Q_k & 0 \\ 0 & U_k \end{pmatrix}\delta_{kj} = \Theta_k\delta_{kj} \\ E[\boldsymbol{\epsilon}_{\boldsymbol{M}k}\boldsymbol{\epsilon}_{\boldsymbol{M}j}^T] &= R_k\delta_{kj} \\ E[\boldsymbol{w}_k\boldsymbol{\epsilon}_{\boldsymbol{M}k}^T] &= 0 \end{aligned}$$

At the kth instant define the pre-update state estimate as $\boldsymbol{\xi}_{\text{est}k}^-$ and the post-update state estimate $\boldsymbol{\xi}_{\text{est}k}^+$. These are given by

$$\begin{aligned} \boldsymbol{\xi}_{\text{est}k}^- &= \tilde{A}_k\boldsymbol{\xi}_{\text{est}k-1}^+ \\ \boldsymbol{\xi}_{\text{est}k}^+ &= \boldsymbol{\xi}_{\text{est}k}^- + K_k(\boldsymbol{y}_k - \tilde{H}_k\boldsymbol{\xi}_{\text{est}k}^-) \end{aligned}$$

where K_k is the filter gain to be determined.

Now, define the pre-update error, $\boldsymbol{e}_k^-$, and post-update error, $\boldsymbol{e}_k^+$ as

$$\begin{aligned}\boldsymbol{e}_k^- &= \boldsymbol{\xi}_k - \boldsymbol{\xi}_{\text{est}k}^- \\ \boldsymbol{e}_k^+ &= \boldsymbol{\xi}_k - \boldsymbol{\xi}_{\text{est}k}^+.\end{aligned}$$

Expanding we find,

$$\begin{aligned}\boldsymbol{e}_k^- &= \tilde{A}_{k-1}\boldsymbol{\xi}_{k-1} + \boldsymbol{w}_{k-1} - \tilde{A}_{k-1}\boldsymbol{\xi}_{\text{est}k-1}^+ \\ &= \tilde{A}_{k-1}\boldsymbol{e}_{k-1}^+ + \boldsymbol{w}_{k-1}, \\ \boldsymbol{e}_k^+ &= \tilde{A}_{k-1}\boldsymbol{\xi}_{k-1} + \boldsymbol{w}_{k-1} - \tilde{A}_{k-1}\boldsymbol{\xi}_{\text{est}k-1}^+ - K_k(\boldsymbol{y}_k - \tilde{H}_k\boldsymbol{\xi}_{\text{est}k}^-) \\ &= \boldsymbol{e}_k^- - K_k(\tilde{H}_k\boldsymbol{\xi}_k + \boldsymbol{\epsilon}_{\boldsymbol{M}k} - \tilde{H}_k\boldsymbol{\xi}_{\text{est}k}^-) \\ &= \boldsymbol{e}_k^- - K_k(\tilde{H}_k\boldsymbol{e}_k^- + \boldsymbol{\epsilon}_{\boldsymbol{M}k}).\end{aligned}$$

Thus, we have

$$\begin{aligned}\boldsymbol{e}_k^- &= \tilde{A}_{k-1}\boldsymbol{e}_{k-1}^+ + \boldsymbol{w}_{k-1}, \\ \boldsymbol{e}_k^+ &= \boldsymbol{e}_k^- - K_k(\tilde{H}_k\boldsymbol{e}_k^- + \boldsymbol{\epsilon}_{\boldsymbol{M}k}).\end{aligned}$$

Now define the pre-update error covariance matrix as,

$$\begin{aligned}P_k^- = E[\boldsymbol{e}_k^-\boldsymbol{e}_k^{-T}] &= E[(\tilde{A}_{k-1}\boldsymbol{e}_{k-1}^+ + \boldsymbol{w}_{k-1})(\boldsymbol{e}_{k-1}^{+T}\tilde{A}_{k-1}^T + \boldsymbol{w}_{k-1}^T)] \\ &= \tilde{A}_{k-1}E[\boldsymbol{e}_{k-1}^+\boldsymbol{e}_{k-1}^{+T}]\tilde{A}_{k-1}^T + E[\boldsymbol{w}_{k-1}\boldsymbol{w}_{k-1}^T] \\ &= \tilde{A}_{k-1}P_{k-1}^+\tilde{A}_{k-1}^T + \Theta_{k-1}\end{aligned}$$

$$
\begin{aligned}
P_k^+ &= E[\boldsymbol{e}_k^+ \boldsymbol{e}_k^{+T}] \\
&= E\left[\left(\boldsymbol{e}_k^- - K_k(\tilde{H}_k \boldsymbol{e}_k^- + \boldsymbol{\epsilon_M}_k)\right)\left(\boldsymbol{e}_k^{-T} - (\boldsymbol{e}_k^{-T}\tilde{H}_k^T + \boldsymbol{\epsilon_M}_k^T)K_k^T\right)\right] \\
&= P_k^- - P_k^-\tilde{H}_k^T K_k^T - E[\boldsymbol{e}_k^- \boldsymbol{\epsilon_M}_k^T]K_k^T - K_k\tilde{H}_k P_k^- - K_k E[\boldsymbol{\epsilon_M}_k \boldsymbol{e}_k^{-T}] + K_k\tilde{H}_k P_k^-\tilde{H}_k^T K_k^T \\
&\quad + K_k\tilde{H}_k E[\boldsymbol{e}_k^- \boldsymbol{\epsilon_M}_k^T]K_k^T + K_k E[\boldsymbol{\epsilon_M}_k \boldsymbol{e}_k^{-T}]\tilde{H}_k^T K_k^T + K_k E[\boldsymbol{\epsilon_M}_k \boldsymbol{\epsilon_M}_k^T]K_k^T \\
&= P_k^- - P_k^-\tilde{H}_k^T K_k^T - K_k\tilde{H}_k P_k^- + K_k\tilde{H}_k P_k^-\tilde{H}_k^T K_k^T + K_k R_k K_k^T \\
&= (I - K_k\tilde{H}_k)P_k^-(I - K_k\tilde{H}_k)^T + K_k R_k K_k^T
\end{aligned}
$$

The optimal K_k minimizes $J_k = \mathrm{Tr}(P_k^+)$, where

$$J_k = \mathrm{Tr}(P_k^+) = \mathrm{Tr}(P_k^-) - \mathrm{Tr}(P_k^-\tilde{H}_k^T K_k^T) - \mathrm{Tr}(K_k\tilde{H}_k P_k^-) + \mathrm{Tr}(K_k\tilde{H}_k P_k^-\tilde{H}_k^T K_k^T) + \mathrm{Tr}(K_k R_k K_k^T).$$

Noting that for symmetric B, $\frac{\partial}{\partial A}\mathrm{Tr}(ABA^T) = 2AB$ and $\frac{\partial}{\partial A}\mathrm{Tr}(AB^T) = B$, taking $\frac{\partial J_k}{\partial K_k}$ and equating to zero we find

$$\frac{\partial J_k}{\partial K_k} = -P_k^-\tilde{H}_k^T + K_k\tilde{H}_k P_k^-\tilde{H}_k^T + K_k R_k = 0$$

which yields the optimal gain $K_k = K_k^*$, where

$$K_k^* = P_k^-\tilde{H}_k^T(\tilde{H}_k P_k^-\tilde{H}_k^T + R_k)^{-1}.$$

Lastly, we can substitute the pre-update variables into the post-update expressions to yield

$$
\begin{aligned}
\boldsymbol{\xi}_{\mathrm{est}\boldsymbol{k}} &= \tilde{A}_{k-1}\boldsymbol{\xi}_{\mathrm{est}k-1} + K_k(\boldsymbol{y}_k - \tilde{H}_k\tilde{A}_{k-1}\boldsymbol{\xi}_{\mathrm{est}k-1}), \\
K_k^* &= (\tilde{A}_{k-1}P_{k-1}\tilde{A}_{k-1}^T + \Theta_{k-1})\tilde{H}_k^T\left(\tilde{H}_k(\tilde{A}_{k-1}P_{k-1}\tilde{A}_{k-1}^T + \Theta_{k-1})\tilde{H}_k^T + R_k\right)^{-1}, \\
P_k &= (1 - K_k\tilde{H}_k)(\tilde{A}_{k-1}P_{k-1}\tilde{A}_{k-1}^T + \Theta_{k-1})(I - K_k\tilde{H}_k)^T + K_k R_k K_k^T.
\end{aligned}
$$

Appendix C

Glider Simulator Details

In this appendix we describe a glider simulator utilized in the AOSN II simulation experiment presented in Section 5.4. A component of this simulator was also used in the *Glider Simulator* component of the AOSN II VBAP implementation (see Figure 5.3.1). The goal of this simulator was to incorporate the operational behaviors, constraints and communication latencies of the gliders as much as possible. This simulator was designed with the assistance of Pradeep Bhatta at Princeton University.

The glider simulator consists of two modules -

- *Module 1* : Glider in Water - to simulate glider motion during a dive
- *Module 2* : Glider at Surface - to simulate glider motion (drift) when it is at the surface and to update the onboard flow estimate.

C.1 Glider in Water

While in water the gliders are simulated to move at a horizontal speed of 40 cm/s, and a nominal vertical speed of 20 cm/s relative to water, consistent with the assumptions

made in Section 5.2.1. When utilized as part of the *Glider Simulator* (see Figure 5.3.1) the horizontal velocity is added to the *estimated* local horizontal flow velocity, which is provided by each glider at its previous surfacing, to compute the total absolute horizontal velocity of the glider. When this module is used for simulation only, e.g. see Section 5.4, the local horizontal flow velocity is acquired from the ICON data set. Vertical current velocities are not utilized. During the simulations of Section 5.4 a zero-mean white noise is added to the vertical velocity to account for the vertical component of the true local flow field.

The gliders are commanded to start surfacing 2 hours after they dove into the water. Since the glider could be at any depth between the minimum and maximum yo depth limits[1] when it starts surfacing, the total time of implementation of the 'glider in water' module will in general be a little over 2 hours during every cycle.

The glider has a constant estimate of the local flow velocity, which is updated every time it surfaces and obtains a GPS fix. To calculate its absolute velocity the glider adds the local flow velocity estimate to its relative velocity (i.e., relative to water). The relative velocity is computed using the heading measurement, and the assumptions regarding the horizontal and vertical speeds. For the simulations of Section 5.4, a white noise with a nonzero bias is added to the actual heading to simulate the heading sensor. The bias itself is randomly chosen at the start of every dive cycle.

While in the water the glider servos its heading so that it tries to move towards the next waypoint. A three-dimensional, black-box model is used to simulate the experimentally observed input-output relation between the tailfin position (input) and the heading (output). The proportional servo controller is turned off whenever the measured heading is within a fixed deadband (± 0.02 rad) of the continuously changing desired heading.

[1] 0-100 m during AOSN II and 0-200m during the simulations of Section 5.4.

A waypoint is considered reached if the horizontal distance from the waypoint is less than 25 m.

C.2 Glider at Surface

This module was only used during the simulations discussed in Section 5.4 and not as part of the Glider Simulator in the AOSN II VBAP implementation.

The glider is set to drift with the flow when it is on the surface. As described in Section 5.1, the glider does not get a GPS fix immediately after it surfaces. We assume that the first GPS fix is obtained $t_1 = 2$ minutes after surfacing.

We assume that the glider uses a nominal time of $t_2 = 17$ minutes for exchanging data collected during the previous dive. We add a zero mean white noise with an amplitude of 2 minutes to t_2 to account for possible communication problems. During this time the glider also gets several GPS fixes. We use the first and the last GPS fix, and the glider's estimate of the local flow to calculate the actual position of its surfacing.

The glider corrects its flow estimate by comparing the dead reckoned and actual positions of surfacing. The corrected flow estimate is used in the computation of dead reckoned positions during the next dive.

During the data exchange the glider also gets an updated set of waypoints. The glider prepares to dive after the data exchange is completed.

We assume that the glider gets its last GPS fix at the end of data exchange and that it is at the surface for another minute before diving. Thus the total nominal time the glider spends at the surface is 2+17+1=20 minutes.

Appendix D

Virtual Body Steering for Cross Track Error Reduction

In this appendix we present the steering control used during the August 16, 2003 experiment to direct the virtual body. The steering law is devised to direct the virtual body towards the destination waypoints but also to steer the virtual body onto a particular path. In Figure D.1 the dash-dotted line segments comprise the desired virtual body trajectory which is denoted by Γ'. The solid dots at the end points of each segment are the destination waypoints. In the example illustrated in the figure the virtual body is to be directed towards the destination waypoint at $\boldsymbol{b'} \in \mathbb{R}^2$ having already visited the destination waypoint at $\boldsymbol{a'} \in \mathbb{R}^2$. $\boldsymbol{r} \in \mathbb{R}^2$ is the instantaneous position vector of the virtual body center and $\boldsymbol{r_w} = \boldsymbol{b'} - \boldsymbol{r}$. The point $\boldsymbol{p'} \in \mathbb{R}^2$ is defined to be the closest point to $\boldsymbol{r}$ on the line segment with endpoints $\boldsymbol{a'}$ and $\boldsymbol{b'}$. That is,

$$\boldsymbol{p'} = \arg \min_{\tilde{\boldsymbol{p}} \in \Gamma'} \|\boldsymbol{e}\|$$

where $\boldsymbol{e} = \boldsymbol{r} - \tilde{\boldsymbol{p}}$ and $\boldsymbol{e}_{\text{xte}}$ is the cross track error vector given by

$$\boldsymbol{e}_{\text{xte}} = \boldsymbol{r} - \boldsymbol{p'}.$$

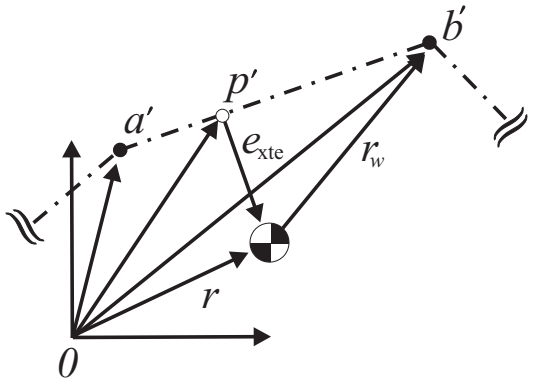

Figure D.1: **Cross Track Error Diagram.** Axes and origin 0 denote inertial frame. Cross track error vector is denoted $\boldsymbol{e}_{\text{xte}}$.

Recall the virtual body heading direction is denoted $\frac{d\boldsymbol{r}}{ds}$. During the August 16, 2003 experiment, prior to being adjusted for the external currents (see Section 5.2.2), the heading was selected as

$$\frac{d\boldsymbol{r}}{ds} = (1 - w_{\text{xte}})\boldsymbol{r_w} - w_{\text{xte}}\boldsymbol{e}_{\text{xte}},$$

where the weight $w_{\text{xte}} \in [0, 1]$. w_{xte} weights the influence of the cross track error vector, $\boldsymbol{e}_{\text{xte}}$, as compared to the destination waypoint vector, $\boldsymbol{r_w}$.

We derive the cross track error vector by noting that

$$\boldsymbol{p'} = \boldsymbol{a'} + m(\boldsymbol{b'} - \boldsymbol{a'})$$

where $m \in [0, 1]$. For $m = 0$, $\boldsymbol{p'} = \boldsymbol{a}$ and for $m = 1, \boldsymbol{p'} = \boldsymbol{b'}$. We can exclude one of these cases by comparing the magnitude of $\boldsymbol{e}_{\text{xte}}$ for these cases. First, let $\boldsymbol{e}'_{\text{xte}} = \min\{\boldsymbol{r} - \boldsymbol{a'}, \boldsymbol{r} - \boldsymbol{b'}\}$. Next we check if $\boldsymbol{p'}$ lies along the line between (but not including) $\boldsymbol{a'}$ and $\boldsymbol{b'}$ by noting that

in this case $\boldsymbol{e}_{\text{xte}}$ is perpendicular to $\boldsymbol{b'} - \boldsymbol{a'}$, i.e.

$$\langle \boldsymbol{e}_{\text{xte}}, \boldsymbol{b'} - \boldsymbol{a'} \rangle = 0.$$

By substitution we have,

$$\begin{aligned} \langle \boldsymbol{r} - \boldsymbol{p'}, \boldsymbol{b'} - \boldsymbol{a'} \rangle &= \langle \boldsymbol{r} - \boldsymbol{a'} - m(\boldsymbol{b'} - \boldsymbol{a'}), \boldsymbol{b'} - \boldsymbol{a'} \rangle \\ &= \langle \boldsymbol{r} - \boldsymbol{a'}, \boldsymbol{b'} - \boldsymbol{a'} \rangle - m\|\boldsymbol{b'} - \boldsymbol{a'}\|^2 = 0. \end{aligned}$$

Therefore,

$$m = \frac{\langle \boldsymbol{r} - \boldsymbol{a'}, \boldsymbol{b'} - \boldsymbol{a'} \rangle}{\|\boldsymbol{b'} - \boldsymbol{a'}\|^2}.$$

If $m \notin (0, 1)$ then it follows that

$$\boldsymbol{e}_{\text{xte}} = \boldsymbol{e'}_{\text{xte}},$$

otherwise, $\boldsymbol{p'}$ lies along Γ' (excluding the endpoints) and the cross track error vector is given by

$$\boldsymbol{e}_{\text{xte}} = \boldsymbol{r} - \boldsymbol{a'} - \frac{\langle \boldsymbol{r} - \boldsymbol{a'}, \boldsymbol{b'} - \boldsymbol{a'} \rangle}{\|\boldsymbol{b'} - \boldsymbol{a'}\|^2}(\boldsymbol{b'} - \boldsymbol{a'}).$$

References

[1] Adaptive Sampling and Prediction (ASAP), collaborative MURI project. `http://www.princeton.edu/~dcsl/asap`.

[2] Autonomous Ocean Sampling Network II (AOSN II), collaborative project. `http://www.mbari.org/aosn/`.

[3] C.O. Alford and S.M. Belyeu. Coordinated control of two robot arms. In *Proc. of IEEE International Conference on Robotics and Automation*, volume 1, pages 468–473, 1984.

[4] D.M. Anderson. Toxic red tides and harmful algal blooms: A practical challenge in coastal oceanography. *Reviews of Geophysics, Supplement*, pages 1189–1200, 1995.

[5] R. Arkin and T. Balch. Cooperative multiagent robotic systems. In D. Kortenkamp, R.P. Bonasso, and R. Murphy, editors, *Artificial Intelligence and Mobile Robots*. MIT/AAAI Press, Cambridge, MA, 1998.

[6] P. Baccou, B. Jouvencel, V. Creuze, and C. Rabaud. Cooperative positioning and navigation for multiple AUV operations. In *Proc. of 2001 IEEE OCEANS Conf*, volume 3, pages 1816–1821, 2001.

[7] R. Bachmayer and N.E. Leonard. Experimental test-bed for multi-vehicle control, navigation and communication. In *Proc. 12th Int. Symposium on Unmanned Untethered Submersible Tech.*, Durham, NH, 2001.

[8] R. Bachmayer and N.E. Leonard. Vehicle networks for gradient descent in a sampled environment. In *Proc. 41st IEEE Conference on Decision and Control*, pages 113–117, 2002.

[9] T. Balch. Learning roles: Behavioral diversity in robot teams. *AAAI Workshop on Multiagent Learning*, 1997.

[10] T. Balch. Behavioral diversity in learning robot teams. *PhD Dissertation*, 1998. College of Computing, Georgia Institute of Technology.

[11] J. Barraquand, B. Langlois, and J. C. Latombe. Robot motion planning with many degrees of freedom and dynamic constraint. In *Proc. 5th Int. Symp. Robotics Research*, pages 74–83, August 1989.

[12] R. Beard and F.Y. Hadaegh. Constellation templates: An approach to autonomous formation flying. In *World Automation Congress*, pages 1771–1776, 1998.

[13] G.S. Begg and J.B. Reid. Spatial variation in seabird density at a shallow sea tidal mixing front in the Irish Sea. *Journal of Marine Science*, 54:552–565, 1997.

[14] A. Blumberg and G. L. Mellor. A description of a three-dimensional coastal ocean circulation model. *Am. Geophys. Un.*, 4:1–16, 1987.

[15] R. Bras and I. Rodriguez-Iturbe. *Random Functions and Hydrology.* Addison-Wesley Publishing Company, first edition, 1994.

[16] E. Burian, D. Yoerger, A. Bradley, and H. Singh. Gradient search with autonomous underwater vehicle using scalar measurements. *Proc. IEEE OES AUV Conf.*, pages 86–98, 1996.

[17] T. Clarke. Robot gliders to watch red tides. *Nature News Service / Macmillan Magazines Ltd*, January 2003.

[18] J. Cortés, S. Martínez, T. Karatas, and F. Bullo. Coverage control for mobile sensing networks: Variations on a theme. In *Proc. Mediterranean Conf. on Control and Automation*, 2002.

[19] I. Couzin, J. Krause, R. James, G. Ruxton, and R. Franks. Collective memory and spatial sorting in animal groups. *Journal of Theoretical Biology*, 2002.

[20] T. B. Curtin, J. G. Bellingham, J. Catipovic, and D. Webb. Autonomous oceanographic sampling networks. *Oceanography*, 6:86–94, 1989.

[21] P.J. Davis and P. Rabinowitz. *Methods of Numerical Integration*. Academic Press, Orlando, FL, 1984.

[22] R. Davis, J. Bellingham, P. Chandler, F. Chavez, N.E. Leonard, and A. Robinson. AOSN II system goals and performance metrics. `http://www.mbari.org/aosn/AOSNNewSite/Documents/AOSNIISystemGoalsandPerformanceMetrics.pdf`, 2003.

[23] J.P. Desai and V. Kumar. Nonholonomic motion planning for multiple mobile manipulators. *Proc. IEEE Int. Conf. Robotics and Automation*, 4:3409 – 3414, 1997.

[24] J.P. Desai, J. Ostrowski, and V. Kumar. Controlling formations of multiple mobile robots. In *Proc. IEEE Int. Conf. Robotics and Automation*, pages 2864–2869, May 1998.

[25] W.B. Dunbar and R.M. Murray. Distributed receding horizon control with application to multi-vehicle formation stabilization. 2004. Submitted to Automatica.

[26] M. Erdmann and T. Lazano-Perez. On multiple moving objects. In *Proc. of IEEE International Conference on Robotics and Automation*, volume 3, pages 1419–1424, 1986.

[27] T. Eren, P.N. Belhumeur, and S.A. Morse. Closing ranks in vehicle formations based on rigidity. In *Proc. 41th IEEE Conf. Decision and Control*, pages 2959–2964, 2002.

[28] C. C. Eriksen, T. J. Osse, T. Light, R. D. Wen, T. W. Lehmann, P. L. Sabin, J. W. Ballard, and A. M. Chiodi. Seaglider: A long range autonomous underwater vehicle for oceanographic research. *IEEE Journal of Oceanic Engineering*, 26(4):424–436, 2001. Special Issue on Autonomous Ocean-Sampling Networks.

[29] A. Fax and R.M. Murray. Graph Laplacians and vehicle formation stabilization. In *Proc. of the 15th IFAC World Congress*, 2002.

[30] R. Fierro, A.K. Das, V. Kumar, and J.P. Ostrowski. Hybrid control of formations of robots. In *Proc. of International Conf. on Robotics and Automation*, pages 157–162, 2001.

[31] E. Fiorelli, P. Bhatta, N.E. Leonard, and I. Shulman. Adaptive sampling using feedback control of an autonomous underwater glider fleet. In *Proc. of Symposium on Unmanned Utethered Submersible Technology*, 2003.

[32] E. Fiorelli, N.E. Leonard, P. Bhatta, D. Paley, R. Bachmayer, and D. Fratantoni. Multi-AUV control and adaptive sampling in Monterey Bay. In *Proceedings of IEEE AUV 2004 Workshop*, 2004. Under review for IEEE Journal of Oceanic Engineering, 2005.

[33] P. Franks and L. Walstad. Phytoplankton patches at fronts: a model of formation and response to wind events. *Journal of Marine Research*, 55(1), 1997.

[34] D.M. Fratantoni. Woods Hole Oceanographic Institution. Personal Communication, 2004.

[35] V. Gazi and K. Passino. Stability analysis of social foraging swarms. In *Proc. 41st IEEE Conf. Decision and Control*, pages 2848–2853, 2002.

[36] H. Goldstein. *Classical Mechanics*. Addison-Wesley, London, second edition, 1980.

[37] D. Grünbaum. Schooling as a strategy for taxis in a noisy environment. *Evol. Ecol.*, 12(5):503–522, 1998.

[38] B. Jouvencel, V. Creuze, and P. Baccou. A new method for multiple AUV coordination: a reactive approach. In *Proc. of International Conf. Emerging Technologies and Factory Automation*, volume 1, pages 51–55, 2001.

[39] E. Kalnay. *Atmospheric Modeling, Data Assimilation, and Predictability*. Cambridge Univeristy Press, first edition, 2003.

[40] H. Khalil. *Nonlinear Systems*. Prentice Hall, New Jersey, third edition, 2002.

[41] O. Khatib. Real time obstacle avoidance for manipulators and mobile robots. *Int. J. Robotics Research*, 5:90–99, 1986.

[42] O. Khatib, K. Yokoi, K. Chang, D. Ruspini, R Holmberg, A. Casal, and A. Baader. Force strategies for cooperative tasks in multiple mobile manipulation systems. *Int. Symp.of Robotics Research*, 1995.

[43] P. Khosla and R. Volpe. Superquadric artificial potentials for obstacle avoidance. In *Proc. IEEE International Conference on Robotics and Automation*, pages 1778–1784, April 1988.

[44] J.C. Kindle, R. Hodur, S. deRada, J. Paduan, L. K. Rosenfeld, and F. Chavez. A COAMPS reanalysis for the Eastern Pacific: Properties of the diurnal sea breeze along the central California coast. *Geophysical Research Letters*, 29(24), 2002.

[45] T. Krennert, R. Winkler, B. Zeiner, and V. Zwatz-Meise. *Manual of Synoptic Satellite Meterology*. Central Institute of Meteorology and Geomagnetism, fifth edition. `http://www.zamg.ac.at/docu/Manual/SatManu/main.htm`.

[46] J. Lawton, B. Young, and R. Beard. A decentralized approach to elementary formation maneuvers. *IEEE Trans. Robotics and Automation*, 19:933–941, 2003.

[47] J. Le Fevre. Aspects of the biology of frontal systems. *Advances in Marine Biology*, 23:163–299, 1986.

[48] F. Lekien, R. Davis, and N.E. Leonard. Generator for inhomogeneous analytical covariance functions and application to adaptive sampling. `http://www.lekien.com/~francois/presentations#2005-07-12`.

[49] F. Lekien and E. Fiorelli. Multi-vehicle control and front tracking. `http://www.lekien.com/~francois/presentations#2004-03-22`.

[50] F. Lekien, D. Paley, and N.E. Leonard. Stability and robustness of sampling arrays subject to intermittent feedback. In preparation, Princeton University, 2005.

[51] N.E. Leonard and E. Fiorelli. Virtual leaders, artificial potentials and coordinated control of groups. In *Proc. 40th IEEE Conf. Decision and Control*, pages 2968–2973, 2001.

[52] N.E. Leonard, D. Paley, F. Lekien, R. Sepulchre, and D.M. Fratantoni. Collective motion, sensor networks, and ocean sampling. Submitted to the *Proceedings of the IEEE* (2005).

[53] W. S. Levine and M. Athans. On the optimal error regulation of a string of moving vehicles. *IEEE Trans. Automatic Control*, 11:355–361, 1966.

[54] D. Marthaler and A.L. Bertozzi. Tracking environmental level sets with autonomous vehicles. In *Proc. Conf. Cooperative Control and Optimization*, 2003.

[55] M.J. Mataric. Group behavoir and group learning. In *Proc. of IEEE From Perception to Action Conference*, pages 326–329, 1994.

[56] C.R. McInnes. Potential function methods for autonomous spacecraft guidance and control. *Advances in Astronautical Sciences*, 90:2093–2109, 1996.

[57] S.M. Melzer and B.C. Kuo. A closed-form solution for the optimal error regulation of a string of moving vehicles. *IEEE Trans. Automatic Control*, 16:50–52, 1971.

[58] A. Mogilner, L. Edelstein-Keshet, L. Bent, and A. Spiros. Mutual interactions, potentials, and individual distance in a social aggregation. *Journal of Mathematical Biology*. In Press (2003).

[59] L. Moreau, R. Bachmayer, and N.E. Leonard. Coordinated gradient descent: A case study of Lagrangian dynamics with projected gradient information. In *2nd IFAC Workshop on Lagrangian and Hamiltonian Methods for Nonlinear Control*, 2003.

[60] W. S. Newman and N. Hogan. High speed robot control and obstacle avoidance using dynamic potential functions. In *Proc. IEEE Int. Conf. Robotics and Automation*, pages 14–24, 1987.

[61] P. Ögren. Formations and obstacle avoidance in mobile robot control. *PhD Dissertation*, 2003. Royal Institute of Technology, Sweden.

[62] P. Ögren, M. Egerstedt, and X. Hu. A control Lyapunov function approach to multiagent coordination. In *Proc. 40th IEEE Conf. Decision and Control*, pages 1150–1155, 2001.

[63] P. Ögren, M. Egerstedt, and X. Hu. A control Lyapunov function approach to multiagent coordination. *IEEE Trans. Robotics and Automation*, 18(5):847–851, 2002.

[64] P. Ögren, E. Fiorelli, and N. E. Leonard. Cooperative control of mobile sensor networks: Adaptive gradient climbing in a distributed environment. *IEEE Trans. Automatic Control*, 49(8), August 2004.

[65] P. Ögren, E. Fiorelli, and N.E. Leonard. Formations with a mission: Stable coordination of vehicle group maneuvers. In *Proc. Symposium of Mathematical Theory of Networks and Systems*, 2002.

[66] A. Okubo. Dynamical aspects of animal grouping: swarms, schools, flocks and herds. *Adv. Biophysics*, 22:1–94, 1986.

[67] R. Olfati-Saber and R.M. Murray. Distributed cooperative control of multiple vehicle formations using structural potential functions. In *The 15th IFAC World Congress*, 2002.

[68] R. Olfati-Saber and R.M. Murray. Graph rigidity and distributed formation stabilization of multi-vehicle systems. In *Proc. 41th IEEE Conf. Decision and Control*, 2002.

[69] J.K. Parrish, S.V. Viscido, and D. Grümbaun. Self-organized fish schools: An examination of emergent properties. *The Biological Bulletin*, 202:296–305, June 1 2002.

[70] J.D. Pearson. On controlling a string of moving vehicles. *IEEE Trans. Automatic Control*, 12:328–329, 1967.

[71] W. Press, S. Teukolsky, W. Vetterling, and B. Flannery. *Numerical Recipes in C*. Cambridge Univeristy Press, second edition, 2002.

[72] G. Ramanathan and S. Alagar. Algorithmic motion planning in robotics: Coordinated motion of several disks amidst polygonal obstacles. In *Proc. of IEEE International Conference on Robotics and Automation*, volume 2, 1985.

[73] J.H. Reif and H. Wang. Social potential fields: A distributed behavioral control for autonomous robots. *Robotics and Autonomous Systems*, 27:171–194, 1999.

[74] C. Reynolds. Flocks, herds, and schools: a distributed behavioral model. In *Proc. ACM SIGGRAPH*, 1987.

[75] E. Rimon and D. E. Koditschek. Exact robot navigation using artificial potential functions. *IEEE Transactions on Robotics and Automation*, pages 501–518, 1992.

[76] J. Roach and M. Boaz. Coordinating the motions of robot arms in a common workspace. In *Proc. of IEEE International Conference on Robotics and Automation*, volume 2, pages 494–499, 1985.

[77] C.W. Rowley. Princeton university. Personal Communication, 2003.

[78] D.L. Rudnick, R.E. Davis, C.C. Eriksen, D.M. Fratantoni, and M.J. Perry. Underwater gliders for ocean research. *Journal of the Marine Technology Society*, 38(1):48–59.

[79] B. Schultz, B. Hobson, M. Kemp, J. Meyer, R. Moody, H. Pinnix, and M. St. Clair. Multi-UUV missions using RANGER MicroUUVs. In *Proc. Unmanned Untethered Submersible Tech.*, 2003.

[80] J.T. Schwartz and M. Sharir. On the piano movers' problem: III. coordinating the motion of several independent bodies. *International Journal of Robotics Research*, 2:46–75, 1983.

[81] M. Serreze, A. Lynch, and M. Clark. The arctic frontal zone as seen in the NCEPN-CAR reanalysis. *Journal of Climate*, 14, 2000.

[82] J. Sherman, R. E. Davis, W. B. Owens, and J. Valdes. The autonomous underwater glider 'Spray'. *IEEE Journal of Oceanic Engineering*, 26(4):437–446, 2001. Special Issue on Autonomous Ocean-Sampling Networks.

[83] I. Shulman, C. R. Wu, J. K. Lewis, J. D. Paduan, L. K. Rosenfeld, J. C. Kindle, S. R. Ramp, and C.A. Collins. High resolution modeling and data assimilation in the Monterey Bay area. *Continental Shelf Research*, 22:1129–1151, 2002.

[84] I. Shulman, C. R. Wu, J. D. Paduan, J. K. Lewis, L. K. Rosenfeld, and S. R. Ramp. High frequency radar data assimilation in the Monterey Bay. In M. L. Spaulding, editor, *Estuarine and Coastal Modeling*, pages 434–446, 2001.

[85] T.R. Smith, H. Hanssmann, and N.E. Leonard. Orientation control of multiple underwater vehicles. In *Proc. 40th IEEE Conf. Decision and Control*, pages 4598–4603, 2001.

[86] R.F. Stengel. *Optimal Control and Estimation*. Dover Publications, first edition, 1994.

[87] G. Strang. *Linear Algebra and its Applications*. Brooks/Cole, Thomson Learning Inc., 1988.

[88] P. Tabuada, G.J. Pappas, and P. Lima. Feasible formations of multi-agent systems. In *Proc. American Control Conference*, pages 56–61, 2001.

[89] M.A. Tan, K.H.and Lewis. Virtual structures for high-precision cooperative mobile robotic control. In *Proc. International Conference on Intelligent Robots and Systems*, 1997.

[90] H. Tanner, A. Jadbabaie, and G.J. Pappas. Stable flocking of mobile agents, part I: Fixed topology. In *Proc. 42nd IEEE Conf. Decision and Control*, pages 2010 – 2015, 2003.

[91] H. Tanner, U.K. Kyriakopoulos, and N.J. Krikelis. Modeling of multiple mobile manipulators handling a common deformable object. *Journal of Robotic Systems*, 1998.

[92] MBARI MUSE Data Team. MOOS upper-water-column science experiment (MUSE). `http://www.mbari.org`, 2001.

[93] P. Tournassoud. A strategy for obstacle avoidance and its applications to multi-robot systems. In *Proc. of IEEE International Conference on Robotics and Automation*, volume 3, 1986.

[94] S. Uryasev. Derivatives of probability functions and some applications. *Annals of Operation Research*, 56:287–311, 1995.

[95] E. Van Marcke. *Random Fields: Analysis and Synthesis*. MIT Press, first edition, 1983.

[96] P.K.C. Wang. Interaction dynamics of multiple mobile robots with simple navigation strategies. *Journal of Robotic Systems*, 6:77—101, 1989.

[97] P.K.C. Wang. Navigation strategies for multiple autonomous mobile robots moving in formation. *Journal of Robotic Systems*, 8:177–195, 1991.

[98] C.W. Warren. Multiple robot path coordination using artificial potential fields. In *Proc. IEEE Int. Conf. Robotics and Automation*, pages 500–505, May 1990.

[99] D. C. Webb, P. J. Simonetti, and C.P. Jones. SLOCUM: An underwater glider propelled by environmental energy. *IEEE Journal of Oceanic Engineering*, 26(4):447–452, 2001. Special Issue on Autonomous Ocean-Sampling Networks.

[100] J.S. Willcox. Oceanographic surveys with autonomous vehicles: Performance metrics and survey design. *Masters of Science Dissertation*, 1998. MIT.

[101] B.J. Young, R.W. Beard, and J.M. Kelsey. A control scheme for improving multi-vehicle formation maneuvers. In *Proc. American Control Conf.*, pages 704–709, 2001.

[102] F. Zhang and N.E. Leonard. Generating contour plots using multiple sensor plots. In *Proc. of 2005 IEEE Swarm Intelligence Symposium*, pages 309–314, June 2005.